



**UNIVERSIDAD DE CONCEPCIÓN**  
**Dirección de Postgrado**  
**FACULTAD DE CIENCIAS NATURALES Y OCEANOGRÁFICAS**  
**Programa de Doctorado en Oceanografía**

**VARIACIONES EN LA PRODUCTIVIDAD Y EN LA  
INTENSIDAD DE LA CORRIENTE CIRCUMPOLAR  
ANTÁRTICA EN EL PASO DE DRAKE DURANTE LOS  
ÚLTIMOS 1.3 MILLONES DE AÑOS: IMPLICACIONES  
EN LA CIRCULACIÓN TERMOHALINA**

**(Changes in productivity and in the strength of the  
Antarctic Circumpolar Current through the Drake Passage  
over the past 1.3 million years, and its global implications  
on the meridional overturning circulation)**

Tesis presentada a la Facultad de Ciencias Naturales y Oceanográficas  
de la Universidad de Concepción para para optar al grado de Doctor en  
Oceanografía

POR: María H. Toyos Simón  
Profesor Guía: Carina B. Lange  
Depto de Oceanografía, Facultad de Ciencias Naturales y  
Oceanográficas  
Profesor Co-guía: Frank Lamy  
Alfred Wegener Institut, Bremerhaven, Alemania

Concepción, Chile 2021

© 2021 María H Toyos Simón

Se autoriza la reproducción total o parcial, con fines académicos, por cualquier medio o procedimiento, incluyendo la cita bibliográfica del documento.



Universidad de Concepción  
Dirección de Postgrado

La Tesis de “*Doctorado en Oceanografía*” titulada “*Variaciones en la productividad y en la intensidad de la Corriente Circumpolar Antártica en el Paso de Drake durante los últimos 1.3 millones de años: implicaciones en la circulación termohalina*”, de la Srta. “*María H. Toyos Simón*” y realizada bajo la Facultad de Ciencias Naturales y Oceanográficas, Universidad de Concepción, ha sido aprobada por la siguiente Comisión de Evaluación:

Dr. Carina B. Lange  
Profesor Guía  
Universidad de Concepción

---

Dr. Frank Lamy  
Profesor Co-guía  
Alfred Wegener Institut



---

Dr. Wolfgang Schneider  
Miembro Comité de Tesis  
Universidad de Concepción

---

Dr. Fabrice Lambert  
Evaluador Externo  
Pontífica, Universidad Católica de Chile

---

Dr. Pamela Hidalgo  
Directora  
Programas de Postgrados en Oceanografía  
Universidad de Concepción

---



A todas las mujeres científicas cuya actividad ha sido acallada en muchas ocasiones a lo largo de la historia. En particular, a Eunice Foote, por ser la primera científica en teorizar sobre el efecto invernadero allá por el año 1856.

## AGRADECIMIENTOS

Al finalizar este proyecto quisiera agradecer a todas las personas e instituciones que han hecho posible la realización de este proyecto de investigación.

El desarrollo de esta tesis doctoral ha sido posible gracias al apoyo de los centros IDEAL: Investigación Dinámica de Ecosistemas Marinos de Altas Latitudes (FONDAP-IDEAL 1500003), COPAS Sur-Austral (AFB170006), Alfred Wegener Institut (AWI) y Lamont-Doherty Earth Observatory. Mi manutención y gastos de matrícula corrieron a cargo de la beca REDOC, beca Conicyt de Doctorado Nacional (CONICYT-PCHA/Doctorado Nacional/2016-21160454) y de la Escuela de Postgrado de la Universidad de Concepción. Los congresos y pasantías en el extranjero han sido financiados a través de los beneficios complementarios de la Beca Conicyt de Doctorado Nacional, la beca Asistencia a eventos y cursos cortos convocatoria 2019 (N° folio 81190303) y Beca Red Cima REC para pasantías cortas en el extranjero 2018 (a través de los programas de Doctorado en Oceanografía y Doctorado MaReA de la Universidad de Concepción).

En primer lugar quisiera agradecer de manera especial a la Dra. Carina Lange por su excepcional dirección académica, por transmitirme sus conocimientos, por todo su apoyo, orientación, dedicación y paciencia infinita. Igualmente agradezco de forma especial al Dr. Frank Lamy por recibirme en Bremerhaven (Alemania), por su orientación y curiosidad, siendo un ejemplo de dedicación a la ciencia. Agradezco también al Dr. Wolfgang Schneider (miembro del comité), al Dr. Fabrice Lambert (evaluador externo) y a la Dra. Pamela Hidalgo (directora del Programa de Doctorado en Oceanografía) por su interés en este trabajo.

Agradezco a la Dra. Gisela Winckler por recibirme en la sección de geoquímica del Lamont-Doherty Earth Observatory (Nueva York), abrirme las puertas de su laboratorio y transmitir sus inestimables conocimientos siempre con una sonrisa. Quiero agradecer también a los otros co-autores de los trabajos científicos derivados de esta tesis, en especial al Dr. Lester Lembke-Jene, Dr. Helge Arz y Dra. Mariem Saavedra por su dedicación y las muchas horas de enriquecedoras discusiones científicas tanto en persona como en línea.

Muchas gracias a todos los miembros del laboratorio de Paleooceanografía (PALEO) de la Universidad de Concepción, Alejandro Ávila, Paola Cárdenas y Victor Acuña, además de los integrantes del laboratorio de Geoquímica Orgánica Marina (GOM), nuestro laboratorio “hermano”, en especial al Dr. Benjamin Srain y a Cristóbal Castillo, por todas las horas compartidas, el excelente ambiente de trabajo y los cafés. Agradezco también a mis compañeros de generación del Programa de Postgrado, así como a otros muchos compañeros del Departamento de Oceanografía por todos los momentos compartidos, especiales gracias van para Nicolás Mayorga, Dra. Ainoha Bernal, María Lorena González, Dra. Odette Vergara, Eliana Velasco, Eduardo Emiliano Navarro, Dra. Liliana Espinosa, Dra. Bibiana Jara, Sofía Martínez y Carlos Cantergiani. Deseo expresar también mi gratitud a Fabiola Gaete, secretaria del

Programa de Postgrado en Oceanografía, así como también a Pedro Mario Torres por todas las gestiones y ayuda.

Esta tesis no habría sido posible sin las estancias en la Sección de Geología Marina del AWI (dirigida por el Dr. Ralf Tiedemann) y en la Sección de Geoquímica del Lamont-Doherty Earth Observatory. Por lo tanto, quiero agradecer a todos los responsables que me brindaron la oportunidad de tener un espacio en ambos institutos, al personal técnico e investigador que me ayudó y guió en el tratamiento de muestras, en especial a Susanne Wieve (AWI), Rita Fröhlking (AWI), Valea Schumacher (AWI), Roseanne Schwarz (Lamont) y al Dr. Martin Q. Fleisher (Lamont), además de a los compañeros y amigos de vivencias en ambos institutos.

Me gustaría agradecer también a los grandes amigos chilenos y españoles que han aparecido durante esta etapa de mi vida y que ya son mi familia Penquista. Muchas gracias a Paula Friz, Grisnery Jerez, Dr. Adrian Garrido, Cristian Vera, Luis Petersen, Cristóbal Gatica, Juan Oliva, Dr. Ramón Díaz Noriega, Dr. Roberto Gómez Espina, Dra. Delia Rodríguez Oroz, Gabriela Farias, Claudio Catalan, Carlos Romero y a mis compañeros de vivencias del “Torreón”.

Muchas gracias a Hodei Muñoz, Danann Pacheco y Lucía Corripio, ya que sus palabras fueron el empujón que hicieron que no renunciase. Parafraseando a una conocidísima banda de rock “*It’s a long way to the top*”, especialmente siendo mujer en un mundo en el que la conciliación e igualdad de oportunidades son todavía una utopía.

Por último, quiero agradecer a mi familia por confiar en mí y apoyarme siempre en todas las decisiones que he tomado a lo largo de mi vida, en especial a mi compañero de vida, Dr. Henrik Sadatzki, y a mi hija Deva por su sonrisa pura y sincera.

## ***Curriculum Vitae***

María H. Toyos Simón

Nacida el 7 de agosto, 1988, en Villaviciosa, Asturias, España

**2006–2012:** Licenciatura en Geología, Universidad de Oviedo, España. Premio fin de carrera 2012 al mejor expediente académico.

**2012–2014:** Máster en Geología Ambiental y Recursos Geológicos (Especialidad cuencas sedimentarias y recursos energéticos). Universidad Complutense de Madrid, España.

**2015–2021:** Doctor en Oceanografía, Universidad de Concepción, Chile.

### **PUBLICACIONES**

**Toyos, M. H.,** Medialdea, T., León, R., Somoza, L., González, F. J., & Meléndez, N. (2016). Evidence of episodic long-lived eruptions in the Yuma, Ginsburg, Jesús Baraza and Tasyo mud volcanoes, Gulf of Cádiz. *Geo-Marine Letters*, 36 (3), 197–214. <https://doi.org/10.1007/s00367-016-0440-z>

**Toyos, M. H.,** Lamy, F., Lange, C. B., Lembke-Jene, L., Saavedra-Pellitero, M., Esper, O., & Arz, H. W. (2020). Antarctic Circumpolar Current Dynamics at the Pacific Entrance to the Drake Passage Over the Past 1.3 Million Years. *Paleoceanography and Paleoclimatology*, 35 (7), 1–20. <https://doi.org/10.1029/2019PA003773>

**Toyos, M. H.,** Winckler, G., Arz, H.W., Lembke-Jene, L., Lange, C.B., Kuhn, G., Lamy, F. (2021). Variations in export production, lithogenic sediment transport and iron fertilization in the Pacific sector of the Drake Passage over the past 400 ka. *Clim. Past Discuss.* (preprint), <https://doi.org/10.5194/cp-2021-85>, accepted.

**Toyos, M. H.,** Lamy, F., Lange, C.B., Arz, H.W., Lembke-Jene, L., Winckler, G. 1.34 Ma productivity reconstruction at the Subantarctic Drake Passage entrance determined from mass accumulation rates corrected for syndepositional redistribution of sediments. Manuscrito en preparación para *Paleoceanography and Paleoclimatology*.

### **ÁREAS DE INVESTIGACIÓN**

Principal: Oceanografía Geológica

Secundaria: Paleoceanografía

Otras: Cuencas sedimentarias

## **EXPERIENCIA DOCENTE Y DE DIVULGACIÓN**

**Semestre II 2016:** Ayudante Asignatura Fundamentos de la Investigación Científica. Carrera Biología Marina, Universidad de Concepción, Chile.

**Febrero 2021:** Ponencia “Geología Marina como herramienta para el estudio del cambio climático”. American Association of Petroleum Geologist, AAPG Student Chapter.

**Julio 2021:** Co-fundador y miembro de la junta directiva de la Asociación de Divulgación Científica “Villaviciosa ConCiencia”. (Registro de Asociaciones del Principado de Asturias-España).

## **CRUCEROS OCEANOGRÁFICOS**

**2014.** Crucero Oceanográfico SUBVENT-02 a bordo del Buque Oceanográfico Sarmiento de Gamboa. Organismos participantes: Instituto geológico y minero de España, Instituto español de oceanografía y Universidad de Cádiz. España.

## **ESTADÍAS DE INVESTIGACIÓN**

**Julio – Octubre 2011.** Internship en EGI (Energy and Geoscience Institute), Bratislava (Eslovaquia), con el Dr. Cameron R. Sheya.

**Septiembre 2013 – Agosto 2014.** Estadía de Investigación en la Sección de Geología Marina del Instituto Geológico y Minero de España, Madrid (España), con el Dr. Ricardo León y la Dr. Teresa Medialdea.

**Mayo – Noviembre 2017.** Pasantía en la Sección de Geología Marina del Alfred-Wegener-Institut (AWI), Bremerhaven (Alemania). Beca Conicyt-PCHA (Doctorado Nacional/2016-21160454). Avance Tesis Doctoral con el Dr. Frank Lamy.

**Junio – Agosto 2018.** Pasantía en la Sección de Geoquímica del Lamont-Doherty Earth Observatory of Columbia University (LDEO), Nueva York (Estados Unidos). Beca “Red Clima Rec” pasantías cortas en el extranjero para tesis y ayuda de estipendio por parte del Centro FONDAP-IDEAL (1500003). Avance Tesis Doctoral con la Dr. Gisela Winckler.

**Septiembre 2018 – Enero 2019.** Pasantía en la Sección de Geología Marina del Alfred-Wegener-Institut (AWI), Bremerhaven (Alemania). Beca Conicyt-PCHA (Doctorado Nacional/2016-21160454). Avance Tesis Doctoral con el Dr. Frank Lamy.



## Tabla de contenidos

Índice de tablas.....	xii
Índice de figuras.....	xiv
Resumen.....	xxv
Abstract.....	xxix
1. INTRODUCTION/INTRODUCCIÓN .....	1
1.1. The Southern Ocean and the Antarctic Circumpolar Current, an overview .....	1
1.2. Oceanography and geomorphological features of the Drake Passage .....	8
1.3. Changes in the intensity of the ACC and SO export production through time .....	14
1.4. Orbital configuration of the Earth over the past 1.3 Ma. ....	17
1.5. Motivation of this study .....	20
2. HYPOTHESES AND OBJECTIVES/ HIPÓTESIS Y OBJETIVOS .....	23
2.1. Hypotheses .....	23
2.2. Objectives .....	24
3. MATERIAL AND METHODS/ MATERIALES Y MÉTODOS .....	28
3.1. Sediment core material .....	29
3.2. XRF core scanning .....	30
3.3. Geochemistry and bulk sediment parameter .....	31
3.4. Age model .....	35
3.5. Grain size measurements .....	37
3.5.1. Principles of Sortable Silt as a paleoflow-speed proxy .....	37
3.5.2. Sample preparation and sortable silt measurements .....	39
3.5.3. Zr/Rb ratio as a current speed proxy .....	40
3.6. Thorium isotopes analyses .....	41
3.6.1. Principles of mass accumulation rates reconstructions by Thorium normalization .....	41
3.6.2. U/Th isotope measurements .....	44
3.6.3. Mass accumulation rate calculations .....	44

3.6.3. Calculation of focusing factor ( $\Psi$ )	45
3.7. Lithogenic content	47
4. RESULTS/ RESULTADOS	49
4.1. Chapter 1/Capítulo 1: Manuscript 1 (published): Antarctic Circumpolar Current dynamics at the Pacific entrance to the Drake Passage over the past 1.3 million years.	49
4.2. Chapter 2/ Capítulo 2: Manuscript 2 (accepted): Variations in export production, lithogenic sediment transport and iron fertilization in the Pacific sector of the Drake Passage over the past 400 ka	77
4.3. Chapter 3/ Capítulo: Manuscript 3 (in preparation): 1.4 Ma productivity reconstruction at the Pacific entrance of the Drake Passage determined from mass accumulation rates corrected for syndepositional redistribution of sediments	123
5. DISCUSSION/ DISCUSIÓN	154
5.1. Glacial-Interglacial changes in ACC flow strength and its global implications	154
5.2. Sedimentation patterns related to near-bottom current speeds.	159
5.3. Glacial-Interglacial productivity pattern based on $^{230}\text{Th}_{\text{xs}}$ -normalized mass accumulation rates	162
5.3.1. Role of Fe as a driver of export production	164
5.3.2. Impact of frontal shifts and $\text{Si(OH)}_4$ availability on the export production patterns	166
5.4. Orbital scale fluctuation in current strength and productivity over the past 1.3 Ma.	168
5.4.1. Changes across the Mid-Pleistocene Transition in the Drake Passage	168
5.4.2. Ocean circulation and productivity during the 100-Kyr world and the Mid-Brunhes event	172
6. GENERAL CONCLUSIONS/ CONCLUSIONES GENERALES	175
7. PERSPECTIVES/ PERSPECTIVAS PARA FUTURAS INVESTIGACIONES	179

8. REFERENCES/REFERENCIAS .....	182
9. APPENDICES/ANEXOS .....	205
A.1. Core photos .....	205
A.2. Onboard core description .....	207
A.3. Onboard physical properties .....	211



## Índice de Tablas

### **Manuscript 1 (published): Antarctic Circumpolar Current dynamics at the Pacific entrance to the Drake Passage over the past 1.3 million years**

Table 1 Summary of biostratigraphic markers of calcareous nannofossils and diatoms used to build the preliminary Age Model of Core PS97/093-2. ....57

Table S1 Core PS97/093-2 calcareous nannofossils biostratigraphic markers and taxonomical notes. ....73

Table S2 Microfossil abundance (mainly diatoms), diatom taxa and preservation in core PS97/093-2. ....74

Table S3 Tie-points used for the age model of core PS97/093-2. See main text for details. ....75

### **Manuscript 2 (accepted): Variations in export production, lithogenic sediment transport and iron fertilization in the Pacific sector of the Drake Passage over the past 400 ka**

Table 1 Comparison between the average MAR and BMARs for the intervals with high (0–15 kyr, 324–334 kyr) and low (212–243 kyr, 243–279 kyr ) focusing factors. ....93

Table S1 Correlation matrix between <sup>230</sup>Th-normalized MARs of export production proxies and lithogenic indicators for core PS97/093-2. ....119

### **Manuscript 3 (in preparation): 1.4 Ma productivity reconstruction at the Pacific entrance of the Drake Passage determined from mass accumulation rates corrected for syndepositional redistribution of sediments**

Table 1 Comparison between the statistical parameters of the correlations between the accumulation rates (g/cm<sup>2</sup>/kyr) MAR (<sup>230</sup>Th-based) from Toyos et al. (accepted), BMAR (stratigraphy-based) from Toyos et al. (accepted), and BMAR-corr

(stratigraphy-based corrected by syndepositional redistribution, this study). BMAR were calculated multiplying the dry bulk density ( $\text{g/cm}^3$ ) by the sedimentation rates ( $\text{cm/kyr}$ ), and BMAR-corr were obtained dividing the BMAR by the focusing factor.  
.....142



## Índice de Figuras

**Figure 1.1** Main oceanographic and bathymetric elements of the Southern Ocean. White arrows illustrate the eastward flow of the ACC around Antarctica. White and purple lines indicate the ACC oceanographic fronts and boundaries (Orsi et al., 1995): STF, Subtropical Front; SAF, Subantarctic Front; PF, Polar Front, SACCF, Southern Front of the ACC; SB, Southern Boundary of the ACC. Red arrows mark the main exit points of the ACC through the deep western boundary currents (DWBC). Blue and brown arrows mark the “cold” and “warm” water routes (Rühs et al., 2019). Black dashed line denotes the maximum extent of sea ice averaged over the 1979/80 to 2007/08 winter seasons taken from Deppeler & Davidson (2017). Green lines indicate the extension of the biogeochemical provinces: AZ, Antarctic Zone; POOZ, Permanently Open Ocean Zone; PFZ, Polar Front Zone; SAZ, Subantarctic Zone. The topography data for the base map was taken from Becker et al. (2009). .....2

**Figure 1.2** (a) Bathymetric map of the Drake Passage area showing the location of the modern SO fronts (Orsi et al., 1995; White lines), and the main geomorphological features: SFZ, Shackleton Fracture Zone; HFZ, Hero Fracture Zone. Black dashed lines a–a’ and b–b’ are two hydrographic transects shown in (c) and (d). (b) Map of the Drake Passage mean chlorophyll-*a* concentrations for the years 2009–2019 showing the trajectories of the Antarctic Circumpolar Current (ACC), South Pacific Current (SPC), Cape Horn Current (CHC), Humboldt Current (Strub et al., 2019), and Antarctic Coastal Current (AACC, Deacon, 1984; white arrows). Black lines mark ACC modern fronts (Orsi et al., 1995). SAF, Subantarctic Front; PF, Polar Front; SACCF, Southern Antarctic Circumpolar Current. Cyan area indicates the extension of the Patagonian Ice Sheet at the Last Glacial Maximum based on Glasser et al. (2008). (c) Salinity section across the Drake Passage (data from Gouretski & Koltermann, 2004). LCDW, Lower Circumpolar Deep Water; UCDW, Upper Circumpolar Deep Water; AAIW, Antarctic Intermediate Water; SAMW, Subantarctic Mode Water. (d) Geostrophic flow velocities across the Drake Passage from Renault et al. (2011). .....10

**Figure 1.3** Evolution of some key records over the past 1.4 million years that show the global and oceanographic changes across the Mid-Pleistocene Transition and the Mid-Brunhes Event. From top to bottom: red, LR04 benthic  $\delta^{18}\text{O}$  stack (Lisiecki & Raymo, 2005), as a reference record of global ice volume fluctuations, numbers indicate interglacial stages; blue, Antarctic air temperature changes (Jouzel et al., 2007); green, Southern Ocean ODP site 1094 Sea Surface Temperature (SST) derived from *N. Pachyderma* (s.) Mg/Ca (Hasenfratz et al., 2019); dust and iron deposition records, Antarctic Dust flux (brown, Lambert et al., 2008), and mass accumulation rates of iron at ODP site 1090 (grey, Martínez-García et al., 2011). Blue shadows mark the Mid-Brunhes Event and the Mid-Pleistocene Transition.....18

**Figure 2.1** Southern Ocean map showing the location of sediment core PS97/093-2 (yellow), and all cores used for comparison and discussion (blue indicates the location of the SO current strength reconstructions; red color marks the location of the export production reconstructions based on  $^{230}\text{Th}_{\text{xs}}$  normalized mass accumulation rates; green indicates long-term paleoproductivity and  $\text{CaCO}_3$  reconstruction; green circles with red rim refer to those core that were used for  $^{230}\text{Th}$ -based and long-term reconstructions. White lines show the ACC oceanographic fronts and boundaries according to Orsi et al. (1995): STF, Subtropical Front; SAF, Subantarctic Front; PF, Polar Front, SACCF, Southern Front of the ACC; SB, Southern Boundary of the ACC. ....27

**Figure 3.1** Schematic workflow diagram of the analytical steps of this thesis. Yellow and purple squares indicate mass accumulation rates of individual components estimated through either the  $^{230}\text{Th}_{\text{xs}}$ - normalization method (purple) or multiplication of the sedimentation rates by the dry bulk density (yellow). ....28

**Figure 3.2** Schematic lithology logs of core PS97/093-2 (Lamy, 2016). .....30

**Figure 3.3** Pointers (blue triangles), and age–depth relationship for core PS97/093-2; red line indicates the initial age model (published in Toyos et al. (2020), and blue line marks the final age model used in manuscript 3. ....36

**Figure 3.4** Simplified radioactive decay chain of  $^{238}\text{U}$ . Red texts indicate the half-life of the radioactive isotopes involved in this decay chain. ....43

**Figure 3.5** Echo sounder profile on a section parallel to the coast of Namibia showing wide variations in the thickness of layered sediments deposited in the same area, providing graphical evidence of focusing and winnowing. This figure was taken from Mollenhauer et al. (2002), and it has been previously used in the literature as a classical example to illustrate processes of sediment redistribution (e.g., Francois et al., 2004). ....46

**Manuscript 1 (published): Antarctic Circumpolar Current dynamics at the Pacific entrance to the Drake Passage over the past 1.3 million years.**

**Figure 1** (a) Map of the Drake Passage area showing the location of core PS97/093-2 (yellow star) and core sites studied by Lamy et al. (2015), McCave et al. (2014), and Roberts et al. (2017) (blue points). White lines mark ACC modern fronts (Orsi et al., 1995). SAF, Subantarctic Front; PF, Polar Front; SACCF, Southern Antarctic Circumpolar Current Front; SB, southern boundary of the ACC. Black dashed lines a–a' and b–b' are two hydrographic transects shown in (b) and (c). SFZ, Shackleton Fracture Zone; HFZ, Hero Fracture Zone. (b) Salinity section across the Drake Passage with the projected core position (data from Gouretski & Koltermann, 2004). LCDW, Lower Circumpolar Deep Water; UCDW, Upper Circumpolar Deep Water; AAIW, Antarctic Intermediate Water; SAMW, Sub-Antarctic Mode Water. (c) Geostrophic flow velocities through the Drake Passage from Renault et al. (2011) with the projected core position; positive velocities are eastward, and negative velocities are westward. ....54

**Figure 2** Age model for core PS97/093-2. From top to bottom: LR04 benthic  $\delta^{18}\text{O}$  stack (Lisiecki & Raymo, 2005), numbers indicate marine isotope stages; XRF Fe scanner counts (blue);  $\text{CaCO}_3$  content (orange) and XRF Ca scanner counts



(black); age control points based on biostratigraphic markers (purple asterisks), sedimentation rate (brown), and tie points (red). .....57

**Figure 3** (a) Linear regression between  $\overline{SS}$  ( $\mu\text{m}$ ) mean and  $\overline{SS}$  percentage of PS97/093-2 samples. Linear relations between Zr/Rb and SS ( $\mu\text{m}$ ) of PS97/093-2 samples. (b) All measured samples. (c) All samples with the exception of those that belong to the Holocene, MIS 5, and MIS 11. (d) Silt distribution of the Holocene, MIS 5, MIS 11, and selected interglacials (MIS 13, MIS 19, MIS 29, and MIS 39). .....59

**Figure 4** Multiproxy reconstruction of ACC current strength fluctuation at the PS97/093-2 site. (a) LR04 benthic  $\delta^{18}\text{O}$  stack (Lisiecki & Raymo, 2005). (b) XRF scanner five-point smoothed Zr/Rb variations. (c) Measured sortable silt ( $\overline{SS}$ ) results. (d) High-resolution SS record based on XRF 5-point smoothed Zr/Rb transformation (black line) compared with measured  $\overline{SS}$  record (pink line) (see text for details). (e, f) Linear regressions between XRF Zr/Rb and  $\overline{SS}$  used to obtain high-resolution SS record. (g) Core PS97/093-2 scalar flow speed fluctuations (cm/s) based on McCave et al. (2017) (blue) and Wu et al. (2019) (gray) equations. Gray bars indicate interglacial stages. Cyan bar indicates MIS 14. ....60

**Figure 5** Drake Passage throughflow change (in %) between the Holocene and the LGM. Yellow (blue) arrows denote Holocene increase (decrease) at PS97/093-2, MD07-3128 and MR0806-PC09 (Lamy et al., 2015), GC528 (Roberts et al., 2017), and Scotia Sea core sites from McCave et al. (2014). White lines mark ACC modern fronts (Orsi et al., 1995): SAF, PF, SACCF, and SB as in Figure 1. ....62

**Figure 6** Marine isotope stage 11. (a) Evolution of the global ice volume (Lisiecki & Raymo, 2005). (b) Estimated changes in ACC strength based on the XRF Zr/Rb ratio and the  $\overline{SS}$  record of core PS97/093-2. (c)  $\text{CaCO}_3$  content (orange) and XRF Ca scanner counts (black). (d) Coccolithophore paleoproductivity proxies of sediment core PS75/059-2 (Saavedra-Pellitero, Baumann, Ullermann, et al., 2017):

Coccolith accumulation rate (blue; note log scale) and Coccolith Sr/Ca residuals using the *Gephyrocapsa oceanica* correction (gray). .....64

**Figure 7** Spectral analysis and comparison between the SS record of core PS97/093-2 (green) and LR04 benthic  $\delta^{18}\text{O}$  stack (Lisiecki & Raymo, 2005) (red). (a) Cross-spectral analysis of high-resolution  $\overline{\text{SS}}$  record based on XRF Zr/Rb transformation of core PS97/093-2 and the Lisiecki and Raymo stack. Coherency indicates the correlation between the pair of variables as a function of frequency; nonzero coherence is higher than 0.38 (red dashed line). Phase refers to the relationship of the pair of variables with the same frequency. If the phase is  $180^\circ$ , the two signals are out of phase with each other. (b) Evolution of the global ice volume during the last ~1.3 Ma (red); numbers indicate marine isotope stages (Lisiecki & Raymo, 2005), and estimated changes in ACC strength (green) are based on the  $\overline{\text{SS}}$  record of PS97/093-2. Vertical gray bars mark Lisiecki and Raymo interglacial stages. MBE, mid-Brunhes event; MPT, mid-Pleistocene transition. B-Tukey tests of the  $\overline{\text{SS}}$  PS97/093-2 record divided into three different time intervals: (c) the entire record, (d) from MIS 21 to the Holocene, and (e) from 1.3 Ma to MIS 21. ....65

**Figure 8** (a) Reconstructed changes in current strength during the past 1.3 Myr: at PS97/093 (green) and ODP 1123 (purple) sites. Vertical gray bars mark Lisiecki and Raymo interglacial stages. Numbers indicate some of the marine isotope stages (Lisiecki & Raymo, 2005). Horizontal dashed lines mark the mean  $\overline{\text{SS}}$  values for the periods used by Hall et al. (2001) and the ones chosen for the core PS97/093-2 record (MIS 1 to MIS 11, MIS 12 to MIS 21, MIS 22 to MIS 35 and MIS 1 to MIS 14, MIS 14 to MIS 21, MIS 22 to MIS 43, respectively). (b) Cross-spectral analyses of  $\overline{\text{SS}}$  results of core PS97/093-2 (this study) and ODP1123 (Hall et al., 2001). .....67

**Figure S1** Linear regression between XRF core scanner-derived Ti, K and Zr in core PS97/093-2. ....76

**Manuscript 2 (accepted): Variations in export production, lithogenic sediment transport and iron fertilization in the Pacific sector of the Drake Passage over the past 400 ka.**

**Figure 1:** (a) Map of the Southern Ocean mean chlorophyll-*a* concentrations for the years 2009–2019 with core locations. Yellow diamond indicates the location of core PS97/093-2 (this study), and white diamonds the location of published records discussed in the text: PS75/076 and PS75/059 (Lamy et al. 2014); PS2498-1, TN057-21, and TN057-06 (Anderson et al., 2014); ODP1090 (Martínez-García et al. 2014); PS2082-1 (Frank et al. 1999; Nürnberg, 1997); MD11-3357 (Thöle et al., 2019), and EPICA Dome C ice Core (Lambert et al., 2008). (b) Map of the Drake Passage mean chlorophyll-*a* concentrations for the years 2009–2019 showing the location of PS97/093-2 (this study), MD07-3128 (Caniupán et al., 2011), PS75/034-2 (Ho et al., 2012), GeoB3325-5 (Tapia et al., 2021), and ODP Site 1233 (Lamy et al., 2010; yellow diamonds); cyan area indicates the extension of the Patagonian Ice Sheet at the Last Glacial Maximum based on Glasser et al. (2008), white arrows show trajectories of the Antarctic Circumpolar Current (ACC), South Pacific Current (SPC), Cape Horn Current (CHC), Humboldt Current (Strub et al., 2019), and Antarctic Coastal Current (AACC, Deacon, 1984). Black lines mark ACC modern fronts (Orsi et al., 1995). SAF, Subantarctic Front; PF, Polar Front; SACCF, southern Antarctic Circumpolar Current Front, and SB, southern boundary of the ACC. We used the MODIS-Aqua Level-3 Mapped Chlorophyll-*a* Data Version 2018 (data/10.5067/AQUA/MODIS/L3M/CHL/2018), in 4 km resolution monthly mean chlorophyll-*a* concentrations between March 2009 and March 2019 (available from NASA Ocean Color website, <https://oceancolor.gsfc.nasa.gov/13/>) and Ocean Data View for visualization (Schlitzer 2021). .....84

**Figure 2** Southeast Pacific (PS97/093-2) stratigraphy-based mass accumulation rates (BMAR) and percentages of individual components compared to dust flux in the EPICA Dome C (EDC) ice core (Lambert et al. 2008). (a) EDC dust flux; (b) Lithogenic content (wt. %; calculated from:  $100 - [\text{opal wt. \%} + \text{CaCO}_3 \text{ wt. \%}]$ ).

%+2xTOC wt. %], grey line) and lithogenic content based on  $^{232}\text{Th}$  (grey stars); lithogenic BMAR (purple line); (c) Fe content (grey line) and Fe BMAR (green line); (d)  $\text{Ba}_{\text{xs}}$  content (grey line) and  $\text{Ba}_{\text{xs}}$  BMAR (pink line); (e) TOC content (light grey line) and TOC BMAR (light blue line); (f) Opal content (wt. %; grey line) and opal BMAR (blue line); (g)  $\text{CaCO}_3$  content (grey line) and  $\text{CaCO}_3$  BMAR (orange line). Numbers in the lower part of the figure indicate Marine Isotope Stages (MIS). Vertical grey bars mark glacial stages according to Lisiecki and Raymo (2005). .....90

**Figure 3** Southeast Pacific (PS97/093-2)  $^{230}\text{Th}_{\text{xs}}$ -normalized mass accumulation rates (MAR) compared to dust flux in the EDC ice core (Lambert et al. 2008) and bottom current strengths of core PS97/093-2 (Toyos et al., 2020). (a) EDC dust flux, (b)  $^{232}\text{Th}$  based lithogenic MAR; (c) Fe MAR; (d) changes in bottom current strength as indicated by the sortable silt record of core PS97/093-2 (note that Y-axis is reversed); (e)  $\text{Ba}_{\text{xs}}$  MAR; (f) TOC MAR; (g) biogenic opal MAR; and (h)  $\text{CaCO}_3$  MAR. Shaded areas indicate associated errors. Numbers in the lower part of the figure indicate Marine Isotope Stages (MIS). Grey bars denote glacial stages according to Lisiecki & Raymo (2005). Dashed lines during MIS 6 denote the interval of extreme winnowing where MAR might be overestimated, and for MIS 10 they indicate uncertainty due to the lack of data points. ....91

**Figure 4** Comparison of sediment mass accumulation rates, focusing factors, bottom current strength and sedimentation rates of core PS97/093-2 for the last 400 ka. (a) Changes in bottom current strength based on the Sortable Silt grain size record (lilac line, Toyos et al., 2020) compared to (b) focusing factors (red line, black dashed line marks focusing factor=1); (c) sedimentation rates; (d)  $^{230}\text{Th}_{\text{xs}}$ -normalized mass accumulation rate (MAR, black line and dots) and associated errors ( $2\sigma$ ; pink shadow), which grow with the age of the sample, dashed lines indicate intervals with uncertainties due to extreme winnowing (Marine Isotope Stage 6) or lack of data (Marine Isotope Stage 10); (e) Stratigraphy-based bulk mass accumulation rates (BMAR) obtained by multiplying sedimentation rates by dry bulk densities. Numbers in the lower part of the figure indicate Marine Isotope

Stages (MIS). Grey bars denote glacial stages according to Lisiecki & Raymo (2005). .....92

**Figure 5** Changes in <sup>230</sup>Th-normalized lithogenic MARs in the subantarctic Southern Ocean (see Fig 1 for location of sites discussed). From top to bottom: Cores PS75/076 and PS75/059 (Lamy et al., 2014); Core PS97/093-2 (this study); Core PS2498 (Anderson et al., 2014); Cores TN057-21 and TN056-06 (Anderson et al., 2014), and ODP1090 (Martínez-García et al., 2009); Core MD11-3357 (Thöle et al., 2019), and dust MAR in the EPICA Dome C ice core (Lambert et al., 2008). Marine Isotope Stage (MIS); grey bars denote glacial stages. Continental masses are located in their relative longitudinal position to the marine sediment cores and represent the primary source of terrigenous inputs to the Subantarctic Zone. ....95

**Figure 6** Comparison of MAR across the Subantarctic Southern Ocean, during the Holocene (0–10 ka, red), the Last Glacial Maximum (19–27 ka, blue), Marine Isotope Stage 5e (119–124 ka, yellow), and late Marine Isotope Stage 6 (132–150 ka, green): Maps of surface water nitrate (a) and silicate (b) concentrations (data from WOCE, Global Hydrographic Climatology, Gouretski and Koltermann, 2004); black lines indicate the modern location of the Subantarctic Front (SAF), and Polar Front (PF, Orsi et al., 1995); white diamonds refer to core locations (PS75/076 and PS75/059, Lamy et al. 2014; PS97/093-2, this study; PS2498-1, TN057-21 and TN056-06, Anderson et al., 2014; ODP1090, Martínez-García et al. 2014; PS2082-1, Nürnberg, 1997 and Frank, 2002; MD11-3357, Thöle et al., 2019); (c) lithogenic flux; (d) Fe flux; (e) Ba<sub>xs</sub> flux; (f) total organic carbon flux; (g) opal flux; (h) CaCO<sub>3</sub> flux. Grey bars indicate the projected core positions. ....100

**Figure S1** a, b, c: Linear regressions between XRF and measured element concentrations (Fe, Ba, Ti) used to obtain high-resolution element content records. d: Linear regression between lithogenic content obtained by subtraction (Litho %= 100 – [CaCO<sub>3</sub> % + opal % + (2xTOC %)]), and lithogenic content

obtained by  $^{232}\text{Th}$  concentrations. e: Linear regression between XRF Ca and measured  $\text{CaCO}_3$  percentage used to obtain a high-resolution carbonate content record. ....120

**Figure S2** Left: Changes in  $^{230}\text{Th}$ -normalized Lithogenic MARs of core PS97/093-2 compared to dust fluxes in the EPICA Dome C ice core (Lambert et al., 2008). The inset texts indicate the chronology of the ice advances in Patagonia and Tierra del Fuego according to Rabassa (2008). Vertical grey bars mark glacial stages according to Lisiecki & Raymo (2005). Marine Isotope Stage (MIS). Right: Linear correlation between PS97/093-2 lithogenic MARs and EDC dust flux. ....121

**Figure S3** Southern Ocean average surface concentration of phosphate (data from Gouretski & Koltermann, 2004); Black lines indicate the modern location of the Subantarctic Front (SAF), and Polar Front (PF, Orsi et al., 1995); White diamonds indicate the core locations (PS75/076 and PS75/059, Lamy et al. 2014; PS97/093-2, this study; PS2498-1, TN057-21 and TN057-06, Anderson et al., 2014; ODP1090, Martínez-García et al. 2014; PS2082-1, Nürnberg, 1997 and Frank, 2002; MD11-3357, Thöle et al., 2019). ....121

**Manuscript 3 (in preparation): 1.4 Ma productivity reconstruction at the Pacific entrance of the Drake Passage determined from mass accumulation rates corrected for syndepositional redistribution of sediments**

**Figure 1** Map of Southern Ocean mean chlorophyll-*a* concentrations for the years 2009–2019 with core locations. Yellow diamond indicates the location of core PS97/093-2 (this study), and white diamonds the location of published records discussed in the text: PS75/079, PS75/076 and PS75/059 (Saavedra-Pellitero, 2017a); TN057-10, TN057-21 and ODP 1089 (Gottschalk et al., 2018); ODP 1088 (Farmer et al., 2019a); ODP 1090 (Farmer et al., 2019a; Lawrence et al., 2013; Martínez-García et al., 2011), and ODP 1094 (Jaccard et al., 2013). Black lines mark ACC modern fronts (Orsi et al., 1995). SAF, Subantarctic Front; PF, Polar Front; SACCF, southern Antarctic Circumpolar Current Front, and SB, southern

boundary of the ACC. We used the MODIS-Aqua Level-3 Mapped Chlorophyll Data Version 2018 (data/10.5067/AQUA/MODIS/L3M/CHL/2018), in 4 km resolution monthly mean chlorophyll-*a* concentrations between March 2009 to March 2019 (available from NASA Ocean Color website, <https://oceancolor.gsfc.nasa.gov/13/>). .....128

**Figure 2** a: Age–depth relationship for core PS97/093-2, red line indicates the original age model from Toyos et al. (2020), and blue line marks the modified age model (this study), the blue triangles are the pointers. b, c: Sedimentation rates of core PS97/093-2 according to the update age model (b), and to the initial age model from Toyos et al. (2020) (c). .....135

**Figure 3** Multiproxy reconstruction at site PS97/093. **a:** Reconstructed current strength based on  $\overline{\delta\delta}$  proxy (Toyos et al., 2020); **b:** Focusing factor (Toyos et al., accepted); **c:** Exponential regression between focusing factor and  $\overline{\delta\delta}$  used to obtain focusing factors beyond the 400 ka.; **d:** High resolution focusing factors (grey line) compared to measured focusing factor (black dots). Red lines in (b) and (d) indicate focusing factor=1, values above 1 are in the focusing intervals, whereas below 1 denote winnowing. ....141

**Figure 4** Comparison between PS97/093-2's BMAR (thick grey lines) and BMAR-corr (fine colored lines) of Fe,  $B_{axs}$ , TOC, opal and  $CaCO_3$ . a: LR04 benthic  $\delta^{18}O$  stack (Lisiecki & Raymo, 2005), numbers indicate interglacial Marine Isotope Stages; b: Fe BMAR-corr and BMAR; c:  $B_{axs}$  BMAR-corr and BMAR; d: TOC BMAR-corr and BMAR; e: biogenic opal BMAR-corr and BMAR; f:  $CaCO_3$  BMAR-corr and BMAR; g: Focusing factor (calculated) over the past 1.37 Ma.; red line indicates focusing factor=1, values above 1 are in the focusing intervals, whereas below 1 denote winnowing. Vertical bars mark the Mid-Pleistocene Transition (green), Mid-Brunhes Event (green), and Marine Isotope Stage 16 (blue). ....143

**Figure 5** SE Pacific (PS97/093-2) stratigraphy-based mass accumulation rate corrected for syndepositional redistribution (BMAR-corr) of individual

components compared to the evolution of the global ice volume (Lisiecki & Raymo, 2005), and bottom current strength fluctuations at core site (Toyos et al., 2020). **a:** LR04 benthic  $\delta^{18}\text{O}$  stack (Lisiecki & Raymo, 2005), numbers indicate interglacial Marine Isotope Stages; **b:** Fe BMAR-corr; **c:**  $\text{Ba}_{\text{xs}}$  BMAR-corr; **d:** TOC BMAR-corr; **e:** biogenic opal BMAR-corr; **f:**  $\text{CaCO}_3$  BMAR-corr; **g:** Changes in bottom current strength as indicated by the sortable silt record of site PS97/093-2. Vertical bars mark the Mid-Pleistocene Transition (green), Mid-Brunhes Event (green), and Marine Isotope Stage 16 (blue). .....146

**Figure 5.1** Scheme of the hypothesized interglacial (left) and glacial (right) conditions in the Drake Passage area based on previous studies and the new paleoceanographic records presented in this thesis. Black lines indicate the expected Subantarctic Front (SAF) and Polar Front (PF) positions in each scenario. Note that we use the modern ACC front position from Orsi et al. (1995) for interglacial stages, and for glacials, we projected the Last Glacial position proposed by Roberts et al. (2017). Blue arrows show the ACC frontal jets; Red shadow areas indicate the current extension of the Patagonian and Cordillera Darwin Icefields (left) and the Patagonian Ice Sheet during the last glacial (right, taken from Glasser et al. (2008)). Purple lines mark the average modern winter sea ice position (Comiso et al., 2003). Yellow dots indicate the location of core PS97/093-2. ....157

**Figure 5.2** Accumulation rates of Fe, and export production in the SAZ, at the SE Pacific (core PS97/093-2) and in the Atlantic (ODP 1090) sectors. **a:** LR04 benthic  $\delta^{18}\text{O}$  stack (Lisiecki & Raymo, 2005), numbers indicate interglacial Marine Isotope Stages; **b:** Fe BMAR-corr (core PS97/093-2, this study); **c:**  $\text{Ba}_{\text{xs}}$  BMAR-corr (core PS97/093-2, this study); **d:** biogenic opal BMAR-corr (core PS97/093-2, this study); **e:** accumulation rates of Fe (ODP 1090; Martínez-García et al., 2011); **f:** accumulation rates of  $\text{C}_{37}$  Alkenone (ODP 1090; Lawrence et al., 2013; Martínez-García et al., 2009). Vertical blue bars indicate Lisiecki and Raymo glacial stages, and glacials from the Mid Pleistocene Transition are marked in green. ....171



## Resumen

Variaciones en la productividad y en la intensidad de la Corriente Circumpolar Antártica en el Paso de Drake durante los últimos 1.3 millones de años:  
implicaciones en la circulación termohalina

María H. Toyos Simón

Doctorado en Oceanografía

Universidad de Concepción, 2021

Dr. Carina B. Lange, Profesora Guía

Dr. Frank Lamy, Profesor Co-guía

El Océano Austral (*SO*, por sus siglas en inglés) que rodea al continente Antártico es un océano singular en numerosos sentidos. En primer lugar, por él fluye la Corriente Circumpolar Antártica (CCA), el mayor sistema de corrientes del mundo, que conecta las cuencas oceánicas Pacífica, Atlántica e Índica. Además, el límite norte de la zona de influencia del *SO* viene dado por la posición del Frente Subtropical, que depende netamente de la CCA. La CCA tiene influencia en la circulación termohalina y se considera un componente importante del sistema climático de la Tierra. En segundo lugar, el *SO* también es importante porque juega y ha jugado un papel trascendental en la regulación del CO<sub>2</sub> atmosférico debido a que a lo largo de la historia ha actuado como captador o emisor de este gas de efecto invernadero. Uno de los motivos de la captación de CO<sub>2</sub> en el *SO* durante periodos glaciales es un aumento en la productividad primaria en la Zona Subantártica. Las causas residen en un incremento en los flujos de polvo eólico depositados por los vientos, y como consecuencia, la fertilización con hierro que habría estimulado la productividad primaria.

La CCA presenta tres frentes en el *SO*, de norte a sur: Frente Subantártico, Frente Polar y Frente Sur de la Corriente Circumpolar Antártica. Su ubicación no ha sido estática a lo largo de la historia ya que los frentes han sufrido desplazamientos latitudinales a diferentes escalas temporales. Dentro del *SO*, la región entre el Frente Subantártico y el Frente Subtropical se denomina Zona Subantártica. Geográficamente dentro del *SO*,

el Paso de Drake separa el continente americano de la península Antártica y constituye el paso más estrecho en el flujo de la CCA, por lo tanto en este área la ubicación de los frentes oceanográficos cobra vital importancia.

Al inicio del desarrollo de esta tesis, los datos disponibles no habían proporcionado información concluyente acerca de cuál sería el papel del Paso de Drake en los cambios en la circulación oceánica global a escalas temporales glacial/interglacial. Además, hoy en día apenas se dispone de información acerca de los cambios en la productividad ni de su conexión con los procesos de fertilización con hierro en la zona Subantártica a la entrada del Paso de Drake. Asimismo, en esta zona tampoco existe información relacionada con los cambios de la intensidad de la CCA, ni en los patrones de productividad primaria que incluyan la Transición del Pleistoceno Medio (desde 1.25 a 0.7 millones de años) y el *Mid-Brunhes Event*. En este contexto, el objetivo general de esta tesis ha sido reconstruir la intensidad de la CCA y la producción marina exportada en los últimos 1.3 millones de años en la Zona Subantártica a la entrada del Paso de Drake. Para ello se ha utilizado un enfoque multi-*proxy* en el testigo de sedimento PS97/093-2 (57° 29.9'S; 70° 16.56'W; recuperado a 3781 m de profundidad, 16,45 m de longitud). Esta tesis incluye tres capítulos de resultados:

En el capítulo 1, se presenta el modelo de edad del testigo de sedimento PS97/093-2, y la reconstrucción de las variaciones en la intensidad de la CCA utilizando como indicadores la media del limo uniforme de la fracción terrígena del sedimento ( $\overline{\text{SS}}$ , 10–63 $\mu\text{m}$ ) en combinación con las concentraciones de elementos sensibles al tamaño de grano (Zr/Rb). Los resultados obtenidos en este capítulo muestran variaciones medias en la CCA de un 6–16% a escala glacial/interglacial durante el último 1.3 millón de años. Además, se ha observado un patrón consistente de mayor (menor) intensidad en el flujo de la CCA durante periodos interglaciares (glaciales). Por último, en este capítulo también se reportan cambios en la ciclicidad en las fluctuaciones de la CCA, pasando de ciclos de 41.000 años a ciclos de 100.000 años en la Transición del Pleistoceno Medio. Los resultados presentados en el capítulo 1 han sido publicados en la revista *Paleoceanography and Paleoclimatology*: **Toyos, M. H.**, Lamy, F., Lange, C. B., Lembke-Jene, L., Saavedra-Pellitero, M., Esper, O., & Arz, H. W. (2020). Antarctic Circumpolar Current Dynamics at the Pacific Entrance to the Drake Passage

Over the Past 1.3 Million Years. *Paleoceanography and Paleoclimatology*, 35 (7), 1–20.

El capítulo 2 incluye una evaluación de los cambios y patrones en la producción marina exportada durante los últimos 400.000 años, basándose en las tasas de acumulación de material litogénico, hierro, opal biogénico, carbonatos, exceso de bario, y carbono orgánico normalizadas por  $^{230}\text{Th}$ . Se demuestra que las variaciones en productividad biológica han estado fuertemente condicionadas por la disponibilidad de hierro y ácido silícico. Durante periodos glaciales, el aumento en la productividad biológica se debe a incrementos en las concentraciones de hierro procedentes de los campos de hielo patagónicos, y de ácido silícico a causa de una migración hacia el norte de los frentes de la CCA. Por otro lado, durante los períodos interglaciales, se infieren menores niveles de productividad sostenidos por organismos con esqueletos de carbonato de calcio. En este estudio se ha podido comprobar también que, a diferencia de lo que acontece en el Atlántico sur, el polvo eólico no ha jugado un papel importante en la estimulación de la productividad marina. En este capítulo también se demuestra que la intensidad del flujo de la CCA ha ocasionado redistribución lateral de los sedimentos, dando lugar a la sub(sobre)-estimación de las tasas de acumulación obtenidas de manera tradicional (aquellas derivadas de la multiplicación de las tasas de sedimentación por la densidad). Estos resultados se encuentran en un manuscrito aceptado en la revista *Climate of the Past*: **Toyos, M. H.**, Winckler, G., Arz, H.W., Lembke-Jene, L., Lange, C.B., Kuhn, G., Lamy, F. (2021). Variations in export production, lithogenic sediment transport and iron fertilization in the Pacific sector of the Drake Passage over the past 400 ka. *Clim. Past Discuss.* (preprint), <https://doi.org/10.5194/cp-2021-85>, accepted.

Por último en el capítulo 3 de esta tesis, con el objetivo de estimar los cambios en la productividad marina más allá de los últimos 400.000 años, y basándose en los resultados del capítulo 2, hemos corregido el efecto de la sub(sobre)-estimación de las tasas de acumulación en los indicadores de productividad y hierro para el último 1.3 millón de años. Estos resultados servirán de base para un manuscrito que actualmente se encuentra en preparación.

En suma, los resultados obtenidos en esta tesis se han integrado con estudios previos realizados en el *SO*, contribuyendo así con nuevo conocimiento a un mejor entendimiento de la evolución de este océano y la CCA a lo largo del Cuaternario.



## **Abstract**

Changes in productivity and the strength of the Antarctic Circumpolar Current through the Drake Passage over the past 1.3 million years, and its global implications on the meridional overturning circulation

María H. Toyos Simón

PhD. in Oceanography

Universidad de Concepción, 2021

Dr. Carina B. Lange, Advisor

Dr. Frank Lamy, Co-advisor

The Southern Ocean (SO) is the broad ocean region surrounding the Antarctic Peninsula, and it is crucial in many ways. Firstly, its flow is driven by the Antarctic Circumpolar Current (ACC), the world's largest current system that connects the Atlantic, Pacific, and Indian ocean basins. The ACC affects the global meridional overturning circulation, and is considered a key component of the Earth's climate system. Secondly, the SO is also important because of its critical role in controlling how much CO<sub>2</sub> is in the atmosphere through time. Precisely, increased Subantarctic biological export production during glacials, fueled by enhanced iron fertilization, is thought to have been a key driver of increased deep marine carbon storage.

Three major oceanographic fronts are seen within the ACC, from north to south: Subantarctic Front, Polar Front, and Southern ACC Front. Their position is not stationary and has changed through time at various time scales. The Subtropical Front is the northern oceanographic boundary of the SO, and the area between the Subantarctic Front and the Subtropical Front is known as the Subantarctic Zone. The narrowest constriction of the SO and the ACC flow is the Drake Passage, located between South America and the Antarctic Peninsula. As the Drake Passage is the only bottleneck for the ACC flow, in this area the location of the fronts is crucial.

At the beginning of this thesis, the knowledge of the ACC changes in the Drake Passage area and the role of this region in driving changes in the global ocean

circulation at glacial-interglacial timescales was still unclear. Furthermore, past export production in the subantarctic Southeast Pacific was poorly documented, and its connection to Fe fertilization, potentially related to Patagonian Ice Sheet dynamics, was unknown. Besides, there was no information on changes in the ACC flow strength and productivity at timescales encompassing the Mid-Pleistocene Transition (between 1.25 to 0.7 Ma) and the Mid-Brunhes Event. On this matter, the general objective of this thesis is to reconstruct the intensity of the ACC, and export production over the past ~1.3 Ma in the Subantarctic Zone, at the Drake Passage entrance. To achieve this goal, a multi-proxy approach of core PS97/093-2 (57° 29.9'S; 70° 16.56'W, 3781 water depth, 16.45 m length) has been used. This thesis includes three chapters:

Chapter 1 includes the development of the age model for core PS97/093-2, and an estimation of changes in the ACC current strength through the last 1.3 Ma, based on the mean sortable silt grain size ( $\overline{SS}$ , 10–63 $\mu$ m) combined with X-ray fluorescence scanner-derived Zr/Rb ratios. Our results show that at the core site, ACC strength varied by ~6–16% on glacial-interglacial time scales, with higher current speeds during interglacial times and reduced current speeds during glacials. This section also reveals that the cyclicity in the current strength changes largely follows the global climate changes from 41-kyr cycles across the Mid-Pleistocene Transition to 100-kyr cycles into the late Pleistocene. The results shown in chapter 1 have been published in the journal *Paleoceanography and Paleoclimatology*: **Toyos, M. H.**, Lamy, F., Lange, C. B., Lembke-Jene, L., Saavedra-Pellitero, M., Esper, O., & Arz, H. W. (2020). Antarctic Circumpolar Current Dynamics at the Pacific Entrance to the Drake Passage Over the Past 1.3 Million Years. *Paleoceanography and Paleoclimatology*, 35 (7), 1–20.

In chapter 2, based on a combination of stratigraphy-based and  $^{230}\text{Th}_{\text{xs}}$ -normalized mass accumulation rates of paleoproductivity indicators, lithogenic and iron, we report on export production changes at glacial/interglacial timescales over the past 400,000 years. We suggest that glacial-interglacial variability in export production responds to glaciogenic Fe supply from Patagonia and silica availability due to shifts in oceanic fronts, whereas dust, as a source of lithogenic material, plays a minor role. Furthermore, due to the strong bottom current dynamics at the core site, a bias in the

stratigraphy-based mass accumulation rates has been reported, resulting in variable sediment focusing or winnowing. These results were accepted for publication in the journal *Climate of the Past*: **Toyos, M. H.**, Winckler, G., Arz, H.W., Lembke-Jene, L., Lange, C.B., Kuhn, G., Lamy, F. (2021). Variations in export production, lithogenic sediment transport and iron fertilization in the Pacific sector of the Drake Passage over the past 400 ka. *Clim. Past Discuss.* (preprint), <https://doi.org/10.5194/cp-2021-85>, accepted.

Lastly, to reconstruct export production changes beyond the last 400,000 years, and based on the excellent agreement between the sediment focusing and the estimated bottom current strengths (chapter 2), in chapter 3 it is shown stratigraphy-based mass accumulation rates corrected for syndepositional redistribution. Therefore, the results included in this work reveal that productivity proxies varied according to some of the Mid-Pleistocene Transition and Mid-Brunhes Event characteristic features. This section as well as the discussion of the thesis will serve as a basis for a manuscript in preparation for submission (December 2021).

The findings of this thesis were compared and integrated with previous works in the SO, providing hitherto new knowledge on SO Quaternary paleoceanography.

# 1. INTRODUCTION/INTRODUCCIÓN

## 1.1. The Southern Ocean and the Antarctic Circumpolar Current, an overview

The Southern Ocean (SO) is a major component of the Earth's global ocean and climate since it connects the three major ocean basins, Pacific, Atlantic and Indian, *via* the Antarctic Circumpolar Current (ACC, figure 1.1). In addition, the SO plays a major role in global ocean heat and carbon uptake and storage. Estimations suggest that the SO is storing *ca.* 75 % of the excess of heat associated with global warming, and *ca.* 35% of the global uptake of excess carbon from the atmosphere (Sallée, 2018). Without this, the atmospheric CO<sub>2</sub> concentration would be *ca.* 50% higher than it is today (Frölicher et al., 2015).

In the SO, circulation is carried by the ACC. Flowing from west to east, the ACC is the longest current in the world, with an estimated pathway of *ca.* 24.000 km circling Antarctica (Whitworth, 1988). It extends from the sea surface to near the bottom of the ocean and, as mentioned above, and plays an essential role in the global distribution of heat, salt and gases.



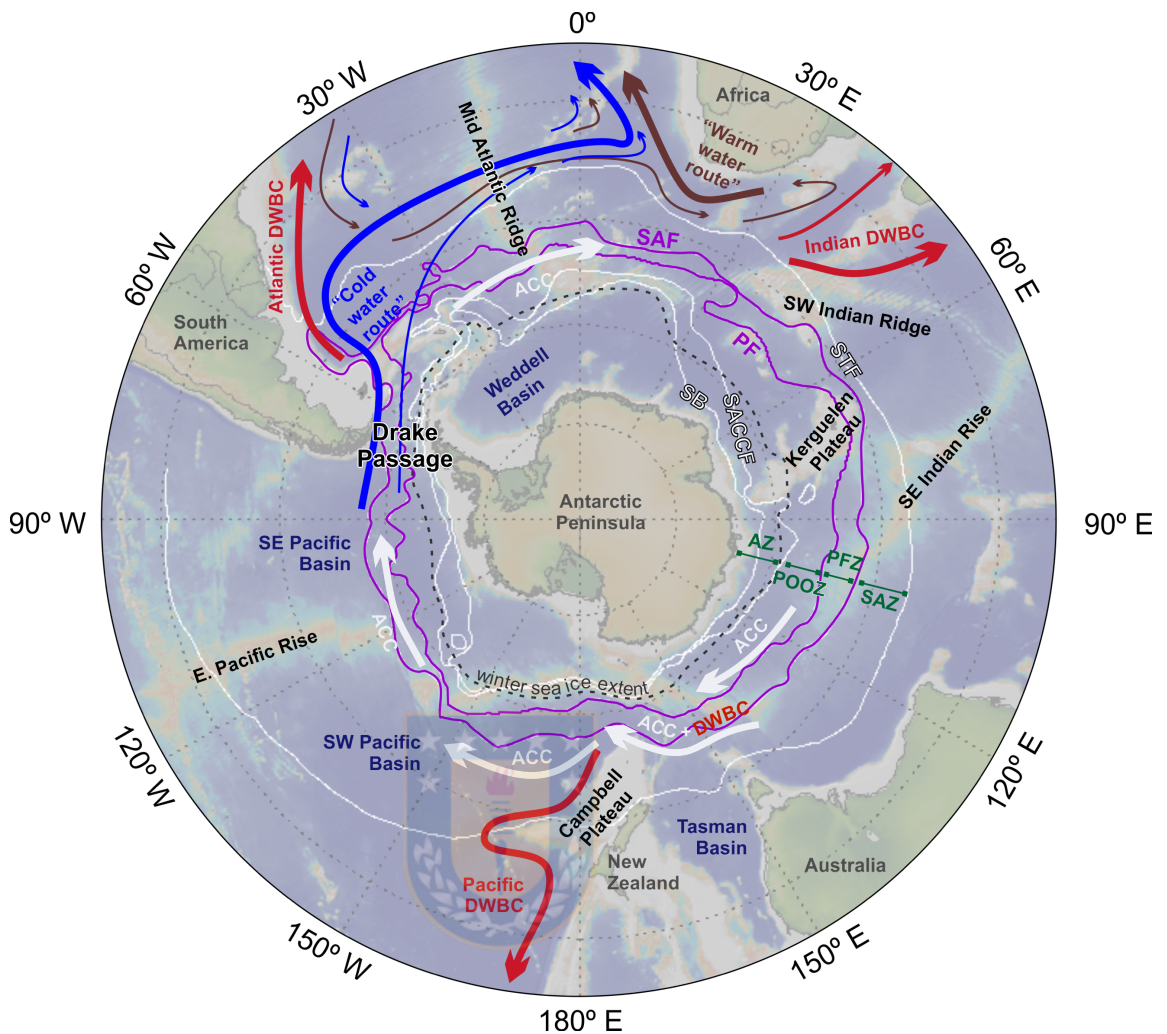


**Figure 1.1** Main oceanographic and bathymetric elements of the Southern Ocean. White arrows illustrate the eastward flow of the ACC around Antarctica. White and purple lines indicate the ACC oceanographic fronts and boundaries (Orsi et al., 1995): STF, Subtropical Front; SAF, Subantarctic Front; PF, Polar Front, SACCF, Southern Front of the ACC; SB, Southern Boundary of the ACC. Red arrows mark the main exit points of the ACC through the deep western boundary currents (DWBC). Blue and brown arrows mark the “cold” and “warm” water routes (Rühs et al., 2019). Black dashed line denotes the maximum extent of sea ice averaged over the 1979/80 to 2007/08 winter seasons taken from Deppeler & Davidson (2017). Green lines indicate the extension of the biogeochemical provinces: AZ, Antarctic Zone; POOZ, Permanently Open Ocean Zone; PFZ, Polar Front Zone; SAZ, Subantarctic Zone. The topography data for the base map was taken from Becker et al. (2009).

It is widely believed that the strong southern westerly winds (SWW) are the main driver of the ACC. However, calculations for a purely wind-driven ACC yielded overestimating transport compared to

observations (Carter et al., 2008; Rintoul & da Silva, 2019; Whitworth, 1988). Therefore, nowadays, the three-dimensional circulation in the ACC is comprehended to reflect the interplay of wind and buoyancy exchange with the atmosphere, water mass modification, eddy fluxes of heat and momentum, and strong interactions between the flow and bathymetry (Rintoul & da Silva, 2019).

Rather than a uniform flow, the ACC is a system of deep-reaching zonal jets that separate zones of relatively calm water, known as oceanic fronts. The SO fronts are narrow regions (50 to 100 km wide) where there is an abrupt change in the properties of the water (Deacon, 1984; Orsi et al., 1995; Whitworth, 1988). They are traditionally termed Subantarctic Front (SAF), Polar Front (PF), and Southern ACC Front (SACCF; Orsi et al., 1995; figure 1.1). The southern limit of the ACC domain is known as the Southern Boundary of the ACC (SB) and coincides with the southern border of Upper Circumpolar Deep Water (UCDW; Orsi et al., 1995), whereas to the north, the Subtropical Front (STF), interrupted only by South America, indicates the northernmost extent of subantarctic waters (Orsi et al., 1995; figure 1.1). The ACC transport can be highly variable, changing over a range of timescales. However, most of the transport takes place within the SO fronts, particularly at the SAF and PF. The relative

contribution of these two fronts to the total transport varies around the circumpolar path (Sokolov & Rintoul, 2009). It is suggested that currently, the zonal acceleration on the northern flank of the ACC is due to anthropogenic ocean warming north of the SAF, which is increasing the heat gradient between north and south of the SAF (Shi et al., 2021).

Circulation cells of the SO also play an essential role in the global-scale overturning circulation because the SO imports deep water from the basins to the north and exports bottom water and intermediate water. The main inflows to the Atlantic, Indian and Pacific oceans are *via* the strong and narrow deep western boundary currents (DWBC, figure 1.1), which mainly carry Lower Circumpolar Deep Water (LCDW) from the northern boundaries of the ACC (Carter et al., 2008; Mantyla & Reid, 1983). These inflows disperse Antarctic and northern-sourced waters throughout the world ocean. In the Atlantic Ocean, the DWBC is located on the continental margin of South America below the southward-moving North Atlantic Deep Water. The inflow consists of a mixture of Weddell Sea Bottom Water and Circumpolar Deep Water from the Drake Passage (DP) (see the review in Carter et al. (2008) and references therein; figure 1.1). In contrast, the Pacific DWBC inflow overlaps with the ACC along the Macquarie Ridge and through the high flanks of the Campbell Plateau. In

this region, around 49° S, the ACC and the DWBC separate leaving the DWBC to continue northwards into the Pacific Ocean at depths between ~5000 and ~2000 m (Carter et al., 2004; Leg 181 synthesis, McCave et al., 2008) and the ACC diverges eastwards into the South Pacific (along the SAF) (McCave et al., 2008; figure 1.1).

At present, the SO symbolizes the main leak in the efficiency of the biological carbon pump. Although upwelling of deep waters supplies the SO with large quantities of macronutrients, the SO is a known high-nutrient low-chlorophyll (HNLC) zone because of high overturning rates together with Fe co-limitation on phytoplankton growth (Boyd et al., 2012; Chapman et al., 2020; Moore et al., 2013). However, downstream of several islands scattered throughout the SO and near the South American continental shelf, phytoplankton concentrations can be relatively high (Chapman et al., 2020; Graham et al., 2015; Venables & Moore, 2010).

The existence of marked gradients in physical and chemical properties, and the separation of water masses provided a powerful tool to interpret observed distributions of phytoplankton stocks (Boyd, 2002). Usually, these gradients are related to the position of the SO fronts, which are thought to play a key role in the global distribution of nutrients through

two primary mechanisms (Palter et al., 2013): 1) the fronts act as sites of intense upwelling, and 2) the “mixing barrier effect” for frontal jets inhibits the exchange of these upwelled waters with neighboring nutrient-poor water masses, forming the limits between biogeochemical provinces (Chapman et al., 2020; Palter et al., 2013; Paparazzo, 2016). Accordingly, the SO is divided into four main biogeochemical regions, namely (from north to south) the i) Subantarctic Zone (SAZ), ii) Polar Frontal Zone (PFZ), iii) Permanently Open Ocean Zone (POOZ), and iv) Antarctic Zone (Deppeler & Davidson, 2017; Tréguer & Jacques, 1992; figure 1.1).

The SAZ is the area between the Subtropical front and the SAF, and it is the largest HNLC province in the world’s ocean. Over the year, phytoplankton is limited by iron, silicic acid, and light (Deppeler & Davidson, 2017). Iron is the main limiting factor here, despite inputs from dust, shelf sediments, and hydrothermal vents (Boyd et al., 2012). Silica is replete in spring, but becomes limiting by autumn (Pollard et al., 2002). Additionally, light levels experienced by phytoplankton can be very low due to cloudiness (Rintoul & Trull, 2001). Overall, the SAZ is defined as a carbonate-dominated regime (Honjo, 2004). Thus, diatom production is relatively low, and coccolithophores, cyanobacteria, dinoflagellates, and

lightly silicified diatoms control primary production (Rigual-Hernández et al., 2015).

The region between the SAF and the PF, known as the PFZ, forms an important transitional boundary between the dominance of coccolithophores to the north and diatoms to the south (Honjo, 2004). Macro- and micronutrients are more abundant than in the SAZ. The region is characterized by a significant increase in phytoplankton biomass in the frontal area and by high abundances of large diatoms (Kopczynska et al., 2001). From the PF to the south, up to two-thirds of the opal burial in the world takes place in the so-called opal belt (e.g., Chase et al., 2015; Geibert et al., 2005; Tréguer & Jacques, 1992).

Between the PF and the northern limit of the Seasonal Ice Zone, the well-mixed POOZ is located. In this area, waters are predominantly HNLC, showing even less chlorophyll-*a* concentrations than the SAZ (Kopczynska et al., 2001). However, in some areas of the POOZ, primary production is enhanced due to increased iron concentrations *via* upwelling or sediment input from sub-Antarctic islands (Pollard et al., 2002).

South of the POOZ is the Antarctic Zone, which can be sub-divided into the i) Seasonal Sea Ice Zone, that encompasses the region between the winter maximum and summer minimum of sea ice cover, where

productivity varies greatly at small spatial and temporal scales due to changes in snow cover, ice thickness, surface flooding, and ice rafting; ii) Marginal Ice Zone, where the dense sea ice pack transitions to open ocean defines it as an area of high export production, accounting for the majority of the spring-summer phytoplankton blooms, and iii) the highly productive Antarctic Coastal and Continental Shelf Zones (Deppeler & Davidson, 2017).

## **1.2. Oceanography and geomorphological features of the Drake Passage**



The DP, named after Sir Francis Drake, who carried out the second circumnavigation of the world in the 16<sup>th</sup> century, is the separation between South America and the Antarctic Peninsula (figure 1.2). It is *ca.* 850 km wide and represents the only bottleneck for the flow of the ACC. Here, the fronts of the ACC are squeezed together, resulting in *ca.* 350 km between the SAF and the PF instead of the *ca.* 900 and *ca.* 500 km of distance reached in certain areas of the Indian and Pacific sectors, respectively. In the DP, the bulk of the geostrophic transport of the ACC is associated with these two fronts, as indicated by strong surface and bottom velocities (e.g., Provost et al., 2011; Renault et al., 2011; figure

1.2), and by a mean near-bottom transport of 45.6 Sv between 2007 and 2011 (Donohue et al., 2016).

The opening of the DP, together with the opening of the Tasmanian gateway, led to the development of the ACC at *ca.* 24 Ma (Pfuhl & McCave, 2005), which is thought to have contributed to the thermal isolation of Antarctica (Barker, 2001) and to the abrupt growth of extensive Antarctic ice sheets during the Eocene-Oligocene climate deterioration (Livermore et al., 2005). However, other works have questioned the importance of the ACC in developing full Antarctic glaciation (e.g., Barker et al., 2007).

Geologically, the main structure of the DP is the Shackleton Fracture Zone, an intra-oceanic ridge in the center that separates the Scotia Plate to the east from the Antarctic Plate to the west. The Shackleton Fracture Zone intersects two extinct spreading centers, the West Scotia Ridge and the Phoenix Antarctic Ridge, the latter limits in the southwest with the Hero Fracture Zone (Bohoyo et al., 2019; figure 1.2).



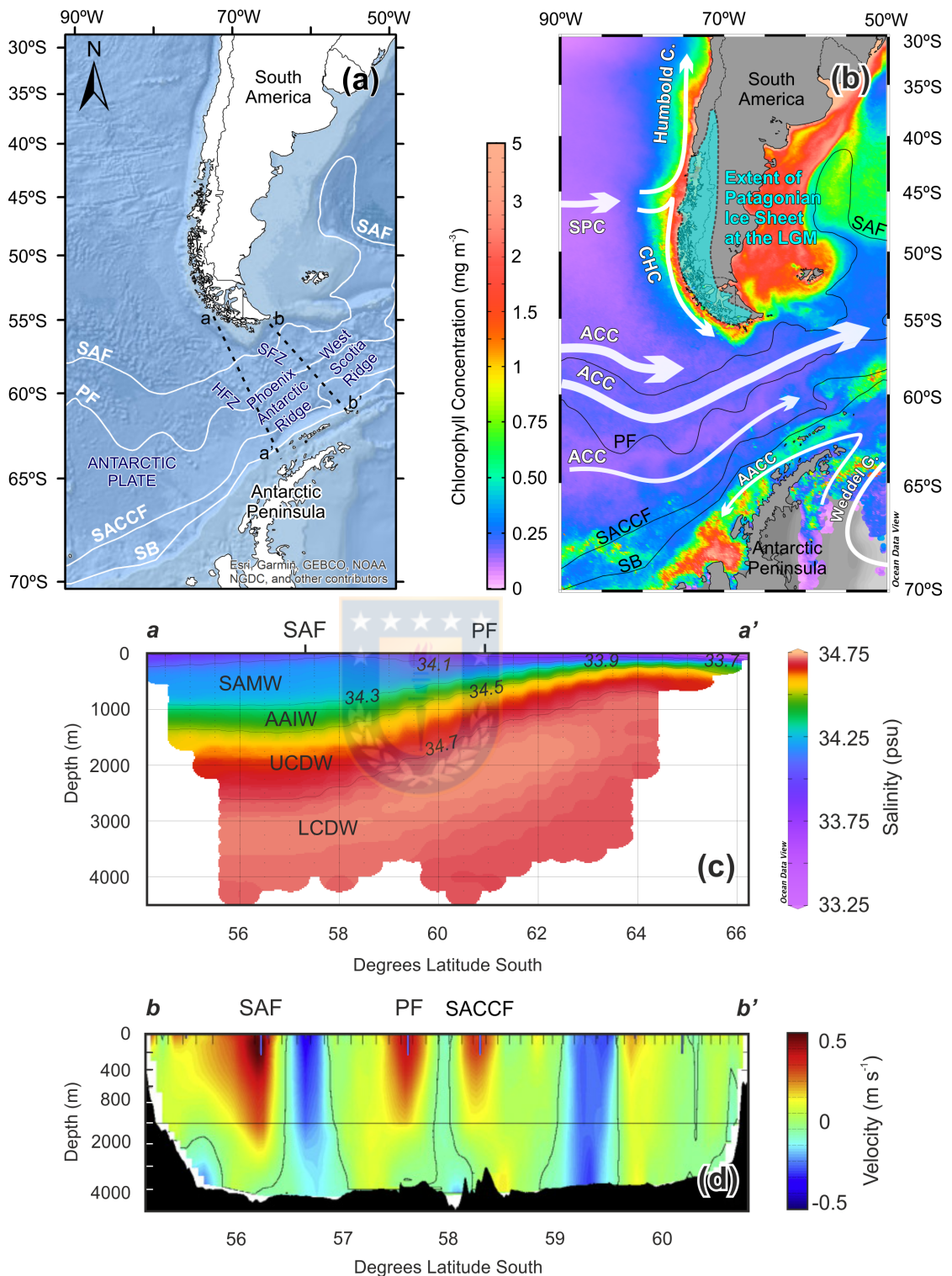


**Figure 1.2** (a) Bathymetric map of the Drake Passage area showing the location of the modern SO fronts (Orsi et al., 1995; White lines), and the main geomorphological features: SFZ, Shackleton Fracture Zone; HFZ, Hero Fracture Zone. Black dashed lines a–a' and b–b' are two hydrographic transects shown in (c) and (d). (b) Map of the Drake Passage mean chlorophyll-*a* concentrations for the years 2009–2019

showing the trajectories of the Antarctic Circumpolar Current (ACC), South Pacific Current (SPC), Cape Horn Current (CHC), Humboldt Current (Strub et al., 2019), and Antarctic Coastal Current (AACC, Deacon, 1984; white arrows). Black lines mark ACC modern fronts (Orsi et al., 1995). SAF, Subantarctic Front; PF, Polar Front; SACCF, Southern Antarctic Circumpolar Current. Cyan area indicates the extension of the Patagonian Ice Sheet at the Last Glacial Maximum based on Glasser et al. (2008). (c) Salinity section across the Drake Passage (data from Gouretski & Koltermann, 2004). LCDW, Lower Circumpolar Deep Water; UCDW, Upper Circumpolar Deep Water; AAIW, Antarctic Intermediate Water; SAMW, Sub-Antarctic Mode Water. (d) Geostrophic flow velocities across the Drake Passage from Renault et al. (2011).

The main deep and intermediate water masses that bathe the DP are shown in figure 1.2c: i) The most voluminous water mass is the Circumpolar Deep Water, which is subdivided in LCDW and UPCW. The LCDW is characterized by a salinity maximum (34.70–34.75 psu) (Gordon, 1975; Orsi et al., 1995). It consists of a mixture of North Atlantic Deep Water (NADW) that enters the SO through the Atlantic and is transported east around the Antarctic continent while mixing with waters from the Indian and Pacific oceans and dense waters from Antarctica (Carter et al., 2008). The UCDW, located above the LCDW at a depth range of ~1400 to 2500 m, is characterized by an oxygen minimum and high nutrient concentrations. At depths shallower than 1400 m, we find ii) the Antarctic Intermediate Water (AAIW), and iv) the Sub-Antarctic Mode Water (Carter et al., 2008). In the DP, the export of fresh and cold AAIW and Sub-Antarctic Mode Water *via* the “Cold Water Route” strongly influences the upper limb of the Atlantic Meridional Overturning

Circulation (AMOC), together with the inflow of warm and salty water masses through the Agulhas Current System into the South Atlantic (“Warm Water Route”, Gordon, 1986; Rühls et al., 2019; figure 1.1). Below the depth of AAIW, the deep-water masses tend to return equatorward across the relatively strong and narrow Atlantic DWBC.

In the DP, the mean annual chlorophyll-*a* concentrations are very low, suggesting that it is not an area of intensive phytoplankton growth (Graham et al., 2015). Here, primary production is strongly controlled by Fe availability, and phytoplankton blooms occur in austral spring (de Baar et al., 1995; Demidov et al., 2011). Additionally, north of the PF, the lack of dissolved silica limits the phytoplankton species' growth dependent on this nutrient (mainly diatoms, Demidov et al., 2011; Freeman et al., 2019). Accordingly, an analysis of surface sediments shows that sediment composition varies latitudinally, conforming to the oceanographic fronts and sea-ice dynamics close to Antarctica. Thus, there is a N-S gradual change from sediments low in organic carbon and high carbonate contents in the SAZ to opal-rich sediments in the PF and POOZ (Cárdenas et al., 2019).

The provenance of terrigenous materials that settle on the ocean floor of the DP is from regional sources, specifically Patagonia in the

northern part and the West Antarctic Peninsula in the south (Wu et al., 2019). Given the direction of the SWW, Patagonian dust is predominantly transported eastward to the SO's Atlantic sector (Li et al., 2008, 2010). Furthermore, analysis of surface sediments of the eastern Pacific sector of the SO and the DP excludes a significant modern dust contribution (Wengler et al., 2019; Wu et al., 2019). Therefore, we assume minor dust transport and impact either from southern South American or Australia/New Zealand sources.

Given that in the northern part of the DP, the provenance of the terrigenous material is restricted to southern Patagonia (Wu et al., 2019), we expect temporal changes in the nature of sediments that reached the seafloor since the Patagonian Andes were covered by a continuous mountain ice sheet at least five times during the last millions of years (e.g., Rabassa et al., 2011). Studies suggest that the ice cover extended from 37°S to the Cape Horn and the Pacific Ocean on the western side, south of Chiloe island (Davies et al., 2020; Rabassa, 2008; Rabassa et al., 2011; figure 1.2b).

### **1.3. Changes in the intensity of the ACC and SO export production through time**

The grain size of the sortable silt fraction of the sediments has been used to reconstruct past ACC flow speed in the DP area and downstream (Lamy et al., 2015; McCave et al., 2014; Roberts et al., 2017; Wu et al., 2021). For the last glacial cycle, the reconstruction by Lamy et al. (2015) based on sediment records from the Chilean and southernmost Argentinean continental margins, shows a significant glacial decrease in DP throughflow over the past 65 kyr. A similar glacial decrease was found by Wu et al. (2021) in the central DP near the PF, for the past 140,000 years. On the Atlantic side, south of the Falkland/Malvinas Islands and immediately downstream of the subantarctic DP, Roberts et al. (2017) also reported a reduction in current speed during the LGM. In contrast, McCave et al. (2014), based on sediment cores from the Scotia Sea, concluded that there was no significant change in the ACC flow strength between the LGM and the Holocene. On longer timescales, the two available current speed reconstructions suggest a weakening of the ACC during glacials; one of these records is from the Subantarctic Indian sector (Mazaud et al., 2010), and the other from the DWBC east of New Zealand

(Hall et al., 2001), whose signal is thought to be directly connected to ACC changes (Carter & McCave, 1997).

Overall, the SO is characterized by two modes of glacial/interglacial change in marine productivity (Jaccard et al., 2013). In the Antarctic Zone, export production decreased during glacials, coinciding with declining atmospheric CO<sub>2</sub> concentrations, indicating a reduced exchange of CO<sub>2</sub> between the ocean interior and the atmosphere (Jaccard et al., 2013). This reduction in glacial export production was documented in marine cores of the Atlantic (Jaccard et al., 2013), Pacific (Studer et al., 2015) and Indian (Thöle et al., 2019) sectors of the SO. In contrast, the SAZ experienced a glacial increase in export production, coinciding with increased dust fluxes, suggesting iron fertilization of subantarctic phytoplankton (Jaccard et al., 2013; Martínez-García et al., 2009). This hypothesis is supported by other studies showing that the availability of Fe controls carbon export production in the Atlantic (Anderson et al., 2014; Martínez-García et al., 2014), central Pacific (Lamy et al., 2014) and Indian (Thöle et al., 2019) subantarctic sectors of the SO. Furthermore, it has been suggested that such changes in the SO biological carbon pump efficiency could be one of the main sources of the

glacial/interglacial variability in atmospheric CO<sub>2</sub> (e.g., Anderson et al., 2002; Kohfeld et al., 2005; Sarmiento & Toggweiler, 1984).

Under open ocean conditions, iron fertilization can occur through increased dust input, upwelling of Fe replete deep water, cross-shelf export, release of terrigenous Fe from icebergs (Shaw et al., 2011), and hydrothermal venting (Fitzsimmons et al., 2014; Klunder et al., 2011). If we focus on the SAZ, it is widely believed that the main mechanism of Fe fertilization during glacials is primarily dust deposition (Martínez-García et al., 2014; Martínez-García et al., 2009). Reconstruction of the past glacial-interglacial variability of the SWW belt supports this idea. Several authors (Ho et al., 2012; Kohfeld et al., 2013; Lamy et al., 2014) have shown a glacial strengthening and an equatorward migration of the wind belt. On orbital timescales, the major step in the SO dust deposition occurs across the Mid-Pleistocene Transition (MPT; figure 1.3, Martínez-García et al., 2011)), when dust flux increased during the stronger ice ages of the post-MPT time as well as opal mass accumulation rates in the Atlantic sector of the SO (Cortese & Gersonde, 2008).

Apart from dust, an increasing number of studies have shown that icebergs could provide a significant amount of bioavailable Fe to the SO, and therefore have an impact on export production (Hopwood et al., 2019;

Wu & Hou, 2017). For instance, Wadham et al. (2019) have recently suggested that a combination of high ice discharge and slower iceberg melting might have increased the supply of Fe-rich terrigenous material in the SAZ during the LGM.

#### **1.4. Orbital configuration of the Earth over the past 1.3 Ma.**

This thesis encompasses a space of time of 1.37 Ma., which includes two main climatic transitions (figure 1.3): 1) the Mid-Pleistocene Transition (MPT, between 1.25 and 0.7 Ma., Clark et al., 2006; Elderfield et al., 2012), and 2) the Mid-Brunhes Event (MBE), at Marine Isotope Stage (MIS) 12/11 boundary, *ca.* 430 ka. ago (Holden et al., 2011).

During the MPT, the cyclicity of ice ages switched from occurring every 41,000-year to every 100,000-year in the absence of substantial change in orbital forcing (figure 1.3; e.g., Farmer et al., 2019a), representing a fundamental reorganization of Earth's internal climate system. Approximately 900 ka. ago, glacial-interglacial cycles started to occur with a longer duration and a marked increase in the amplitude of global ice volume variations (Elderfield et al., 2012), and by 700 ka ago, the change in amplitude was complete in most records (Past Interglacials Working Group of PAGES, 2016, and references therein).



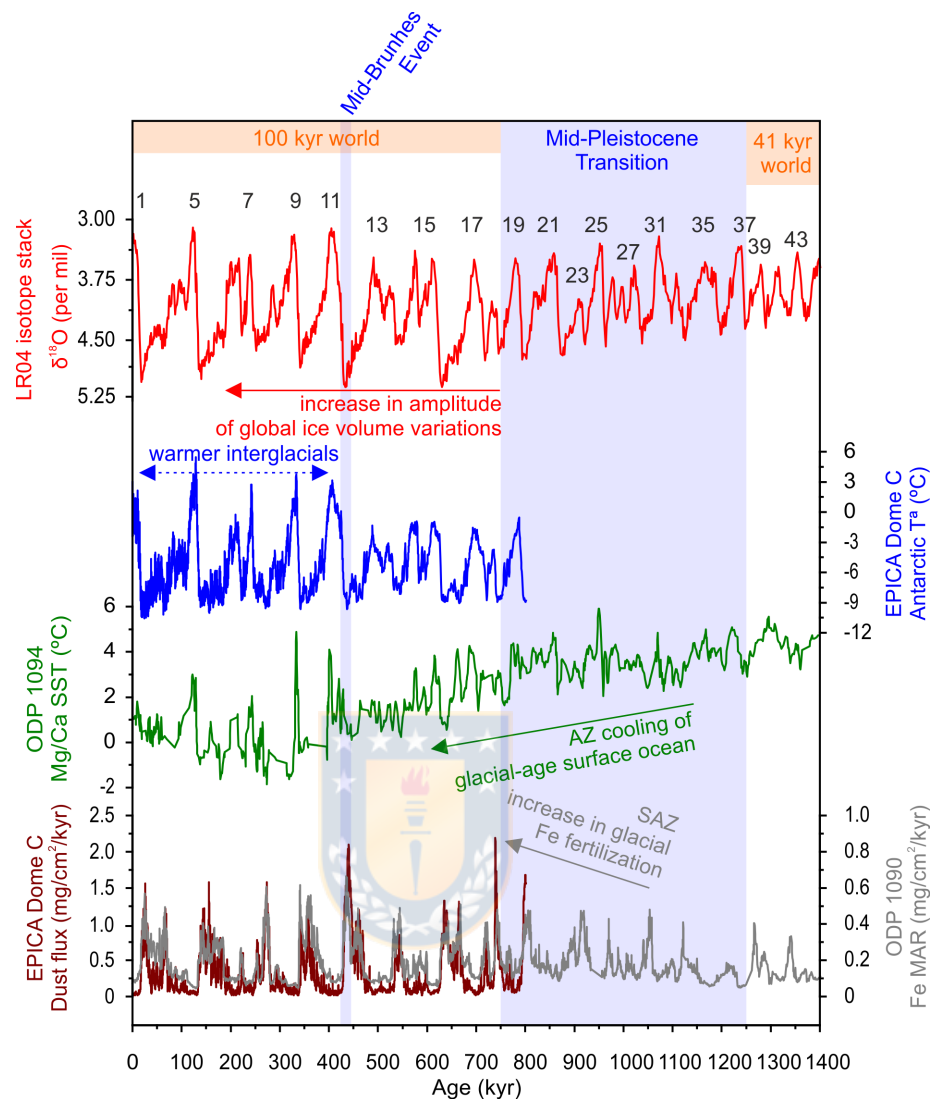


**Figure 1.3** Evolution of some key records over the past 1.4 million years that show the global and oceanographic changes across the Mid-Pleistocene Transition and the Mid-Brunhes Event. From top to bottom: Red, LR04 benthic  $\delta^{18}\text{O}$  stack (Lisiecki & Raymo, 2005), as a reference record of global ice volume fluctuations, numbers indicate interglacial stages; Blue, Antarctic air temperature changes (Jouzel et al., 2007); Green, Southern Ocean ODP site 1094 Sea Surface Temperature (SST) derived from *N. pachyderma* (s.) Mg/Ca (Hasenfratz et al., 2019); Dust and iron deposition records, Antarctic Dust flux (brown, Lambert et al., 2008), and mass accumulation rates of iron at ODP site 1090 (grey, Martínez-García et al., 2011). Blue shadows mark the Mid-Brunhes Event and the Mid-Pleistocene Transition.

In the SO, some of the changes linked to the MPT are: i) An increase in stratification and reduced upwelling during glacial times (Hasenfratz et al., 2019); ii) enhanced nutrient export in the eastern equatorial Pacific

potentially caused by a northward migration of fronts (Robinson et al., 2019); and iii) an equatorward extension of polar surface water masses (Martínez-García et al., 2011). Furthermore, across the MPT, there is evidence of a global increase in productivity, but the changes were not synchronous worldwide and likely reflected regional hydrographic variability (Diester-Haass et al., 2018).

The main characteristic feature of the MBE is that interglacials after this event (post-MBE) were substantially warmer with higher CO<sub>2</sub> concentrations than previous interglacials (Holden et al., 2011; Yin & Berger, 2012). Specifically, atmospheric CO<sub>2</sub> levels during interglacials before the MBE were around 40 ppm lower than post-MBE (Bouttes et al., 2018). Furthermore, after the MBE, the amplitude of glacial-interglacial climate cycles increased significantly as recorded in marine oxygen isotope and Antarctic ice core records (Jouzel et al., 2007; Lisiecki & Raymo, 2005), indicating that pre-MBE interglacials experienced a colder climate than the more recent ones (post-MBE). This trend is supported by records of  $\delta^{18}\text{O}$  and SST from marine sediment cores (e.g., Lang & Wolff, 2011; PAGES, 2016, and references therein). The MBE also represents a period of global carbonate dissolution, which paradoxically is also distinguished by increased CaCO<sub>3</sub> accumulation at

low latitudes (Barker et al., 2006). Specifically, in the SO, the MBE is characterized as a period of amplified carbonate accumulation (Hodell et al., 2000). As is the case for the MPT, the processes that triggered the MBE are still under debate (figure 1.3).

### **1.5. Motivation of this study**

The DP is the only constriction in the ACC flow pathway, and therefore the most important oceanic gateway of the SO (e.g., Rintoul & da Silva, 2019). Within the DP, one-half of the total modern throughflow transport occurs in the SAZ (Koenig et al., 2016), thus resolving glacial-interglacial changes in the ACC throughflow here is crucial for a better understanding of the global climate system. Consequently, this thesis is based on a core collected at the Pacific entrance of the DP, in the vicinity of the SAF within the main flow of the ACC.

In addition, the potential role of the Subantarctic DP throughflow in driving changes in global MOC on glacial-interglacial is not well constrained, leading up to disagreements between published works, as mentioned before (Lamy et al., 2015; McCave et al., 2014; Roberts et al., 2017). To sum it up, there are remarkably few records (only two) of ACC flow in the SO older than the last two glacial-interglacial cycles, despite the importance of the ACC for the global climate system. Constraining the

ACC's temporal variations during glacial-interglacial cycles in the Pleistocene is one of the motivations of this thesis.

Enhanced biological export production in the SAZ of the SO during glacials, fueled by enhanced dust-borne Fe fertilization, is thought to be one of the key mechanisms that contributed to the lowering of atmospheric CO<sub>2</sub>. However, a substantial contribution of dust in the Subantarctic southeastern Pacific is not expected due to prevailing westerly winds (Wengler et al., 2019; Wu et al., 2019). On the other hand, the proximity of Patagonia to the study area, as a potential source of Fe *via* meltwater and/or icebergs, and the lack of past export production reconstructions in the area constitutes a second motivation. Thus, we set out to explore the Patagonian Icefield's potential role as a direct source of Fe for the fertilization of the southeastern Pacific during glacial intervals. In addition, we investigated the role of frontal shifts related to the Si(OH)<sub>4</sub> inventory and ACC dynamics.

Lastly, resolving ACC changes and the degree of sediment redistribution by using two independent proxies gives us the unprecedented opportunity to explore the potential of bottom-current circulation affecting the sedimentation patterns at the DP entrance.

Therefore, based on the discrepancies exposed above in relation to ACC flow intensity and the scarcity of paleoproductivity reconstruction studies in the DP area, the following key questions motivated this thesis: How has the flow of circumpolar bottom water through the DP changed over and beyond the last million years? Have these changes impacted the dynamics of the Meridional Overturning Circulation? How has the ACC bottom current dynamics affected sedimentation patterns in the DP through time? Was dust-borne iron fertilization the main driver of export production in the Subantarctic Drake Passage during glacials? Are there differences in the amplitude and strength of ACC bottom current and export production changes related to the Mid-Pleistocene Transition and the Mid-Brunhes Event?

## 2. HYPOTHESES AND OBJECTIVES/ HIPÓTESIS Y

### OBJETIVOS

#### 2.1. Hypotheses

In order to answer the previous questions, the following null-hypotheses have been tested:

- **Hypothesis A0:** At the Drake Passage entrance, the strength of the Antarctic Circumpolar Current does not vary significantly at glacial-interglacial timescales, and therefore, changes in the global Meridional Overturning Circulation originating from the ACC are not expected.
- **Hypothesis B0:** Although the subantarctic Drake Passage is an area of highly dynamic bottom currents, sediment accumulation rates are not influenced by redistribution processes (focusing/winnowing).
- **Hypothesis C0:** Dust-borne iron fertilization is the main driver of enhanced export production during glacial times in the subantarctic Drake Passage.
- **Hypothesis D0:** The amplitude and pattern of glacial-interglacial changes in the Antarctic Circumpolar Current strength and export production in the subantarctic Drake Passage have not been influenced by the Earth's major climate changes (Mid-Pleistocene Transition and Mid-Brunhes Event) over the past 1.3 Ma.

## 2.2. Objectives

The general objective of this thesis is to reconstruct fluctuations in the intensity of ACC flow and past productivity changes in the subantarctic SE Pacific over the past ca.1.3 Myr based on a multi-proxy approach of core PS97/093- 2 (figure 2.1). This core was collected at the Pacific entrance of the DP, in the vicinity of the SAF within the main flow of the ACC. It represents the only record in the DP area that reaches beyond the longest Antarctic ice-core record (800,000 years), giving us the unprecedented opportunity to study glacial-interglacial changes in ACC strength and productivity, and thus contributing with new knowledge on Southern Ocean Quaternary paleoceanography. This study of longer-term paleoceanographic changes in the SO will become even more important in the future, as international initiative to prolong ice-core records beyond 1 Ma are currently underway (Beyond EPICA – Oldest Ice (BE-OI)).

To reach these goals and address the hypotheses, the specific objectives are as follows:

- i) To develop an age model for core PS97/093-2, providing the stratigraphic framework for ACC flow strength, lithogenic and productivity records. This will be based on biostratigraphic time markers

from calcareous nannofossils and diatoms, and tuning of the X-ray fluorescence (XRF)-scanner Fe and Ca counts to the benthic  $\delta^{18}\text{O}$  stack (Lisiecki & Raymo, 2005).

ii) To use the  $\overline{\text{SS}}$  proxy in core PS97/093-2, to reconstruct changes in ACC strength. These data will be combined with XRF scanner-derived Zr/Rb ratios to obtain a high-resolution record of bottom water circulation changes for the last *ca.* 1.3 Ma.

iii) To reconstruct and characterize past ocean productivity changes in core PS97/093-2 using carbonates, biogenic opal, total organic carbon, and excess of barium mass accumulation rates. To achieve the additional goal of evaluating if glacial productivity was fueled by iron fertilization at site PS97/93, lithogenic and Fe records will be generated for comparison with the productivity data.

iv) To use  $^{230}\text{Th}$  normalized mass accumulation rates over the first *ca.* 400 kyr of core PS97/093-2 to correct for the effect of syndepositional redistribution.

v) To document and integrate the consequences of past current strength and productivity changes in the subantarctic SE Pacific. This will be achieved by comparing the results of this thesis with selected works of  
i) Southern Ocean current strength reconstructions (Cores and Sites



ODP1123, MD07-3128, MR0806-PC09, MD00-2375G, 1 to 12 McCave et al (2014), and GC528; Hall et al., 2001; Lamy et al., 2015; Mazaud et al., 2010; McCave et al., 2014; Roberts et al., 2017; figure 2.1); ii) Subantarctic export production reconstructions based on  $^{230}\text{Th}_{\text{xs}}$ -normalized mass accumulation rates (Cores and Sites PS2498-1, TN057-06, TN057-21, PS75/059, PS75/076, ODP 1090, and MD11-3357; Anderson et al., 2014; Lamy et al., 2014; Martínez-Garcia et al., 2009; Thöle et al., 2019; figure 2.1), and iii) long-term export production reconstructions in the SO (Cores and Sites ODP 1088, ODP 1089, TN057-21, TN057-10, ODP 1094, ODP 1090, PS75/059, PS75/076, and PS75/079; Farmer et al., 2019b; Gottschalk et al., 2018; Jaccard et al., 2013; Lawrence et al., 2013; Martínez-Garcia et al., 2011; Saavedra-Pellitero et al., 2017a; figure 2.1).

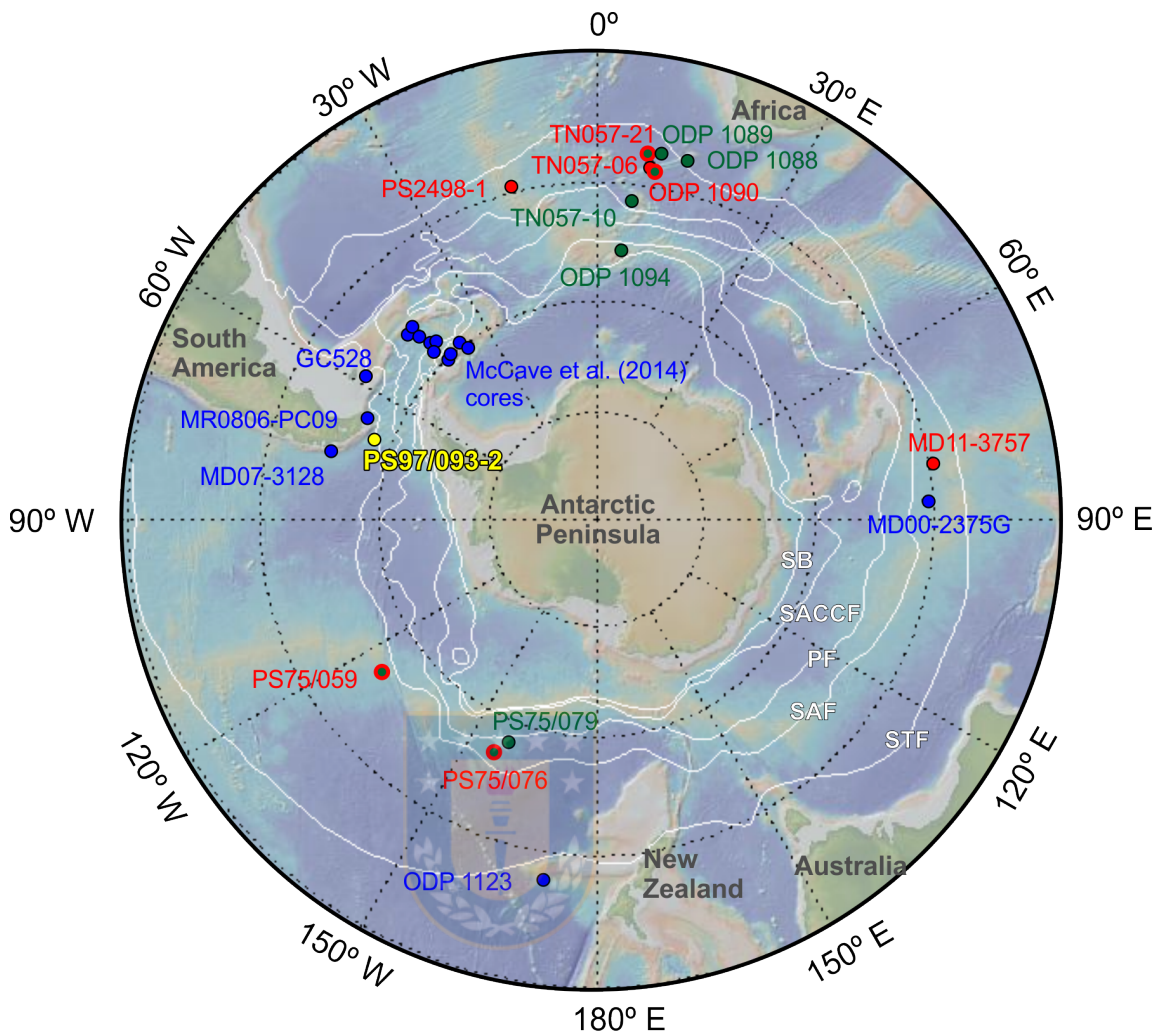


**Figure 2.1** Southern Ocean map showing the location of sediment core PS97/093-2 (yellow), and all cores used for comparison and discussion (blue indicates the location of the SO current strength reconstructions; red color marks the location of the export production reconstructions based on  $^{230}\text{Th}_{\text{xs}}$  normalized mass accumulation rates; green indicates long-term paleoproductivity and  $\text{CaCO}_3$  reconstruction; green circles with red rim refer to those core that were used for  $^{230}\text{Th}$ -based and long-term reconstructions. White lines show the ACC oceanographic fronts and boundaries according to Orsi et al. (1995): STF, Subtropical Front; SAF, Subantarctic Front; PF, Polar Front, SACCF, Southern Front of the ACC; SB, Southern Boundary of the ACC.

### 3. MATERIAL AND METHODS/ MATERIALES Y

#### MÉTODOS

The methodological approach of this thesis relies on the measurements of numerous geochemical and physical proxies in the marine sediments of core PS97/093-2 (figure 3.1).

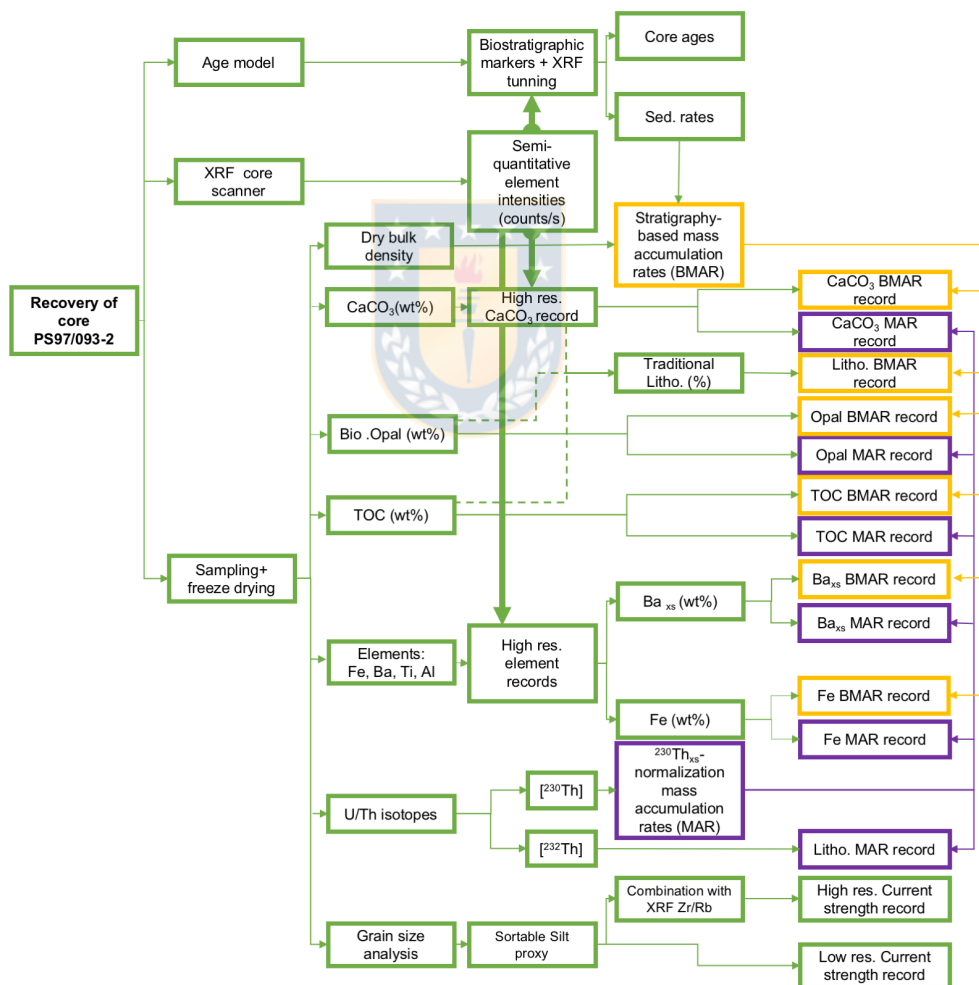


**Figure 3.1** Schematic workflow diagram of the analytical steps of this thesis. Yellow and purple squares indicate mass accumulation rates of individual components estimated through either the  $^{230}\text{Th}_{\text{xs}}$ - normalization method (purple) or multiplication of the sedimentation rates by the dry bulk density (yellow).

### 3.1. Sediment core material

Piston core PS97/093-2 (57° 29.94' S; 70° 16.48' W; 16.45 m in length) was recovered on March 20, 2016 onboard R/V Polarstern during expedition PS97 “Paleo Drake” (Lamy, 2016). The core site is located *ca.* 40 km NW of the present-day position of the SAF, within the main flow of the ACC, and bathed in LCDW.

After opening and splitting of the core, the core sections were photographed onboard (see appendix A.1.). Additionally, core description (color, lithology, texture) was performed on the archive half at sea (figure 3.2, and appendix A.2.). Overall, whitish-gray to white calcareous oozes (nannofossil or foraminifera-nannofossil oozes) with only minor concentrations of diatoms characterize the interglacial sediments. Dark clayey silts with rare biogenic components and intercalated diatomaceous fine-grained clayey silts constitute the glacial and transitional sediments. Some of these intervals, described as diatomaceous silt, are moderately bioturbated, and more greenish-gray in color. Within the sediment core, ten well-defined calcareous oozes were identified. For more information, see appendix A.2.

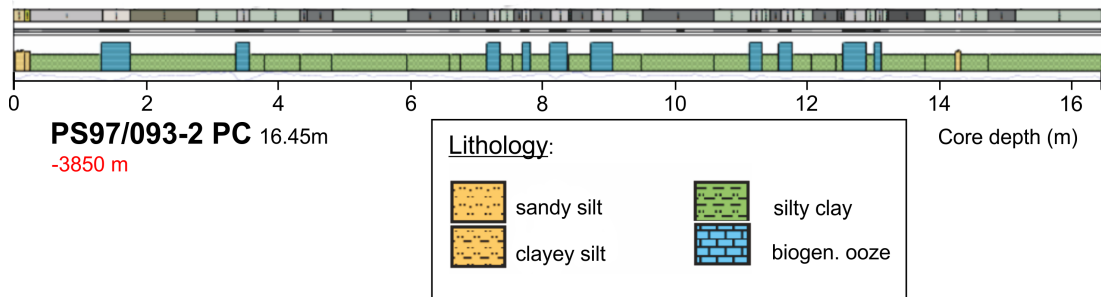


**Figure 3.2** Schematic lithology logs of core PS97/093-2 (Lamy, 2016).

After collection, the physical properties of core PS97/093-2 (gamma ray density and magnetic susceptibility) were measured onboard (density and magnetic susceptibility records are shown in appendix A.3). The working half of core PS97/093-2 was sampled onboard every 10 cm for bulk sediment parameters (density, water content, carbonates and total organic carbon).

### 3.2. XRF core scanning

XRF core scanning provides rapid high-resolution records of chemical composition on split sediment cores; the measurements are non-destructive and cover the atomic mass range from Al to U (Richter et al., 2006). The XRF core scanner results are inherently semi-quantitative, yet it provides reliable records of the variability in elemental composition downcore (Richter et al., 2006).

Therefore, for high-resolution of semi-quantitative element intensities, the archive half of core PS97/093-2 was measured with an

AVAATECH XRF Core Scanner at the Alfred Wegener Institut (AWI), Bremerhaven, at 0.5 cm resolution. The core scanning preparation was carried out following Richter et al. (2006), which included careful flattening of the sediment surface to remove irregularities from core slicing and covering of the sediment surface with a 4  $\mu\text{m}$  thick Ultralene film to protect the probe of the scanner from contamination and to prevent desiccation of the sediment. Each section was triple-scanned at different tube voltages (10, 30, and 50 kV) with 30 seconds of counting time to cover a wider range of elements. Raw data were processed using Canberra *Eurisys* ' interactive least squares software (WIN AXIL) package.

In this study, we use the 3-point smoothed XRF Ca, Fe, Ba, and Ti counts to calibrate and get high-resolution records of  $\text{CaCO}_3$ , Fe, Ba, and Ti (wt%), and the 5-point smoothed XRF scanning-derived Zr/Rb count ratio as a proxy for fine sediment grain size variations and calibration with the sortable silt proxy.

### **3.3. Geochemistry and bulk sediment parameter**

Once on land, the sediment core was stored at 4°C in the core storage facilities of AWI. Core PS97/93-2 was sampled with metal spatulas every cm and immediately frozen at minus 20 °C for several days. Then, the frozen samples were freeze-dried.

For dry bulk density determination, we used a total of 162 freeze-dried and homogenized samples, chosen at 10 cm intervals. The analyses were performed with a gas pycnometer (Micromeritics AccPyc II 1340) at AWI.

Total carbon and nitrogen (TC, TN) were quantified using a CNS analyzer (Elementar Varia EL III) at AWI using 100 mg of freeze-dried and homogenized sediments. Total organic carbon (TOC) contents were measured with a carbon-sulfur determinator (CS-2000, ELTRA) after the removal of inorganic carbon (total inorganic carbon) by adding 37% (vol/vol) of hydrochloric acid.  $\text{CaCO}_3$  was calculated employing the standard equation:

$$\text{CaCO}_3 \text{ [wt.\%]} = (\text{TC [wt.\%]} - \text{TOC [wt.\%]}) * 8.333.$$

Samples for TOC and  $\text{CaCO}_3$  analysis were taken at 10 cm intervals. To get a high-resolution record of  $\text{CaCO}_3$ , we calibrated the 3-point smoothed XRF Ca intensities with the bulk sediment  $\text{CaCO}_3$  ( $r^2=0.91$ ;  $P<0.0001$ ;  $n=157$ ) measurements.

A total of 770 samples collected at 2-cm resolution were used for biogenic opal content (wt%) analysis at the Laboratory of Paleooceanography, University of Concepción (UdeC), Chile. The alkaline extraction was conducted following the procedure described by

Mortlock & Froelich, (1989), but using NaOH as a digestion solution (Müller & Schneider, 1993). Between fifty to seventy milligrams of freeze-dried sediment were first treated with 10% H<sub>2</sub>O<sub>2</sub> and 1N HCl, and then extracted with 1M NaOH (40 mL; pH~13) at 85 °C for five hours. The analysis was carried out by molybdate-blue spectrophotometry. Values are expressed as biogenic opal by multiplying the Si (%) by 2.4 (Mortlock & Froelich, 1989). We did not correct for the release of extractable Si from coexisting clay minerals, and thus biogenic opal values could be overestimated (Schlüter & Rickert, 1998). Biogenic opal was also measured at AWI Bremerhaven using the sequential leaching method of Müller & Schneider (1993) at much lower temporal resolution, and offsets between the overlapping data sets were observed. For terrigenous contents exceeding 70%, opal concentrations measured at UdeC are consistently 3–5% higher than those measured at AWI. When the lithogenic content was below 40%, the inter-lab difference was less than 1%. Despite the difference in values, both records show a similar pattern of variability. Given the importance of high-resolution data, we here use the opal results from UdeC.

For measuring element concentrations of Fe, Ba, and Ti, approximately 100 mg of 132 freeze-dried samples were treated by



complete acid digestion following Fleisher & Anderson (2003). After digestion, 0.4 ml were diluted again in 0.5 HNO<sub>3</sub> to get a total dilution of 2000x for sediment sample, that was used for determination of Fe, Ti and Ba concentrations. Element concentrations were measured on an Element 2 ICP-MS. All chemical sample preparations and measurements were performed at Lamont-Doherty Earth Observatory (LDEO). To get high-resolution records of Fe, Ba, and Ti, we calibrated the 3-point smoothed XRF Fe, Ba, and Ti intensities with the bulk sediment Fe ( $r^2=0.90$ ;  $P<0.0001$ ;  $n=132$ ), Ba ( $r^2=0.76$ ;  $P<0.0001$ ;  $n=132$ ), and Ti ( $r^2=0.79$ ;  $P<0.0001$ ;  $n=132$ ) measurements.

Excess of barium ( $Ba_{xs}$ ) has been used in many studies to infer past productivity changes after the seminal work of Dymond et al. (1992) (e.g., Frank et al., 1999; Nürnberg et al., 1997; Winckler et al., 2016).  $Ba_{xs}$  was calculated as:

$$Ba_{xs} = Ba_{total} - (Ti_{total} * [Ba/Ti]_{detrital}).$$

$Ba_{xs}$  (total barium minus the fraction associated with terrigenous material) was determined from the total Ba concentration in the sediment after subtracting the Ba associated with terrigenous material, which is calculated from total Ti, and normalization to a constant detrital Ba/Ti ratio. In this thesis we used 0.126 for the  $[Ba/Ti]_{detrital}$  after Turekian &

Wedepohl (1961). Calculation of  $Ba_{xs}$  assumes that 1) the major source of elemental Ba to deep sea sediments is marine barite, and 2) terrigenous material has a known and constant Ba/Ti ratio.

### 3.4. Age model

The sediment record of core PS97/093-2 reached back to ~1.37 Ma and thus covers MIS 1 to MIS 44. To establish the age model, we used a two-step approach. First, we obtained a preliminary age based on onboard physical properties data and biostratigraphic time markers from calcareous nannofossils and diatoms (see Table 1 in Toyos et al., 2020). Secondly, we used the high-resolution XRF scanner-derived records of Fe and Ca counts and the measured  $CaCO_3$  contents to fine-tune the PS97/093-2 record within the age ranges of the biostratigraphic dates to the benthic  $\delta^{18}O$  stack (Lisiecki & Raymo, 2005). For tuning, we assumed that low Fe contents characterize interglacial periods, whereas high values represent glacials. Additionally, we used XRF Ca counts and  $CaCO_3$  percentages for finer tuning in the intervals where they are present. Note that the initial age model published in Toyos et al. (2020) was revisited because from the bottom-core to *ca.* 1.2 Ma. the sedimentation rates increased substantially. To solve this issue, we went back over the initial age model following the steps described above and updated the age model

accordingly. The final age model has 37 tie points, all of them within the biostratigraphic datums' age ranges. The new sedimentation rates range between *ca.* 0.5 and 2.5 cm/kyr, showing less variability over time (figure 3.3). All correlations were performed with the AnalySeries software (Paillard et al., 1996).

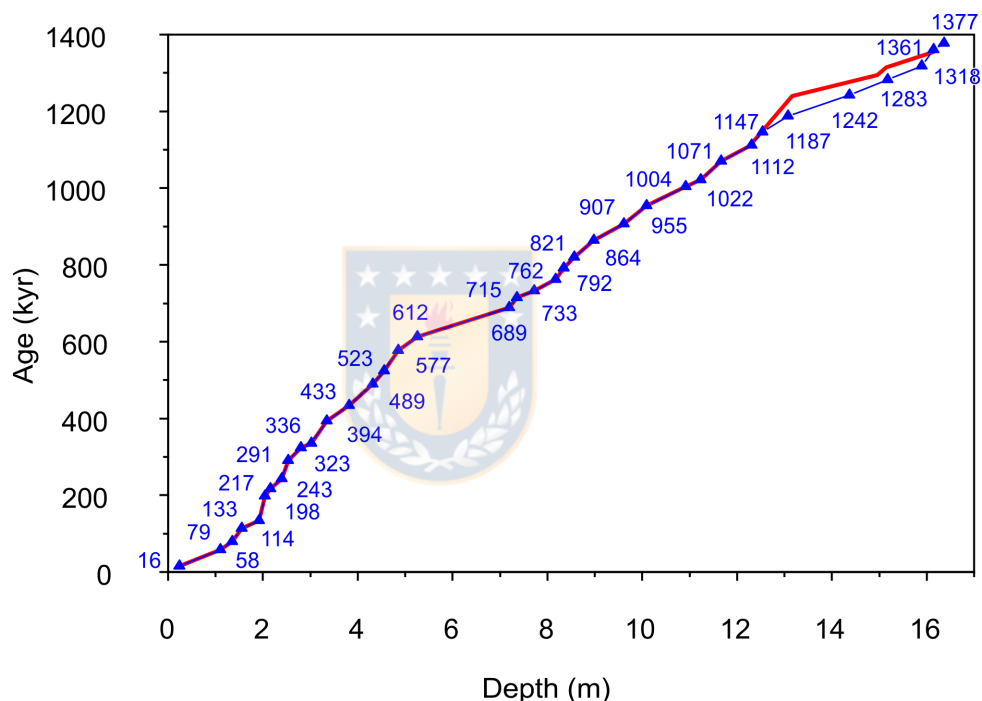


**Figure 3.3** Pointers (blue triangles), and age–depth relationship for core PS97/093-2; red line indicates the initial age model (published in Toyos et al.,2020), and blue line marks the final age model used in manuscript 3.

### 3.5. Grain size measurements

The relationship between grain size variations and current velocities has been widely investigated in geological sciences. The Hjulström curve, developed by Filip Hjulström in his doctoral thesis in

1935, constitutes the first approach of reconciling grain size fluctuations and flow speeds, establishing the relationship between grain size and horizontal velocities that result in erosion, transportation, and deposition of a sedimentary particle. Since then, numerous studies have investigated the influence of grain size in a given sedimentary record on the velocity of past currents systems (e.g., triangles of Shepard and Folk, stratification, and bedforms in sand-sized sediments such as ripples and dunes; Miller et al., 1977). In general, higher current velocities move larger grain size sediments. However, in pelagic and hemipelagic sediments, the sand fraction is mainly biogenic; thus, to examine deep-sea currents, the best approach is to focus on the fine grain sizes.

### **3.5.1. Principles of Sortable Silt as a paleoflow-speed proxy**

The sortable silt ( $\overline{SS}$ ) is a proxy for estimating paleoflow speeds of near-bottom currents; it was developed by McCave et al. (1995).  $\overline{SS}$  is the mean size of the terrigenous re-deposited silt (10–63  $\mu\text{m}$ ). Within this size range, deposition of coarser material under faster currents also involves suppression of deposition of finer sediments (McCave et al., 1995). The source of potential uncertainties regarding the applicability of the  $\overline{SS}$  proxy are ice rafted debris deposits, fine tails of turbidity deposits, or local sediment movement and redeposition caused by changes in mud waves

(McCave et al., 1995, 2017; McCave & Hall, 2006). A test for whether the sortable silt data is recording flow (rather than input) is to plot  $\overline{SS}$  versus SS% (the percentage of the <63  $\mu\text{m}$  fraction that lies in the 10-63  $\mu\text{m}$  range). Under a current sorted regime,  $\overline{SS}$  correlates positively with SS%, whereas unsorted sediments show no correlation (McCave & Hall, 2006).

Several types of instruments are available to measure grain size distributions. However, the Sedigraph is the instrument of choice for the study of deep-sea sediments as proxies for current intensity, since it is based on the settling velocity principle, and therefore measures a dynamical grain size distribution closely related to transport and depositional processes (McCave & Hall, 2006). The instrumental precision of the Sedigraph for pure standard analysis ranges from  $\pm 0.3$  to  $\pm 1.9\%$  (Bianchi et al., 1999).

### **3.5.2. Sample preparation and sortable silt measurements**

With the goal of covering all the maxima and minima of the XRF Zr/Rb curve and intervals of special interest (e.g., MIS 11, MIS 5, Holocene, where the sampling frequency is higher), we chose a total of 144 samples spacing *ca.* 15 cm along the entire sediment core for grain

size determinations. Firstly, the freeze-dried and homogenized samples were separated by size. The separation of the 63–150  $\mu\text{m}$  fine-sand portion was carried out by wet sieving. The silt (2–63  $\mu\text{m}$ ) and clay fractions (<2 $\mu\text{m}$ ) were separated by application of Stokes' law settling using Atterberg tubes (this procedure was repeated 12 to 20 times to get almost complete separation of the two fractions). Once the silt fraction is separated and to get the terrigenous fraction, we removed the organic matter, biogenic silica, and carbonates. Organic matter was eliminated with (vol/vol)  $\text{H}_2\text{O}_2$ . Opal leaching was carried out by adding 250 ml of 20% NaOH and heating to 85– 90°C for 60 minutes; thereafter, rinsing was done until the pH of the solution reached the pH of DI water (~6.5). To dissolve carbonates, we used 150 ml of 25% (vol/vol) of acetic acid. Rinsing was repeated after carbonate dissolution until the pH of the sample reached the pH of DI water again. Finally, to avoid the coagulation of particles, we added sodium polyphosphate.

A detailed grain size analysis of 2 to 8 g of the silt fraction was performed with a Micrometric Sedigraph 5010. To measure the instrumental error of the Sedigraph 5100 for our sediment samples, we repeated the analyses of 10 samples for 2 to 3 times, and 10 of the tests were replicated in the two different devices available (Unit 1 and Unit 2).

Thus, for the  $\overline{SS}$  parameter, the average error within the same instrument is  $\pm 0.18 \mu\text{m}$  (Unit 1) and  $\pm 0.13 \mu\text{m}$  (Unit 2). All chemical preparations and measurements were performed at AWI.

### **3.5.3. Zr/Rb ratio as a current speed proxy**

Previous studies showed that fluctuations in the Zr/Rb ratio could be explained by grain size variations of fine grains. In marine and lacustrine sediments, Zr is commonly associated with the relatively coarse-grained fraction of fine-grained siliciclastic sediments and with heavy minerals like zircon (Fralick & Kronberg, 1997). In contrast, Rb is usually related to fine silt and clay mineral assemblages (Fralick & Kronberg, 1997; Kylander et al., 2011). Consequently, Zr/Rb ratio has largely been used as a proxy for grain size fluctuations (e.g., Dypvik & Harris, 2001). In addition, a recent study tested the relationship between high-resolution grain-size measurements and the XRF Zr/Rb on a series of sediment cores from different SO regions, founding a good correspondence between these two parameters (Wu et al., 2020). Therefore, it supports using the Zr/Rb ratio as an indicator of bottom current strength in cases where the sediment is current sorted (Wu et al., 2020).

To increase the temporal resolution of the estimations for near-bottom current strength changes, we obtained a high-resolution record based on the significant and positive correlation between our sortable silt data and the Zr/Rb ratios. Thus, we used a linear equation between XRF core scanner-derived Zr/Rb, smoothed with a 5-point moving average, and the sortable silt data obtained with the Sedigraph.

### **3.6. Thorium isotopes analyses**

#### **3.6.1. Principles of mass accumulation rates reconstructions by**

##### **Thorium normalization**

Efforts to construct geochemical mass budgets in many areas of paleoceanographic research rely on an accurate evaluation and interpretation of particle fluxes and of sediment accumulation rates. Ocean currents transport particles laterally throughout the ocean. Therefore, geochemical mass budgets and paleoceanographic interpretations may both suffer significant errors if lateral redistribution of particles by ocean currents is not taken into account (Francois et al., 2004). Thus, in several works it has been argued that by using the particle-reactive  $^{230}\text{Th}$  radionuclide, the lateral sediment redistribution could be quantified, and the vertical rain rates reconstructed accurately (e.g., Bacon, 1984; Costa et al., 2020; Francois et al., 2004).



Here we describe the basis of the  $^{230}\text{Th}_{\text{xs}}$  normalization method (Bacon, 1984; Francois et al., 2004):

$^{230}\text{Th}$  is produced in the water column by the decay of  $^{234}\text{U}$  (figure 3.4). Uranium is highly soluble in seawater with a fairly constant concentration. The long residence time of uranium (400 kyr) leads to a relatively uniform and known production of  $^{230}\text{Th}$  across the ocean. Unlike uranium, thorium is practically insoluble in seawater, has a short residence time in the water column (20–40 years, Nozaki et al., 1981), and settles fast to the underlying sediments by proximal scavenging. The small residence time of the  $^{230}\text{Th}$  in the ocean compared to its half-life (75.5 kyr; Cheng et al., 2013) allows to consider that the flux  $^{230}\text{Th}$  scavenged from the water column is nearly equal to its production rate.

Thus, the  $^{230}\text{Th}$  normalized particle mass accumulation rates (MAR) are calculated by applying the following equation:

$$MAR = \frac{\beta \times z}{[^{230}_{\text{xs}}\text{Th}]}$$

Where  $\beta \times z$  is the integrated  $^{230}\text{Th}$  production in the overlying water column that depends on the water depth in meters ( $z$ ), and  $^{230}_{\text{xs}}\text{Th}$  is the measured  $^{230}\text{Th}$  activity after corrections for i)  $^{230}\text{Th}$  supported by  $^{238}\text{U}$  in detrital sediments, ii)  $^{230}\text{Th}$  supported by authigenic  $^{238}\text{U}$  from the seawater, and iii) radioactive decay of  $^{230}\text{Th}$  since deposition.

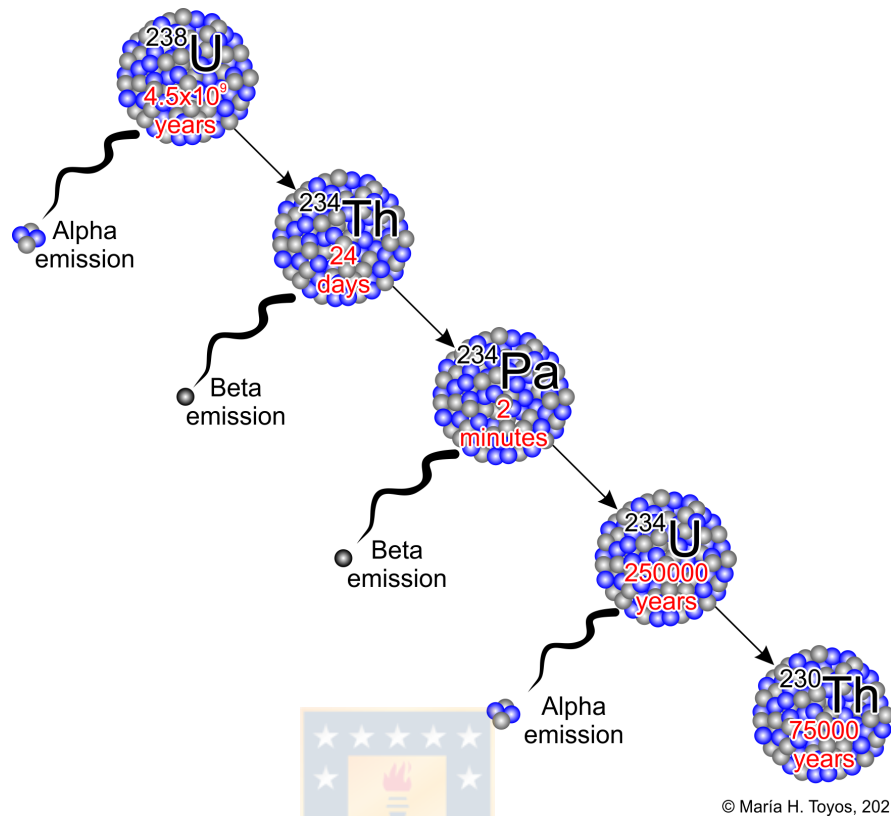


**Figure 3.4** Simplified radioactive decay chain of  $^{238}\text{U}$ . Red texts indicate the half-life of the radioactive isotopes involved in this decay chain.

### 3.6.2. U/Th isotope measurements

Sixty-eight freeze-dried and homogenized samples were used for U/Th isotopic analysis; 100 mg of each sample were spiked with a known  $^{236}\text{U} - ^{229}\text{Th}$  solution, followed by complete acid digestion (Fleisher & Anderson, 2003), and digests were taken up in  $\sim 9.6$  ml of 0.5 M  $\text{HNO}_3$ . The dilutions were processed with Fe-coprecipitation, and purification of U and Th was carried out *via* column chromatography following the methodology of Fleisher & Anderson (2003). To check for reproducibility and for quality control purposes, an internal sediment standard (VOICE

Internal MegaStandard, VIMS) was run in each batch. U/Th isotopes were measured on an Element 2 ICP-MS. All chemical sample preparations and measurements were performed at Lamont-Doherty Earth Observatory (LDEO).

### **3.6.3. Mass accumulation rate calculations**

For the last ca. 400 kyr., reconstructions of MAR of individual components (Fe, Ba<sub>xs</sub>, TOC, CaCO<sub>3</sub> and biogenic opal) were calculated as the product of the concentration of each component and the <sup>230</sup>Th<sub>xs</sub> normalized MAR (See equation in section 3.6.1).

Additionally, to cover all the timeframe of core PS97/093-2, stratigraphy-based bulk mass accumulation rates (BMAR) of individual components were obtained by multiplying the concentration of the respective constituent by the linear sedimentation rate (cm/kyr) and by the dry bulk density (g/cm<sup>3</sup>).

### **3.6.3. Calculation of focusing factor ( $\Psi$ )**

It has long been recognized that sediment is not always distributed equally over the floor of a sedimentary basin. Redistribution of recently deposited material from zones of erosion to deposition areas can affect the accumulation rates without disrupting the chronology and can be easily overlooked (e.g., Francois et al., 2004).

After Likens and Davis (1975), who developed the terminology, sediment **focusing** is the nomenclature used to describe conditions when ocean currents produce a net lateral transport of particles to a reference site. That is, the rate of particle deposition on the seabed at a site experiencing sediment focusing is higher than the regional average rate of particles settling through the water column (figure 3.5). On the other hand, the term **winnowing** is applied when currents lead to a net lateral transport of particles away from a reference site. In this case, the rate of sediment deposition at the reference site is less than the regional average rate of settling particles (figure 3.4).

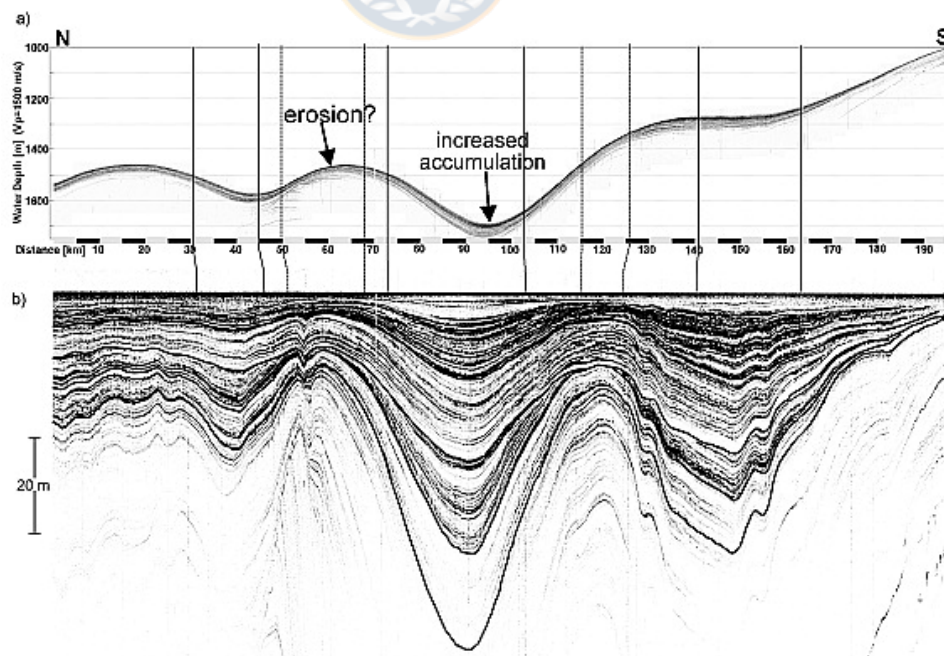


**Figure 3.5** Echo sounder profile on a section parallel to the coast of Namibia showing wide variations in the thickness of layered sediments deposited in the same area, providing graphical evidence of focusing and winnowing. This figure was taken from

Mollenhauer et al. (2002), and it has been previously used in the literature as a classical example to illustrate processes of sediment redistribution (e.g., Francois et al., 2004).

For core PS97/093-2, the degree of sediment focusing ( $\Psi$ ) was calculated following Suman & Bacon (1989):

$$\Psi = \left( \int_{r_1}^{r_2} {}^{230}\text{Th}_{xs}^0 \rho_r dr \right) / \beta_z (t_2 - t_1)$$

where  $\rho_r$  is the dry bulk density ( $\text{g/cm}^3$ ),  ${}^{230}\text{Th}_{xs}^0$  is the concentration of excess  ${}^{230}\text{Th}$  in the sediment corrected for decay since deposition,  $t_1$  and  $t_2$  are the corresponding ages (kyr) of sediment depths  $r_1$  and  $r_2$  (cm).  $\beta_z$  ( $\text{dpm/cm}^2/\text{kyr}$ ) is the integrated  ${}^{230}\text{Th}$  production in the overlying water column from  ${}^{234}\text{U}$  decay ( $0.0267 \text{ dpm/m}^3/\text{yr}$ ) that was obtained by multiplying  ${}^{234}\text{U}$  decay in the water column with the water depth (m) divided by 10. Thus,  $\Psi > 1$  indicates sediment focusing whereas  $\Psi < 1$  denotes sediment winnowing and values of  $\Psi = 1$  mean that the amount of  ${}^{230}\text{Th}$  buried in the sediment is equivalent to the amount of  ${}^{230}\text{Th}$  produced in the water column.

### 3.7. Lithogenic content

For the past 400 kyr, the concentrations of lithogenic material were calculated using  ${}^{232}\text{Th}$ . The key assumptions of this methodology are i)  ${}^{232}\text{Th}$  has exclusively a detrital origin (e.g., Kienast et al., 2016), and ii) the  ${}^{232}\text{Th}$  concentration of terrigenous material is relatively constant (e.g.,

McGee et al., 2016). Thus,  $^{232}\text{Th}$ -derived lithogenic MAR ( $\text{g}/\text{cm}^2/\text{kyr}$ ) were calculated by dividing the  $^{232}\text{Th}$  MAR ( $\mu\text{g}/\text{cm}^2/\text{kyr}$ ) by the constant average  $^{232}\text{Th}$  concentration of lithogenic material from Patagonia ( $9 \pm 1 \mu\text{g}/\text{g}$ , McGee et al., 2016).

Additionally, to cover all the timeframe of core PS97/093-2, lithogenic content (wt% Lith) was determined by subtraction:  $100 - (\text{wt}\% \text{Biogenic opal} + \text{wt}\% \text{CaCO}_3 + 2 \times \text{wt}\% \text{TOC})$ . Thus, lithogenic BMARs were obtained by multiplying the lithogenic content with linear sedimentation rates ( $\text{cm}/\text{kyr}$ ) and dry bulk density ( $\text{g}/\text{cm}^3$ ).



## 4. RESULTS/ RESULTADOS

### 4.1. Chapter 1/Capítulo 1

**Manuscript 1 (published): Antarctic Circumpolar Current dynamics at the Pacific entrance to the Drake Passage over the past 1.3 million years.**

Toyos, M. H., Lamy, F., Lange, C. B., Lembke-Jene, L., Saavedra-Pellitero, M., Esper, O., & Arz, H. W. (2020). Antarctic Circumpolar Current dynamics at the Pacific entrance to the Drake Passage over the past 1.3 million years. *Paleoceanography and Paleoclimatology*, 35(7), 1–20. <https://doi.org/10.1029/2019PA003773>

#### **Resumen:**

**Dinámica de la Corriente Circumpolar Antártica en la entrada del Pacífico al Paso de Drake durante los últimos 1,3 millones de años.**

La Corriente Circumpolar Antártica (*ACC*, por sus siglas en inglés) es el sistema de corriente más grande del mundo que conecta las tres principales cuencas del océano global. Nuestro conocimiento de los cambios glacial-interglacial en la dinámica de la *ACC* en el Pacífico sureste es restringido y se basa en reconstrucciones que solo abarcan el último ciclo glacial. Aquí usamos una combinación de la media de limo

uniforme ( $\overline{SS}$ , 10–63  $\mu\text{m}$ ) de la fracción terrígena y razones de Zr/Rb derivadas del escáner de fluorescencia de rayos X como *proxies* de intensidad de flujo para examinar las variaciones de la ACC en la entrada del Pacífico al Pasaje Drake (*DP*, por sus siglas en inglés) en la vecindad del frente subantártico. Nuestros resultados indican que en la entrada del *DP*, la intensidad de la ACC varió entre un 6–16% en escalas de tiempo glacial-interglacial, produciendo velocidades de corriente más altas durante los tiempos interglaciares y velocidades de corriente reducidas durante los glaciales. Proporcionamos evidencia de que las observaciones previas de una reducción en el flujo a través del Paso Drake durante el último período glacial son parte de un patrón constante que se extiende por al menos el último 1,3 millones de años. La ciclicidad a escala orbital sigue los cambios climáticos globales conocidos desde los ciclos de 41 kyr en la primera parte del registro (1.3 Ma a 850 ka; estadio isotópico marino 21) a través de la Transición del Pleistoceno medio, al mundo de los “100 kyr” del Pleistoceno medio y tardío. Por último, la comparación del registro de corrientes generado con uno previo de la corriente de fondo al oeste de Nueva Zelanda (ODP *Site* 1123) muestra que ambos se han comportado de manera opuesta a lo largo del último millón de años. Es decir, debilitamientos en el flujo de la CCA en el *DP* se corresponden con



aumentos de la intensidad de la corriente de fondo en el occidente del  
Pacífico Sur.



# Paleoceanography and Paleoclimatology

RESEARCH ARTICLE  
10.1029/2019PA003773

**Key Points:**

- The strength of ACC flow in the SE Pacific varied strongly on glacial-interglacial time scales
- Over the past 1.3 Ma, our results show a consistent pattern of stronger (weaker) flow during interglacials (glacials)
- The sortable silt record largely follows orbital-scale cyclicity, changing from ca. 41-kyr cycles into a 100-kyr world after the MPT

**Supporting Information:**

- Supporting Information S1

**Correspondence to:**

M. H. Toyos,  
mtoyos@udec.cl

**Citation:**

Toyos, M. H., Lamy, F., Lange, C. B., Lembke-Jene, L., Saavedra-Pellitero, M., Esper, O., & Arz, H. W. (2020). Antarctic circumpolar current dynamics at the Pacific entrance to the Drake Passage over the past 1.3 million years. *Paleoceanography and Paleoclimatology*, 35, e2019PA003773. <https://doi.org/10.1029/2019PA003773>






Received 23 SEP 2019

Accepted 3 JUN 2020

Accepted article online 11 JUN 2020

©2020. American Geophysical Union.  
All Rights Reserved.

## Antarctic Circumpolar Current Dynamics at the Pacific Entrance to the Drake Passage Over the Past 1.3 Million Years

María H. Toyos<sup>1,2</sup> , Frank Lamy<sup>3</sup> , Carina B. Lange<sup>2,4,5,6</sup> , Lester Lembke-Jene<sup>3</sup> , Mariem Saavedra-Pellitero<sup>7,8</sup> , Oliver Esper<sup>3</sup>, and Helge W. Arz<sup>9</sup>

<sup>1</sup>Programa de Postgrado en Oceanografía, Departamento de Oceanografía, Facultad de Ciencias Naturales y Oceanográficas, Universidad de Concepción, Concepción, Chile, <sup>2</sup>Centro de Investigación Dinámica de Ecosistemas Marinos de Altas Latitudes, Universidad Austral de Chile, Valdivia, Chile, <sup>3</sup>Alfred-Wegener-Institut, Helmholtz-Zentrum für Polar und Meeresforschung, Bremerhaven, Germany, <sup>4</sup>Centro Oceanográfico COPAS Sur-Austral, Universidad de Concepción, Concepción, Chile, <sup>5</sup>Departamento de Oceanografía, Universidad de Concepción, Concepción, Chile, <sup>6</sup>Scripps Institution of Oceanography, La Jolla, CA, USA, <sup>7</sup>Geowissenschaften, Universität Bremen, Bremen, Germany, <sup>8</sup>Now at School of Geography, Earth and Environmental Sciences, University of Birmingham, Birmingham, UK, <sup>9</sup>Leibniz-Institut für Ostseeforschung Warnemünde, Rostock, Germany

**Abstract** The Antarctic Circumpolar Current (ACC) is the world's largest current system connecting all three major basins of the global ocean. Our knowledge of glacial-interglacial changes in ACC dynamics in the southeast Pacific is not well constrained and presently only based on reconstructions covering the last glacial cycle. Here we use a combination of mean sortable silt grain size of the terrigenous sediment fraction (10–63  $\mu\text{m}$ ,  $\overline{SS}$ ) and X-ray fluorescence scanner-derived Zr/Rb ratios as flow strength proxies to examine ACC variations at the Pacific entrance to the Drake Passage (DP) in the vicinity of the Subantarctic Front. Our results indicate that at the DP entrance, ACC strength varied by ~6–16% on glacial-interglacial time scales, yielding higher current speeds during interglacial times and reduced current speeds during glacials. We provide evidence that previous observations of a reduction in DP throughflow during the last glacial period are part of a consistent pattern extending for at least the last 1.3 Ma. The orbital-scale cyclicity follows well-known global climate changes from prevailing ca. 41-kyr cycles in the early part of the record (1.3 Ma to 850 ka; marine isotope stage 21) across the mid-Pleistocene transition into the middle and late Pleistocene 100-kyr world. A comparison to a bottom water flow record from the deep western boundary current off New Zealand (Ocean Drilling Program Site 1123) reveals anti-phased changes between the two sites. The enhanced supply of deep water along the DP and into the Atlantic Ocean during interglacials corresponds to a weakened flow of the SW Pacific deep western boundary current.

### 1. Introduction

The Antarctic Circumpolar Current (ACC) is the main oceanographic feature of the Southern Ocean, flowing clockwise around Antarctica and connecting the Atlantic, Pacific, and Indian Ocean basins. It is the world's largest and strongest current system driven by strong southern westerly winds (SWW), buoyancy forcing, and large-scale changes in thermohaline circulation (Rintoul et al., 2018). The ACC flow is constrained by bathymetric boundaries (Gordon et al., 1978), with the Drake Passage (DP) being the region of narrowest and shallowest constriction of its flow path (e.g., Meredith et al., 2011). Three major oceanographic fronts have been described within the ACC, traditionally termed the Subantarctic Front (SAF), the Polar Front (PF), and the Southern ACC Front (SACCF; Orsi et al., 1995). The southern limit of Upper Circumpolar Deep Water (UCDW) marks the southern boundary of the ACC (Orsi et al., 1995). The location of these fronts is not stationary and changes on seasonal and interannual (e.g., Freeman & Lovenduski, 2016; Gille, 2014) to orbital time scales (e.g., Gersonde et al., 2003, 2005; Kemp et al., 2010). Frontal positions were likely displaced northward during the Last Glacial Maximum (LGM; Gersonde et al., 2005; Kohfeld et al., 2013) and, more generally, in glacial intervals (Howard & Prell, 1992). At the DP, the position of the SAF is crucial, because it controls the volume of Antarctic Intermediate Water (AAIW) and Circumpolar Deep Water (CDW) transported from the Indo-Pacific into the Atlantic via the “cold water route,” and as

such, has implications for the southern-sourced Atlantic deep return flow in the global Meridional Overturning Circulation (MOC; Gordon, 1986).

There is substantial disagreement about ACC flow speed changes in response to glacial and interglacial climates during the Quaternary. Recent studies reconstructing ACC flow speed focused on the DP area (Lamy et al., 2015; Roberts et al., 2017) and the downstream Scotia Sea (McCave et al., 2014). For the last glacial cycle, Lamy et al. (2015) reconstructed DP throughflow based on sediment records from the Chilean margin at the entrance to the DP and the southernmost Argentinean continental slope located directly at the northern margin of the DP and found a significant glacial decrease in DP throughflow. On the Atlantic side south of the Falkland/Malvinas Islands, immediately downstream of the subantarctic DP, Roberts et al. (2017) reported a similar reduction in current speed. These findings are consistent with generally reduced current velocities of the ACC during the last glacial and concomitant reduction in interbasin exchange in the Southern Ocean, most likely regulated by variations in the SWW field over the Subantarctic Zone and changes in Antarctic sea ice extent (Lamy et al., 2015). In contrast, sediment records from the Scotia Sea (McCave et al., 2014) suggest minor ACC speed variations between the LGM and the Holocene near the PF and a small decrease southward, most likely due to increased sea ice cover. Density reconstructions across the ACC south of Australia based on benthic foraminifera demonstrate a moderate overall increase of the ACC flow during the LGM (Lynch-Stieglitz et al., 2016). Likewise, a 1.2-Ma-long sediment record of grain sizes in the sortable silt fraction from the subantarctic southwest Pacific indicates intensification of the deep western boundary current (DWBC) east of New Zealand during glacial periods (Hall et al., 2001). Finally, in the Indian sector of the Southern Ocean, a magnetic grain size record suggests that the ACC was weak during warm stages and strong during glacial epochs throughout the past ~500 kyr (Mazaud et al., 2010).

Between 1.25 and 0.7 Ma, Earth's climate underwent a fundamental change when the dominant periodicity of orbital-scale climate cycles changed from primarily 41 to 100 kyr (e.g., Clark et al., 2006; Elderfield et al., 2012; Maslin & Brierley, 2015). This period is known as the mid-Pleistocene transition (MPT). In the Southern Ocean, the MPT is linked to a variety of important atmosphere-ocean changes leading to an equatorward extension of polar surface water masses (Martínez-García et al., 2011), an increase in stratification and reduced upwelling during glacial times (Hasenfratz et al., 2019), and enhanced nutrient export to the eastern equatorial Pacific potentially caused by a northward migration of fronts (Robinson et al., 2019). Together, these changes are thought to contribute to the increasing amplitudes of glacial to interglacial CO<sub>2</sub> concentrations (Chalk et al., 2017) with lower atmospheric CO<sub>2</sub> concentrations during glacial times (Hasenfratz et al., 2019).

Little is known about changes in the dynamics of the subantarctic ACC and its interplay with SWW fluctuations across multiple glacial/interglacial cycles including the MPT with its widespread change in orbital cyclicity (Clark et al., 2006) and the Mid-Brunhes Event (MBE). The MBE took place at marine isotope stage (MIS) 12/11 and is characterized by an increase in the glacial/interglacial amplitudes and warmer interglacials thereafter, as well as changes in insolation, CO<sub>2</sub> concentrations, and carbon storage in the ocean (e.g., Bouttes et al., 2018; Yin & Berger, 2012). Atmosphere-ocean changes in the subantarctic ACC region likely affected the global MOC as well as the exchange of heat, salt, and nutrients zonally across the Southern Hemisphere and meridionally between high and low latitudes. Reconstructions of past ACC dynamics may thus provide important baseline data on the physical configuration of a region critical for understanding orbital-scale atmospheric CO<sub>2</sub> fluctuations and the storage of CO<sub>2</sub> in the deep ocean.

In this study, we reconstruct changes in the intensity of ACC flow in the subantarctic SE Pacific over the past 1.3 Myr, based on grain size analyses and X-ray fluorescence (XRF) scanner data from a sediment core located near the SAF at the DP entrance (Figure 1). We provide evidence that the previously observed pattern of a glacial reduction of the ACC upstream and downstream of the DP throughflow extends to glacial intervals across the past 1.3 Ma. A comparison with variations of deep Pacific inflow in the SW Pacific basin (Hall et al., 2001) reveals contrasting flow pattern in the core of the ACC and the deep boundary current in the SW Pacific.

## 2. Study Area

The DP is located between South America and Antarctica; it is 850 km wide and represents the major geographical constriction for the transport of the ACC into the Atlantic. The exact timing of the opening of this

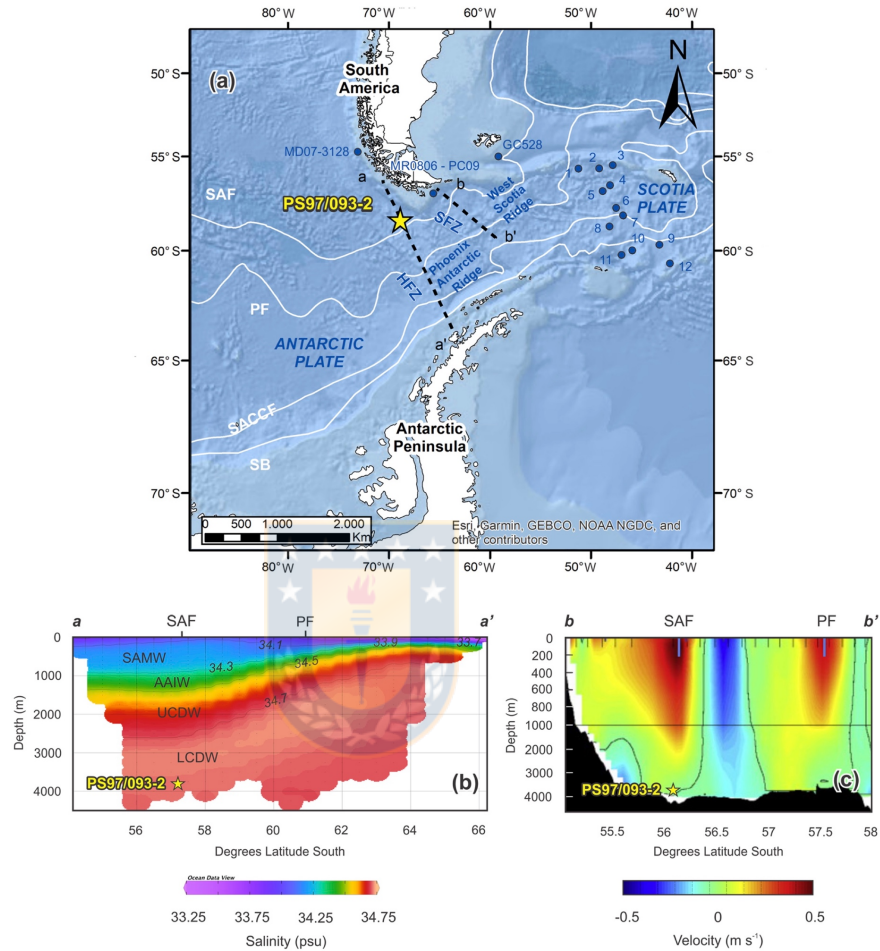


**Figure 1.** (a) Map of the Drake Passage area showing the location of core PS97/093-2 (yellow star) and core sites studied by Lamy et al. (2015), McCave et al. (2014), and Roberts et al. (2017) (blue points). White lines mark ACC modern fronts (Orsi et al., 1995). SAF, Subantarctic Front; PF, Polar Front; SACCF, Southern Antarctic Circumpolar Current Front; SB, southern boundary of the ACC. Black dashed lines a-a' and b-b' are two hydrographic transects shown in (b) and (c). SFZ, Shackleton Fracture Zone; HFZ, Hero Fracture Zone. (b) Salinity section across the Drake Passage with the projected core position (data from Gouretski & Koltermann, 2004). LCDW, Lower Circumpolar Deep Water; UCDW, Upper Circumpolar Deep Water; AAIW, Antarctic Intermediate Water; SAMW, Sub-Antarctic Mode Water. (c) Geostrophic flow velocities through the Drake Passage from Renault et al. (2011) with the projected core position; positive velocities are eastward, and negative velocities are westward.

oceanic gateway is still discussed controversially; it occurred during the Eocene to Oligocene (between ~45 and ~22 Ma). The opening resulted from the breakup of the continental connection between South America and the Antarctic Peninsula along the final steps of Gondwana separation (e.g., Barker & Burrell, 1977; Eagles & Jokat, 2014; Livermore et al., 2005). The opening of the DP together with the Tasmanian gateway allowed the extensive exchange of water between the main ocean basins and the development of the ACC at ~24 Ma (Pfuhl & McCave, 2005), which contributed to the thermal isolation of Antarctica (Barker, 2001). In the DP, the main tectonic and morphological feature is the Shackleton Fracture Zone (an intra-oceanic

ridge in the center that separates the Scotia Plate to the east and the Antarctic Plate to the west). The West Scotia ridge also intersects with the Shackleton Fracture Zone to the east and with the Phoenix-Antarctic ridge to the west; the latter borders in the south with the Hero Fracture Zone. The spreading of the Phoenix-Antarctic Ridge ended at ca. 3.6 to 2.6 Ma, when the Phoenix Plate became part of the Antarctic Plate (Bohoyo et al., 2019). Core PS97/093-2 is located in the oceanic domain of the Antarctic Plate, north of the Phoenix-Antarctic ridge ~80 km SW of the southern end of the Chile Trench (Figure 1a).

The oceanographic boundaries of the ACC are defined by zonal variations in water mass properties of the Southern Ocean. The three major fronts associated with the ACC, namely, the SAF, PF and SACCF, are closely spaced in the DP (Figure 1a). The bulk of the geostrophic transport of the ACC is associated with the SAF and PF, where strong surface and bottom velocities have been observed (e.g., Renault et al., 2011) (Figure 1c). Site PS97/093 is bathed in Lower Circumpolar Deep Water (LCDW), which is characterized by a salinity maximum (34.70–34.75 psu) (Gordon, 1975; Orsi et al., 1995). It consists of a mixture of North Atlantic Deep Water that enters the Southern Ocean through the Atlantic and is transported east around the Antarctic continent, while mixing with waters from the Indian and Pacific Oceans and dense waters from Antarctica (e.g., Carter et al., 2008). The UCDW is located at a depth range of ~1,400 to 2,500 m, above the LCDW. It is characterized by an oxygen minimum and high nutrient concentrations. At depths shallower than 1,400 m, AAIW, identified by a salinity minimum, and the low-density Sub-Antarctic Mode Water occur (Figure 1b). The export of fresh and cold UCDW, AAIW, and Sub-Antarctic Mode Water via the cold water route strongly influences the upper limb of Atlantic MOC, together with the “warm water route” (inflow of the warm and salty water masses through the Agulhas Current System into the South Atlantic; Gordon, 1986). Below the depth of AAIW, the deep water masses tend to return equatorward as a relatively strong and narrow DWBC. In the Atlantic Ocean, the DWBC is located on the continental margin off South America below the southward moving North Atlantic Deep Water, and the inflow consists of a mixture of Weddell Sea Bottom Water and CDW from the DP.

### 3. Material and Methods

Piston core PS97/093-2 (57°29.94'S; 70°16.48'W; 16.45 m in length) was recovered in 2016 on board R/V *Polarstern* during expedition PS97 “Paleo Drake” (Lamy, 2016). The coring site is located approximately 40 km NW of the SAF, within the main flow of the ACC at the Pacific entrance to the DP, at 3,781-m water depth and is bathed in LCDW (Figure 1).

#### 3.1. Bulk Sediment Parameter and Geochemistry

The archive half of core PS97/093-2 was measured with an AVAATECH XRF Core Scanner at the Alfred-Wegener-Institut (AWI, Bremerhaven) for high-resolution element intensities of Ca, Fe, Zr, Rb, Ti, and K at 0.5 cm resolution. Total carbon (TC) and total nitrogen were quantified using a CNS analyzer (Elementar Varia EL III) at AWI using 100 mg of freeze-dried and homogenized sediments. Total organic carbon (TOC) contents were determined with a carbon-sulfur determinator (CS-2000, ELTRA) after the removal of inorganic carbon (total inorganic carbon) by adding 37% (vol/vol) hydrochloric acid. Calcium carbonate content (CaCO<sub>3</sub>) was calculated employing the standard equation  $\text{CaCO}_3 [\text{wt.}\%] = (\text{TC} [\text{wt.}\%] - \text{TOC} [\text{wt.}\%]) * 8.333$ . A high-resolution CaCO<sub>3</sub> record was obtained calibrating the Ca intensities with the bulk sediment CaCO<sub>3</sub> measurements ( $r^2 = 0.92$ ).

#### 3.2. Grain Size Analysis

A total of 144 samples distributed along the entire sediment core were taken for grain size analysis. The separation of the 63- to 150- $\mu\text{m}$  fine-sand fraction was carried out by wet sieving, whereas the silt (2–63  $\mu\text{m}$ ) and clay fractions (<2  $\mu\text{m}$ ) were separated by application of Stokes' law settling using Atterberg tubes. This procedure was repeated 12 to 20 times to get an almost complete separation of the two fractions. In order to get the terrigenous silt fraction, organic matter was removed with 35% (vol/vol) H<sub>2</sub>O<sub>2</sub>. To dissolve the carbonates, sediment samples were placed in a 500-ml beaker with 150 ml of 25% (vol/vol) acetic acid (this procedure was repeated two times). Rinsing was done until the pH of the solution reached the pH of deionized water (~6.5). Opal leaching was carried out adding 250 ml of 20% NaOH and heated to 85–90 °C for 60 min. Rinsing was repeated after this leaching step for at least four times, until the pH of

the sample reached the pH of deionized water again. Before the samples in the Sedigraph device were introduced, sodium polyphosphate was added to avoid coagulation of particles.

A detailed grain size analysis with 2 to 8 g of the silt fraction was performed with a Micrometric Sedigraph 5010 at AWI. The Sedigraph measures the particle size distribution using the sedimentation method and provides a high-resolution grain size distribution in steps of  $0.1\phi$ . The instrumental precision of the Sedigraph for pure standard analysis ranges from  $\pm 0.3\%$  to  $\pm 1.9\%$  (Bianchi et al., 1999). The way of measuring grain size distribution by the Sedigraph devices is closely related to the transport and depositional processes and estimations of current intensity (McCave & Hall, 2006). The coarse fraction of silt (size spectrum between 10 and 63  $\mu\text{m}$ ) is referred to as sortable silt (SS) because of its noncohesive behavior. SS is considered as a proxy for estimating relative changes in the near-bottom flow speed in deep-sea sediments (McCave et al., 1995).

We repeated measurements of 10 samples for two to three times in order to measure the instrumental error of the Sedigraph 5100 for our sediment samples, and 10 of the analyses were replicated in the two different devices available at AWI (Unit 1 and Unit 2). For the SS parameter, the average error within the same device is  $\pm 0.18$  and  $\pm 0.13$   $\mu\text{m}$  regarding the two devices. A high-resolution SS record was obtained using the linear equation describing the relationship between XRF core scanner-derived Zr/Rb, smoothed with a 5-point moving average, and the sortable silt data obtained with the Sedigraph (see section 5.1 for more details).

### 3.3. Biostratigraphic Time Markers

Smear slides were prepared by mounting small portions of bulk sediment on glass slides following standard International Ocean Discovery Program procedures. Thirty-six slides were examined for calcareous nannofossils, and 18 for siliceous microfossils (Tables S1 and S2). Calcareous nannofossils were observed with a Leica DMRM polarized light (LM) microscope (at the University of Bremen, Germany) and a Nikon Eclipse 80i (at the University of Salamanca, Spain) at 1,000X magnification. Calcareous nannofossils were classified following the compilations of Raffi et al. (2006) and Anthonissen and Ogg (2012). Bio-event ages were assigned based on the occurrence (or absence) of calcareous nannofossil biostratigraphical markers in selected samples from core sections of the archive half (Tables 1 and S1). Additional age markers for sediment core PS97/093-2 were obtained from diatom biostratigraphy (Tables 1 and S2). Qualitative analysis of diatom assemblages was conducted on discrete sediment samples. Diatom counting and identification was performed with a Zeiss microscope at 1,000X magnification and followed the methods of Schrader and Gersonde (1978). The taxonomy of diatom species followed Hasle and Syvertsen (1997) and Zielinski and Gersonde (1997). The biostratigraphic zonations and diatom occurrence ranges suggested by Zielinski and Gersonde (2002) were applied.

### 3.4. Stratigraphic Tuning and Spectral Analyses

We used the AnalySeries software (Paillard et al., 1996) for stratigraphic fine-tuning and spectral analyses to derive the relative power of the major cycles in the Milankovitch band. Linear trends were removed and values normalized. The frequency scale was resampled from 0 to 0.1 with a step of 0.0002. We used a Bartlett window, and the bandwidth is  $\sim 0.005$ .

## 4. Age Model

A two-step approach was used to establish the age model for core PS97/093-2. First, a preliminary age was derived based on onboard physical property data and biostratigraphic time markers from calcareous nannofossils and diatoms (Table 1 and Figure 2). Second, the high-resolution XRF scanner-derived records of Fe and Ca counts and the measured  $\text{CaCO}_3$  contents were used to fine-tune the PS97/093-2 record within the age ranges of the biostratigraphic dates to the benthic  $\delta^{18}\text{O}$  stack (Lisiecki & Raymo, 2005, LR04 hereafter).

Although the presence of nannofossils is discontinuous and preservation varies strongly, Zones NN21 through NN19 are recognized based on the first occurrence of *Emiliania huxleyi* at 0.29 Ma (between 143 and 43 cm) and the last occurrence (LO) of *Pseudoemiliania lacunosa* at 0.44 Ma (between 726 and 643 cm). Additionally, an ooze of *Gephyrocapsa caribbeanica* was recorded at 343 cm. This characteristic ooze has been previously observed at other locations in the Pacific sector of the Southern Ocean (Gersonde, 2011; Saavedra-Pellitero, Baumann, Ullermann, et al., 2017, Saavedra-Pellitero, Baumann,

**Table 1**  
Summary of Biostratigraphic Markers of Calcareous Nannofossils and Diatoms Used to Build the Preliminary Age Model of Core PS97/093-2

Depth (cm)	Calcareous nannofossil			Diatoms		Age model (Ma)
	Zonation (Martini, 1971)	Marker/taxa	Age (Myr)	Marker/taxa	Age (Ma)	
1	NN21	<i>Emiliana huxleyi</i>	$x < 0.29$			0.004
43		<i>E. huxleyi</i>	$x < 0.29$			0.025
343	NN20	<i>Gephyrocapsa caribbeanica</i> (ooze) <sup>a</sup>	MIS 11 <sup>a</sup>	LO <i>Actinocyclus ingens</i>	MIS 11	0.40
543				LAO <i>A. ingens</i>	~0.64	0.62
726	NN19	<i>Pseudoemiliana lacunosa</i>	$x > 0.44$			0.70
1,044				FAO <i>Thalassiosira elliptipora</i>	~1.04	0.98
1,120		<i>Reticulofenestra asanoi</i>	$x > 0.91$			1.02
1,164		<i>R. asanoi</i>	$0.91 < x < 1.14$			1.07
1,545				LO <i>Fragilariopsis barronii</i>	~1.3	1.33
1,645						1.37

Note. FAO = first abundance occurrence; LAO, last abundance occurrence; LO, last occurrence.

<sup>a</sup>Note that the monospecific assemblage of *Gephyrocapsa caribbeanica* is not a formal calibrated datum. However, this ooze can be tied to MIS 11 based on previous research (Geronde, 2011; Saavedra-Pellitero, Baumann, Ullermann, et al., 2017, Saavedra-Pellitero, Baumann, Lamy, et al., 2017).

Lamy, et al., 2017), suggesting MIS 11 for this acme. Although several of the studied samples are devoid of calcareous nannofossils, the LO of *Reticulofenestra asanoi* at 0.91 Ma (between 1,120- and 894-cm depth in core) and the first common occurrence of *R. asanoi* at 1.14 Ma (between 1,230 and 1,164 cm) provide

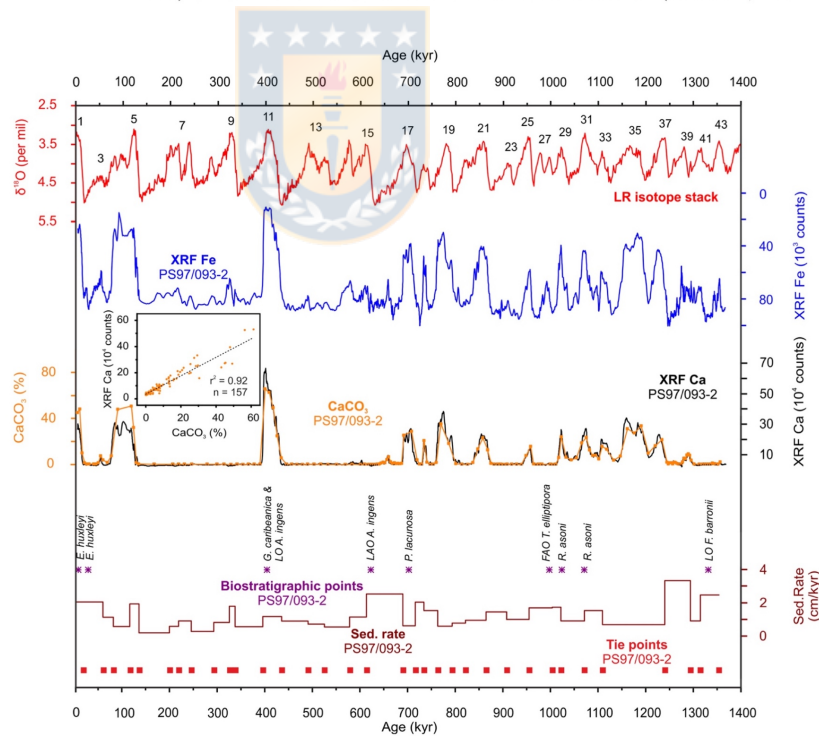


**Figure 2.** Age model for core PS97/093-2. From top to bottom: LR04 benthic  $\delta^{18}\text{O}$  stack (Lisiecki & Raymo, 2005), numbers indicate marine isotope stages; XRF Fe scanner counts (blue);  $\text{CaCO}_3$  content (orange) and XRF Ca scanner counts (black); age control points based on biostratigraphic markers (purple asterisks), sedimentation rate (brown), and tie points (red).

good age control for the Pleistocene sequence. Furthermore, the absence of *Gephyrocapsa* spp. large (>5.5  $\mu\text{m}$ ) and *Helicosphaera sellii* suggests an age younger than 1.24 Ma at 1,461-cm depth in core.

Within the stratigraphic range of this study, the LO of the diatom species *Fragilariopsis barronii* at about 1,545-cm depth in core constrains the transition from the *Actinocyclus ingens* Zone A to *A. ingens* Zone B at ca. 1.3 Ma. A first abundance occurrence of *Thalassiosira elliptipora* at 1,144 cm points to the transition from *A. ingens* Zone B to *A. ingens* Zone C. The top of *A. ingens* Zone C is constrained by the last abundance occurrence of *A. ingens* at 543 cm. The LO of *A. ingens* at 343 cm marks the transition from MIS 12 to MIS 11. XRF Fe counts show clear orbital-scale variability along most of the record (Figure 2). We tuned the PS97/093-2 Fe content to the LR04 benthic  $\delta^{18}\text{O}$  stack (Lisiecki & Raymo, 2005) assuming low Fe contents during interglacials and high contents during glacials. The Fe content is generally representative for the siliciclastic fraction of the sediment. This fraction is most likely controlled by a combination of factors including dilution with biogenic material (primarily  $\text{CaCO}_3$ ; Figure 2) and thus preservation and/or biological production, together with varying eolian and/or glaciogenic sediment input from South America, in addition to winnowing by the ACC. We additionally used XRF-derived Ca and  $\text{CaCO}_3$  percentages for a finer-tuning with the LR04 benthic  $\delta^{18}\text{O}$  stack as a reference curve only in the intervals where Ca and  $\text{CaCO}_3$  (%) are present (Figure 2). Thus, the resulting age model has 34 tie points that consist of a combination of indicators for glacial/interglacials and biostratigraphic points (Table S3).

## 5. Results and Discussion

Core PS97/093-2 consists of hemipelagic sediments and comprises distinct lithological changes (Lamy, 2016) reoccurring on orbital time scales. Interglacial sediments are primarily composed of whitish gray to white calcareous oozes (nannofossil ooze or foraminifera-nannofossil ooze) with only minor concentrations of diatoms.  $\text{CaCO}_3$  contents above 40% occur during MIS 1 and MIS 5, approximately 70% during MIS 11, and 20–40% during most interglacials before MIS 17. Glacial and transitional sediments are weakly bioturbated, dark clayey silt with rare biogenic components and intercalated diatomaceous fine-grained clayey silts. Some intervals are moderately bioturbated and more greenish gray in color and characterized as diatomaceous silt. Sedimentation rates are 1.3 cm/kyr on average and range from approximately 0.5 to 3.5 cm/kyr (Figure 2). Higher sedimentation rates occur during MIS 1–5, MIS 15–19, and MIS 37–43. Lower sedimentation rates characterize the intervals MIS 6–10 and MIS 14.

### 5.1. Sortable Silt, Zr/Rb Records, and Flow Speed Reconstruction

The key assumption of the  $\overline{\text{SS}}$  proxy for estimating relative changes in the near-bottom flow speed in deep-sea sediments is that the sediment is primarily controlled by current sorting during deposition (McCave et al., 1995); coarser mean size reflects stronger flow through selective deposition (McCave & Hall, 2006). The sources of potential uncertainties regarding the applicability of the  $\overline{\text{SS}}$  proxy are ice rafted debris deposits, fine tails of turbidity deposits, or local sediment movement and redeposition caused by changes in mud waves (McCave et al., 1995). A way to test if the sediments are current sorted consists of plotting  $\overline{\text{SS}}$  against the percentage of the 10- to 63- $\mu\text{m}$  fraction (SS%; McCave & Hall, 2006) (Figure 3). Under a current-sorted regime, a positive correlation exists between  $\overline{\text{SS}}$  and SS%, whereas unsorted sediments show no correlation. Sortable silt values of core PS97/093-2 display a significant positive correlation ( $r^2 = 0.78$ ,  $P \ll 0.001$ ,  $n = 148$ ) (Figure 3a).

In order to increase the temporal resolution of our sortable silt record, we established the relationship between measured  $\overline{\text{SS}}$  values with the XRF-based Zr/Rb record (Figure 4). Changes in Zr/Rb ratios have been previously interpreted as a proxy for grain size variations (Dypvik & Harris, 2001), though mainly in lake sediments. Zr is enriched in heavy minerals (especially in zircon) (Fralick & Kronberg, 1997) and is associated with the coarser tail in grain size distributions of silty-clayey siliciclastic sediments. Rb is associated with clay and fine silt because Rb occurs in clay minerals (Fralick & Kronberg, 1997; Taylor, 1965). Our  $\overline{\text{SS}}$  data and Zr/Rb ratios show a significant positive linear correlation (Figure 3b;  $r^2 = 0.50$ ,  $P \ll 0.001$ ,  $n = 148$ ), supporting the assumption that Zr/Rb ratios are strongly related to current strength in our deep-sea record as well. Consequently, we transformed the XRF core scanner-derived Zr/Rb data into  $\overline{\text{SS}}$  using a linear regression (Figure 4).



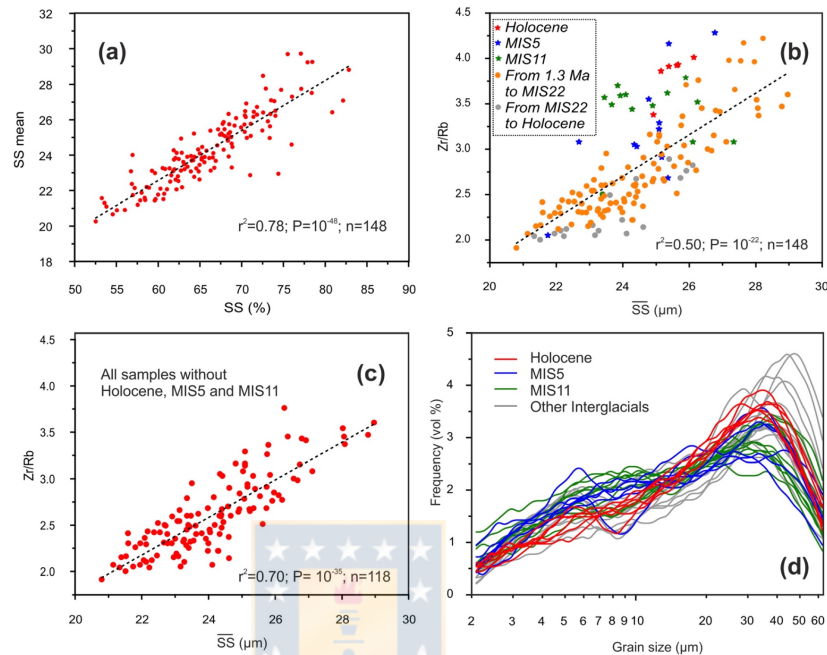


**Figure 3.** (a) Linear regression between  $\overline{SS}$  ( $\mu\text{m}$ ) mean and SS percentage of PS97/093-2 samples. Linear relations between Zr/Rb and  $\overline{SS}$  ( $\mu\text{m}$ ) of PS97/093-2 samples. (b) All measured samples. (c) All samples with the exception of those that belong to the Holocene, MIS 5, and MIS 11. (d) Silt distribution of the Holocene, MIS 5, MIS 11, and selected interglacials (MIS 13, MIS 19, MIS 29, and MIS 39).

Some values fall outside the general linear trend (Figure 3b). These occur particularly during the  $\text{CaCO}_3$ -rich interglacials MIS 1, MIS 5, and MIS 11, characterized by very high Zr/Rb values that are not accompanied by equally high maxima in the  $\overline{SS}$  data. When the data of these three intervals ( $n = 30$ ) are removed, the correlation between SS and Zr/Rb increases significantly (Figure 3c;  $r^2 = 0.70$ ,  $P \ll 0.001$ ,  $n = 118$ ). When we compare Holocene, MIS 5, and MIS 11 to other interglacials in our record, we do not observe any significant difference in the silt distributions (Figure 3d). Therefore, we suggest that the Zr/Rb record is affected by noncurrent-related factors during these intervals. One possibility is the occurrence of K-feldspars. Though Rb is usually more common in clay minerals and fine silt than in medium to coarse silts, this element has the ability to act as a substitute for K in K-feldspars, which are usually associated with the coarse silt and sand fractions (Kylander et al., 2011). To rule out this possibility, we followed Kylander et al. (2011) and examined the relationship to Ti, which is representative of fine size fractions, with Rb and K. We found significant positive correlations using all data points ( $n = 3,254$ ) (Figure S1), suggesting that coarser grain sizes are not important hosts for Rb and K. Finally, it is conceivable that the high Zr/Rb values during these peak interglacials reflect strong currents at our site and thus enhancement of the ACC during the interglacials because there could be a shift to coarser grain sizes that might result in a relative increase of fine sand, which is excluded from the definition of sortable silt. This might result in a possible limitation of the  $\overline{SS}$  as a bottom current indicator. The high fine-sand contents in intervals with extremely high current strength as measured in Lamy et al. (2015) at the Chilean continental margin would generally support this interpretation.

To get the best adjustment to the  $\overline{SS}$ -Zr/Rb recalculation, as a first step, we looked for the best fit regions, establishing MIS 14 as the most suitable crop mark at the expense of MBE, which shows slightly worse statistical parameters ( $r^2 = 0.717$ ,  $P \ll 0.001$ ,  $n = 92$  for samples older than MBE and  $r^2 = 0.648$ ,  $P \ll 0.001$ ,

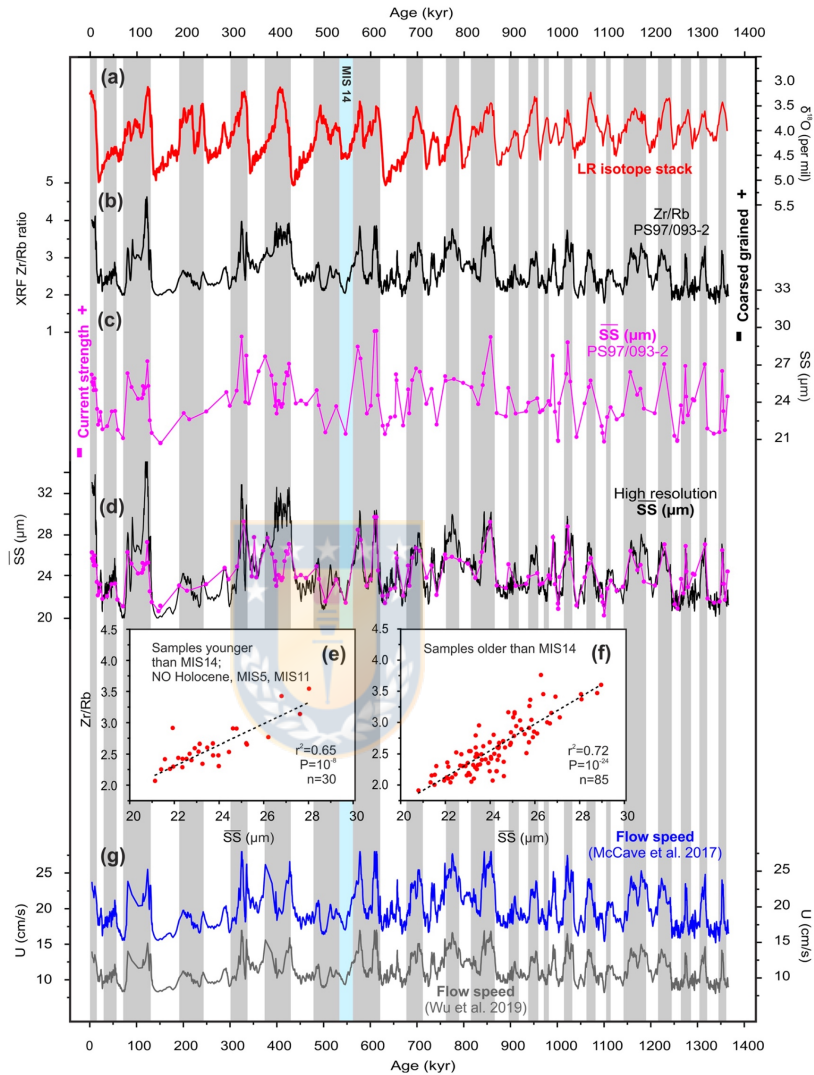


**Figure 4.** Multiproxy reconstruction of ACC current strength fluctuation at the PS97/093-2 site. (a) LR04 benthic  $\delta^{18}\text{O}$  stack (Lisiecki & Raymo, 2005). (b) XRF scanner five-point smoothed Zr/Rb variations. (c) Measured sortable silt ( $\overline{\text{SS}}$ ) results. (d) High-resolution  $\overline{\text{SS}}$  record based on XRF 5-point smoothed Zr/Rb transformation (black line) compared with measured SS record (pink line) (see text for details). (e, f) Linear regressions between XRF Zr/Rb and  $\overline{\text{SS}}$  used to obtain high-resolution  $\overline{\text{SS}}$  record. (g) Core PS97/093-2 scalar flow speed fluctuations (cm/s) based on McCave et al. (2017) (blue) and Wu et al. (2019) (gray) equations. Gray bars indicate interglacial stages. Cyan bar indicates MIS 14.

$n = 23$  for samples younger than MBE). Therefore, for the  $\overline{\text{SS}}$ -Zr/Rb recalculation, two linear regressions were used, one for the samples older than MIS 14 ( $Zr/Rb = 0.21 \overline{\text{SS}} - 2.39$ ;  $r^2 = 0.720$ ,  $P \ll 0.001$ ,  $n = 85$ , and a second one for samples younger than MIS 14, excluding the Holocene, MIS 5, and MIS 11, where

the direct high-resolution  $\overline{SS}$  measurements obtained with the Sedigraph were used ( $Zr/Rb = 0.15 \overline{SS} - 1.09$ ;  $r^2 = 0.651$ ,  $P \ll 0.001$ ,  $n = 30$ ) (Figure 4(e), (f)).

Based on the positive and significant correlation between  $\overline{SS}$  data and  $Zr/Rb$  ratios, we calculated ACC flow speed on the transformed XRF core scanner-derived  $Zr/Rb$  data into  $\overline{SS}$ . Using the calibration of  $\overline{SS}$  for the Scotia-Weddell Sea region ( $\overline{SS} = 0.59U + 12.23$ , McCave et al., 2017), the calculated current speed values of core PS97/093-2 vary from 15 to 28 cm/s, with a Holocene average of approximately 22 cm/s (Figure 4g). These values are rather high for a 3,800-m-deep current when compared to modern deep observations of ACC flow speeds of 10 to 20 cm/s in the vicinity of the SAF in the DP (Donohue et al., 2016; Renault et al., 2011). This difference between the estimated and measured modern values could be due to a deficit of coarser silt at the deeper sites of the calibration line, leading to a finer mean size for the same speed (McCave et al., 2017). However, this difference is smaller when using the most recent calibration of Wu et al. (2019;  $\overline{SS} = 0.86U + 14.49$ ), yielding values ranging from 8 to 17 cm/s, with a Holocene average of 12 cm/s (Figure 4g). Although the Wu et al. (2019) calibration might be biased by the fact that surface sediment data (multicore samples) and bottom current data are not from exactly the same locations; the data were retrieved directly within the DP and thus close to our site. The McCave et al. (2017) calibration, on the other hand, uses records from the Scotia Sea downstream of the DP and at or south of the PF.

## 5.2. LGM to Holocene Changes in the DP Throughflow

Between the LGM (19–27 ka, sensu lato: Clark et al., 2009) and the Holocene,  $\overline{SS}$  ranges from a minimum value of 21.4  $\mu\text{m}$  at ~26 ka to a maximum of 26.2  $\mu\text{m}$  in the uppermost part of the core (~4 kyr ago). The increase between the LGM mean value (23.1  $\mu\text{m}$ ) and the Holocene mean value (25.5  $\mu\text{m}$ ) is approximately 10%. A much larger LGM/Holocene difference is observed in all cores located in the northern part of the DP: core MD07-3128 at 1,032-m water depth shows approximately 40% difference, core MR0806-PC09 at 684-m water depth with approximately 20% (Lamy et al., 2015), and core GC528 at 598 m indicates approximately 50% difference (Roberts et al., 2017) (Figure 5). We suggest that these strong increases compared to our core PS97/093-2 might be related to (i) shallower depths of continental margin cores and stronger currents and/or (ii) a reestablishment of the SAF by general southward frontal movement between the LGM and the Holocene, as suggested by Roberts et al. (2017).

Furthermore, when comparing our LGM/Holocene  $\overline{SS}$  record to other deep cores retrieved along a transect in the Scotia Sea (2,000- to 4,323-m water depth; McCave et al., 2014), we notice that the  $\overline{SS}$  proxy for ACC throughflow is overall larger and more variable at the Pacific DP entrance (core PS97/093-2, LGM mean 23.1  $\mu\text{m}$  and Holocene mean 25.5  $\mu\text{m}$ ) than in the Scotia Sea (17.1 and 17.4  $\mu\text{m}$ , respectively). This difference could be explained by the latitudinal distribution of the core locations; all Scotia Sea cores stem from south of the PF (cf. Orsi et al., 1995), whereas core PS97/093-2 is located in the Subantarctic Zone close to the SAF, where one half of the total modern DP throughflow transport occurs (Koenig et al., 2016; Well & Roether, 2003). Earlier reconstructions of bottom current speeds also based on the  $\overline{SS}$  proxy show a 7–10% speed increase for the Holocene at core sites located in the vicinity of the PF and SACCF (McCave et al., 2014), whereas cores between these two oceanographic fronts show a slight increase for the LGM (2–5%; Figure 5). With the exception of McCave's southernmost core, sites that were covered by the LGM summer sea ice extent (Collins et al., 2012) show a 1–5% Holocene increase in current strength (Figure 5).

Our record is consistent with the reduced current velocities of the ACC during the last glacial on the Chilean margin at the entrance of the DP (Lamy et al., 2015). Proxy reconstructions of the SWW belt in the southern Chilean margin show a decrease of the westerly winds during colder intervals (Kohfeld et al., 2013; Lamy et al., 2010). Therefore, our observed glacial reduction could be associated with a weakening and equatorward shift of the SWW belt consistent with oceanographic observations and models that show that the strength of the ACC is related to the position and intensity of the SWW belt (Völker & Köhler, 2013).

In summary, the cores located at the Chilean-Argentinian margin and in the vicinity of the SAF in the DP area show higher flow speeds during the Holocene than during the LGM in terms of absolute values and regardless of water depth, corroborating the finding that more than one half of total DP transport takes place in the Subantarctic Zone. The higher Holocene flow speeds are suggested to respond to changes in the strength of the subantarctic ACC flow (Roberts et al., 2017). The LGM-Holocene change is greater in shallower cores but is still significant in deep cores that are near the ACC fronts.

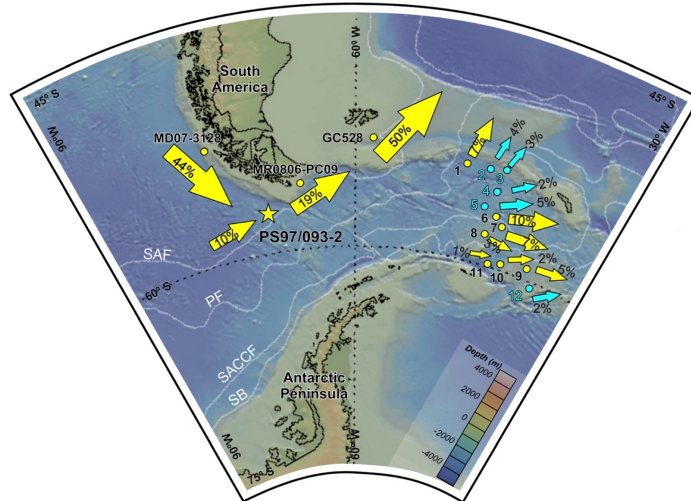


**Figure 5.** Drake Passage throughflow change (in %) between the Holocene and the LGM. Yellow (blue) arrows denote Holocene increase (decrease) at PS97/093-2, MD07-3128 and MR0806-PC09 (Lamy et al., 2015), GC528 (Roberts et al., 2017), and Scotia Sea core sites from McCave et al. (2014). White lines mark ACC modern fronts (Orsi et al., 1995): SAF, PF, SACCF, and SB as in Figure 1.

### 5.3. Glacial-Interglacial Changes in ACC Flow Strength

In contrast to the other available records from the DP region that only cover the last glacial and the Holocene, core PS97/093-2 provides a longer, orbital-scale perspective on the current dynamics that occur at the entrance of the DP gateway. Despite the importance of the ACC for the global climate system, its temporal variations are still largely unknown during glacial-interglacial cycles in the Pleistocene. Apart from our study, only two other records extend beyond ~500 ka, one in the Indian sector (Mazaud et al., 2010) and a second record from the SW Pacific (Hall et al., 2001).

At the location of core PS97/093-2, the mean  $\overline{SS}$  is 25.3  $\mu\text{m}$  during interglacials and 23.9  $\mu\text{m}$  during glacials (Figure 4), indicating an overall mean average glacial/interglacial variability of 6% over the last ca. 1.3 Myr. This difference is not very large, amounting to about 2 cm/s on the McCave et al. (2017) calibration. Because this value underestimates the major shifts during glacial terminations, we considered the difference between the  $\overline{SS}$  minimum value of each preceding glacial and the maximum of the following interglacial (Lisiecki & Raymo, 2005), resulting in a mean interglacial increase of approximately 16%.

The consistent pattern of higher bottom water current speeds during interglacials contrasts with the 500-ka-long ACC record from the subantarctic Indian Southern Ocean sector that is based on variations in size and abundance of magnetic grains and suggests an intensified ACC during glacials (Mazaud et al., 2010). However, caution in the interpretation of this record is advised since, in addition to current strength fluctuations, variations in magnetic properties could also reflect changes in bacterial production, ice-rafted debris input, and the source of the magnetic minerals (Channell et al., 2016). Stronger glacial near-bottom flow speeds (inferred from elevated  $\overline{SS}$ ) attributed to enhanced ACC influence have also been reported for the southern Agulhas Plateau (core MD02-2589 0–170 ka; Molyneux et al., 2007) and the western slope of the Agulhas Bank off South Africa (core MD96-2080 0–350 ka; Martínez-Méndez et al., 2008). On a longer time scale,  $\overline{SS}$  data from ODP Site 1123 in the southwest Pacific indicate that the DWBC east of New Zealand intensified during glacials over the past 1.2 Ma (Hall et al., 2001). If we accept that (i) the changes in the abundance of magnetic grains studied by Mazaud et al. (2010) reflect current strength fluctuations and, (ii) at ODP 1123, DWBC current strength fluctuations would reflect strength fluctuations connected to

ACC changes (Carter & McCave, 1997), then both studies would support the traditional view of a faster ACC flow during glacials due to a general glacial intensification of atmospheric ocean circulation (Gersonde et al., 2005; Lynch-Stieglitz et al., 2016; Toggweiler et al., 2006). Nevertheless, the interpretation of the DWBC is complex and most likely controlled by a combination of factors (see section 5.6)

Core PS97/093-2 data show that this general intensification of the subantarctic ACC does not extend to the SE Pacific and the DP where current strength is overall enhanced during interglacials. We suggest that in the DP, the northward shift of fronts and particularly of the SAF (Roberts et al., 2017) accompanied by an expansion of sea ice during glacial times likely decreased the DP throughflow of ACC, thus weakening the cold water route into the Atlantic. This shortfall in the supply of deep water to the Atlantic basin through the DP during glacial times might be compensated by a strong recirculation within the South Pacific causing a stronger South Pacific Gyre (Lamy et al., 2015). Concomitantly, the recirculation in the South Atlantic/Indian Ocean sectors may have weakened through a reduced Agulhas leakage along the warm water route (Beal et al., 2011).

#### 5.4. Marine Isotope Stage 11

MIS 11 was an outstanding interglacial period in the Earth's Pleistocene climate history that was characterized by longer and warmer interglacial conditions, 6–13 m higher sea level than that during the Holocene, and an unusual increase in carbonate production at high southern latitudes (e.g., Barker et al., 2006; Droxler et al., 1999; Hearty et al., 1999; Hodell et al., 2000; Raymo & Mitrovica, 2012).

Unlike for most interglacials in core PS97/093-2, where a consistent pattern of higher ACC strength emerges, the  $\overline{SS}$  values during the peak MIS 11 show a different behavior (Figure 6). We observe an initial rise in  $\overline{SS}$  during the MIS 12–11 transition (Termination V) followed by a decrease in the  $\overline{SS}$  that continues until the MIS 11–10 transition, where there is a short increase again. The most likely explanation is that the high Zr/Rb values during MIS 11 reflect extraordinarily strong currents at the PS97/93 site and thus additional enhancement of the ACC during this warmest interglacial as discussed in section 5.1.

The timing of the low  $\overline{SS}$  coincides with a 20-cm-thick nannofossil ooze in the core (Lamy, 2016) and matches the increase in coccolith accumulation rates during this time interval observed in the western and eastern flanks of the southern East Pacific Rise (Saavedra-Pellitero, Baumann, Lamy, et al., 2017) (Figure 6). This increase was associated with a very high production of coccolithophores in the water column triggered by a poleward retreat of the Southern Ocean fronts and associated variations in the nutrient regime and higher than modern sea surface temperatures. Assuming that for MIS 11 the measurements obtained with the Sedigraph are indeed reflecting reduced current strength, an alternative explanation could be a response to an exceptional southward movement of the ACC fronts during this extreme warm interval leading to an increased distance of core PS97/093-2 to the SAF and a respective flow speed reduction. Another alternative explanation could be that the opening of a marine seaway between the Amundsen and the Weddell Sea caused by a significant ice loss of the West Antarctic ice sheet (Vaughan et al., 2011) possibly deviated part of the ACC flow into the Weddell Sea, reducing ACC throughflow in the DP area. Whether such a mechanism can be invoked for the exceptionally warm MIS 11 needs to be explored in future work.

#### 5.5. Long-Term Modulation of Orbital-Scale ACC Variations Over the Past 1.3 Ma

Beyond glacial-interglacial ACC variations, our 1.3-Ma record allows to address the response and role of changes in the subantarctic ACC during major periods of global climate reorganizations when large atmosphere-ocean-ice and carbon cycle changes took place. Such is the case for the MPT (shift in ice-volume cyclicity from the 41- to 100-kyr world) and the MBE (major climatic transition ca. 430 ka ago with amplified 100-kyr cycles and warmer interglacials thereafter; Bouttes et al., 2018; Clark et al., 2006; Holden et al., 2011).

Our  $\overline{SS}$  record indicates that major shifts in amplitudes and pattern of ~41- and ~100-kyr cycles took place over both the MPT and the MBE (Figure 7). Overall, across the complete ~1.3-Ma record, we find a strong spectral coherence to the global benthic oxygen isotope stack in the ~41-kyr band (Figures 7a and 7b). These cycles dominate from 1.3 Ma to ~850 ka (MIS 21) and continued their influence thereafter (Figures 7c and 7d); this result largely agrees with that by Bajo et al. (2020), who found a strong influence of the obliquity on glacial terminations after the MPT. After MIS 21, the spectral power in the ~100-kyr

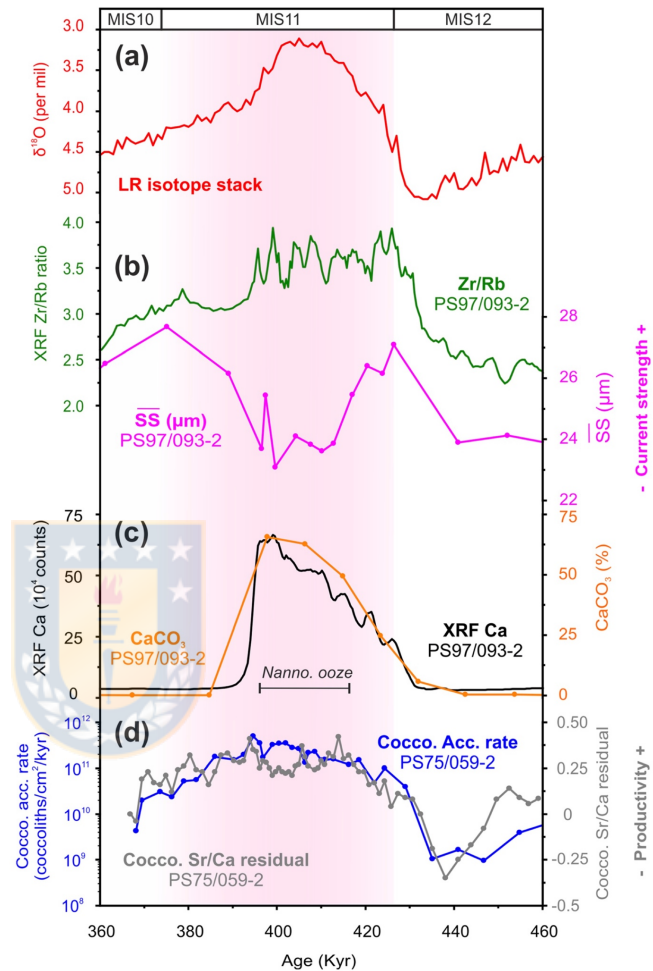


**Figure 6.** Marine isotope stage 11. (a) Evolution of the global ice volume (Lisiecki & Raymo, 2005). (b) Estimated changes in ACC strength based on the XRF Zr/Rb ratio and the SS record of core PS97/093-2. (c) CaCO<sub>3</sub> content (orange) and XRF Ca scanner counts (black). (d) Coccolithophore paleoproductivity proxies of sediment core PS75/059-2 (Saavedra-Pellitero, Baumann, Ullermann, et al., 2017): Coccolith accumulation rate (blue; note log scale) and Coccolith Sr/Ca residuals using the *Gephyrocapsa oceanica* correction (gray).

band becomes stronger across the MPT, and after a few subdued cycles during MIS 12–14, ~100-kyr cycles reappear after the MBE (Figures 7c–7e). There are two intervals (MIS 6–8 and MIS 12–14) during which the amplitudes of our SS record diminished strongly and show no correspondence with either the amplitudes in the LR04 stack (Figure 7b) or in Antarctic ice core records (Jouzel et al., 2007). The distinctly reduced sedimentation rates during these times (0.2–0.9 cm/kyr for MIS 6–8 and 0.5–0.9 cm/kyr for MIS 12–14; Figure 2) might be an indication of pronounced winnowing and subsequent bioturbation that could have reduced the glacial-interglacial amplitudes in our record.

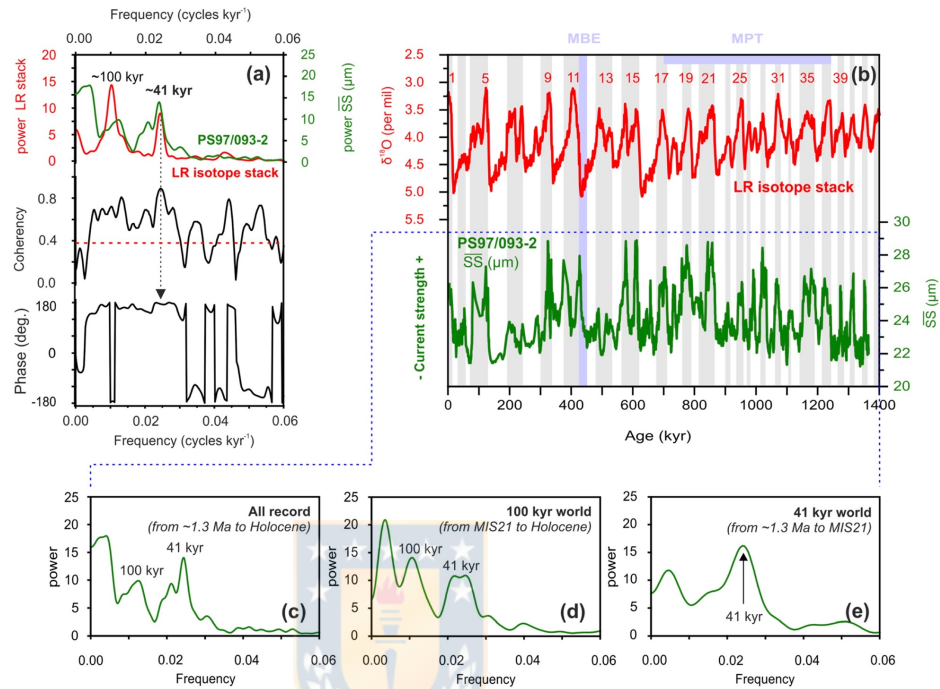


**Figure 7.** Spectral analysis and comparison between the  $\overline{SS}$  record of core PS97/093-2 (green) and LR04 benthic  $\delta^{18}O$  stack (Lisiecki & Raymo, 2005) (red). (a) Cross-spectral analysis of high-resolution  $\overline{SS}$  record based on XRF Zr/Rb transformation of core PS97/093-2 and the Lisiecki and Raymo stack. Coherency indicates the correlation between the pair of variables as a function of frequency; nonzero coherence is higher than 0.38 (red dashed line). Phase refers to the relationship of the pair of variables with the same frequency. If the phase is 180°, the two signals are out of phase with each other. (b) Evolution of the global ice volume during the last ~1.3 Ma (red); numbers indicate marine isotope stages (Lisiecki & Raymo, 2005), and estimated changes in ACC strength (green) are based on the  $\overline{SS}$  record of PS97/093-2. Vertical gray bars mark Lisiecki and Raymo interglacial stages. MBE, mid-Brunhes event; MPT, mid-Pleistocene transition. B-Tukey tests of the  $\overline{SS}$  PS97/093-2 record divided into three different time intervals: (c) the entire record, (d) from MIS 21 to the Holocene, and (e) from 1.3 Ma to MIS 21.

Neodymium isotopes have been used as a paleo-ocean circulation proxy across the MPT in the South Atlantic (Farmer et al., 2019; Pena & Goldstein, 2014). Both studies hypothesize that the rise of the 100-kyr ice age cycles was facilitated by enhanced deep-ocean carbon storage associated with a weakened Atlantic MOC. Between MIS 25 and 21 (~950 to 860 ka), Pena and Goldstein (2014) documented a major disruption of the MOC that seems to match with a reduced ACC strength at the entrance of the DP (seen as a strong diminution in the amplitude of the cycles in PS97/093-2; Figure 7b). In our record, MIS 21 (ca. 850 ka) marks the emergence of the first high-amplitude 100-kyr glacial cycle. Pena and Goldstein (2014) also stated that the vigor of the Atlantic MOC pre- and post-MPT has remained similar during interglacials. However, based on the PS97/093-2 record (Figure 7b), interglacials younger than 850 ka are characterized by somewhat higher values compared to interglacials before the MPT. We suggest that higher interglacial  $\overline{SS}$  values after the MPT could reflect a change in the southward position of the Southern Ocean fronts that may be associated with a stronger drawdown of nutrients and atmospheric  $CO_2$  in the Southern Ocean (Robinson et al., 2019). The interglacial increase in values coincides with the observed rise in deep-ocean  $\delta^{13}C$  values in the Southern Ocean, indicating an increase in the variability of deep water circulation that included well-ventilated interglacials and poorly ventilated glacials (Venz & Hodell, 2002). Both changes were in unison with the amplified strength of the 100-kyr cycle in ice volume change. In summary, the  $\overline{SS}$  PS97/093-2

record reflects the documented major disruption in the MOC during the MPT (Pena & Goldstein, 2014). The higher  $\overline{SS}$  values after the MPT could be caused by a change in the southward position of the Southern Ocean fronts and/or an increase in the variability of deep water circulation.

### 5.6. Comparing Deep Water Dynamics Across the South Pacific

The well-dated high-resolution sortable silt record from ODP Site 1123 documenting changes in strength of the DWBC off New Zealand back to ~1.2 Ma uniquely allows us to compare deep-ocean circulation changes across the Pacific Southern Ocean.

Both the ACC and the DWBC are major components of the global MOC. The DWBC is constituted of CDW, similar to ACC water masses. As the ACC approaches the Pacific sector from the Indian Ocean, it passes around and through gaps in Macquarie Ridge and then flows northeast along and around the eastern edge of the Campbell Plateau. In this region, the DWBC overlaps with the ACC and is strongly reinforced by the ACC, especially in the vicinity of the SAF that carries a mean transport of 90 Sv in this region (McCave et al., 2008). Thus, a strong coupling and positive reinforcement of the ACC and the DWBC occurs here. At ~45°S, the ACC and the DWBC separate and the ACC diverges eastward into the open South Pacific (along the SAF). The DWBC continues to flow northward at depths between ~5,000 and ~2,000 m, across the Bounty Fan, around the eastern end of the Chatham Rise through the Valerie Passage, northwestward across the eastern boundary of the Hikurangi Plateau, and finally northward toward the equator along the Tonga-Kermadec Ridge (Carter et al., 2004; Leg 181 synthesis, McCave et al., 2008). Based on this modern oceanographic setting, a mechanistic link between the main ACC and the DWBC is conceivable as the ACC presently reinforces the DWBC, suggesting the current strength in both systems could vary in parallel. However, the direct comparison of our record to the sortable silt data set at ODP Site 1123 (Hall et al., 2001) at orbital time scales indicates the opposite, i.e., a glacial weakening of the ACC at our SE Pacific site and a strengthening of the DWBC off New Zealand (Figure 8). Furthermore, if we divide our record into three similar intervals of differing inferred mean flow speeds as done by Hall et al. (2001), we find that relatively high (low) mean flows in the SW Pacific are correlated with relatively low (high) mean flows in the SE Pacific (Figure 8a).

B-Tukey's test of the records of core PS97/093-2 (this work) and Site ODP1123 (Hall et al., 2001) show high coherence and a phase close to 180° at the 41-kyr frequency band (Figure 8b), providing evidence that current strength fluctuations are out of phase between the eastern (core PS97/093-2) and western (ODP1123) Pacific. However, at the 100-kyr frequency, the spectral power of the PS97/093-2 record is distributed in two small peaks (at ~110- and 85-kyr frequencies, respectively) that lead to an absence of a coherent peak at the 100-kyr frequency in the PS97/093-2 record (Figure 8b). This might be originated either by (i) the lack of a 100-kyr peak during the "41-kyr world" from 1.3 Ma to 850 ka (Figure 7d) or by (ii) a change in the spacing of the interglacial peak value during the last 800 kyr that could cause a shift in the 100-kyr power band from ~110- to 85-kyr frequencies (Past Interglacial Working Group of PAGES, 2016). Therefore, we did not carry out the comparison at the 100-kyr frequency between the PS97/093-2 and ODP1123 records.

We suggest three different possible scenarios that could explain the disparity between both sides of the Pacific: (i) If we assume that our eastern record is representative for the Pacific ACC, following Hall et al. (2001) and the Leg 181 synthesis (Carter et al., 2004), the carbon isotope and sortable silt data at Site 1123 are consistent with greater DWBC flow, and therefore enhanced formation of AABW and greater Pacific ventilation, as a persistent feature of glacial periods over the past 1.2 Myr. In contrast, at the same time, the supply of deep water along the DP and into the Atlantic Ocean (via the CDW) was reduced during glacials. We speculate that these opposite changes in deep water flow across the South Pacific reflect a separation of deep water masses and enhanced recirculation in the deep Pacific. Such enhanced glacial recirculation coinciding with reduced DP transport is consistent with earlier findings of stronger glacial recirculation of Subantarctic Surface Water into the South Pacific Gyre (Lamy et al., 2015) during the LGM. Together with the glacial occurrence of the ~2,000-m bathyal front in the Pacific (Herguera et al., 1992, 2010; Keigwin & Lehman, 2015), this separation could have contributed to the isolation and aging of deep Pacific water masses, fostering enhanced glacial carbon storage (Ronge et al., 2016; Skinner et al., 2010). (ii) ACC changes in the SW Pacific are opposite to those recorded at our site at the entrance of the DP. This might indicate that the signal in the SW Pacific could be imported from the Indian sector were evidence for enhanced glacial ACC strength had been presented (Mazaud et al., 2010). This would imply an enhanced



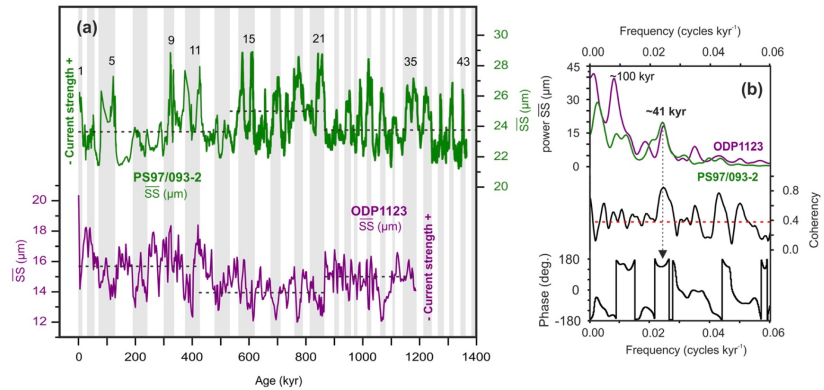


**Figure 8.** (a) Reconstructed changes in current strength during the past 1.3 Myr: at PS97/093 (green) and ODP 1123 (purple) sites. Vertical gray bars mark Lisiecki and Raymo interglacial stages. Numbers indicate some of the marine isotope stages (Lisiecki & Raymo, 2005). Horizontal dashed lines mark the mean  $\overline{SS}$  values for the periods used by Hall et al. (2001) and the ones chosen for the core PS97/093-2 record (MIS 1 to MIS 11, MIS 12 to MIS 21, MIS 22 to MIS 35 and MIS 1 to MIS 14, MIS 14 to MIS 21, MIS 22 to MIS 43, respectively). (b) Cross-spectral analyses of SS results of core PS97/093-2 (this study) and ODP1123 (Hall et al., 2001).

southern Pacific gyre recirculation but would impose questions about a shortage in the Atlantic water budget. (iii) Our record indicates that glacial northward shifts of the SAF in the SE Pacific (though potentially restricted by the DP) are coupled with changes in the southern westerlies, and it would be plausible that the SAF likewise moved northward in the SW Pacific. This might move the strong reinforcement of the DWBC by the ACC presently occurring at  $\sim 45^\circ\text{S}$  northward, i.e., closer to ODP Site 1123, where stronger bottom currents are recorded (Hall et al., 2001). Off New Zealand, the Campbell Plateau and Chatham Rise limited the shift of the SAF and particularly fixed the Subtropical Front at the Chatham Rise, thus enhancing oceanographic gradients in this area. Further east in the SW Pacific basin, both fronts might have been located further to the north (Bostock et al., 2013). From this point of view, a glacial northward displacement of the SAF could have both increased bottom water flow at ODP Site 1123 and reduced bottom water flow at site PS97/093.

## 6. Conclusions

We present a new high-resolution ACC strength record from the Subantarctic Zone of the Pacific entrance to the DP covering the last 1.3 Ma. An excellent correlation between measured  $\overline{SS}$  data and XRF scanner-derived Zr/Rb ratios in core PS97/093-2 demonstrates that in this area the latter are a reliable bottom current flow strength proxy. Our reconstruction shows consistently higher ACC speeds during interglacial times over the entire middle-late Pleistocene record.

Whereas shallower sites of the Chilean and Argentinian continental margins show a substantial 20–40% glacial reduction in ACC strength that was associated with a weakening of the cold water route, our data point to a smaller, but still significant (approximately 6% overall and 16% when considering major shifts), reduction in deep circulation during glacial times.

Our estimated ACC strength fluctuations upstream of the DP largely follow orbital-scale variations of climate and ice volume as expressed in the LR04 stack (Lisiecki & Raymo, 2005). The  $\overline{SS}$  record of core PS97/093-2 shows a dominance of the  $\sim 41$ -kyr cycles from 1.3 Ma to ca. 850 ka (MIS 21), followed by an increase of the spectral power of  $\sim 100$ -kyr cycles thereafter (from MIS 21 to the Holocene).

We hypothesize that the observed variations in strength are linked to the northward shift of Southern Ocean frontal systems during glacial times, potentially locating our site south of the strongest ACC flow in the vicinity of the SAF. Therefore, our record most likely records both limited local northward shifts and changes in

general ACC flow in the vicinity of the SAF. Together with an expected glacially extended sea ice zone and the geographic constriction of the DP, the reduced subantarctic ACC flow likely contributed to a glacial weakening of the total DP throughflow. This somewhat diminished inflow of CDW into the Atlantic through the DP could have affected the strength of the global MOC at time scales before the last glacial.

When comparing the  $\overline{SS}$  record of our site PS97/093 (SE Pacific) with the one at ODP Site 1123 (SW Pacific), we found that a clear opposite trend is evident: The weakened supply of deep water along the DP and into the Atlantic Ocean during glacials corresponds to an enhanced flow of the SW Pacific DWBC. This might indicate that the signal in the SW Pacific could be imported from the Indian sector or that a northward migration of the SAF during glacials increased the bottom water flow at ODP site 1123 and, at the same time, reduced bottom water flow at site PS97/093.

### Data Availability Statement

All data are available in PANGAEA repository: doi.pangaea.de/10.1594/PANGAEA.905998; doi.pangaea.de/10.1594/PANGAEA.905996; doi.pangaea.de/10.1594/PANGAEA.905994.

### Acknowledgments

This work was funded by AWI Helmholtz-Zentrum für Polar- und Meeresforschung. Additional support was provided by the Chilean oceanographic centers FONDAP-IDEAL (project 1500003) and COPAS Sur-Austral (project AFB170006 to C. B. L. and M. H. T.) and the Deutsche Forschungsgemeinschaft (DFG project BA 1648/30-1 to M. S-P). M. H. T. acknowledges support from scholarship CONICYT-PCHA/Doctorado Nacional/2016-21160454. We thank Dr. David Wilson and two anonymous reviewers for their comments and suggestions that helped improve the revised version of this manuscript. We wish to thank the captain, crew, and scientific party of R/V *Polarstern* for a successful PS97 cruise. We acknowledge S. Wiebe, R. Fröhling, and V. Schumacher for technical support at AWI. We also thank M. Wengler, L. Dumm, S. Wu, and G. Kuhn for fruitful discussions during the development of this work.

### References

- Anthonsen, D. E., & Ogg, J. G. (2012). Cenozoic and Cretaceous biochronology of planktonic foraminifera and calcareous nannofossils. In F. M. Gradstein, J. G. Ogg, M. D. Schmitz, & G. M. Ogg (Eds.), *The Geologic Time Scale 2012* (Vol. 1, pp. 1083–1127). Oxford: Elsevier. <https://doi.org/10.1016/b978-0-444-59425-9.15003-6>
- Bajo, P., Drysdale, R. N., Woodhead, J. D., Hellstrom, J. C., Hodell, D., Ferretti, P., et al. (2020). Persistent influence of obliquity on ice age terminations since the middle Pleistocene transition. *Science*, *367*(6483), 1235–1239. <https://doi.org/10.1126/science.aaw1114>
- Barker, P. F. (2001). Scotia Sea regional tectonic evolution: Implications for mantle flow and palaeocirculation. *Earth-Science Reviews*, *55*, 1–39. [https://doi.org/10.1016/S0012-8252\(01\)00055-1](https://doi.org/10.1016/S0012-8252(01)00055-1)
- Barker, P. F., & Burrell, J. (1977). The opening of Drake Passage. *Marine Geology*, *25*, 15–34.
- Barker, S., Archer, D., Booth, L., Elderfield, H., Henderiks, J., & Rickaby, R. E. M. (2006). Globally increased pelagic carbonate production during the Mid-Brunhes dissolution interval and the CO<sub>2</sub> paradox of MIS 11. *Quaternary Science Reviews*, *25*(23–24), 3278–3293. <https://doi.org/10.1016/j.quascirev.2006.07.018>
- Beal, L. M., De Ruijter, W. P. M., Biastoch, A., Zahn, R., & SCOR/WCRP/IAPSO Working Group 136 (2011). On the role of the Agulhas system in ocean circulation and climate. *Nature*, *472*(7344), 429–436. <https://doi.org/10.1038/nature09983>
- Bianchi, G. G., Hall, I. R., McCave, I. N., & Joseph, L. (1999). Measurement of the sortable silt current speed proxy using the Sedigraph 5100 and Coulter Multisizer IIe: Precision and accuracy. *Sedimentology*, *46*, 1001–1014. <https://doi.org/10.1046/j.1365-3091.1999.00256.x>
- Bohoyo, F., Larter, R. D., Galindo-Zaldívar, J., Leat, P. T., Maldonado, A., Tate, A. J., et al. (2019). Morphological and geological features of Drake Passage, Antarctica, from a new digital bathymetric model. *Journal of Maps*, *15*(2), 49–59. <https://doi.org/10.1080/17445647.2018.1543618>
- Bostock, H. C., Barrows, T. T., Carter, L., Chase, Z., Cortese, G., Dunbar, G. B., et al. (2013). A review of the Australian-New Zealand sector of the Southern Ocean over the last 30ka (Aus-INTIMATE project). *Quaternary Science Reviews*, *74*, 35–57. <https://doi.org/10.1016/j.quascirev.2012.07.018>
- Bouttes, N., Swingedouw, D., Roche, D. M., Sanchez-Goni, M. F., & Crosta, X. (2018). Response of the carbon cycle in an intermediate complexity model to the different climate configurations of the last nine interglacials. *Climate of the Past*, *14*(2), 239–253. <https://doi.org/10.5194/cp-14-239-2018>
- Carter, L., & McCave, I. N. (1997). The sedimentary regime beneath the deep western boundary current inflow to the southwest Pacific Ocean. *Journal of Sedimentary Research, Section B: Stratigraphy and Global Studies*, *67*(6), 1005–1017. <https://doi.org/10.1306/d42686b2-2b26-11d7-8648000102c1865d>
- Carter, L., McCave, I. N., & Williams, M. J. M. (2008). Chapter 4 Circulation and water masses of the Southern Ocean: A review. In F. Florindo, & M. Siebert (Eds.), *Developments in Earth and Environmental Sciences* (Vol. 8, pp. 85–114). Amsterdam: Elsevier B.V. [https://doi.org/10.1016/S1571-9197\(08\)00004-9](https://doi.org/10.1016/S1571-9197(08)00004-9)
- Carter, R. M., McCave, I. N., & Carter, L. (2004). Leg 181 synthesis: Fronts, flows, drifts, volcanoes, and the evolution of the southwestern gateway to the Pacific Ocean, eastern New Zealand. In C. Richter (Ed.), *Proc. ODP, Sci. Results* (Vol. 181, pp. 1–111). College Station, TX: ocean drilling program. <https://doi.org/10.2973/odp.proc.sr.181.210.2004>
- Chalk, T. B., Hain, M. P., Foster, G. L., Rohling, E. J., Sexton, P. F., Badger, M. P. S., et al. (2017). Causes of ice age intensification across the mid-Pleistocene transition. *Proceedings of the National Academy of Sciences*, *114*(50), 13,114–13,119. <https://doi.org/10.1073/pnas.1702143114>
- Channell, J. E. T., Harrison, R. J., Lascu, I., McCave, I. N., Hibbert, F. D., & Austin, W. E. (2016). Magnetic record of deglaciation using FORC-PCA, sortable-silt grain size, and magnetic excursion at 26 ka, from the Rockall Trough (NE Atlantic). *Geochemistry, Geophysics, Geosystems*, *17*, 4517–4533. <https://doi.org/10.1002/2015GC006171>
- Clark, P. U., Archer, D., Pollard, D., Blum, J. D., Rial, J. A., Brovkin, V., et al. (2006). The middle Pleistocene transition: Characteristics, mechanisms, and implications for long-term changes in atmospheric pCO<sub>2</sub>. *Quaternary Science Reviews*, *25*(23–24), 3150–3184. <https://doi.org/10.1016/j.quascirev.2006.07.008>
- Clark, P. U., Dyke, A. S., Shakun, J. D., Carlson, A. E., Clark, J., Wohlfarth, B., et al. (2009). The Last Glacial Maximum. *Science*, *325*(5941), 710–714. <https://doi.org/10.1126/science.1172873>
- Collins, L. G., Pike, J., Allen, C. S., & Hodgson, D. A. (2012). High-resolution reconstruction of southwest Atlantic sea-ice and its role in the carbon cycle during marine isotope stages 3 and 2. *Paleoceanography*, *27*, PA3217. <https://doi.org/10.1029/2011PA002264>
- Donohue, K. A., Tracey, K. L., Watts, D. R., Chidichimo, M. P., & Chereskin, T. K. (2016). Mean Antarctic Circumpolar Current transport measured in Drake Passage. *Geophysical Research Letters*, *43*, 11,760–11,767. <https://doi.org/10.1002/2016GL070319>

- Droxler, A. W., Poor, R., & Burckle, L. (1999). Data on past climate warmth may lead to better model of warm future. *Eos, Transactions of the American Geophysical Union*, 80(26), 289–290. <https://doi.org/10.1029/99EO00211>
- Dypvik, H., & Harris, N. B. (2001). Geochemical facies analysis of fine-grained siliciclastics using Th/U, Zr/Rb and (Zr + Rb)/Sr ratios. *Chemical Geology*, 181(1–4), 131–146. [https://doi.org/10.1016/S0009-2541\(01\)00278-9](https://doi.org/10.1016/S0009-2541(01)00278-9)
- Eagles, G., & Jokat, W. (2014). Tectonic reconstructions for paleobathymetry in Drake Passage. *Tectonophysics*, 611, 28–50. <https://doi.org/10.1016/j.tecto.2013.11.021>
- Elderfield, H., Ferretti, P., Greaves, M., Crowhurst, S. J., McCave, I. N., Hodell, D., & Piotrowski, A. M. (2012). Evolution of ocean temperature and ice volume through the mid-Pleistocene climate transition. *Science*, 337(6095), 704–709. <https://doi.org/10.1126/science.1219431>
- FARMGAEA.786205
- Farmer, J. R., Hönisch, B., Haynes, L. L., Kroon, D., Jung, S., Ford, H. L., et al. (2019). Deep Atlantic Ocean carbon storage and the rise of 100,000-year glacial cycles. *Nature Geoscience*, 12(5), 355–360. <https://doi.org/10.1038/s41561-019-0334-6>
- Fralick, P. W., & Kronberg, B. I. (1997). Geochemical discrimination of clastic sedimentary rock sources. *Sedimentary Geology*, 113(1–2), 111–124. [https://doi.org/10.1016/S0037-0738\(97\)00049-3](https://doi.org/10.1016/S0037-0738(97)00049-3)
- Freeman, N. M., & Lovenduski, N. S. (2016). Mapping the Antarctic Polar Front: Weekly realizations from 2002 to 2014. *Earth System Science Data*, 8(1), 191–198. <https://doi.org/10.5194/essd-8-191-2016>
- Gersonde, R. (2011). The expedition of the research vessel “Polarstern” to the polar South Pacific in 2009/2010 (ANT-XXVI/2 - BIPOMAC). *Berichte zur Polar- und Meeresforschung (Rep. Polar Marine Res.)*, 632, 330
- Gersonde, R., Abelmann, A., Brathauer, U., Becquey, S., Bianchi, C., Cortese, G., et al. (2003). Last glacial sea surface temperatures and sea-ice extent in the Southern Ocean (Atlantic-Indian sector): A multiproxy approach. *Paleoceanography*, 18(3), 1061. <https://doi.org/10.1029/2002PA000809>
- Gersonde, R., Crosta, X., Abelmann, A., & Armand, L. (2005). Sea-surface temperature and sea ice distribution of the Southern Ocean at the EPILOG Last Glacial Maximum—A circum-Antarctic view based on siliceous microfossil records. *Quaternary Science Reviews*, 24, 869–896. <https://doi.org/10.1016/j.quascirev.2004.07.015>
- Gille, S. T. (2014). Meridional displacement of the Antarctic Circumpolar Current. *Philosophical Transactions of the Royal Society*, 372, 20,130,273. <https://doi.org/10.1098/rsta.2013.0273>
- Gordon, A. L. (1975). An Antarctic oceanographic section along 170°E. *Deep Sea Research and Oceanographic Abstracts*, 22, 357–377. [https://doi.org/10.1016/0011-7471\(75\)90060-1](https://doi.org/10.1016/0011-7471(75)90060-1)
- Gordon, A. L. (1986). Inter-ocean exchange of thermocline water. *Journal of Geophysical Research*, 91(C4), 5037–5046. <https://doi.org/10.1063/1.475313>
- Gordon, A. L., Molinelli, E., & Baker, T. (1978). Large-scale relative dynamic topography of the Southern Ocean. *Journal of Geophysical Research*, 83(C6), 3023. <https://doi.org/10.1029/JC083i06p03023>
- Gouretski, V. V., & Koltermann, K. P. (2004). *WOCE Global Hydrographic Climatology. 35/2004, Berichte des Bundesamtes für Seeschifffahrt und Hydrographie* (52 pp.). Retrieved from <http://rda.ucar.edu/datasets/ds2854/>
- Hall, I. R., McCave, I. N., Shackleton, N. J., Weedon, G. P., & Harris, S. E. (2001). Intensified deep Pacific inflow and ventilation in Pleistocene glacial times. *Nature*, 412(6849), 809–812. <https://doi.org/10.1038/35090552>
- Hasenfratz, A. P., Jaccard, S. L., Martínez-García, A., Sigman, D. M., Hodell, D. A., Vance, D., et al. (2019). The residence time of Southern Ocean surface waters and the 100,000-year ice age cycle. *Science*, 363(6431), 1080–1084. <https://doi.org/10.1126/science.aat7067>
- Hasle, G. R., & Syvertsen, E. E. (1997). Marine Diatoms. In C. R. Tomas (Ed.), *Identifying marine phytoplankton* (pp. 5–385). Florida: Elsevier. <https://doi.org/10.1016/B978-012693018-4/50004-5>
- Hearty, P. J., Kindler, P., Cheng, H., & Edwards, R. L. (1999). A +20 m middle Pleistocene sea-level highstand (Bermuda and the Bahamas) due to partial collapse of Antarctic ice. *Geology*, 27(4), 375–378. [https://doi.org/10.1130/0091-7613\(1999\)027<0375:AMMPSL>2.3.CO;2](https://doi.org/10.1130/0091-7613(1999)027<0375:AMMPSL>2.3.CO;2)
- Herguera, J. C., Herbert, T., Kashgarian, M., & Charles, C. (2010). Intermediate and deep water mass distribution in the Pacific during the Last Glacial Maximum inferred from oxygen and carbon stable isotopes. *Quaternary Science Reviews*, 29(9–10), 1228–1245. <https://doi.org/10.1016/j.quascirev.2010.02.009>
- Herguera, J. C., Jansen, E., & Berger, W. H. (1992). Evidence for a bathyal front at 2000 m depth in the glacial Pacific, based on a depth transect on Ontong Java Plateau. *Paleoceanography*, 7(3), 273–288. <https://doi.org/10.1029/92PA00869>
- Hodell, D. A., Charles, C. D., & Ninnemann, U. S. (2000). Comparison of interglacial stages in the South Atlantic sector of the Southern Ocean for the past 450 kyr: Implications for marine isotope stage (MIS) 11. *Global and Planetary Change*, 24(1), 7–26. [https://doi.org/10.1016/S0921-8181\(99\)00069-7](https://doi.org/10.1016/S0921-8181(99)00069-7)
- Holden, P. B., Edwards, N. R., Wolff, E. W., Valdes, P. J., & Singarayer, J. S. (2011). The mid-Brunhes event and West Antarctic ice sheet stability. *Journal of Quaternary Science*, 26(5), 474–477. <https://doi.org/10.1002/jqs.1525>
- Howard, W. R., & Prell, W. L. (1992). Late Quaternary surface circulation of the southern Indian Ocean and its relationship to orbital variations. *Paleoceanography*, 7(1), 79–117. <https://doi.org/10.1029/91PA02994>
- Jouzel, J., Masson-Delmotte, V., Cattani, O., Dreyfus, G., Falourd, S., Hoffmann, G., et al. (2007). Orbital and millennial Antarctic climate variability over the past 800,000 years. *Science*, 317(5839), 793–796. <https://doi.org/10.1126/science.1141038>
- Keigwin, L. D., & Lehman, S. J. (2015). Radiocarbon evidence for a possible abyssal front near 3.1 km in the glacial equatorial Pacific Ocean. *Earth and Planetary Science Letters*, 425, 93–104. <https://doi.org/10.1016/j.epsl.2015.05.025>
- Kemp, A. E. S., Grigorov, I., Pearce, R. B., & Naveira Garabato, A. C. (2010). Migration of the Antarctic Polar Front through the mid-Pleistocene transition: Evidence and climatic implications. *Quaternary Science Reviews*, 29(17–18), 1993–2009. <https://doi.org/10.1016/j.quascirev.2010.04.027>
- Koenig, Z., Provost, C., Park, Y.-H., Ferrari, R., & Sennechael, N. (2016). Anatomy of the Antarctic Circumpolar Current volume transports through Drake Passage. *Journal of Geophysical Research: Oceans*, 121, 1626–1639. <https://doi.org/10.1002/2015JC011486>
- Kohfeld, K. E., Graham, R. M., de Boer, A. M., Sime, L. C., Wolff, E. W., Le Quéré, C., & Bopp, L. (2013). Southern Hemisphere westerly wind changes during the Last Glacial Maximum: Paleo-data synthesis. *Quaternary Science Reviews*, 68, 76–95. <https://doi.org/10.1016/j.quascirev.2013.01.017>
- Kylander, M. E., Ampel, L., Wohlfarth, B., & Veres, D. (2011). High-resolution X-ray fluorescence core scanning analysis of les Echets (France) sedimentary sequence: New insights from chemical proxies. *Journal of Quaternary Science*, 26(1), 109–117. <https://doi.org/10.1002/jqs.1438>
- Lamy, F. (2016). The expedition PS97 of the research vessel POLARSTERN to the Drake Passage in 2016. Reports on polar and marine research. Bremerhaven, Germany. [https://doi.org/10.2312/BzPM\\_0702\\_2016](https://doi.org/10.2312/BzPM_0702_2016)

- Lamy, F., Arz, H. W., Kilian, R., Lange, C. B., Lembke-Jene, L., Wengler, M., et al. (2015). Glacial reduction and millennial-scale variations in Drake Passage throughflow. *Proceedings of the National Academy of Sciences*, *112*(44), 13,496–13,501. <https://doi.org/10.1073/pnas.1509203112>
- Lamy, F., Kilian, R., Arz, H. W., Francois, J. P., Kaiser, J., Prange, M., & Steinke, T. (2010). Holocene changes in the position and intensity of the southern westerly wind belt. *Nature Geoscience*, *3*(10), 695–699. <https://doi.org/10.1038/ngeo959>
- Lisiecki, L. E., & Raymo, M. E. (2005). A Pliocene-Pleistocene stack of 57 globally distributed benthic  $\delta^{18}\text{O}$  records. *Paleoceanography*, *20*, PA1003. <https://doi.org/10.1029/2004PA001071>
- Livermore, R., Nankivell, A., Eagles, G., & Morris, P. (2005). Paleogene opening of Drake Passage. *Earth and Planetary Science Letters*, *236*, 459–470. <https://doi.org/10.1016/j.epsl.2005.03.027>
- Lynch-Stieglitz, J., Ito, T., & Michel, E. (2016). Antarctic density stratification and the strength of the circumpolar current during the Last Glacial Maximum. *Paleoceanography and Paleoclimatology*, *31*(5), 539–552. <https://doi.org/10.1002/2015PA002915>
- Martinez-Garcia, A., Rosell-Melé, A., Jaccard, S. L., Geibert, W., Sigman, D. M., & Haug, G. H. (2011). Southern Ocean dust-climate coupling over the past four million years. *Nature*, *476*(7360), 312–315. <https://doi.org/10.1038/nature10310>
- Martínez-Méndez, G., Zahn, R., Hall, I. R., Pena, L. D., & Cacho, I. (2008). 345,000-year-long multi-proxy records off South Africa document variable contributions of northern versus southern component water to the deep South Atlantic. *Earth and Planetary Science Letters*, *267*(1–2), 309–321. <https://doi.org/10.1016/j.epsl.2007.11.050>
- Martini, E. (1971). Standard tertiary and quaternary calcareous nanoplankton zonation. *Proceedings of the 2<sup>nd</sup> Planktonic Conference*, Roma, 1970, 739–785.
- Maslin, M. A., & Brierley, C. M. (2015). The role of orbital forcing in the early middle Pleistocene transition. *Quaternary International*, *389*, 47–55. <https://doi.org/10.1016/j.quaint.2015.01.047>
- Mazaud, A., Michel, E., Dewilde, F., & Turon, J. L. (2010). Variations of the Antarctic circumpolar current intensity during the past 500 ka. *Geochemistry, Geophysics, Geosystems*, *11*, Q08007. <https://doi.org/10.1029/2010GC003033>
- McCave, I. N., Carter, L., & Hall, I. R. (2008). Glacial-interglacial changes in water mass structure and flow in the SW Pacific Ocean. *Quaternary Science Reviews*, *27*(19–20), 1886–1908. <https://doi.org/10.1016/j.quascirev.2008.07.010>
- McCave, I. N., Crowhurst, S. J., Kuhn, G., Hillenbrand, C.-D., & Meredith, M. P. (2014). Minimal change in Antarctic circumpolar current flow speed between the last glacial and Holocene. *Nature Geoscience*, *7*(2), 113–116. <https://doi.org/10.1038/ngeo2037>
- McCave, I. N., & Hall, I. R. (2006). Size sorting in marine muds: Processes, pitfalls, and prospects for paleoflow-speed proxies. *Geochemistry, Geophysics, Geosystems*, *7*, Q10N05. <https://doi.org/10.1029/2006GC001284>
- McCave, I. N., Manighetti, B., & Robinson, S. G. (1995). Sortable silt and fine sediment size/composition slicing: Parameters for paleo-current speed and paleoceanography. *Paleoceanography*, *10*(3), 593–610.
- McCave, I. N., Thormalley, D. J. R., & Hall, I. R. (2017). Relation of sortable silt grain-size to deep-sea current speeds: Calibration of the 'Mud Current Meter'. *Deep-Sea Research Part I*, *127*, 1–12. <https://doi.org/10.1016/j.dsr.2017.07.003>
- Meredith, M. P., Woodworth, P. L., Chereskin, T. K., Marshall, D. P., Allison, L. C., Bigg, G. R., et al. (2011). Sustained monitoring of the Southern Ocean at Drake Passage: Past achievements and future priorities. *Reviews of Geophysics*, *49*, RG4005. <https://doi.org/10.1029/2010RG000348>
- Molyneux, E. G., Hall, I. R., Zahn, R., & Diz, P. (2007). Deep water variability on the southern Agulhas Plateau: Interhemispheric links over the past 170 ka. *Paleoceanography*, *22*, PA4209. <https://doi.org/10.1029/2006PA001407>
- Orsi, H., Whitworth, T., & Worth, D. N. (1995). On the meridional extent and fronts of the Antarctic Circumpolar Current. *Deep Sea Research*, *42*(5), 641–673. [https://doi.org/10.1016/0967-0637\(95\)00021-W](https://doi.org/10.1016/0967-0637(95)00021-W)
- Paillard, D., Labeyrie, L., & Yiou, P. (1996). Macintosh program performs time-series analysis. *Eos, Transactions American Geophysical Union*, *77*(39), 379–379. <https://doi.org/10.1029/96EO00259>
- Past Interglacial Working Group of PAGES (2016). Interglacials of the last 800,000 years. *Reviews of Geophysics*, *54*, 162–219. <https://doi.org/10.1002/2015RG000482>
- Pena, L. D., & Goldstein, S. L. (2014). Thermohaline circulation crisis and impacts during the mid-Pleistocene transition. *Science*, *345*(6194), 318–322. <https://doi.org/10.1126/science.1249770>
- Pfuhl, H. A., & McCave, I. N. (2005). Evidence for late Oligocene establishment of the Antarctic Circumpolar Current. *Earth and Planetary Science Letters*, *235*(3–4), 715–728. <https://doi.org/10.1016/j.epsl.2005.04.025>
- Raffi, I., Backman, J., Fornaciari, E., Pälike, H., Rio, D., Lourens, L., & Hilgen, F. (2006). A review of calcareous nannofossil astrochronology encompassing the past 25 million years. *Quaternary Science Reviews*, *25*(23–24), 3113–3137. <https://doi.org/10.1016/j.quascirev.2006.07.007>
- Raymo, M. E., & Mitrovica, J. X. (2012). Collapse of polar ice sheets during the stage 11 interglacial. *Nature*, *483*(7390), 453–456. <https://doi.org/10.1038/nature10891>
- Renault, A., Provost, C., Sennéchal, N., Barré, N., & Kartavtseff, A. (2011). Two full-depth velocity sections in the Drake Passage in 2006—Transport estimates. *Deep Sea Research, Part II*, *58*(25–26), 2572–2591. <https://doi.org/10.1016/j.dsr2.2011.01.004>
- Rintoul, S. R., Chown, S. L., DeConto, R. M., England, M. H., Fricker, H. A., Masson-Delmotte, V., et al. (2018). Choosing the future of Antarctica. *Nature*, *558*(7709), 233–241. <https://doi.org/10.1038/s41586-018-0173-4>
- Roberts, J., McCave, I. N., McClymont, E. L., Kender, S., Hillenbrand, C.-D., Matano, R., et al. (2017). Deglacial changes in flow and frontal structure through the Drake Passage. *Earth and Planetary Science Letters*, *474*, 397–408. <https://doi.org/10.1016/j.epsl.2017.07.004>
- Robinson, R. S., Jones, C. A., Kelly, R. P., Rafer, P., Etourneau, J., & Martinez, P. (2019). A cool, nutrient-enriched eastern equatorial Pacific during the mid-Pleistocene transition. *Geophysical Research Letters*, *46*, 2187–2195. <https://doi.org/10.1029/2018GL081315>
- Ronge, T. A., Tiedemann, R., Lamy, F., Köhler, P., Alloway, B. V., De Pol-Holz, R., et al. (2016). Radiocarbon constraints on the extent and evolution of the South Pacific glacial carbon pool. *Nature Communications*, *7*(1), 11487. <https://doi.org/10.1038/ncomms11487>
- Saavedra-Pellitero, M., Baumann, K. H., Lamy, F., & Köhler, P. (2017). Coccolithophore variability across marine isotope stage 11 in the Pacific sector of the Southern Ocean and its potential impact on the carbon cycle. *Paleoceanography*, *32*, 864–880. <https://doi.org/10.1002/2017PA003156>
- Saavedra-Pellitero, M., Baumann, K. H., Ullermann, J., & Lamy, F. (2017). Marine isotope stage 11 in the Pacific sector of the Southern Ocean: a coccolithophore perspective. *Quaternary Science Reviews*, *158*, 1–14. <https://doi.org/10.1016/j.quascirev.2016.12.020>
- Schrader, H., & Gersonde, R. (1978). Diatoms and silicoflagellates. In: Zachariasse et al. Microplanktonological counting methods and techniques—An exercise on an eight metres section of the lower Pliocene of Capo Rossello, Sicily. *Utrecht Micropaleontological Bulletins*, *17*, 129–176.
- Skinner, L. C., Fallon, S., Waelbroeck, C., Michel, E., & Barker, S. (2010). Ventilation of the deep Southern Ocean and deglacial CO<sub>2</sub> rise. *Science*, *328*(5982), 1147–1151. <https://doi.org/10.1126/science.1183627>

- Taylor, S. R. (1965). The application of trace element data to problems in petrology. In L. A. Ahrens, F. Press, S. K. Runcorn, & C. Urey (Eds.), *Physics and chemistry of the Earth* (Vol. 6, pp. 135–213). New York: Pergamon.
- Toggweiler, J. R., Russell, J. L., & Carson, S. R. (2006). Midlatitude westerlies, atmospheric CO<sub>2</sub>, and climate change during the ice ages. *Paleoceanography*, 21, PA2005. <https://doi.org/10.1029/2005PA001154>
- Vaughan, D. G., Barnes, D. K. A., Fretwell, P. T., & Bingham, R. G. (2011). Potential seaways across West Antarctica. *Geochemistry, Geophysics, Geosystems*, 12, Q10004. <https://doi.org/10.1029/2011GC003688>
- Venz, K. A., & Hodell, D. A. (2002). New evidence for changes in Plio-Pleistocene deep water circulation from Southern Ocean ODP leg 177 site 1090. *Palaeogeography, Palaeoclimatology, Palaeoecology*, 182(3–4), 197–220. [https://doi.org/10.1016/S0031-0182\(01\)00496-5](https://doi.org/10.1016/S0031-0182(01)00496-5)
- Völker, C., & Köhler, P. (2013). Responses of ocean circulation and carbon cycle to changes in the position of the Southern Hemisphere westerlies at Last Glacial Maximum. *Paleoceanography*, 28, 726–739. <https://doi.org/10.1002/2013PA002556>
- Well, R., & Roether, W. (2003). Neon distribution in South Atlantic and South Pacific waters. *Deep-Sea Research Part I: Oceanographic Research Papers*, 50(6), 721–735. [https://doi.org/10.1016/S0967-0637\(03\)00058-X](https://doi.org/10.1016/S0967-0637(03)00058-X)
- Wu, S., Kuhn, G., Diekmann, B., Lembke-Jene, L., Tiedemann, R., Zheng, X., et al. (2019). Surface sediment characteristics related to provenance and ocean circulation in the Drake Passage sector of the Southern Ocean. *Deep-Sea Research Part I*, 154, 103135. <https://doi.org/10.1016/j.dsr.2019.103135>
- Yin, Q. Z., & Berger, A. (2012). Individual contribution of insolation and CO<sub>2</sub> to the interglacial climates of the past 800,000 years. *Climate Dynamics*, 38(3–4), 709–724. <https://doi.org/10.1007/s00382-011-1013-5>
- Zielinski, U., & Gersonde, R. (1997). Diatom distribution in Southern Ocean surface sediments (Atlantic sector): Implications for paleoenvironmental reconstructions. *Palaeogeography, Palaeoclimatology, Palaeoecology*, 129(3–4), 213–250. [https://doi.org/10.1016/S0031-0182\(96\)00130-7](https://doi.org/10.1016/S0031-0182(96)00130-7)
- Zielinski, U., & Gersonde, R. (2002). Plio-Pleistocene diatom biostratigraphy from ODP leg 177, Atlantic sector of the Southern Ocean. *Marine Micropaleontology*, 45, 225–268.



*Paleoceanography and Paleoclimatology*

Supporting Information for

**Antarctic Circumpolar Current dynamics at the Pacific entrance to the Drake Passage over the past 1.3 million years**

María H. Goyos<sup>1,2</sup>, Frank Lamy<sup>3</sup>, Carina B. Lange<sup>2,4,5,6</sup>, Lester Lembke-Jene<sup>3</sup>,  
Mariem Saavedra-Pellitero<sup>7,†</sup>, Oliver Esper<sup>3</sup> and Helge W. Arz<sup>8</sup>

1 Programa de Postgrado en Oceanografía, Departamento de Oceanografía, Facultad de Ciencias Naturales y Oceanográficas, Universidad de Concepción, Concepción, Chile

2 Centro de Investigación Dinámica de Ecosistemas Marinos de Altas Latitudes (IDEAL), Universidad Austral de Chile, Valdivia, Chile

3 Alfred-Wegener Institut, Helmholtz Zentrum für Polar und Meeresforschung, Bremerhaven, Germany

4 Centro Oceanográfico COPAS Sur-Austral, Universidad de Concepción, Concepción, Chile

5 Departamento de Oceanografía, Universidad de Concepción, Chile

6 Scripps Institution of Oceanography, La Jolla, California 92037

7 Geowissenschaften, Universität Bremen, 28334 Bremen, Germany

† School of Geography, Earth and Environmental Sciences, University of Birmingham, UK

8 Leibniz-Institut für Ostseeforschung Warnemünde (IOW), Rostock-Warnemünde, Germany

**Contents of this file**

Tables S1 to S3

Figure S1

PS97/093-2		Markers	Age (Ma)		Notes
Section	Depth (cm)		Minimum age (Ma)	Maximum age (Ma)	
a	1	<i>Emiliana huxleyi</i>	0	0.29	
sec17	43	<i>E. huxleyi</i>	0	0.29	
sec16	143				Small-sized <i>Gephyrocapsa</i> (ooze)
sec15	243				Barren
b	300				Barren
c	334				Small-sized <i>Reticulofenestra</i>
sec14	343				<i>Gephyrocapsa caribbeanica</i> ooze (*) MIS 11
d	410				Barren
sec13	443				Barren
e	500				Barren
sec12	543				Barren
f	620				Barren
sec11	643				Absence of <i>Pseudoemiliana lacunosa</i>
g	726	<i>Pseudoemiliana lacunosa</i>	0.44	0.91	Absence of <i>Reticulofenestra asanoi</i>
sec10	744				Almost barren
h	771				Presence of CaCO <sub>3</sub> but absence of calcareous nannofossils
i	820				Small-sized <i>Gephyrocapsa</i> and <i>Reticulofenestra</i>
sec09	844				Almost barren
j	854				Barren
sec08	944				Barren
sec07	1044				Barren
k	1090				Barren
l	1120	<i>Reticulofenestra asanoi</i>	0.91	1.14	The assemblage is dominated by <i>Coccolithus pelagicus</i>
sec06	1144				Almost barren
m	1164	<i>R. asanoi</i>	0.91	1.14	The assemblage is dominated by <i>Coccolithus pelagicus</i>
n	1230				
sec05	1245				Barren
o	1280				
sec04	1345				Barren
p	1425				Barren
sec03	1445	Absence of <i>R. asanoi</i>	1.14	1.24	Absence of large <i>Gephyrocapsa</i>
q	1461				
sec02	1545				Barren
r	1620				Barren
CC	1645				Barren

**Table S1.** Core PS97/093-2 calcareous nannofossils biostratigraphic markers and taxonomical notes.

PS97/093-2																												
Section	Depth (cm)	<i>Act. actinodihulus</i>	<i>Act. ingens</i>	<i>Azpt. tabularis</i>	<i>E. antarctica</i>	<i>H. caneformis</i>	<i>F. barronii</i>	<i>F. keguelensis</i>	<i>Steph. turris</i>	<i>T. nitz group</i>	<i>T. nitz. var. parva</i>	<i>Thal. elliptipora</i>	<i>Thal. fassliata</i>	<i>Thal. lentiginosa</i>	<i>Thal. oestrupii</i>	<i>Thal. oliverana</i>	<i>Thaltr. antarctica</i>	<i>Disteph. speculum</i>	Chaetoceros spores	Nannos	Diatoms:	Silicoflagellates:	Sponge Spicules:	Foraminifera:	IRD:	Radiolarians	Preservation	Age Zone
sec17	1				R			A						F			F		R		A			F		T	M	<i>T. lentiginosa</i> Zone C (<0.19 Ma)
sec16	43				R	T		D		F				F			F		R		D			F		T	M/G	<i>T. lentiginosa</i> Zone C (<0.19 Ma)
sec15	143			R	R			D						F		R					C						M	<i>T. lentiginosa</i> Zone B
sec14	243		R	F		R		A		F	T			F			R			D	F						G/M	<i>T. lentiginosa</i> Zone A- MIS11 (nanno ooze)
sec13	343	T	R	T	R			A	T			T		F			T				C					T	M/P	<i>A. ingens</i> Zone A
sec12	543		F		R			A				R		R	T		R				A						M	<i>A. ingens</i> Zone A (0.65>X<1.04)
sec11	643		F		R			C									R				C						P	<i>A. ingens</i> Zone A (<1.04 Ma)
sec10	744		F	T	R			A	R					F			F				A					R	M/P	<i>A. ingens</i> Zone A (<1.04 Ma)
sec09	844	T	C	T	T			C	R			R		R			F				A					R	M	<i>A. ingens</i> Zone A (<1.04 Ma)
sec08	944		C					C	T			F					F				A					F	M	<i>A. ingens</i> Zone A (<1.04 Ma)
sec07	1044		F					C				F					F				A					F	G/M	<i>A. ingens</i> Zone B/A (<1.1 Ma)
sec06	1144		F					A	R					F			C				A					F	M	<i>A. ingens</i> Zone B (<1.3 Ma)
sec05	1245		F	T				C	R					F			C				A	T				F	M	<i>A. ingens</i> Zone B (<1.3 Ma)
sec04	1345		C					C	T								C				A					G/M	<i>A. ingens</i> Zone B (<1.3 Ma)	
sec03	1445		C	R				C	R			T		R		T	C				A					F	M	<i>A. ingens</i> Zone B (<1.3 Ma)
sec02	1545		F				R	R	T			T	T				C				C						P	<i>A. ingens</i> Zone A/B (about 1.3 Ma)
CC	1645		F				R	F	R				T			T	C	R	F		C	R					M/P	<i>A. ingens</i> Zone A/B (about 1.3 Ma)

**Table S2.** Microfossil abundance (mainly diatoms), diatom taxa and preservation in core PS97/093-2.



Tie point number	Depth (m)	Age model age (kyr)	Tie point number	Depth (m)	Age model age (kyr)	Tie point number	Depth (m)	Age model age (kyr)
1	0.24	15.54	13	3.82	433.43	25	9.61	907.27
2	1.10	57.54	14	4.32	489.03	26	10.09	954.74
3	1.35	79.19	15	4.56	523.38	27	10.92	1003.69
4	1.55	114.15	16	4.85	576.75	28	11.23	1021.71
5	1.92	133.43	17	5.26	612.33	29	11.67	1071.01
6	2.04	197.63	18	7.20	688.89	30	12.26	1109.24
7	2.16	216.69	19	7.36	715.03	31	13.16	1240.28
8	2.40	243.08	20	7.72	732.83	32	14.96	1294.20
9	2.53	290.63	21	8.17	762.21	33	15.15	1315.12
10	2.80	323.46	22	8.35	792.36	34	16.12	1354.32
11	3.02	335.59	23	8.57	820.76			
12	3.35	393.72	24	8.98	863.73			

**Table S3.** Tie-points used for the age model of core PS97/093-2. See main text for details.



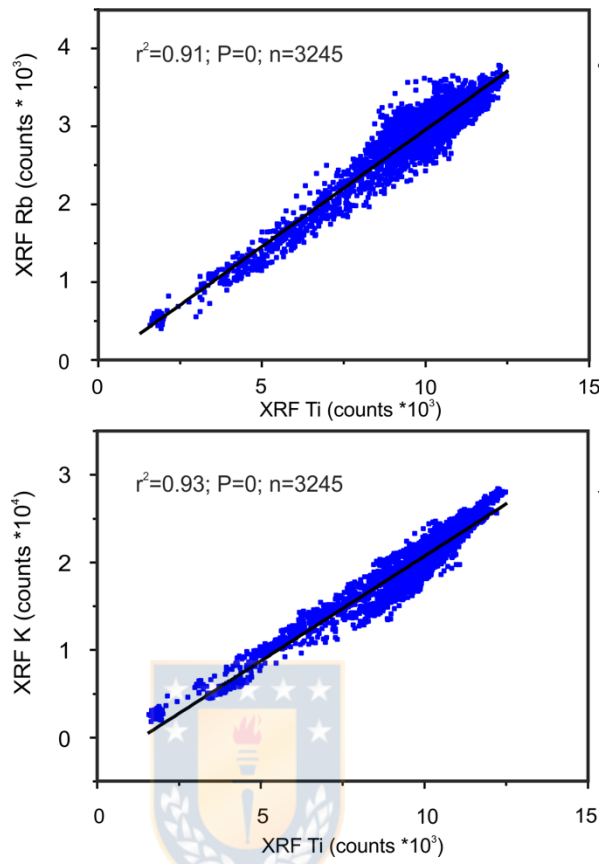
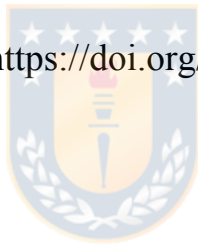


**Figure S1.** Linear regression between XRF core scanner-derived Ti, K and Rb in core PS97/093-2.

## 4.2. Chapter 2/ Capítulo 2

### **Manuscript 2 (accepted): Variations in export production, lithogenic sediment transport and iron fertilization in the Pacific sector of the Drake Passage over the past 400 ka**

Toyos, M. H., Winckler, G., Arz, H.W., Lembke-Jene, L., Lange, C.B., Gerhard Kuhn, and Lamy, F. (2021). Variations in export production, lithogenic sediment transport and iron fertilization in the Pacific sector of the Drake Passage over the past 400Ka. *Climate of the Past Discuss.* (preprint). <https://doi.org/10.5194/cp-2021-85>.



#### **Resumen:**

**Cambios en la producción biológica exportada, transporte de sedimentos litogénicos y fertilización con hierro en el sector Pacífico del Pasaje Drake durante los últimos 400,000 años.**

Los cambios en la productividad biológica en el Océano Austral tienen grandes repercusiones biogeoquímicas y climáticas. Específicamente, en la Zona Subantártica, la fertilización con hierro ha facilitado la utilización de nutrientes, aumentando la eficiencia de la bomba biológica durante periodos glaciales. Sin embargo, las variaciones pasadas en la productividad biológica y su vinculación con la fertilización

con hierro, potencialmente relacionado con avances y retrocesos de los campos de hielo Patagónicos en la Zona Subantártica del Pacífico Suroriental son todavía desconocidas. Para evaluar los principales mecanismos de productividad y la influencia de la fertilización con hierro durante los últimos 400.000 años, se han reconstruido tasas de acumulación basadas en  $^{230}\text{Th}$  normalizado (*MAR*, por sus siglas en inglés) y derivadas del modelo de edad (*BMAR*, por sus siglas en inglés) de opal biogénico,  $\text{CaCO}_3$ , exceso de bario, carbono orgánico, hierro y material litogénico de un testigo de sedimento recuperado en la Zona Subantártica a la entrada del Paso de Drake ( $57.5^\circ \text{ S}$ ;  $70.3^\circ \text{ W}$ ). Los resultados obtenidos indican que las *BMAR* han estado muy influenciadas por la dinámica de corrientes, ocasionando redistribución lateral de los sedimentos depositados en el sitio de estudio. Excepto por el Holoceno, MIS 5 y MIS 11, la ausencia de carbonatos en el testigo de sedimentos sería indicativo de disolución de los mismos. Por su parte el resto de los indicadores de productividad aumentaron en periodos glaciales, coincidiendo con incrementos en los flujos de hierro, muy probablemente procedentes de material glaciogénico Patagónico. Además, los aumentos en la productividad biológica son consistentes con una migración hacia el norte de los frentes Subantártico y Polar, que habrían dado lugar a que el testigo de sedimento se sitúe al

sur del frente Subantártico, en aguas más ricas en  $\text{Si(OH)}_4$ . No obstante, la productividad biológica en nuestra zona de estudio es menor que en otros sectores Subantárticos del Océano Austral, debido probablemente a un consumo de todo el  $\text{Si(OH)}_4$  en nuestra zona de estudio. Los resultados de este trabajo resaltan la importancia de la utilización de micronutrientes que habrían llegado del continente americano a través de transporte lateral en vez de polvo eólico. Además, nuestros resultados ejemplifican el papel que han jugado la migración de los frentes de la Corriente Circumpolar Antártica y la limitación de nutrientes en la regulación de los cambios en la productividad biológica en el sector Pacífico a la entrada del Paso de Drake en el pasado.



# Variations in export production, lithogenic sediment transport and iron fertilization in the Pacific sector of the Drake Passage over the past 400 ka

María H. Toyos<sup>1,2,3</sup>, Gisela Winckler<sup>4,5</sup>, Helge W. Arz<sup>6</sup>, Lester Lembke-Jene<sup>3</sup>, Carina B. Lange<sup>2,7,8</sup>, Gerhard Kuhn<sup>3</sup>, and Frank Lamy<sup>3</sup>

<sup>1</sup> Programa de Postgrados en Oceanografía, Departamento de Oceanografía, Facultad de Ciencias Naturales y Oceanográficas, Universidad de Concepción, Concepción, Chile

<sup>2</sup> Centro de Investigación Dinámica de Ecosistemas Marinos de Altas Latitudes (IDEAL), Universidad Austral de Chile, Valdivia, Chile

<sup>3</sup> Alfred-Wegener-Institut, Helmholtz-Zentrum für Polar und Meeresforschung, Bremerhaven, Germany

<sup>4</sup> Lamont-Doherty Earth Observatory, Columbia University, Palisades, NY 10964, United States

<sup>5</sup> Department of Earth and Environmental Sciences, Columbia University, New York, NY 10027, United States

<sup>6</sup> Leibniz-Institut für Ostseeforschung Warnemünde (IOW), Rostock-Warnemünde, Germany

<sup>7</sup> Departamento de Oceanografía and Centro Oceanográfico COPAS Sur-Austral, Universidad de Concepción, Chile

<sup>8</sup> Scripps Institution of Oceanography, La Jolla, California 92037, United States

*Correspondence to:* Maria H Toyos (mtoyos@udec.cl)

**Abstract.** Changes in Southern Ocean export production have broad biogeochemical and climatic implications. Specifically, iron fertilization likely increased subantarctic nutrient utilization and enhanced the efficiency of the biological pump during glacials. However, past export production in the subantarctic Southeast Pacific is poorly documented, and its connection to Fe fertilization, potentially related to Patagonian Ice Sheet dynamics is unknown. We report biological productivity changes over the past 400 ka, based on a combination of <sup>230</sup>Th<sub>xs</sub>-normalized and stratigraphy-based mass accumulation rates of biogenic barium, organic carbon, biogenic opal, and calcium carbonate as indicators of paleo-export production in a sediment core upstream of the Drake Passage (57.5° S; 70.3° W). In addition, we use fluxes of iron and lithogenic material as proxies for terrigenous input, and thus potential micronutrient supply. Stratigraphy-based mass accumulation rates are strongly influenced by bottom-current dynamics, which result in variable sediment focussing or winnowing at our site. Carbonate is virtually absent in the core, except during peak interglacial intervals of the Holocene, and Marine Isotope Stages (MIS) 5 and 11, likely caused by transient decreases in carbonate dissolution. All other proxies suggest that export production increased during most glacial periods, coinciding with high iron fluxes. Such augmented glacial iron fluxes at the core site were most likely derived from glaciogenic input from the Patagonian Ice Sheet promoting the growth of phytoplankton. Additionally, glacial export production peaks are also consistent with northward shifts of the Subantarctic and Polar Fronts, which positioned our site south of the Subantarctic Front and closer to silicic acid-rich waters of the Polar Frontal Zone. However, glacial export production near the Drake Passage was lower than

in the Atlantic and Indian sectors of the Southern Ocean, which may relate to complete consumption of silicic acid in the study area. Our results underline the importance of micro-nutrient fertilization through lateral terrigenous input from South America rather than aeolian transport, and exemplify the role of frontal shifts and nutrient limitation for past productivity changes in the Pacific entrance to the Drake Passage.

## 1 Introduction

The Southern Ocean (SO) plays an essential role in modulating glacial-interglacial variations of atmospheric  $p\text{CO}_2$  (Sigman et al., 2010). Increased biological export production, fueled by enhanced iron (Fe) fertilization in a more stratified glacial SO, is thought to have been a key driver of increased deep marine carbon storage (Jaccard et al., 2013). In the SO, the wind-driven, eastward flowing Antarctic Circumpolar Current (ACC) enhances the air-sea exchange of  $\text{CO}_2$  and the upwelling of nutrient- and  $\text{CO}_2$ -rich subsurface water masses (e.g., Marshall and Speer, 2012). Its flow is concentrated along several fronts, which are the Subantarctic Front (SAF), Polar Front (PF), and Southern ACC Front (SACCF; Orsi et al., 1995). These fronts act as barriers, inhibiting the exchange of the upwelled waters and their associated nutrients with neighboring fronts, and therefore also represent the limits between geochemical provinces (Chapman et al., 2020; Paparazzo, 2016). Nevertheless, in some regions of the SO with weaker jets the mixing barrier effect is lower, allowing some degree of meridional exchange of nutrients and upwelled waters by eddy fields (Naveira Garabato et al., 2011). Furthermore, these SO fronts are not stationary and their positions have been shown to change on seasonal to orbital timescales (e.g. Gille, 2014; Kemp et al., 2010). The Drake Passage (DP), located between the southern tip of South America and the Antarctic Peninsula, is a major constriction for the ACC flow and SO fronts. At the DP entrance, a consistent pattern of glacial reduction of the ACC throughflow has been previously linked to a northward shift of the SAF (Lamy et al., 2015; Toyos et al., 2020).

Today, the SO represents the major region in the world ocean where the efficiency of the biological carbon pump, the processes by which marine organisms consume inorganic nutrients and  $\text{CO}_2$  during photosynthesis and transform these elements into organic material into the deep sea, is low. Incomplete nutrient utilization arises from a combination of high overturning rates, yielding fast replenishment of most macronutrients to the photic zone, and Fe limitation, restricting phytoplankton growth (Boyd et al., 2012; Moore et al., 2013). Therefore, mean chlorophyll-*a* concentrations above  $2 \text{ mg m}^{-3}$  are only found within 50 km off a continental or island coastline (Fig 1, Graham et al., 2015). Specifically, in the Subantarctic Zone (SAZ; the area between the SAF and the Subtropical Front), waters feature excess nitrate relative to silicate (Dugdale et al., 1995) and Fe limits phytoplankton growth (Boyd et al., 1999). Thus, diatom production is relatively low, coccolithophores control primary production (Rigual-Hernández et al., 2015), and the biological pump is predominantly driven by carbonate producing organisms (Honjo, 2004). In contrast, the region between the SAF and the PF, known as the Polar

Frontal Zone (the PFZ), is characterized by high abundances of large diatoms (Kopczynska et al., 2001), and by relatively low mean chlorophyll-*a* concentrations (Fig 1, Graham et al., 2015).

The modern low export production in the SAZ contrasts with increased biological activity during glacials, predominantly fueled by enhanced Fe fertilization (e.g., Anderson et al., 2014; Jaccard et al., 2013; Kohfeld et al., 2005; Lamy et al., 2014; Martínez-García et al., 2009; Thöle et al., 2019). However, other mechanisms such as a more efficient diatom growth, shifts in the dominant plankton types, and increased nutrient utilization due to the lack of Fe limitation may also explain the glacial increase in export production, which may lead to an increase in the biological carbon pump's efficiency in the SAZ (François et al., 1997; Galbraith and Skinner, 2020; Matsumoto et al., 2014). Of the proposed mechanisms, only Fe fertilization contributed significantly to the lowering of atmospheric CO<sub>2</sub>, explaining 30 to 50 ppm of atmospheric CO<sub>2</sub> drawdown during the last glacial period (Kohfeld et al. 2005, Martin, 1990). It is widely believed that the Fe driving this fertilization of the glacial subantarctic SO is primarily delivered via aeolian dust (e.g., Martínez-García et al., 2009, 2014). This idea has been corroborated by reconstructions of past glacial-interglacial variability in the southern westerly wind belt, which indicate a glacial strengthening and an equatorward migration and/or extension (Ho et al., 2012; Kohfeld et al., 2013; Lamy et al., 2014).

In addition to dust input, especially in the vicinity of continents, Fe may also be brought to the surface ocean via continental runoff, iceberg transport or meltwater, and coastal upwelling (De Baar and De Jong, 2001). An increasing number of studies have recently shown that icebergs could provide a comparable or larger amount of bioavailable Fe than dust to the SO (e.g., Hopwood et al., 2019), and therefore significantly influence primary productivity (Wu and Hou, 2017). For instance, Fe associated with subglacial meltwater and icebergs stimulates and enhances marine primary productivity in ecosystems around the Antarctic Ice Sheet (Laufkötter et al., 2018; Vernet et al., 2011), and in the SAZ during the Last Glacial Maximum (LGM), where a combination of high ice discharge and slower iceberg melting due to colder sea surface temperatures increased the supply of Fe-rich terrigenous material (Wadham et al., 2019). It is well known that during glacial stages, erosion increased significantly, enhancing physical weathering and, in turn, the sediment supply to the deep ocean. However, despite comprising a non-trivial portion of the SO, past export production in the Southeast Pacific, and its connection to direct Fe fertilization via meltwater or icebergs, potentially related to Patagonian Ice sheet (PIS) dynamics, remains unexplored. The subantarctic Pacific in the vicinity of the entrance to the DP is proximal to Patagonia, but likely does not receive substantial dust from this region, given the prevailing wind direction of the southern westerlies. In fact, Patagonian dust is predominantly transported eastward to the SO's Atlantic sector (Li et al., 2008, 2010). Therefore, the DP entrance location might provide a unique opportunity to explore the PIS's potential as a direct source of Fe for fertilization of the southeastern Pacific during glacial intervals.

In this study, we reconstruct and characterize export production changes off southernmost Patagonia in the subantarctic Southeast Pacific over the past 400 ka and investigate their link to Fe fertilization and SO frontal shifts. We use a combination of <sup>230</sup>Th<sub>xs</sub>-normalized and stratigraphy-based mass



accumulation rates of the lithogenic fraction, Fe, excess Barium ( $Ba_{xs}$ ), i.e. the fraction of Ba that is not supplied by terrigenous material, total organic carbon (TOC), biogenic opal, and carbonate ( $CaCO_3$ ) from sediment core PS97/093-2 located near the SAF at the DP entrance (Fig 1). While  $Ba_{xs}$  and TOC reflect the integrated total export production,  $CaCO_3$  and biogenic opal indicate changes in the export production related to specific organisms. These are mainly coccolithophores and foraminifera for  $CaCO_3$  and diatoms and radiolarians for opal (Dymond et al., 1992; Paytan, 2009). We show that variations in export production were closely linked to terrigenous sediment and Fe delivery from the Patagonian hinterland, glacier dynamics and fundamental climate/ocean changes in the region. Lastly, we discuss potential underlying mechanisms, and evaluate our results with respect to published SAZ paleoproductivity reconstructions from other SO sectors.

## 2 Study area

Our site PS97/093 is located in the subantarctic Southeast Pacific, at the western entrance to the DP ( $57^\circ 29.94'$  S;  $70^\circ 16.48'$  W, 3781 m water depth). The DP, located between South America and the Antarctic Peninsula, is 850 km wide and represents the major geographical constriction for ACC transport into the Atlantic (Gordon et al., 1978). At present, the geostrophic transport of the ACC in the DP is associated with the SAF and PF, where strong surface and bottom velocities have been observed (Meredith et al., 2011; Renault et al., 2011). Furthermore, glacial-interglacial variability in bottom current circulation of *ca.* 16% during the last 1.3 Ma. has been reported at our coring site (Toyos et al., 2020). At present, Site PS97/093 is bathed in Circumpolar Deep Water (CDW), which consists of a mixture of aged North Atlantic Deep Water that enters the SO through the Atlantic, recirculated Pacific and Indian Deep waters, and dense bottom waters from Antarctica (e.g., Carter et al., 2008). The carbonate ion concentration of CDW is nearly constant at  $85 \pm 5 \mu\text{mol/kg}$  (Broecker and Clark, 2001), and it is slightly undersaturated with respect to calcium (Key et al., 2004). In the DP, the seafloor features, the position of the core southern westerly wind belt, and nutrient concentrations define the location of the ACC fronts (e.g., Ferrari et al., 2014; Meredith et al., 2011; Paparazzo et al., 2016). Here, the PF is associated with the northern expression of the silicate front, indicating the geographical boundary between silicate-poor waters to the north and silicate-rich waters to the south of it (Freeman et al., 2018, 2019). Our sediment core was retrieved *ca.* 40 km NW of the present-day position of the SAF, and *ca.* 350 km NW of the PF, within the main flow of the ACC (Fig 1b).

The DP is the region of the SO with the largest vertical velocities associated with topographically induced upwelling (Graham et al., 2015). Nevertheless, the DP is not considered an area of intensive phytoplankton growth, as illustrated by low chlorophyll-*a* concentrations (Fig 1; Demidov et al., 2011). Primary production is characterized by phytoplankton blooms in austral spring (Demidov et al., 2011), when Fe availability is the critical factor for the occurrence of the blooms (De Baar et al., 1995). Additionally, a lack of dissolved silica compared to phosphorus may limit the growth of siliceous phytoplankton species north of the PF (mainly diatoms, Demidov et al., 2011; Freeman et al., 2019).

An analysis of the composition of the surface sediments shows that in the DP a gradual change occurs from low organic carbon and high CaCO<sub>3</sub> content in the SAZ to opal-rich sediments at the Polar Front zone and in the Permanently Open Ocean Zone (Cárdenas et al., 2019).

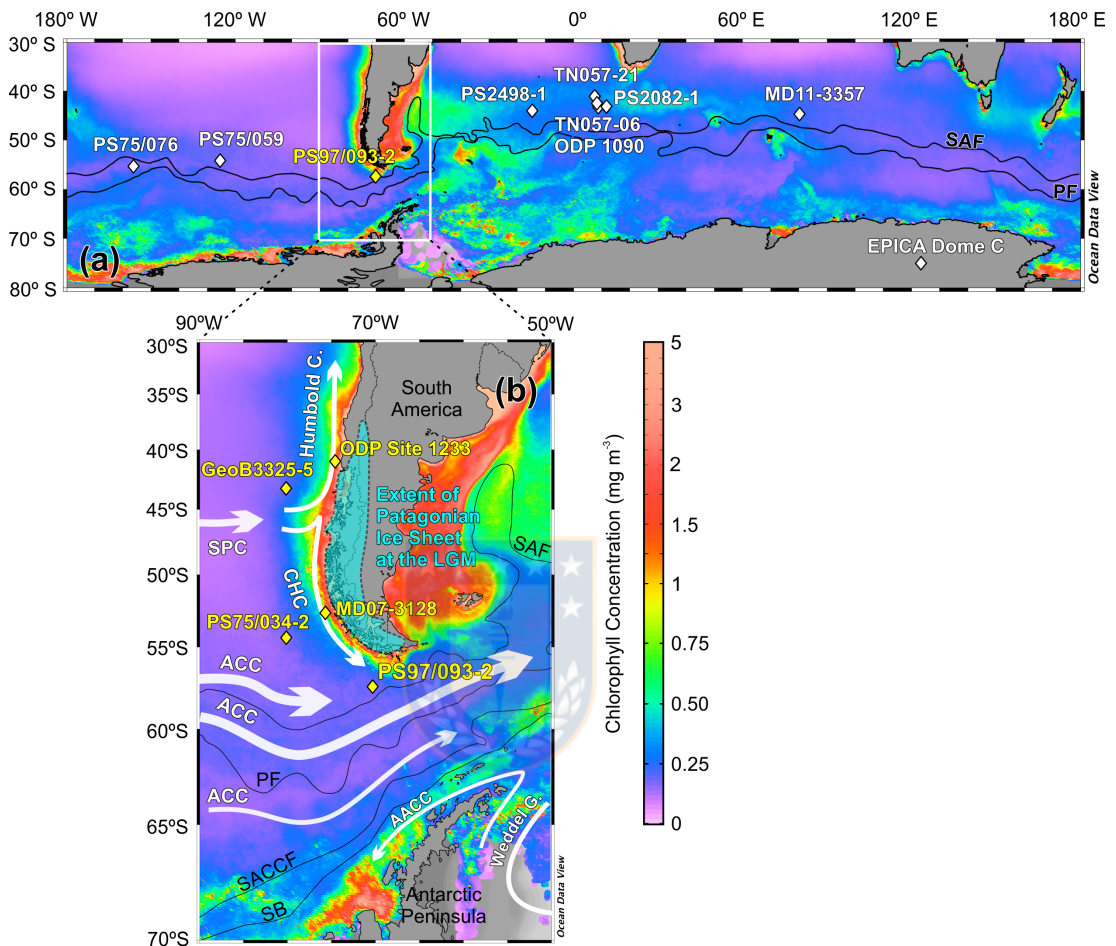


**Figure 1:** (a) Map of the Southern Ocean mean chlorophyll-*a* concentrations for the years 2009–2019 with core locations. Yellow diamond indicates the location of core PS97/093-2 (this study), and white diamonds the location of published records discussed in the text: PS75/076 and PS75/059 (Lamy et al. 2014); PS2498-1, TN057-21, and TN057-06 (Anderson et al., 2014); ODP1090 (Martínez-García et al. 2014); PS2082-1 (Frank et al. 1999; Nürnberg, 1997); MD11-3357 (Thöle et al., 2019), and EPICA Dome C ice Core (Lambert et al., 2008). (b) Map of the Drake Passage mean chlorophyll-*a* concentrations for the years 2009–2019 showing the location of PS97/093-2 (this study), MD07-3128 (Caniupán et al., 2011), PS75/034-2 (Ho et al., 2012), GeoB3325-5 (Tapia et al., 2021), and ODP Site 1233 (Lamy et al., 2010; yellow diamonds); cyan area indicates the extension of the Patagonian Ice Sheet at the Last Glacial Maximum based on Glasser et al. (2008), white arrows show trajectories of the Antarctic Circumpolar Current (ACC), South Pacific Current (SPC), Cape Horn Current (CHC), Humboldt Current (Strub et al., 2019), and Antarctic Coastal Current (AACC, Deacon, 1984). Black lines mark ACC modern fronts (Orsi et al., 1995). SAF, Subantarctic Front; PF, Polar Front; SACCF, southern Antarctic Circumpolar Current Front, and SB, southern boundary of the ACC. We used the MODIS-Aqua Level-3 Mapped Chlorophyll-*a* Data Version 2018 (data/10.5067/AQUA/MODIS/L3M/CHL/2018), in 4 km resolution monthly mean chlorophyll-*a* concentrations between March 2009 and March 2019 (available from NASA Ocean Color website, <https://oceancolor.gsfc.nasa.gov/l3/>) and Ocean Data View for visualization (Schlitzer 2021).

In the northern part of the DP, the provenance of terrigenous materials is restricted to proximal source regions, specifically southern Patagonia (Wu et al., 2019). Furthermore, analyses of surface sediments

from the eastern South Pacific and DP have excluded both a westward dust transport pathway from southern South America dust sources to this region (Wengler et al., 2019), and a substantial modern dust contribution from either Patagonia or Australia to the DP (Wu et al., 2019). After the Great Patagonian Glaciation (*ca.* 1 Ma), in at least five major glaciations, the Patagonian Andes were covered by a continuous mountain ice sheet, extending from 37°S to the Cape Horn and onto the Pacific Patagonian Shelf, with most ice likely calving into the Pacific Ocean on the western side, south of Chiloe island (Fig. 1; Davies et al., 2020; Gowan et al., 2021; Rabassa, 2008; Rabassa et al., 2011). As a result, at the southernmost Chilean continental margin, higher ice-rafted debris (IRD) contents occurred during cold intervals, interpreted as advances of the PIS (Caniupán et al., 2011). The distance between core PS97/093-2 and the PIS during the last glacial (situated at ~56°S at that time, Glasser et al., 2008) was *ca.* 180 km (Fig 1b).

### 3 Material and methods

Piston core PS97/093-2 was retrieved from the Pacific entrance of the Drake Passage (57° 29.94' S; 70° 16.48' W; 3781 m water depth; 16.45 m length; Fig. 1) during expedition PS97 "Paleo Drake" with R/V Polarstern (Lamy, 2016). Lithologically, different types of hemipelagic sediments occur at this location that vary in composition on orbital timescales (Lamy, 2016). Sediments from the interglacials MIS 11, MIS 5 and the Holocene are primarily composed of calcareous oozes (nannofossil or foraminifera-nannofossil oozes) with minor concentrations of diatoms. In contrast, glacial and sediments from MIS 9, 7 and 3 are clayey silt with rare biogenic components, intercalated with some layers of diatomaceous fine-grained clayey silts.

#### 3.1 Age model

The age model for core PS97/093-2 was developed by Toyos et al. (2020) using the AnalySeries software (Paillard et al., 1996), and is based on a two-step approach: 1) establishment of a preliminary age model based on shipboard physical property data and biostratigraphic time markers from calcareous nannofossils and diatoms, and 2) fine-tuning of the high-resolution XRF-derived elemental Fe and Ca counts and CaCO<sub>3</sub> contents to the LR04 benthic  $\delta^{18}\text{O}$  stack (Lisiecki and Raymo, 2005). The iron content is generally representative of the sediment's siliciclastic fraction, which is most likely controlled by a combination of factors, including dilution of biogenic material (primarily CaCO<sub>3</sub>) together with varying eolian and/or glaciogenic sediment input from South America. CaCO<sub>3</sub> content usually is lower during glacial stages when enhanced detrital fluxes suppress the relative amount of carbonate (e.g., Diekmann, 2007). For tuning, we assumed that low Fe contents characterize interglacial periods, whereas high contents represent glacial. Additionally, XRF Ca counts and CaCO<sub>3</sub> contents were used for additional tuning in the intervals where they are present.

### 3.2 Bulk sediment parameters and geochemistry

Total carbon and nitrogen (TC, TN) were quantified using a CNS analyzer (Elementar Varia EL III) at the Alfred-Wegener-Institute, Bremerhaven (AWI) using 100 mg of freeze-dried and homogenized sediment. Total organic carbon (TOC) contents were measured with a carbon-sulfur determinator (CS-2000, ELTRA) after the removal of inorganic carbon (total inorganic carbon) by adding 37% (vol/vol) of hydrochloric acid.  $\text{CaCO}_3$  was calculated employing the standard equation Eq. (1):

$$\text{CaCO}_3[\text{wt}\%] = (\text{TC}[\text{wt}\%] - \text{TOC}[\text{wt}\%]) * 8.333 \quad (1)$$

Biogenic opal was determined at the Laboratory of Paleoceanography, University of Concepción (UdeC), Chile. The alkaline extraction was conducted following the procedure described by Mortlock and Froelich, (1989), but using NaOH as a digestion solution (Müller and Schneider, 1993). Between 50 and 70 milligrams of freeze-dried sediment were first treated with 10%  $\text{H}_2\text{O}_2$  and 1N HCl, and then extracted with 1M NaOH (40 mL; pH-13) at 85 °C for five hours. The analysis was carried out by molybdate-blue spectrophotometry. Values are expressed as biogenic opal percent by multiplying the Si (%) by 2.4 (Mortlock and Froelich, 1989). We did not correct for the release of extractable Si from coexisting clay minerals, and thus biogenic opal values could be overestimated (Schlüter and Rickert, 1998). Biogenic opal was also measured at AWI Bremerhaven, though at significantly lower temporal resolution and with smaller sample sizes (30 mg), using the sequential leaching method of Müller and Schneider (1993), and differences between the overlapping data points were observed. For terrigenous contents exceeding 70%, opal concentrations measured at UdeC were consistently 3–5% higher than those measured at AWI. When the lithogenic content was below 40%, the inter-lab difference was less than 1%. The discrepancy between both datasets is most probably due to leaching of clay minerals like smectite (Cárdenas et al., 2019; Wu et al., 2019) and a higher pH base employed at UdeC. Despite the difference in values, both records show a similar pattern of variability. Given the importance of high-resolution data, we here use the opal results from UdeC. Dry bulk densities were quantified on a total of 162 samples with a gas pycnometer (Micromeritics AccPyc II 1340) at AWI Bremerhaven, using the density measurements of freeze-dried and homogenized bulk sediment samples and calculated by incorporating the water content of the samples.

The archive half of core PS97/093-2 was measured with an AVAATECH X-Ray Fluorescence Core Scanner (XRF-CS) at AWI Bremerhaven for high-resolution semi-quantitative element intensities of Ca, Fe, Ba and Ti at 0.5 cm resolution (0.5 x 1.2 cm measurement area, slit size down- and across-core). Three consecutive runs were performed with tube voltages of 10 kV (no filter), 30 kV (Pd-thick filter) and 50 kV (Cu filter), a current of 0.15, 0.175 and 1 mA, acquisition times of 10 s, 15 s and 20 s, respectively. Raw data were processed using Canberra *Eurisys'* iterative least squares software (WIN AXIL) package. To obtain a high-resolution  $\text{CaCO}_3$  record we calibrated the XRF Ca intensities with the bulk sediment  $\text{CaCO}_3$  measurements ( $r^2=0.92$ ,  $n=157$ ,  $P<0.0001$ , Fig S1).

### 3.3 Elements and U/Th isotope analysis

Concentrations of Fe, Ti and Ba, along with U/Th isotopes, were determined at Lamont-Doherty Earth Observatory (LDEO). Freeze dried samples (100 mg) were spiked with a  $^{236}\text{U} - ^{229}\text{Th}$  solution, followed by complete acid digestion (Fleisher and Anderson, 2003). Digests were taken up in 10 ml of 0.5 M  $\text{HNO}_3$ , and subsequently split in two aliquots. First, 0.4 ml was diluted again in 0.5 M  $\text{HNO}_3$  to get a final dilution of 2000x that was used for the determination of Al, Fe, Ti and Ba concentrations. For the determination of U/Th isotopes, the remainder of the initial dilution (~ 9.6 ml) was utilized, with U/Th purification achieved via Fe-coprecipitation and anion exchange chromatography following the methodology of Fleisher and Anderson, (2003). To check for reproducibility and for quality control purposes, an internal sediment standard (VOICE Internal MegaStandard (VIMS)) was run in each batch. U/Th isotopes were measured on a Thermo Scientific Element 2 ICP-MS, and absolute elemental concentrations of Fe, Ti, and Ba were determined using an ICP-OES. Finally, to obtain a high-resolution Fe record, we calibrated the 3-point smoothed Fe XRF intensities with bulk sediment (wt%) Fe from our discrete samples ( $r^2=0.90$ ,  $n=132$ ,  $P<0.0001$ ) (Fig S1).

### 3.4 Excess barium

$\text{Ba}_{xs}$  was calculated as:

$$\text{Ba}_{xs} = \text{Ba}_{total} - \left( \text{Ti}_{total} * \left[ \frac{\text{Ba}}{\text{Ti}} \right]_{detrifal} \right) \quad \text{Eq. (2)}$$

where  $\text{Ba}_{total}$  is the total measured Ba,  $\text{Ti}_{total}$  is the total measured Ti, and  $[\text{Ba}/\text{Ti}]_{detrifal}$  is the ratio of Ba and Ti in crustal material (assumed here to be 0.126 after Turekian and Wedepohl, 1961). This methodology assumes that 1) the major source of elemental Ba to deep-sea sediments is marine barite, and 2) terrigenous material has a known and constant Ba/Ti ratio (e.g., Winckler et al., 2016). Our  $\text{Ba}_{xs}$  record was obtained calibrating the 3-point smoothed Ba and Ti XRF intensities with bulk sediment (wt%) Ba ( $r^2=0.76$ ,  $n=132$ ,  $P<0.0001$ ) and Ti ( $r^2=0.79$ ,  $n=132$ ,  $P<0.0001$ ) (Fig S1).

### 3.5 Mass accumulation rates

Mass accumulation rates of individual sediment components (Fe,  $\text{Ba}_{xs}$ , TOC,  $\text{CaCO}_3$  and biogenic opal) were calculated by using the  $^{230}\text{Th}_{xs}$  normalization method (Bacon, 1984; Francois et al., 2004).  $^{230}\text{Th}$  is produced in the water column by decay of  $^{234}\text{U}$ , and has a short residence time, settling quickly to the underlying sediments by proximal scavenging. As such, the flux of  $^{230}\text{Th}$  scavenged from the water column is considered to be nearly equal to its production rate. Therefore, the  $^{230}\text{Th}_{xs}$ - normalized mass accumulation rate (MAR) for a given sample can be determined by Eq (3):

$$\text{MAR} = \frac{\beta \times z}{[^{230}\text{Th}_{xs}^0]}, \quad (3)$$

where  $\beta \times z$  is the integrated  $^{230}\text{Th}$  production in the overlying water column that depends on the water depth ( $z$ ), and  $^{230}\text{Th}_{xs}^0$  is the measured  $^{230}\text{Th}$  activity after corrections for i)  $^{230}\text{Th}$  supported by  $^{238}\text{U}$  in detrital sediments, ii)  $^{230}\text{Th}$  supported by authigenic  $^{238}\text{U}$  from the seawater, and iii) radioactive decay of  $^{230}\text{Th}$  since deposition. Uncertainties of  $^{230}\text{Th}_{xs}^0$  were propagated by considering analytical errors, uncertainties in the lithogenic and autigenic corrections, and decay corrections. In this study, if a sample has  $^{230}\text{Th}_{xs} \leq 30\%$  of the total  $^{230}\text{Th}$  concentration and a propagated uncertainty  $\geq 60\%$ , it is excluded. We determine MAR back to *ca.* 400 ka, with the relative uncertainties of the  $^{230}\text{Th}_{xs}$  constrained MAR increasing with the age of the sediments.  $^{230}\text{Th}_{xs}$ -normalized mass accumulation rates of individual components were obtained by multiplying their respective concentrations by the  $^{230}\text{Th}$ -derived MAR. Additionally, stratigraphy-based bulk mass accumulation rates (BMAR) of individual components were obtained by multiplying the concentration of the respective component by the linear sedimentation rate and the dry bulk density.

### 3.6 Calculation of focusing factor

The degree of sediment focusing ( $\Psi$ ) was calculated following the approach of Suman and Bacon, (1989) Eq (4):

$$\Psi = \left( \int_{r_1}^{r_2} {}^{230}\text{Th}_{xs}^0 \rho_r dr \right) / \beta_z (t_2 - t_1), \quad (4)$$

where  $\rho_r$  is the dry bulk density ( $\text{g}/\text{cm}^3$ ),  $^{230}\text{Th}_{xs}^0$  is the concentration of excess  $^{230}\text{Th}$  in the sediment corrected for decay since deposition,  $t_1$  and  $t_2$  are the corresponding ages (kyr) of sediment depths  $r_1$  and  $r_2$  (cm), and  $\beta_z$  ( $\text{dpm}/\text{cm}^2/\text{kyr}$ ) is the integrated  $^{230}\text{Th}$  production in the overlying water column from  $^{234}\text{U}$  decay.  $\Psi > 1$  indicates sediment focusing, whereas  $\Psi < 1$  denotes sediment winnowing. Values of  $\Psi = 1$  indicate that the amount of  $^{230}\text{Th}$  buried in the sediment is equivalent to the amount of  $^{230}\text{Th}$  produced in the water column.

### 3.7 Lithogenic content

The concentrations of lithogenic material were calculated using  $^{232}\text{Th}$  (e.g., Anderson et al., 2014; Winckler et al., 2008) assuming that i)  $^{232}\text{Th}$  is exclusively of detrital origin (Francois et al., 2004), and ii) the  $^{232}\text{Th}$  concentration of terrigenous material is relatively constant.  $^{232}\text{Th}$ -derived lithogenic MAR were calculated by dividing the lithogenic material concentration by average  $^{232}\text{Th}$  concentration of lithogenic material from Patagonia ( $9 \mu\text{g}/\text{g}$ , McGee et al., 2016).

Additionally, the lithogenic content was also determined by subtraction of the biogenic sediment components from the total bulk, Eq (5):

$$\text{lithogenic (wt\%)} = 100 - [\text{biogenic opal (wt\%)} + \text{CaCO}_3 \text{ (wt\%)} + (2\text{TOC (wt\%)})], \quad (5)$$

#### 4 Results

CaCO<sub>3</sub> content is almost zero throughout most of the record, peaking only during MIS 11 (~80%, which coincides with a prominent layer of nannofossil ooze, Lamy, 2016), MIS 5 (~40%), and the Holocene (~40%, Fig 2). In contrast, lithogenic content (<sup>232</sup>Th-derived, and those obtained by subtracting biogenic sediment components from the total bulk) and Fe (wt%) show minima during these interglacials, and higher values during the rest of the record. Overall, the <sup>232</sup>Th-based lithogenic fraction is 10% lower than the lithogenic fraction obtained by subtraction (Fig 2b). The Ba<sub>xs</sub> concentrations show glacial-interglacial variability with broadly elevated values during interglacials. Specifically, in our Ba<sub>xs</sub> record, interglacial peaks are more pronounced in MIS 5, 7 and 9 than in MIS 1 and MIS 11 (Fig 2d). The percentage of TOC does not display glacial-interglacial variability, and values increase gradually from MIS 5e to the Holocene. The biogenic opal percentage shows strong similarities with the lithogenic and Fe records with pronounced minima of less than four percent during MIS 11, MIS 5 and the Holocene, and relatively high values during the rest of the record (~ 7.5–10 %).

CaCO<sub>3</sub> and Ba<sub>xs</sub> BMAR records vary in parallel with percentages of CaCO<sub>3</sub> and Ba<sub>xs</sub>, respectively (Fig 2d, g), except for MIS 5e compared to MIS 5a–d, the latter caused by an increase in the sedimentation rates from *ca.* 0.5 to 2 cm/ka during MIS 5e (Figs 2d,g and 4). In contrast to the CaCO<sub>3</sub> and Ba<sub>xs</sub> BMAR records all other BMAR of individual components show no strong similarities with the corresponding percentages (Fig 2b, c, e, f). From MIS 11 to MIS 6/5 transition all other BMAR records generally co-vary, showing two small peaks during MIS 9 and MIS 7, and a larger peak during Termination II that continues through the beginning of MIS 5. However, from MIS 4 to the Holocene there are some differences between all records; the lithogenic, Fe and opal BMAR records increase gradually from MIS 4 to MIS 2, and decrease during the Holocene (Fig 2b, c, f), whereas TOC BMAR increases gradually from MIS 4 to the Holocene (Fig 2e).

<sup>230</sup>Th<sub>xs</sub>-normalized mass accumulation rates (MAR) of individual components show that lithogenics, Fe, Ba<sub>xs</sub>, TOC and opal co-vary and display certain glacial-interglacial variability, whereas CaCO<sub>3</sub> peaks when almost all other fluxes are low (Fig 3). Lithogenic and Fe MARs show a pattern of higher values during glacials than in preceding interglacial stages and reach maxima during the MIS 6/5 transition. In contrast, the lowest lithogenic and Fe MARs are recorded in the Holocene, MIS 5, and possibly during MIS 10-11 (Fig 3b, c). Opal MAR follows the same pattern with three strongest minima during MIS 11, MIS 5 and the Holocene. Opal MAR gradually increases until the end of MIS 6, reaching the highest values at the MIS 6/5 transition (Fig. 3g). Glacial-interglacial variability is not recorded between MIS 4 and MIS 2 in the opal record despite the relatively high values. TOC and Ba<sub>xs</sub> MAR records are in good agreement with opal MAR except for the glacial peaks in the interval MIS 4 to MIS 2, and MIS 11 (Fig. 3e, f). CaCO<sub>3</sub> MAR displays strong increases during MIS 11, MIS 5 and the Holocene only (Fig 3h).

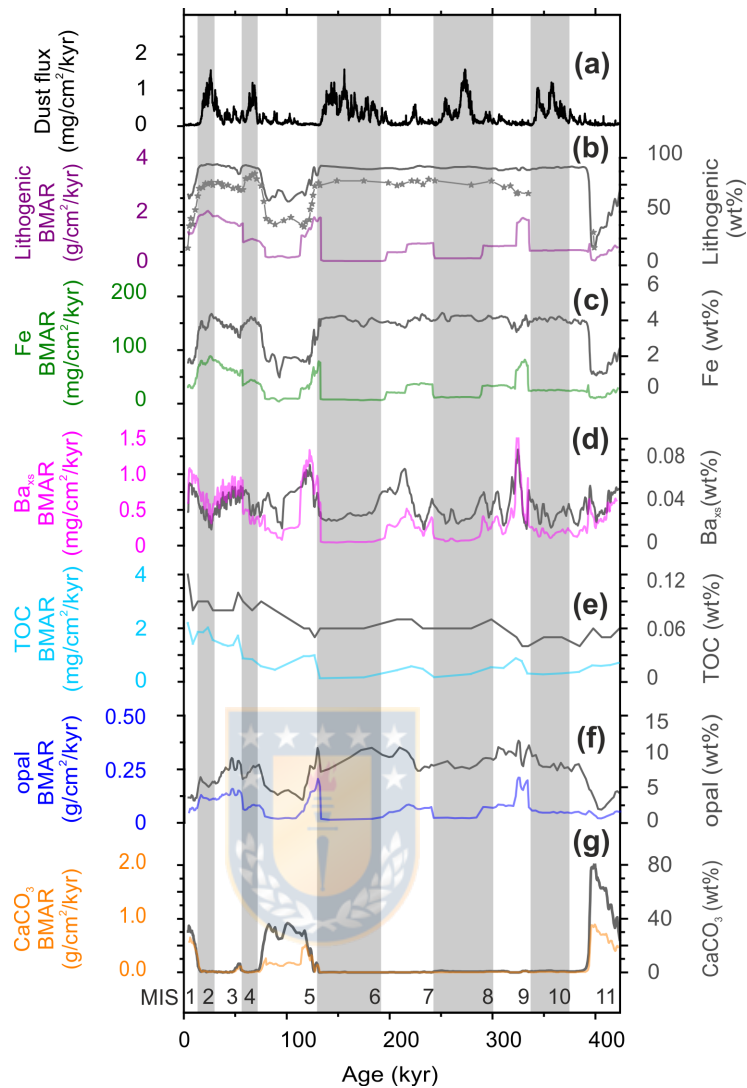


**Figure 2: Southeast Pacific (PS97/093-2) stratigraphy-based mass accumulation rates (BMAR) and percentages of individual components compared to dust flux in the EPICA Dome C (EDC) ice core (Lambert et al. 2008). (a) EDC dust flux; (b) Lithogenic content (wt. %; calculated from:  $100 - [\text{opal wt. \%} + \text{CaCO}_3 \text{ wt. \%} + 2 \times \text{TOC wt. \%}]$ , grey line) and lithogenic content based on  $^{232}\text{Th}$  (grey stars); lithogenic BMAR (purple line); (c) Fe content (grey line) and Fe BMAR (green line); (d)  $\text{Ba}_{\text{ss}}$  content (grey line) and  $\text{Ba}_{\text{ss}}$  BMAR (pink line); (e) TOC content (light grey line) and TOC BMAR (light blue line); (f) Opal content (wt. %; grey line) and opal BMAR (blue line); (g)  $\text{CaCO}_3$  content (grey line) and  $\text{CaCO}_3$  BMAR (orange line). Numbers in the lower part of the figure indicate Marine Isotope Stages (MIS). Vertical grey bars mark glacial stages according to Lisiecki and Raymo (2005).**



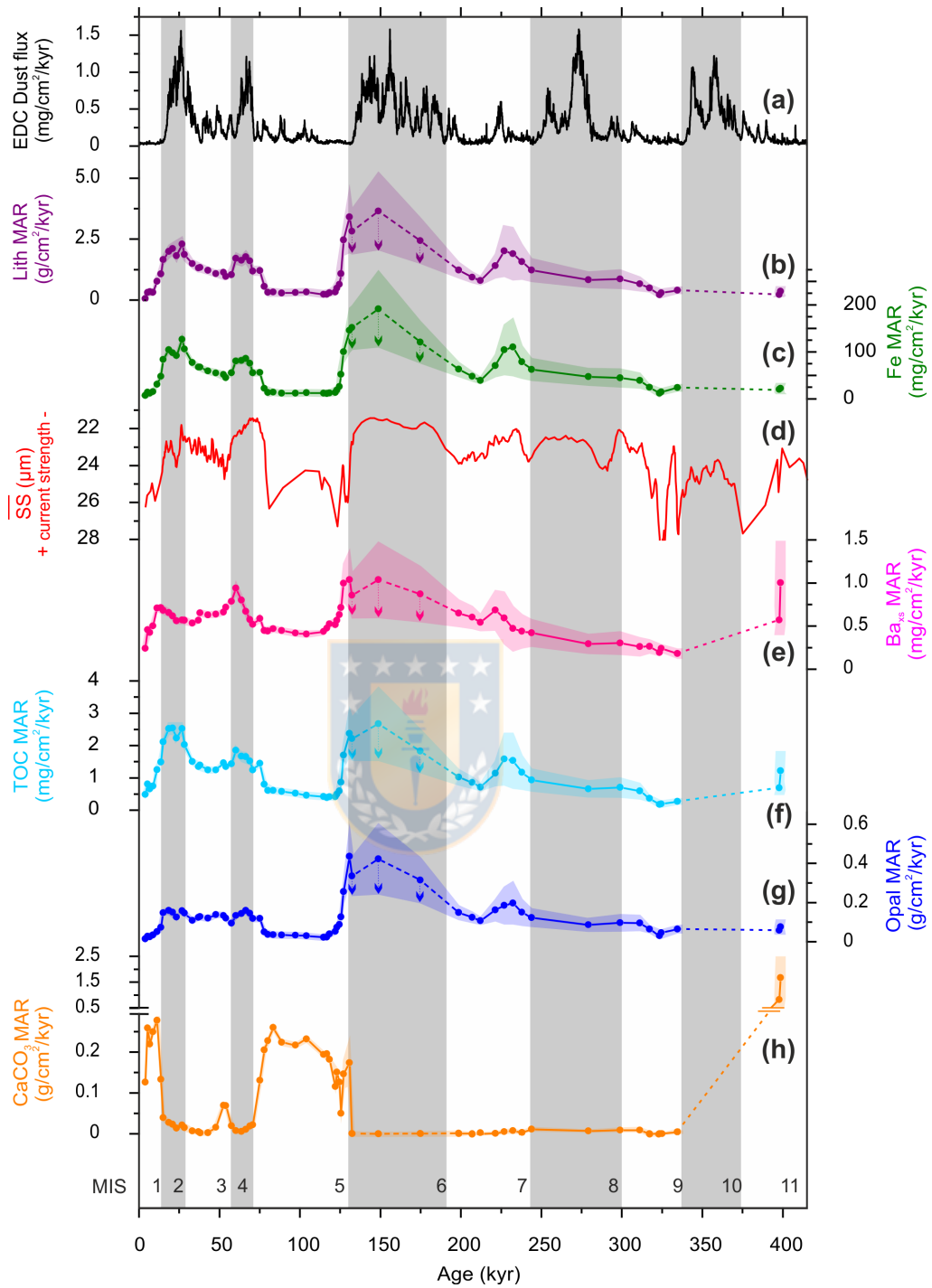
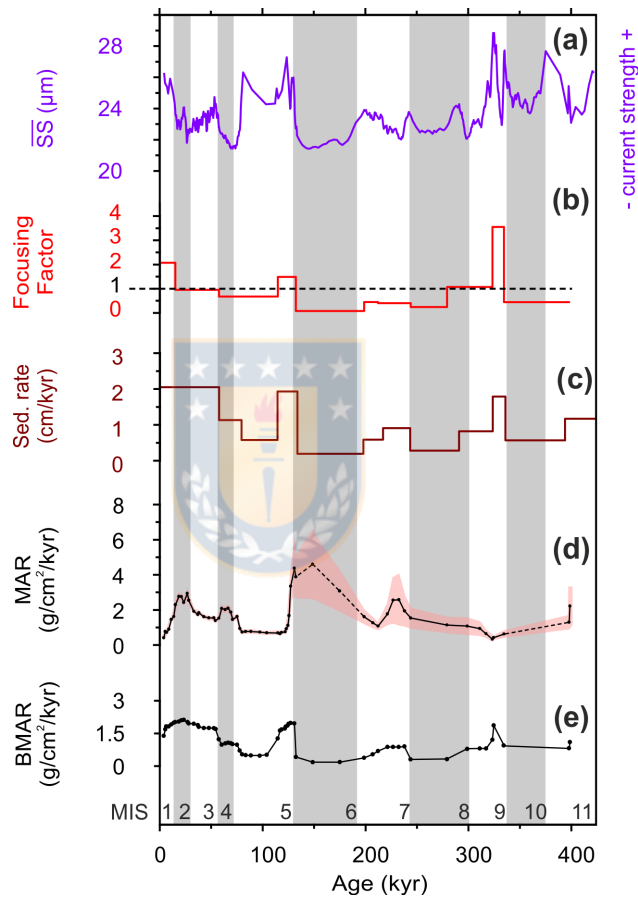


Figure 3: Southeast Pacific (PS97/093-2)  $^{230}\text{Th}_{\text{xs}}$ -normalized mass accumulation rates (MAR) compared to dust flux in the EDC ice core (Lambert et al. 2008) and bottom current strengths of core PS97/093-2 (Toyo et al., 2020). (a) EDC dust flux, (b)  $^{232}\text{Th}$  based lithogenic MAR; (c) Fe MAR; (d) changes in bottom current strength as indicated by the sortable silt record of core PS97/093-2 (note that Y-axis is reversed); (e)  $\text{Ba}_{\text{ss}}$  MAR; (f) TOC MAR; (g) biogenic opal MAR; and (h)  $\text{CaCO}_3$  MAR. Shaded areas indicate associated errors. Numbers in the lower part of the figure indicate Marine Isotope Stages (MIS). Grey bars denote glacial stages according to Lisiecki & Raymo (2005). Dashed lines during MIS 6 denote the interval of extreme winnowing where MAR might be overestimated, and for MIS 10 they indicate uncertainty due to the lack of data points.

Focusing factors range from significant winnowing ( $\Psi=0.08$ ) to considerable focusing ( $\Psi=3.55$ ) throughout the past 400 ka. At the coring site, winnowing dominates, and we only have brief periods of focusing during the peak interglacials MIS 9, MIS 5e and the Holocene. The intervals from MIS 11 to MIS 9 and from mid-MIS 8 to MIS 6 show net winnowing, whereas the interval between mid-MIS 9 to mid-MIS 8 was net neutral, and from MIS 5e to MIS 2 was nearly neutral with moderate winnowing (Fig 4b). Furthermore, the focusing factor record broadly agrees with the sedimentation rates, with winnowing in the intervals of low sedimentation rates and focusing during periods of relatively high sedimentation rates (Fig 4b, c).



**Figure 4: Comparison of sediment mass accumulation rates, focusing factors, bottom current strength and sedimentation rates of core PS97/093-2 for the last 400 ka. (a) Changes in bottom current strength based on the Sortable Silt grain size record (lilac line, Toyos et al., 2020) compared to (b) focusing factors (red line, black dashed line marks focusing factor=1); (c) sedimentation rates; (d)  $^{230}\text{Th}_{\text{xs}}$ - normalized mass accumulation rate (MAR, black line and dots) and associated errors ( $2\sigma$ ; pink shadow), which grow with the age of the sample, dashed lines indicate intervals with uncertainties due to extreme winnowing (Marine Isotope Stage 6) or lack of data (Marine Isotope Stage 10); (e) Stratigraphy-based bulk mass accumulation rates (BMAR) obtained by multiplying sedimentation rates by dry bulk densities. Numbers in the lower part of the figure indicate Marine Isotope Stages (MIS). Grey bars denote glacial stages according to Lisiecki & Raymo (2005).**

A comparison between the MAR and the BMAR (Figs 4d, e) shows discrepancies between both records. For most of the record, MAR is higher than BMAR, except for the focusing intervals (MIS 9, MIS 5e and the Holocene), where an opposite trend is observed. The largest divergence between both records

happens during MIS 6, which is characterized by significant winnowing (Fig 4). As a result, during MIS 9, MIS 6, MIS 5e and the Holocene, the BMAR and MAR of the individual components (lithogenic, Fe, Ba<sub>xs</sub>, TOC, opal, and CaCO<sub>3</sub>) diverge from each other to varying degrees (Table 1), showing only similar values from mid-MIS 5 to MIS 2 and in MIS 9/8 (Figs 2 and 3).

**Table 1: Comparison between the average MAR and BMARs for the intervals with high (0–15 kyr, 324–334 kyr) and low (212–243 kyr, 243–279 kyr ) focusing factors.**

average	Accumulation rate of Fe (mg/cm <sup>2</sup> /kyr)	Accumulation rate of Ba <sub>xs</sub> (mg/cm <sup>2</sup> /kyr)	Accumulation rate of TOC (mg/cm <sup>2</sup> /kyr)	Accumulation rate of opal(mg/cm <sup>2</sup> /kyr)	Accumulation rate of CaCO <sub>3</sub> (mg/cm <sup>2</sup> /kyr)	
0–15 kyr (Ψ=2.07)	30.06	0.53	1.07	53.04	185	MAR
	40.65	0.94	1.82	70.05	411	BMARs
	<b>1.35</b>	<b>1.77</b>	<b>1.70</b>	<b>1.32</b>	<b>2.21</b>	<b>overestimation factor</b>
324–334 kyr (Ψ=3.55)	55.44	0.46	0.59	125.46	11.50	MAR
	72.99	1.32	0.82	184.97	12.53	BMARs
	<b>1.31</b>	<b>2.84</b>	<b>1.38</b>	<b>1.47</b>	<b>1.08</b>	<b>overestimation factor</b>
212–243 kyr (Ψ=0.40)	77.49	0.52	1.17	153.67	4.52	MAR
	34.21	0.30	0.50	69.14	1.40	BMARs
	<b>2.26</b>	<b>1.71</b>	<b>2.35</b>	<b>2.22</b>	<b>3.21</b>	<b>underestimation factor</b>
243–279 kyr (Ψ=0.24)	47.11	0.29	0.66	86.05	6.62	MAR
	12.03	0.07	0.23	22.99	2.07	BMARs
	<b>3.91</b>	<b>3.75</b>	<b>2.83</b>	<b>3.74</b>	<b>3.00</b>	<b>underestimation factor</b>

## 5 Discussion

### 5.1 Influence of current dynamics on sediment redistribution and its effect on proxy record interpretations

The study area at the Pacific entrance of the DP is strongly influenced by the ACC, as documented by highly variable current strengths on millennial and glacial-interglacial timescales (Lamy et al., 2015; Toyos et al., 2020; Wu et al., 2021). Our results indicate that this variability in current strength influenced changes in sedimentation patterns (Fig. 4). Specifically, the focusing factors imply that sediment redistribution is highly variable in our core, encompassing significant winnowing during MIS 6 (Fig 4b). Under these extreme conditions winnowing may bias the <sup>230</sup>Th normalization reconstructions because of a preferential removal of the fine <sup>230</sup>Th-rich grains (Marcantonio et al., 2014). Costa and McManus (2017) documented a potential overestimation of MAR when winnowing is severe (focusing factors of 0.158–0.20). With moderate winnowing Ψ>0.24, this effect is negligible and <sup>230</sup>Th<sub>xs</sub>-normalized accumulation rates are robust. Therefore, the high MAR during MIS 6 in core PS97/093-2 may in part stem from the extreme winnowing (Ψ=0.08) at that time, whereas in all other intervals Ψ exceeds 0.24 and thus estimated MARs are reliable (Fig 4).

In our core, we observe winnowing during glacial periods in intervals with relatively low current strengths, and increased focusing factors contemporaneous with increased sortable silt values in the same core, reflecting strengthened bottom currents during MIS 9, MIS 5e and the Holocene (Toyos et al., 2020; Fig. 4a-c). The consistent pattern of winnowing (focusing) in intervals with relatively low (high) current strength might at first sight seem counterintuitive. We suggest that under strong bottom current conditions, the fine sediment fraction ( $<10\ \mu\text{m}$ ) potentially behaves similarly to the  $>63\ \mu\text{m}$  fraction because of cohesive effects and flocculation of the fine fraction during transport (McCave and Hall, 2006), whereas under slower current conditions a loss of such effects in the fine sediment fraction might trigger the winnowing of such sediment fraction (Marcantonio et al., 2014). We propose that winnowing at our site, in a generally fine-grained sediment setting, is due to current velocities that occasionally overrule the cohesive forces, resulting in the loss of a small amount of the fine fraction. Prior studies have pointed out that in the deep sea, current velocities between *ca.* 6.5 and 10.5 cm/s are enough to trigger surface sediment erosion of the aggregated particulate matter that compose the surface sediments (Peine et al., 2009; Turnewitsch et al., 2008). However, our results suggest that even lower flow speeds of  $\sim 5.5\text{--}6$  cm/s during glacials (Fig 4, Toyos et al., 2020, calibrated following Wu et al., 2019) reached the threshold of intermittent erosion and resuspension of the fine sediment fraction. During interglacial periods MIS 9, MIS 5 and the Holocene, strong currents plausibly caused a gradual mobilization of more and more coarse-grained material that was laterally accumulated in certain areas, resulting in a coarser-grained focusing at our site. A similar pattern, characterized by strengthened bottom currents inferred from grain size analysis, and increased sediment focusing has also been observed for interglacials on the Weddell Sea continental margin (Frank et al., 1996).

The dynamic bottom water circulation appears to have led to frequent syndepositional redistribution. For core PS97/093-2, when comparing MAR and BMAR of Fe,  $\text{Ba}_{\text{xs}}$ , TOC, opal and  $\text{CaCO}_3$  in the intervals with high and low focusing factors (excluding MIS 6, where we cannot discard an overestimation of the  $^{230}\text{Th}_{\text{xs}}^0$ -constrained fluxes because of extreme winnowing), large discrepancies are seen (Table 1, Figs 2 and 3). BMAR of the individual components are up to three times higher than MAR in intervals with highest focusing, and about four times smaller in intervals with pronounced winnowing (Table 1). These differences confirm that the PS97/093-2 BMAR are strongly biased by sediment redistribution due to current dynamics. Given that the PS97/93 site is affected by substantial lateral redistribution of sediment particles, we therefore base our paleoproductivity reconstruction on the MAR, which allows for the quantification of lateral sediment redistribution and accurate vertical rain rates (e.g., Costa et al., 2020; Suman and Bacon, 1989).

## 5.2 Southeast Pacific lithogenic material, sources and iron fertilization potential

A comparison of lithogenic fluxes in core PS97/093-02 with eolian dust records from open ocean sites in the SAZ (Anderson et al., 2014, Lamy et al., 2014; Martínez-García et al., 2009; Thöle et al., 2019) and in Antarctic ice cores (Lambert et al., 2008), shows generally similar patterns (Fig. 5). However, for MIS 10 and MIS 8, some characteristic features are not observed in our sediment core due to a lower

temporal resolution that prevents an accurate evaluation during such intervals (Fig 5). Our glacial lithogenic MAR peaks were one order of magnitude higher than those observed in the open Pacific, Atlantic and Indian SAZ (Fig 5). Furthermore, studies of modern surface sediments do not indicate a substantial contribution of dust to the DP region and the Southeast Pacific north of the SAF (Wengler et al., 2019; Wu et al., 2019). Thus, accounting for these very high lithogenic fluxes in the proximity of the DP requires an additional non-eolian source of terrigenous material.

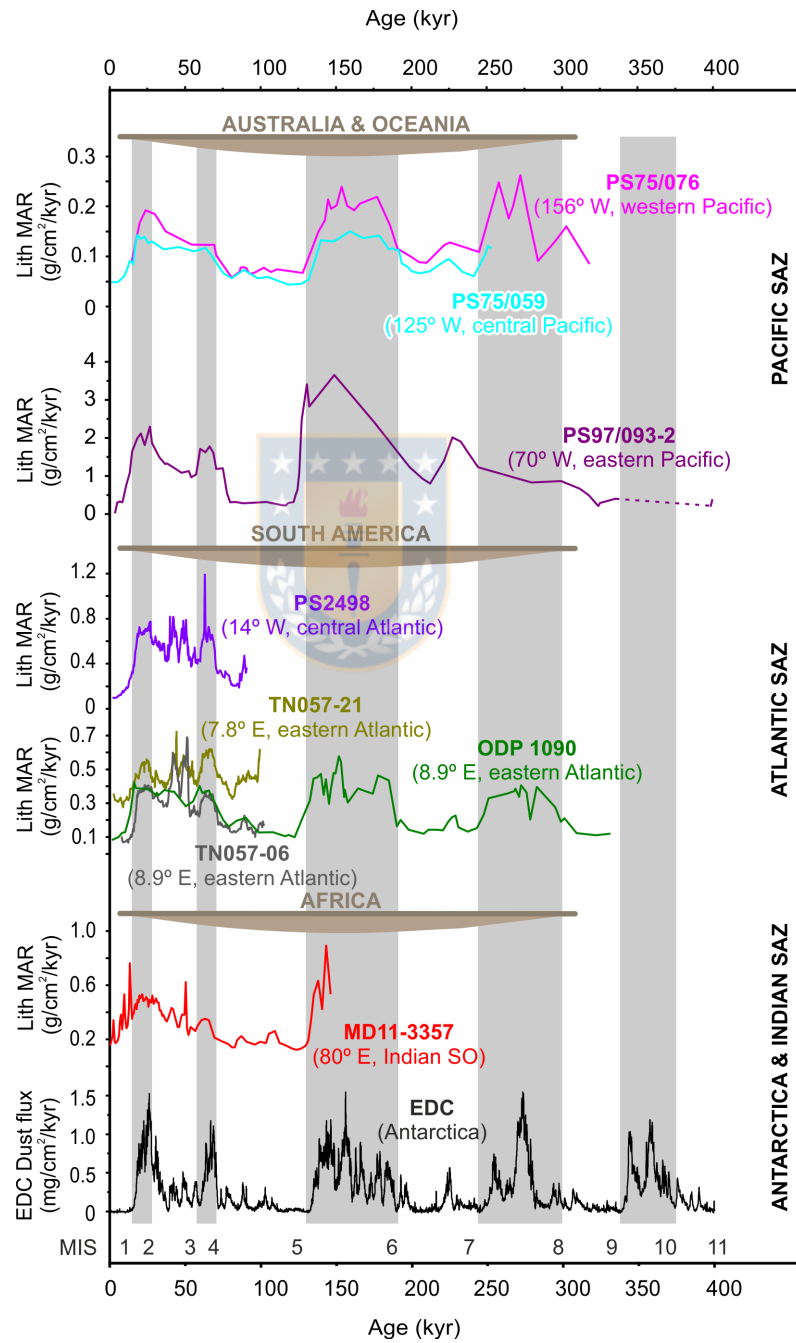


**Figure 5:** Changes in  $^{230}\text{Th}$ -normalized lithogenic MARs in the subantarctic Southern Ocean (see Fig 1 for location of sites discussed). From top to bottom: Cores PS75/076 and PS75/059 (Lamy et al., 2014); Core PS97/093-2 (this study); Core PS2498 (Anderson et al., 2014); Cores TN057-21 and TN056-06 (Anderson et

al., 2014), and ODP1090 (Martínez-García et al., 2009); Core MD11-3357 (Thöle et al., 2019), and dust MAR in the EPICA Dome C ice core (Lambert et al., 2008). Marine Isotope Stage (MIS); grey bars denote glacial stages. Continental masses are located in their relative longitudinal position to the marine sediment cores and represent the primary source of terrigenous inputs to the Subantarctic Zone.

South America is considered a substantial source of runoff-derived and glaciogenic sediments, particularly during glacials when large parts of the southern Andes were covered by the PIS (Fig 1b). Therefore, we suggest that the PS97/093-2's high lithogenic MARs are related to the relative proximity of our site to southern South America. From MIS 6 onwards, PS97/093-2 lithogenic MARs reveal significant increases during glacials. Specifically, the most intense growth occurred during MIS 6, due to a combination of the penultimate local glaciation (Rabassa, 2008) and a possible winnowing bias, followed by a smaller rise during MIS 4, and a gradual increase to higher values in the LGM. This pattern closely corresponds to reported Patagonian ice expansions (e.g., Gowan et al., 2021; Lowell et al., 1995; Rabassa, 2008; Rabassa and Clapperton, 1990; Fig S2). Furthermore, an IRD record from Core MD07-3128, retrieved from the Pacific entrance to the Strait of Magellan (*ca.* 620 km NNW of core PS97/093-2, Fig 1b), shows a consistent pattern of higher IRD contents during cold intervals over the past ~60 kyr, which have been interpreted as advances of the PIS (Caniupán et al., 2011). Moreover, enhanced Fe concentrations linked to PIS advances during colder periods were reported at ODP Site 1233 from the Chilean continental margin (Fig 1b, Kaiser and Lamy, 2010; Lamy et al., 2004), and Antarctic dust maxima and have been mechanistically linked to the presence of active outwash plains in Patagonia (Sugden et al. (2009)). This mechanism explains enhanced dust mobilisation and uptake from these outwash for transport to Antarctica.

It has been suggested that Fe bio-availability depends on the mineralogy of the detrital fraction (Schroth et al., 2009). Therefore, it is unclear which amount of the Fe that reached our site was bioavailable, and how this availability changed through time. Previous studies suggest that physical weathering increases the labile primary Fe (II) content of sediments that is associated with phytoplankton fertilization (Shoenfelt et al., 2017, 2018), indicating that a stronger contribution of glaciogenic sediments might increase the proportion of bioavailable Fe in a given sediment flux (Shoenfelt et al., 2019). As the study site is proximal to the continental sources (tip of South America), which are dominated by physical weathering during both glacial and interglacial intervals, we hypothesize that temporal changes in the proportion of bioavailable Fe in the Southeast Pacific are less pronounced than in more open ocean locations. We thus expect that the Fe supply delivered to our site might have always been relatively enriched in bio-available Fe compared to other oceanographic sectors. In summary, because dust does not seem to be the main source of lithogenic material at site PS97/093, we propose that advances of the PIS and iceberg discharge during glacial intervals (e.g., Kaiser et al., 2007; Rabassa, 2008) could have increased lithogenic fluxes and potentially bio-available Fe reaching the subantarctic Pacific entrance to the DP and thus promoting biological productivity.

In the present-day Atlantic SAZ, chlorophyll-*a* blooms are supported by an advective supply of Fe from the South American coastline along the western boundary current first and the Subtropical Front later, rather than by continental dust sources (Graham et al., 2015). Other studies also invoke this mechanism

for the LGM, where increased supply of glaciogenic debris by expanded Patagonian and Antarctic Peninsula ice sheets travel long distances via the ACC at depth (Noble et al., 2012). However, in the subantarctic region of our core location, the glacial northward shift of the SAF likely decreased the DP throughflow of the ACC, weakening the cold water route into the Atlantic (Lamy et al., 2015; Toyos et al., 2020), which would have hindered the transport of Fe released from the PIS to the Southeast Pacific into the Atlantic. It has been suggested that the reduced supply to the Atlantic basin through the DP during glacials might have been compensated by a stronger recirculation within the South Pacific, causing a stronger South Pacific Gyre recirculation (Lamy et al., 2015). Therefore, the bioavailable Fe might have been transported in the South Pacific gyre, enhancing productivity in this region, which is currently limited by Fe availability (Bonnet et al., 2008). To evaluate the reach of Fe fertilization in the Southeast Pacific linked to PIS dynamics, further reconstructions along the Pacific SAZ and Cape Horn-Humboldt current systems and iron speciation data are needed. Currently, the knowledge is restricted to one recently published record (core GeoB3327-5, located at 43°S, *ca.* 400 km off the Chilean coast) that reportedly featured increases in primary production during MIS 2–4, linked to increased supply of micronutrients via continental runoff, primarily controlled by PIS variability or precipitation (Tapia et al., 2021).



### **5.3 Orbital-scale variations and drivers of export production in the Southeast Pacific SO**

#### **5.3.1 Export production**

Our <sup>230</sup>Th-normalized results show that the proxies for integrated export production ( $Ba_{xs}$  MAR and TOC MAR) generally co-vary and correlate with biogenic opal MAR; all being higher during MIS 6 and MIS 4–2, and lower during the Holocene, and MIS 5 (Table S1, Fig 3).

Usually, variable dissolution in the water column does not significantly affect opal burial in the SO (Chase et al., 2015), suggesting that opal MAR might be only marginally affected by preservation changes, thus providing valid information on past diatom productivity changes (e.g., Bradtmiller et al., 2009; Sprenk et al., 2013). Since the preservation of organic carbon in sediments is globally scarce (only about 1% of the TOC produced in the water column gets preserved in the sediments, Berger et al., 1989), the good correspondence and positive correlation between opal and TOC MARs ( $r^2=0.56$ , Table S1, Fig 3) might imply that the TOC, suggesting that most of the glacial export production was fueled by diatoms. An exception to the strong correlation between the export production proxies occurred from MIS 4 to MIS 2, when TOC and  $Ba_{xs}$  MARs show relatively high values with glacial/interglacial variability, whereas the opal record is rather flat within this interval. Several studies proposed that diatom growth rate was more effective during the LGM compared to today (resulting in higher opal burial during the LGM), as diatoms can reduce their Si/C uptake ratio under Fe-replete conditions (Anderson et al., 2002; Chase et al., 2015). Thus, a glacial increase of Fe input may have created conditions under which relatively more TOC and biogenic barium were exported per unit of opal buried (Fig. 3).

Unlike our other MAR records, high CaCO<sub>3</sub> MAR values are observed only during the Holocene, MIS 5 and MIS 11 (Fig. 3). To explain the different pattern, we have to consider changes in carbonate chemistry and variations in the depth of the lysocline affecting our site's carbonate contents through time. At present, the lysocline is located at *ca.* 4000 m (Sulpis et al., 2018), which is only slightly below the depth of our core (3781 m water depth). Site PS97/093 is bathed in Circumpolar Deep Water, which is characterized by relatively low [CO<sub>3</sub><sup>2-</sup>], being undersaturated with respect to CaCO<sub>3</sub>, and therefore promotes carbonate dissolution (Key et al., 2004). In the SO, the lysocline depth shoaled at least 0.5 km during the glacial stages of the past 500 kyr, triggering enhanced carbonate dissolution and concomitant reduced carbonate MAR (Howard and Prell, 1994). Moreover, poor carbonate preservation has also been observed in another Southeast Pacific core with an alkenone-based SST record (PS75/034-2, 54° 22'S, 80° 05'W, 4425 m water depth; Ho et al., 2012, Fig 1b). Nevertheless, since carbonate preservation is favored in intervals with high sedimentation rates (Gottschalk et al., 2018), in our core the relatively high sedimentation rates during MIS1–3 or MIS 5e (Fig 4c) might allow the burial of carbonates in the sediment before being dissolved during such intervals. On the other hand, we suggest that the absence of carbonates between MIS 10 to MIS 6, and in MIS 4 indicates carbonate dissolution, rather than changes in export production of coccolithophores and foraminifera (Fig. 3). As a result, CaCO<sub>3</sub> MAR in our record are only present in the globally strong interglacials MIS 11, MIS 5 and the Holocene (PAGES, 2016), while during weaker interglacials, such as MIS 7 and MIS 9, carbonate productivity did not offset carbonate dissolution.

### 5.3.2 Drivers of local export production patterns

In the DP, the oceanographic fronts may act as barriers to mixing in the ocean, preventing cross-frontal movement and meridional exchange of water masses and their associated nutrients (Naveira Garabato et al., 2011; Paparazzo, 2016). On longer timescales, studies of sediment cores located upstream and downstream of the northern and central DP suggest a northward shift of the SO frontal system during glacial times, lower ACC flow speed and reduced transport through the DP (Lamy et al., 2015; Roberts et al., 2017; Toyos et al., 2020; Wu et al., 2021). Particularly at site PS97/093, a comparison between the  $\overline{SS}$  record and the opal and TOC MAR records shows that decreases in current strengths correspond with increases in opal and TOC (Fig 3). The inverse correspondence between current strength and opal export supports the idea that the glacial decrease in current vigor, linked to the northward shift of the frontal systems, would locate our coring site south of the strongest ACC flow in the vicinity of the SAF (Toyos et al., 2020) and closer to the Si-rich southern waters. Furthermore, it is likely that the waters between the PF and SAF received an additional supply of dissolved Si(OH)<sub>4</sub> during glacial intervals, as inferred from the displacement of the opal belt north of the present day PF position (e.g., Diekmann, 2007). This pattern is explained by upwelling of dissolved Si(OH)<sub>4</sub> south of the PF as it does today, but due to expanded ice cover during glacials, very little silica was used by diatoms south of the PF, and the upwelled Si(OH)<sub>4</sub> was transported northwards from the PF (Chase et al., 2003; Freeman et al., 2018). At the same time, we discard a substantial arrival at our core site of either hydrothermally sourced Fe



from the East Pacific Rise (Fitzsimmons et al., 2014) or potentially upwelled Fe south of the PF. In case of upwelling of Fe south of the PF, its strong particle reactivity might have caused efficient scavenging of Fe beneath the ice (Chase et al., 2003). In our core, the coeval increase in MAR of lithogenics, Fe, biogenic opal, TOC and  $Ba_{xs}$  suggests that sufficient Fe was transported to our site to consume all the supplied  $Si(OH)_4$  during glacial intervals. Furthermore, under Fe-replete conditions, diatoms take up substantially less silicic acid relative to nitrate (Matsumoto et al., 2014). Modern observations and incubation experiments show that the Si:N uptake ratio lowers from  $\sim 4:1$  to  $\sim 1:1$  (Brzezinski et al., 2002; Franck et al., 2000). Therefore, since our core received enough glacial Fe to relieve the limitation, the enhanced diatom production, indicated by higher biogenic opal MAR, may be the result of a reduced diatom Si:N uptake ratio, combined with an increase of the amount of  $Si(OH)_4$  that reached the core site.

In contrast with this glacial scenario, increases in bottom current strength, usually during interglacials, indicate that the SAF was located south of our site, resulting in a production regime similar to present-day conditions. This area is characterized by low average chlorophyll-*a* concentrations (Fig 1b), where the lack of dissolved silica may limit the growth of diatoms (Demidov et al., 2011; Freeman et al., 2019), Fig 6a and 6b) and might cause coccolithophores and other phytoplankters to become the dominant group (Rigual Hernández et al., 2020; Saavedra-Pellitero et al., 2019). However, the absence of peaks in the TOC and  $Ba_{xs}$  MAR during the Holocene and MIS 5 suggests that the increased  $CaCO_3$  export production did not significantly influence the integrated proxies of export production, implying no noticeable impact by calcareous organisms on the total export during such intervals (Fig 3).

Unlike other interglacials, during MIS 11, a prominent nannofossil ooze, primarily composed of *Geophyrocapsa* coccolithophore and foraminifera has been reported in the area (Lamy, 2016; Toyos et al., 2020) that is mirrored at our site by  $CaCO_3$  MARs one order of magnitude higher than in the Holocene and in MIS 5, and by increases in the  $Ba_{xs}$  and TOC MARs (Fig 3). A similar rise in  $CaCO_3$  accumulation has also been recognized at other SAZ locations in the Atlantic (Hodell et al., 2000) and the Pacific (Gersonde, 2011; Saavedra-Pellitero et al., 2017) sectors of the SO, suggesting that the increase in  $CaCO_3$  MAR during MIS 11 in core PS97/093-2 is part of a general pattern comprising at least the Pacific and Atlantic SAZ, likely caused by an exceptional southward migration of the ACC frontal systems in the Pacific sector of the SO (Saavedra-Pellitero et al., 2017).

### 5.3.3 Comparison of PS97/093-2 export fluxes/MARs to other Southern Ocean SAZ sites

In order to assess the zonal dynamics of productivity and lithogenic flux variations along the Southern Ocean's SAZ, we compare our MAR reconstructions with previously published records from open ocean areas of the SAZ (Anderson et al., 2014; Frank et al., 1999; Lamy et al., 2014; Martínez-García et al., 2014; Nürnberg et al., 1997; Thöle et al., 2019). We use a circum-Antarctic subantarctic transect of MAR of lithogenics, Fe,  $Ba_{xs}$ , TOC, opal and  $CaCO_3$  for the Holocene (0–10 ka), the LGM (19–27 ka; Clark et al., 2009), the last interglacial MIS 5e (119–124 ka), and the end of MIS 6 during full glacial conditions, just before the beginning of the warming in the SO at 132–131 ka (Bianchi and Gersonde,

2002; Fig 6). Overall, our productivity indicators agree with subantarctic records from other locations, displaying higher  $\text{CaCO}_3$  during interglacials and higher opal, TOC and  $\text{Ba}_{\text{xs}}$  during glacials, the latter pattern most likely enabled by an increase of lithogenic Fe fluxes (Martin, 1990; Fig 6). But, as it has previously been reported, it is likely that other factors than Fe played a role in regulating the biological production in the SO (Anderson et al., 2014; Kohfeld et al., 2005).

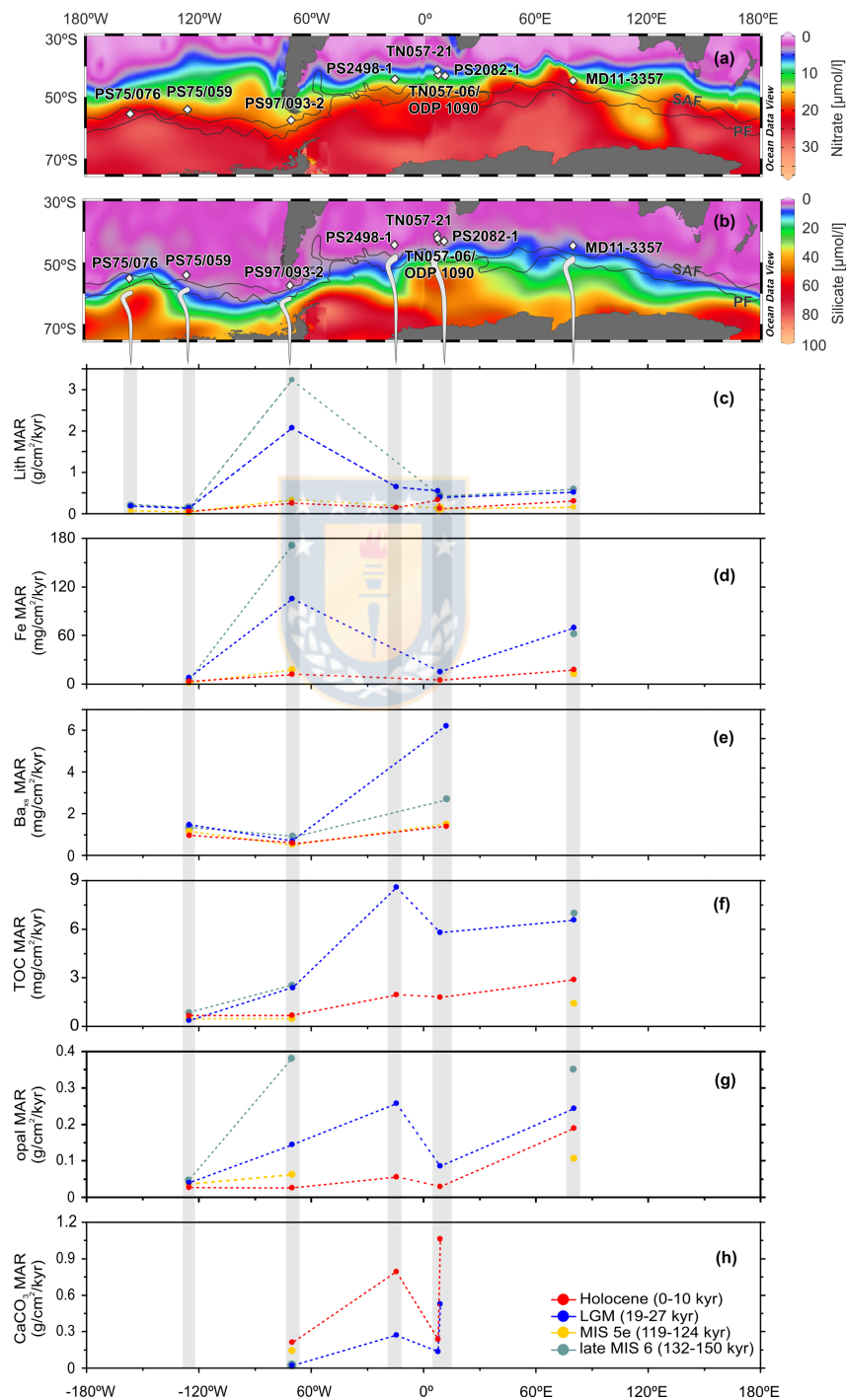


**Figure 6: Comparison of MAR across the Subantarctic Southern Ocean, during the Holocene (0–10 ka, red), the Last Glacial Maximum (19–27 ka, blue), Marine Isotope Stage 5e (119–124 ka, yellow), and late Marine**

**Isotope Stage 6 (132–150 ka, green):** Maps of surface water nitrate (a) and silicate (b) concentrations (data from WOCE, Global Hydrographic Climatology, Gouretski and Koltermann, 2004); black lines indicate the modern location of the Subantarctic Front (SAF), and Polar Front (PF, Orsi et al., 1995); white diamonds refer to core locations (PS75/076 and PS75/059, Lamy et al. 2014; PS97/093-2, this study; PS2498-1, TN057-21 and TN057-06, Anderson et al., 2014; ODP1090, Martínez-García et al. 2014; PS2082-1, Nürnberg, 1997 and Frank, 2002; MD11-3357, Thöle et al., 2019); (c) lithogenic flux; (d) Fe flux; (e)  $Ba_{xs}$  flux; (f) total organic carbon flux; (g) opal flux; (h)  $CaCO_3$  flux. Grey bars indicate the projected core positions.

At our core location, we observe that the LGM lithogenic (Fe) MARs were about eightfold (ninefold) larger than during the Holocene. Furthermore, our site records the highest glacial lithogenic and Fe fluxes of the subantarctic SO; the LGM Indian–Atlantic and Pacific lithogenic fluxes are four to eleven times lower than at the PS97/093 site (Fig 6). However, the corresponding glacial increases in our productivity MARs are not as high as expected when considering the relative increase in the lithogenic MAR. In the Atlantic and Indian sectors, the LGM rise in export production was larger than the increase in lithogenic fluxes, whereas the opposite pattern is observed in our core (Fig 6). Furthermore, the glacial and interglacial export production fluxes are higher in the Atlantic and Indian sectors than at the DP entrance and in the central Pacific (Fig 6). Whereas in the central Pacific, the relatively low export production is explained by weaker Fe fertilization caused by lower local glacial dust fluxes (Lamy et al., 2014), the results at our site indicate that export production did not respond exclusively to glacial Fe fertilization (Fig 6). Since it takes very little bioavailable iron to get out of the Fe-limited conditions (*ca.* 3nM, Boyd et al., 2000), and our core site is proximal to Fe sources, which might facilitate a faster transition from a Fe-deplete to Fe-replete conditions, we suggest that under bioavailable Fe-replete conditions, another mechanism than Fe fertilization might ultimately regulate export production at our site.

The region is currently nitrate and phosphate-rich (Fig 6a; phosphate shown in Fig S3), and previous works north of the PF have shown that productivity increased during the LGM, whereas nitrate utilization decreased only slightly, implying a glacial intensification in the supply of nitrate to surface waters (François et al., 1997; Martínez-García et al., 2014). Since nitrate is not the macronutrient that was limiting export production during glacials, we propose  $Si(OH)_4$  as a suitable candidate.

Under high Fe conditions, a glacial northward migration of the SO frontal system, together with the transport of silicic acid northwards of the PF (Chase et al., 2003), and a reduced Si:N uptake ratio by diatoms (Brzezinski et al., 2002) should have contributed to the relief of silicate limitation in the SAZ, resulting in an increase in export production (predominantly diatom production). Given that LGM (and the possibly overestimated MIS 6) opal fluxes at our site were over fivefold larger than during the Holocene (Fig 6g), to sustain such a diatom productivity implicated by the opal flux would require a supply of  $Si(OH)_4$  much greater than exists today (Anderson et al., 2014). Thus, we propose that if all the  $Si(OH)_4$  brought to our site was consumed entirely, silica (diatom) production would have been inhibited by  $Si(OH)_4$  limitation, as it is happening today in some areas of the Polar Front Zone, where nearly depleted levels of silicic acid have been reported (Mengelt et al., 2001, Fig 6b). This hypothesis might be supported by modern experiments that show that  $Si(OH)_4$  limitation significantly restrict the response of diatom production to Fe in the SAZ (Brzezinski et al., 2005). Consequently, the growth of

other phytoplankton groups (e.g., small flagellates) or small, weakly-silicified diatom species would have been favored, which are strongly affected by remineralization, thus lowering export production (Buesseler, 1998). Alternatively, since increases in productivity at the SO fronts are explained by horizontal advection rather than upwelling (Graham et al., 2015), it might be possible that during past glacials only a portion of the  $\text{Si(OH)}_4$  supplied via upwelling at the PF travelled northwards across the PFZ reaching the core location. The other portion of the upwelled silica might have been advected laterally into the Atlantic via the ACC (Graham et al., 2015), causing a more intensive phytoplankton growth there instead of in the DP. Although the latter scenario is somewhat speculative, both assumptions (a moderate glacial  $\text{Si(OH)}_4$  limitation and dominance of horizontal advection rather than upwelling) are not mutually exclusive; hence the two scenarios would explain the weaker productivity response to Fe at the PS97/093 site compared to other subantarctic records.

## 6 Conclusions

We present a multi-proxy approach for reconstructing paleo-export production in the SAZ at the Pacific entrance to the DP covering the past 400 ka. As our core is located in an area with relatively high bottom current speeds, we show that our site is strongly affected by the lateral redistribution of sediments, with high focusing (winnowing) factors associated with high (low) bottom current speeds. This counterintuitive pattern is most likely due to a dominance of the coarse (fine)-grained fraction together with a preservation (loss) of the flocculation and cohesive effects of the fine sediment fraction under relatively high (slow) bottom currents. As a result, focusing (winnowing) leads to an overestimation (underestimation) of the BMAR by a factor of ca. 3 (4) during such intervals in our core. The frequent syndepositional redistribution emphasizes the importance of the utilization of the  $^{230}\text{Th}_{\text{xs}}$ -normalization method to reconstruct fluxes in the subantarctic SO.

Whereas our lithogenic record follows the temporal pattern of other lithogenic records at open ocean sites in the SAZ and in the Antarctic ice core (EDC dust flux), we present evidence that dust was not the main source of lithogenic material. Instead, advances of the PIS during glacial intervals increased the portion of glaciogenic sediments and therefore released lithogenics.

Our results show orbital-scale variations from a predominantly high opal-rich export production for most glacials to lower levels of export productivity during interglacials dominated by carbonates. We suggest that such fluctuations are responding to glacial-interglacial frontal shifts coupled with nutrient limitation. We hypothesize that during interglacials the SAF was located slightly south of our core location, so that a reduction in Fe and dissolved silica supply may have limited the growth of siliceous phytoplankton (diatoms), leading to calcareous plankton (i.e. coccolithophores) becoming the dominant group. Yet, the reduced total export production during such intervals suggests that export production by calcareous organisms was too small to have a noticeable impact on the total export, except for MIS 11,

where the impact was perceptible, as demonstrated by the occurrence of a prominent calcareous ooze. Conversely, the glacial northward migration of the SO frontal system would have positioned the core south of the SAF and closer to Si-rich waters in an environment characterized by extremely high lithogenic and Fe fluxes from a more extensive PIS as mentioned above. The coeval increase in lithogenic, Fe, opal, TOC, and  $Ba_{xs}$  suggests that our core received sufficient Fe and  $Si(OH)_4$  to fuel higher export production during glacial intervals.

A spatial comparison with previously published records from different locations in the SAZ shows that our core displays the highest glacial lithogenic and Fe MARs. However, the corresponding glacial increases in productivity fluxes are not as high as we expected given the relative increase in lithogenics, suggesting that export production did not respond to glacial Fe fertilization as efficiently as in other sectors of the SAZ. We hypothesize that under these Fe-repleted glacial conditions, a depletion in the silicic acid that was transported northwards of the PF, could explain the glacial export production pattern at our core location.

#### **Data availability**

All data are available in PANGAEA repository: <https://doi.pangaea.de/10.1594/PANGAEA.934588>



#### **Author contribution**

This study is part of MHT's thesis under the supervision of CBL and FL. MHT carried out most of the measurements. MHT, GW and HWA made the mass accumulation rate calculations. MHT, CBL, FL, HWA, LLJ and GW analysed and interpreted the data. MHT wrote the first draft and produced the figures for the manuscript with substantial contributions of GW, HWA, LLJ, CBL and FL. All authors interpreted, edited, and reviewed the manuscript.

#### **Competing interests**

The authors declare that they have no conflict of interest.

#### **Acknowledgements**

This work was funded by the Alfred-Wegener-Institut Helmholtz-Zentrum für Polar- und Meeresforschung through its research programs “PACES-II” and “Changing Earth – Sustaining our Future”. Additional financial support was provided by the Chilean oceanographic centers FONDAP-IDEAL (project number 1500003) and COPAS Sur-Austral (AFB170006) to CBL and MHT, and Lamont-Doherty Earth Observatory. MHT acknowledges support from scholarship CONICYT-PCHA/Doctorado Nacional/2016-21160454, Postgraduate Office of Universidad de Concepción, Red

Clima Red (project number LPR163), and Doctorado MaReA. We acknowledge the comments and suggestions by Dr. Giuseppe Cortese and Dr. Louisa Bradtmiller, which helped us to improve the revised version of this manuscript. We thank the captain, crew and scientific party of R/V Polarstern for a successful PS97 cruise. We acknowledge A. Ávila for technical support at the Paleoceanography lab of Universidad de Concepción, R. Schwarz, M. Fleisher and J. Abell for assistance at Lamont-Doherty Earth Observatory, and S. Wiebe, R. Fröhling and V. Schumacher for technical support at AWI.

## References

Anderson, R. F., Chase, Z., Fleisher, M. Q. and Sachs, J.: The Southern Ocean's biological pump during the Last Glacial Maximum, *Deep. Res. Part II Top. Stud. Oceanogr.*, 49(9–10), 1909–1938, doi:10.1016/S0967-0645(02)00018-8, 2002.

Anderson, R. F., Barker, S., Fleisher, M., Gersonde, R., Goldstein, S. L., Kuhn, G., Mortyn, P. G., Pahnke, K. and Sachs, J. P.: Biological response to millennial variability of dust and nutrient supply in the Subantarctic South Atlantic Ocean, *Philos. Trans. R. Soc. A Math. Phys. Eng. Sci.*, 372(2019), doi:10.1098/rsta.2013.0054, 2014.

de Baar, H. J. W. and De Jong, J. T. M.: Distributions, sources and sinks of iron in seawater, in *The Biogeochemistry of Iron in Seawater*, edited by D. R. Turner and K. A. Hunter, pp. 123–253, John Wiley & Sons Limited., 2001.

de Baar, H. J. W., Bathmann, U., Smetacek, V., Löscher, B. M. and Veth, C.: Importance of iron for plankton blooms and carbon dioxide drawdown in the Southern Ocean, *Nature*, 373(6513), 412–415, doi:10.1038/373412a0, 1995.

Bacon, M. P.: Glacial to interglacial changes in carbonate and clay sedimentation in the Atlantic Ocean estimated from  $^{230}\text{Th}$  measurements., *Isot. Geosci.*, 2(2), 97–111, 1984.

Berger, W. H., Smetacek, V. and Wefer, G.: Ocean Productivity and Paleoproductivity - An Overview, in *Productivity of the Ocean: Present and Past*, edited by W. Berger, V. Smetacek, and G. Wefer, pp. 1–34, John Wiley & Sons Limited., 1989.

Bianchi, C. and Gersonde, R.: The Southern Ocean surface between Marine Isotope Stages 6 and 5d: Shape and timing of climate changes, *Palaeogeogr. Palaeoclimatol. Palaeoecol.*, 187(1–2), 151–177, doi:10.1016/S0031-0182(02)00516-3, 2002.

Bonnet, S., Guieu, C., Bruyant, F., Prášil, O., Van Wambeke, F., Raimbault, P., Moutin, T., Grob, C., Gorbunov, M. Y., Zehr, J. P., Masquelier, S. M., Garczarek, L. and Claustre, H.: Nutrient limitation of

primary productivity in the Southeast Pacific (BIO SOPE cruise), *Biogeosciences*, 5(1), 215–225, doi:10.5194/bg-5-215-2008, 2008.

Boyd, P., LaRoche, J., Gall, M., Frew, R. and McKay, R. M. L.: Role of iron, light, and silicate in controlling algal biomass in subantarctic waters SE of New Zealand, *J. Geophys. Res. Ocean.*, 104(C6), 13395–13408, doi:10.1029/1999JC900009, 1999.

Boyd, P. W., Watson, a J., Law, C. S., Abraham, E. R., Trull, T., Murdoch, R., Bakker, D. C., Bowie, a R., Buesseler, K. O., Chang, H., Charette, M., Croot, P., Downing, K., Frew, R., Gall, M., Hadfield, M., Hall, J., Harvey, M., Jameson, G., LaRoche, J., Liddicoat, M., Ling, R., Maldonado, M. T., McKay, R. M., Nodder, S., Pickmere, S., Pridmore, R., Rintoul, S., Safi, K., Sutton, P., Strzepek, R., Tanneberger, K., Turner, S., Waite, A. and Zeldis, J.: A mesoscale phytoplankton bloom in the polar Southern Ocean stimulated by iron fertilization, *Nature*, 407(6805), 695–702, doi:10.1038/35037500, 2000.

Boyd, P. W., Arrigo, K. R., Strzepek, R. and Van Dijken, G. L.: Mapping phytoplankton iron utilization: Insights into Southern Ocean supply mechanisms, *J. Geophys. Res. Ocean.*, 117(6), 1–18, doi:10.1029/2011JC007726, 2012.

Bradt Miller, L. I., Anderson, R. F., Fleisher, M. Q. and Burckle, L. H.: Comparing glacial and Holocene opal fluxes in the Pacific sector of the Southern Ocean, *Paleoceanography*, 24(2), 1–20, doi:10.1029/2008PA001693, 2009.

Broecker, W. S. and Clark, E.: Glacial-to-Holocene Redistribution of Carbonate Ion in the Deep Sea, *Science*, 294(5549), 2152–2155, doi:10.1126/science.1064171, 2001.

Brzezinski, M. A., Pride, C. J., Franck, V. M., Sigman, D. M., Sarmiento, J. L., Matsumoto, K., Gruber, N., Rau, G. H. and Coale, K. H.: A switch from Si(OH)<sub>4</sub> to NO<sub>3</sub> – depletion in the glacial Southern Ocean, *Geophys. Res. Lett.*, 29(12), 1564, doi:10.1029/2001GL014349, 2002.

Brzezinski, M. A., Jones, J. L. and Demarest, M. S.: Control of silica production by iron and silicic acid during the Southern Ocean Iron Experiment (SOFEX), *Limnol. Oceanogr.*, 50(3), 810–824, doi:10.4319/lo.2005.50.3.0810, 2005.

Buesseler, K. O.: The decoupling of production and particulate export in the surface ocean, *Global Biogeochem. Cycles*, 12(2), 297–310, doi:10.1029/97GB03366, 1998.

Caniupán, M., Lamy, F., Lange, C. B., Kaiser, J., Arz, H., Kilian, R., Baeza Urrea, O., Aracena, C., Hebbeln, D., Kissel, C., Laj, C., Mollenhauer, G. and Tiedemann, R.: Millennial-scale sea surface

temperature and Patagonian Ice Sheet changes off southernmost Chile (53 °s) over the past ~60 kyr, *Paleoceanography*, 26(3), doi:10.1029/2010PA002049, 2011.

Cárdenas, P., Lange, C. B., Vernet, M., Esper, O., Strain, B., Vorrath, M.-E., Ehrhardt, S., Müller, J., Kuhn, G., Arz, H. W., Lembke-Jene, L. and Lamy, F.: Biogeochemical proxies and diatoms in surface sediments across the Drake Passage reflect oceanic domains and frontal systems in the region, *Prog. Oceanogr.*, 174, 72–88, doi:10.1016/j.pocean.2018.10.004, 2019.

Carter, L., McCave, I. N. and Williams, M. J. M.: Chapter 4 Circulation and Water Masses of the Southern Ocean: A Review, in *Developments in Earth and Environmental Sciences*, vol. 8, edited by F. Florindo and M. Soegert, pp. 85–114, Elsevier B.V., Amsterdam., 2008.

Chapman, C. C., Lea, M.-A., Meyer, A., Sallée, J.-B. and Hindell, M.: Defining Southern Ocean fronts and their influence on biological and physical processes in a changing climate, *Nat. Clim. Chang.*, 10(3), 209–219, doi:10.1038/s41558-020-0705-4, 2020.

Chase, Z., Anderson, R. F., Fleisher, M. Q. and Kubik, P. W.: Accumulation of biogenic and lithogenic material in the Pacific sector of the Southern Ocean during the past 40,000 years, *Deep. Res. Part II Top. Stud. Oceanogr.*, 50(3–4), 799–832, doi:10.1016/S0967-0645(02)00595-7, 2003.

Chase, Z., Kohfeld, K. E. and Matsumoto, K.: Controls on biogenic silica burial in the Southern Ocean, *Global Biogeochem. Cycles*, 29(10), 1599–1616, doi:10.1002/2015GB005186, 2015.

Clark, P. U., Dyke, A. S., Shakun, J. D., Carlson, A. E., Clark, J., Wohlfarth, B., Mitrovica, J. X., Hostetler, S. W. and McCabe, A. M.: The Last Glacial Maximum, *Science*, 325(5941), 710–714, doi:10.1126/science.1172873, 2009.

Costa, K. and McManus, J.: Efficacy of <sup>230</sup>Th normalization in sediments from the Juan de Fuca Ridge, northeast Pacific Ocean, *Geochim. Cosmochim. Acta*, 197, 215–225, doi:10.1016/j.gca.2016.10.034, 2017.

Costa, K. M., Hayes, C. T., Anderson, R. F., Pavia, F. J., Bausch, A., Deng, F., Dutay, J. C., Geibert, W., Heinze, C., Henderson, G., Hillaire-Marcel, C., Hoffmann, S., Jaccard, S. L., Jacobel, A. W., Kienast, S. S., Kipp, L., Lerner, P., Lippold, J., Lund, D., Marcantonio, F., McGee, D., McManus, J. F., Mekik, F., Middleton, J. L., Missiaen, L., Not, C., Pichat, S., Robinson, L. F., Rowland, G. H., Roy-Barman, M., Tagliabue, A., Torfstein, A., Winckler, G. and Zhou, Y.: <sup>230</sup>Th Normalization: New Insights on an Essential Tool for Quantifying Sedimentary Fluxes in the Modern and Quaternary Ocean, *Paleoceanogr. Paleoclimatology*, 35(2), 1–36, doi:10.1029/2019PA003820, 2020.



Davies, B. J., Darvill, C. M., Lovell, H., Bendle, J. M., Dowdeswell, J. A., Fabel, D., García, J.-L., Geiger, A., Glasser, N. F., Gheorghiu, D. M., Harrison, S., Hein, A. S., Kaplan, M. R., Martin, J. R. V., Mendelova, M., Palmer, A., Pelto, M., Rodés, Á., Sagredo, E. A., Smedley, R. K., Smellie, J. L. and Thorndycraft, V. R.: The evolution of the Patagonian Ice Sheet from 35 ka to the present day (PATICE), *Earth-Science Rev.*, 204, 103152, doi:10.1016/j.earscirev.2020.103152, 2020.

Deacon, G.: The Antarctic Circumpolar Ocean. Studies in Polar Research Series, viii, in *Geological Magazine*, vol. 122, edited by Cambridge University Press., pp. 306–306, Cambridge, London, New York, New Rochelle, Melbourne, Sydney., 1984.

Demidov, A. B., Mosharov, S. A., Gagarin, V. I. and Romanova, N. D.: Spatial variability of the primary production and chlorophyll-*a* concentration in the drake passage in the austral spring, *Oceanology*, 51(2), 281–294, doi:10.1134/S0001437011020056, 2011.

Diekmann, B.: Sedimentary patterns in the late Quaternary Southern Ocean, *Deep. Res. Part II Top. Stud. Oceanogr.*, 54(21–22), 2350–2366, doi:10.1016/j.dsr2.2007.07.025, 2007.

Dugdale, R. C., Wilkerson, F. P. and Minas, H. J.: The role of a silicate pump in driving new production, *Deep Sea Res. Part I Oceanogr. Res. Pap.*, 42(5), 697–719, doi:10.1016/0967-0637(95)00015-X, 1995.

Dymond, J.: Barium in deep sea sediments: A geo-chemical proxy for paleoproductivity: *Paleoceanography*, *Paleoceanography*, 7, 163–181, doi:0883-8305/92/92PA-00181, 1992.

Ferrari, R., Jansen, M. F., Adkins, J. F., Burke, A., Stewart, A. L. and Thompson, A. F.: Antarctic sea ice control on ocean circulation in present and glacial climates, *Proc. Natl. Acad. Sci.*, 111(24), 8753–8758, doi:10.1073/pnas.1323922111, 2014.

Fitzsimmons, J. N., Boyle, E. A. and Jenkins, W. J.: Distal transport of dissolved hydrothermal iron in the deep South Pacific Ocean, *Proc. Natl. Acad. Sci.*, 111(47), 16654–16661, doi:10.1073/pnas.1418778111, 2014.

Fleisher, M. Q. and Anderson, R. F.: Assessing the collection efficiency of Ross Sea sediment traps using <sup>230</sup>Th and <sup>231</sup>Pa, *Deep. Res.*, 50, 693–712, doi:10.1016/S0967-0645(02)00591-X, 2003.

Franck, V. M., Brzezinski, M. A., Coale, K. H. and Nelson, D. M.: Iron and silicic acid concentrations regulate Si uptake north and south of the Polar Frontal Zone in the Pacific Sector of the Southern Ocean, *Deep Sea Res. Part II Top. Stud. Oceanogr.*, 47(15–16), 3315–3338, doi:10.1016/S0967-0645(00)00070-9, 2000.

Francois, R., Frank, M., Rutgers van der Loeff, M. M. and Bacon, M. P.: 230 Th normalization: An essential tool for interpreting sedimentary fluxes during the late Quaternary, *Paleoceanography*, 19(1), PA1018, doi:10.1029/2003PA000939, 2004.

François, R., Altabet, M. A., Yu, E.-F., Sigman, D. M., Bacon, M. P., Frank, M., Bohrmann, G., Bareille, G. and Labeyrie, L. D.: Contribution of Southern Ocean surface-water stratification to low atmospheric CO<sub>2</sub> concentrations during the last glacial period, *Nature*, 389(6654), 929–935, doi:10.1038/40073, 1997.

Frank, M., Mangini, A., Gersonde, R., Rutgers van der Loeff, M. and Kuhn, G.: Late Quaternary sediment dating and quantification of lateral sediment redistribution applying 230Thex: a study from the eastern Atlantic sector of the Southern Ocean, *Geol. Rundschau*, 85(3), 554–566, doi:10.1007/BF02369010, 1996.

Frank, M., Gersonde, R. and Mangini, A.: Sediment Redistribution, 230Thex- Normalization and Implications for the Reconstruction of Particle Flux and Export Paleoproductivity, in *Use of Proxies in Paleoceanography*, pp. 409–426, Springer Berlin Heidelberg, Berlin, Heidelberg., 1999.

Frank, M.: Accumulation rate and vertical rain rate of sediment core PS2082-1. PANGAEA, <https://doi.org/10.1594/PANGAEA.81101>, 2002.

Freeman, N. M., Lovenduski, N. S., Munro, D. R., Krumhardt, K. M., Lindsay, K., Long, M. C., and Maclennan, M.: The Variable and Changing Southern Ocean Silicate Front: Insights from the CESM Large Ensemble. *Global Biogeochemical Cycles*, 32(5), 752–768. <https://doi.org/10.1029/2017GB005816>, 2018.

Freeman, N. M., Munro, D. R., Sprintall, J., Mazloff, M. R., Purkey, S., Rosso, I., DeRanek, C. A. and Sweeney, C.: The Observed Seasonal Cycle of Macronutrients in Drake Passage: Relationship to Fronts and Utility as a Model Metric, *J. Geophys. Res. Ocean.*, 124(7), 4763–4783, doi:10.1029/2019JC015052, 2019.

Gersonde, R.: The expedition of the research vessel “Polarstern” to the polar South Pacific in 2009/2010 (ANT-XXVI/2 - BIPOMAC), Gersonde, edited by H. Bornemann; and B. Chiaventone, *Berichte zur Polar- und Meeresforschung (Reports on Polar and Marine Research)*, Bremerhaven, Alfred Wegener Institute for Polar and Marine Research, Bremerhaven., 2011.

Gille, S. T.: Meridional displacement of the Antarctic Circumpolar Current, *Philos. Trans. R. Soc.*, 372, 20130273, doi:http://dx.doi.org/10.1098/rsta.2013.0273, 2014.

Glasser, N. F., Jansson, K. N., Harrison, S. and Kleman, J.: The glacial geomorphology and Pleistocene history of South America between 38°S and 56°S, *Quat. Sci. Rev.*, 27(3–4), 365–390, doi:10.1016/j.quascirev.2007.11.011, 2008.

Gordon, A. L., Molinelli, E. and Baker, T.: Large-scale relative dynamic topography of the Southern Ocean, *J. Geophys. Res.*, 83(C6), 3023, doi:10.1029/jc083ic06p03023, 1978.

Gottschalk, J., Hodell, D. A., Skinner, L. C., Crowhurst, S. J., Jaccard, S. L. and Charles, C.: Past Carbonate Preservation Events in the Deep Southeast Atlantic Ocean (Cape Basin) and Their Implications for Atlantic Overturning Dynamics and Marine Carbon Cycling, *Paleoceanogr. Paleoclimatology*, 33(6), 643–663, doi:10.1029/2018PA003353, 2018.

Gouretski, V. V. and Koltermann, K. P.: The World Ocean Circulation Experiment (WOCE) Global Hydrographic Climatology, 35th ed., edited by B. BHS, Hamburg. [online] Available from: <http://rda.ucar.edu/datasets/ds285.4/>, 2004.

Gowan, E. J., Zhang, X., Khosravi, S., Rovere, A., Stocchi, P., Hughes, A. L. C., Gyllencreutz, R., Mangerud, J., Svendsen, J.-I. and Lohmann, G.: A new global ice sheet reconstruction for the past 80 000 years, *Nat. Commun.*, 12(1), 1199, doi:10.1038/s41467-021-21469-w, 2021.

Graham, R. M., De Boer, A. M., van Sebille, E., Kohfeld, K. E. and Schlosser, C.: Inferring source regions and supply mechanisms of iron in the Southern Ocean from satellite chlorophyll data, *Deep. Res. Part I Oceanogr. Res. Pap.*, 104, 9–25, doi:10.1016/j.dsr.2015.05.007, 2015.

Ho, S. L., Mollenhauer, G., Lamy, F., Martínez-García, A., Mohtadi, M., Gersonde, R., Hebbeln, D., Nunez-Ricardo, S., Rosell-Melé, A. and Tiedemann, R.: Sea surface temperature variability in the Pacific sector of the Southern Ocean over the past 700 kyr, *Paleoceanography*, 27(4), PA4202, doi:10.1029/2012PA002317, 2012.

Hodell, D. A., Charles, C. D. and Ninnemann, U. S.: Comparison of interglacial stages in the South Atlantic sector of the Southern Ocean for the past 450 kyr: Implications for Marine Isotope Stage (MIS) 11, *Glob. Planet. Change*, 24(1), 7–26, doi:10.1016/S0921-8181(99)00069-7, 2000.

Honjo, S.: Particle export and the biological pump in the Southern Ocean, *Antarct. Sci.*, 16(4), 501–516, doi:10.1017/S0954102004002287, 2004.

Hopwood, M. J., Carroll, D., Höfer, J., Achterberg, E. P., Meire, L., Le Moigne, F. A. C., Bach, L. T., Eich, C., Sutherland, D. A. and González, H. E.: Highly variable iron content modulates iceberg-ocean fertilisation and potential carbon export, *Nat. Commun.*, 10(1), doi:10.1038/s41467-019-13231-0, 2019.

Howard, W. R. and Prell, W. L.: Late Quaternary CaCO<sub>3</sub> production and preservation in the Southern Ocean: Implications for oceanic and atmospheric carbon cycling, *Paleoceanography*, 9(3), 453–482, doi:10.1029/93PA03524, 1994.

Jaccard, S. L., Hayes, C. T., Martínez-García, A., Hodell, D. A., Anderson, R. F., Sigman, D. M. and Haug, G. H.: Supplementary materials: Two modes of change in Southern Ocean productivity over the past million years, *Science*, 339(6126), 1419–1423, doi:10.1126/science.1227545, 2013.

Kaiser, J. and Lamy, F.: Links between Patagonian Ice Sheet fluctuations and Antarctic dust variability during the last glacial period (MIS 4-2), *Quat. Sci. Rev.*, 29(11–12), 1464–1471, doi:10.1016/j.quascirev.2010.03.005, 2010.

Kaiser, J., Lamy, F., Arz, H. W. and Hebbeln, D.: Dynamics of the millennial-scale sea surface temperature and Patagonian Ice Sheet fluctuations in southern Chile during the last 70 kyr (ODP Site 1233), *Quat. Int.*, 161(1), 77–89, doi:10.1016/j.quaint.2006.10.024, 2007.

Kemp, A. E. S., Grigorov, I., Pearce, R. B. and Naveira Garabato, A. C.: Migration of the Antarctic Polar Front through the mid-Pleistocene transition: evidence and climatic implications, *Quat. Sci. Rev.*, 29(17–18), 1993–2009, doi:10.1016/j.quascirev.2010.04.027, 2010.

Key, R. M., Kozyr, A., Sabine, C. L., Lee, K., Wanninkhof, R., Bullister, J. L., Feely, R. A., Millero, F. J., Mordy, C. and Peng, T. H.: A global ocean carbon climatology: Results from Global Data Analysis Project (GLODAP), *Global Biogeochem. Cycles*, 18(4), 1–23, doi:10.1029/2004GB002247, 2004.

Kohfeld, K. E., Le Quéré, C., Harrison, S. P. and Anderson, R. F.: Role of marine biology in glacial-interglacial CO<sub>2</sub> cycles, *Science*, 308(5718), 74–78, doi:10.1126/science.1105375, 2005.

Kohfeld, K. E., Graham, R. M., de Boer, A. M., Sime, L. C., Wolff, E. W., Le Quéré, C. and Bopp, L.: Southern Hemisphere westerly wind changes during the Last Glacial Maximum: Paleo-data synthesis, *Quat. Sci. Rev.*, 68(April 2013), 76–95, doi:10.1016/j.quascirev.2013.01.017, 2013.

Kopczynska, E. E., Dehairs, F., Elskens, M. and Wright, S.: Phytoplankton and microzooplankton variability between the Subtropical and Polar Fronts south of Australia: Thriving under regenerative and new production in late summer, *J. Geophys. Res. Ocean.*, 106(C12), 31597–31609, doi:10.1029/2000JC000278, 2001.

Lambert, F., Delmonte, B., Petit, J. R., Bigler, M., Kaufmann, P. R., Hutterli, M. A., Stocker, T. F., Ruth, U., Steffensen, J. P. and Maggi, V.: Dust - Climate couplings over the past 800,000 years from the EPICA Dome C ice core, *Nature*, 452(7187), 616–619, doi:10.1038/nature06763, 2008.

Lamy, F.: The expedition PS97 of the research vessel POLARSTERN to the Drake Passage in 2016, Bremerhaven, Germany., 2016, Berichte zur Polar- und Meeresforschung = Reports on Polar and Marine Research, Alfred Wegener Institute for Polar and Marine Research, Bremerhaven, Germany. 701, 571 p., doi:10.2312/BzPM\_0701\_2016, 2016.

Lamy, F., Kaiser, J., Ninnemann, U., Hebbeln, D., Arz, H. W. and Stoner, J.: Antarctic Timing of Surface Water Changes off Chile and Patagonian Ice Sheet Response, *Science*, 304(5679), 1959–1962, doi:10.1126/science.1097863, 2004.

Lamy, F., Gersonde, R., Winckler, G., Esper, O., Jaeschke, A., Kuhn, G., Ullermann, J., Martinez-Garcia, A., Lambert, F. and Kilian, R.: Increased Dust Deposition in the Pacific Southern Ocean During Glacial Periods, *Science*, 343(6169), 403–407, doi:10.1126/science.1245424, 2014.

Lamy, F., Arz, H. W., Kilian, R., Lange, C. B., Lembke-Jene, L., Wengler, M., Kaiser, J., Baeza-Urrea, O., Hall, I. R., Harada, N. and Tiedemann, R.: Glacial reduction and millennial-scale variations in Drake Passage throughflow., *Proc. Natl. Acad. Sci. U. S. A.*, 112(44), 13496–501, doi:10.1073/pnas.1509203112, 2015.

Laufkötter, C., Stern, A. A., John, J. G., Stock, C. A. and Dunne, J. P.: Glacial Iron Sources Stimulate the Southern Ocean Carbon Cycle, *Geophys. Res. Lett.*, 45(24), 13,377–13,385, doi:10.1029/2018GL079797, 2018.

Li, F., Ginoux, P. and Ramaswamy, V.: Distribution, transport, and deposition of mineral dust in the Southern Ocean and Antarctica: Contribution of major sources, *J. Geophys. Res.*, 113(D10), D10207, doi:10.1029/2007JD009190, 2008.

Li, F., Ginoux, P. and Ramaswamy, V.: Transport of Patagonian dust to Antarctica, *J. Geophys. Res. Atmos.*, 115(18), 1–9, doi:10.1029/2009JD012356, 2010.

Lisiecki, L. E. and Raymo, M. E.: A Pliocene-Pleistocene stack of 57 globally distributed benthic  $\delta^{18}\text{O}$  records, *Paleoceanography*, 20(1), PA1003, doi:10.1029/2004PA001071, 2005.

Lowell, T. V., Heusser, C. J., Andersen, B. G., Moreno, P. I., Hauser, A., Heusser, L. E., Schluchter, C., Marchant, D. R. and Denton, G. H.: Interhemispheric Correlation of Late Pleistocene Glacial Events, *Science*, 269(5230), 1541–1549, doi:10.1126/science.269.5230.1541, 1995.

Marcantonio, F., Lyle, M. and Ibrahim, R.: Particle sorting during sediment redistribution processes and the effect on  $^{230}\text{Th}$ -normalized mass accumulation rates, *Geophys. Res. Lett.*, 41(15), 5547–5554, doi:10.1002/2014GL060477, 2014.

Marshall, J. and Speer, K.: Closure of the meridional overturning circulation through Southern Ocean upwelling, *Nat. Geosci.*, 5(3), 171–180, doi:10.1038/ngeo1391, 2012.

Martin, J. H.: Glacial-interglacial CO<sub>2</sub> change: The Iron Hypothesis, *Paleoceanography*, 5(1), 1–13, doi:10.1029/PA005i001p00001, 1990.

Martínez-García, A., Rosell-Melé, A., Geibert, W., Gersonde, R., Masqué, P., Gaspari, V. and Barbante, C.: Links between iron supply, marine productivity, sea surface temperature, and CO<sub>2</sub> over the last 1.1 Ma, *Paleoceanography*, 24(1), PA1207, doi:10.1029/2008PA001657, 2009.

Martínez-García, A., Sigman, D. M., Ren, H., Anderson, R. F., Straub, M., Hodell, D. A., Jaccard, S. L., Eglinton, T. I. and Haug, G. H.: Iron Fertilization of the Subantarctic Ocean During the Last Ice Age, *Science*, 343(6177), 1347–1350, doi:10.1126/science.1246848, 2014.

Matsumoto, K., Chase, Z. and Kohfeld, K.: Different mechanisms of silicic acid leakage and their biogeochemical consequences, *Paleoceanography*, 29(3), 238–254, doi:10.1002/2013PA002588, 2014.

McCave, I. N. and Hall, I. R.: Size sorting in marine muds: Processes, pitfalls, and prospects for paleoflow-speed proxies, *Geochemistry, Geophys. Geosystems*, 7(10), Q10N05, doi:10.1029/2006GC001284, 2006.

McGee, D., Winckler, G., Borunda, A., Sernó, S., Anderson, R. F., Recasens, C., Bory, A., Gaiero, D., Jaccard, S. L., Kaplan, M., McManus, J. F., Revel, M. and Sun, Y.: Tracking eolian dust with helium and thorium: Impacts of grain size and provenance, *Geochim. Cosmochim. Acta*, 175, 47–67, doi:10.1016/j.gca.2015.11.023, 2016.

Mengelt, C., Abbott, M. R., Barth, J. A., Letelier, R. M., Measures, C. I. and Vink, S.: Phytoplankton pigment distribution in relation to silicic acid, iron and the physical structure across the Antarctic Polar Front, 170°W, during austral summer, *Deep. Res. Part II Top. Stud. Oceanogr.*, 48(19–20), 4081–4100, doi:10.1016/S0967-0645(01)00081-9, 2001.

Meredith, M. P., Woodworth, P. L., Chereskin, T. K., Marshall, D. P., Allison, L. C., Bigg, G. R., Donohue, K., Heywood, K. J., Hughes, C. W., Hibbert, A., Hogg, A. M., Johnson, H. L., Jullion, L., King, B. A., Leach, H., Lenn, Y. D., Maqueda, M. A. M., Munday, D. R., Garabato, A. C. N., Provost, C., Sallée, J. B. and Sprintall, J.: SUSTAINED MONITORING OF THE SOUTHERN OCEAN AT DRAKE PASSAGE: PAST ACHIEVEMENTS AND FUTURE PRIORITIES, *Rev. Geophys.*, 49, 8755–1209, doi:10.1029/2010RG000348.1., 2011.

Moore, C. M., Mills, M. M., Arrigo, K. R., Berman-Frank, I., Bopp, L., Boyd, P. W., Galbraith, E. D., Geider, R. J., Guieu, C., Jaccard, S. L., Jickells, T. D., La Roche, J., Lenton, T. M., Mahowald, N. M.,

- Marañón, E., Marinov, I., Moore, J. K., Nakatsuka, T., Oschlies, A., Saito, M. A., Thingstad, T. F., Tsuda, A. and Ulloa, O.: Processes and patterns of oceanic nutrient limitation, *Nat. Geosci.*, 6(9), 701–710, doi:10.1038/ngeo1765, 2013.
- Mortlock, R. A. and Froelich, P. N.: A simple method for the rapid determination of biogenic opal in pelagic marine sediments, *Deep Sea Res. Part A, Oceanogr. Res. Pap.*, 36(9), 1415–1426, doi:10.1016/0198-0149(89)90092-7, 1989.
- Müller, P. J. and Schneider, R.: An automated leaching method for the determination of opal in sediments and particulate matter, *Deep Sea Res. Part I Oceanogr. Res. Pap.*, 40(3), 425–444, doi:10.1016/0967-0637(93)90140-X, 1993.
- Naveira Garabato, A. C., Ferrari, R. and Polzin, K. L.: Eddy stirring in the Southern Ocean, *J. Geophys. Res.*, 116(C9), C09019, doi:10.1029/2010JC006818, 2011.
- Noble, T. L., Piotrowski, A. M., Robinson, L. F., McManus, J. F., Hillenbrand, C. D. and Bory, A. J. M.: Greater supply of Patagonian-sourced detritus and transport by the ACC to the Atlantic sector of the Southern Ocean during the last glacial period, *Earth Planet. Sci. Lett.*, 317–318, 374–385, doi:10.1016/j.epsl.2011.10.007, 2012.
- Nürnberg, C. C., Bohrmann, G., Schlüter, M. and Frank, M.: Barium accumulation in the Atlantic sector of the Southern Ocean: Results From 190,000-year records, *Paleoceanography*, 12(4), 594–603, doi:10.1029/97PA01130, 1997.
- Orsi, H., Whitworth, T. and Jr, W. D. N.: On the meridional extent and fronts of the Antarctic Circumpolar Current, *Deep Sea Res.*, 42(5), 641–673, doi:10.1016/0967-0637(95)00021-W, 1995.
- PAGES, Past Interglacials Working Group of PAGES: Interglacials of the last 800,000years, *Rev. Geophys.*, 54, 162–219, doi:10.1002/2015RG000482.Received, 2016.
- Paillard, D., Labeyrie, L. and Yiou, P.: Macintosh Program performs time-series analysis, *Eos, Trans. Am. Geophys. Union*, 77(39), 379–379, doi:10.1029/96EO00259, 1996.
- Paparazzo, F. E.: Tendencias espaciales y temporales en la distribución de macronutrientes en aguas superficiales del Pasaje Drake, *Ecol. Austral*, 26(1), 027–039, doi:10.25260/EA.16.26.1.0.142, 2016.
- Paytan, A.: Ocean Paleoproductivity, in *Encyclopedia of Paleoclimatology and Ancient Environments. Encyclopedia of Earth Sciences Series.*, edited by V. Gornitz, pp. 643–651, Springer Netherlands, Dordrecht, 2009.

Peine, F., Turnewitsch, R., Mohn, C., Reichelt, T., Springer, B. and Kaufmann, M.: The importance of tides for sediment dynamics in the deep sea—Evidence from the particulate-matter tracer 234Th in deep-sea environments with different tidal forcing, *Deep Sea Res. Part I Oceanogr. Res. Pap.*, 56(7), 1182–1202, doi:10.1016/j.dsr.2009.03.009, 2009.

Rabassa, J.: Late Cenozoic Glaciations in Patagonia and Tierra del Fuego, *Dev. Quat. Sci.*, 11, 151–204, doi:10.1016/S1571-0866(07)10008-7, 2008.

Rabassa, J. and Clapperton, C. M.: Quaternary glaciations in the southern hemisphere: An overview, *Quat. Sci. Rev.*, 9(2–3), 299–304, doi:10.1016/0277-3791(90)90024-5, 1990.

Rabassa, J., Coronato, A. and Martínez, O.: Late Cenozoic glaciations in Patagonia and Tierra del Fuego: An updated review, *Biol. J. Linn. Soc.*, 103(2), 316–335, doi:10.1111/j.1095-8312.2011.01681.x, 2011.

Renault, A., Provost, C., Sennéchaël, N., Barré, N. and Kartavtseff, A.: Two full-depth velocity sections in the Drake Passage in 2006—Transport estimates, *Deep Sea Res. Part II Top. Stud. Oceanogr.*, 58(25–26), 2572–2591, doi:10.1016/j.dsr2.2011.01.004, 2011.

Rigual-Hernández, A. S., Trull, T. W., Bray, S. G., Cortina, A. and Armand, L. K.: Latitudinal and temporal distributions of diatom populations in the pelagic waters of the Subantarctic and Polar Frontal zones of the Southern Ocean and their role in the biological pump, *Biogeosciences*, 12(18), 5309–5337, doi:10.5194/bg-12-5309-2015, 2015.

Rigual Hernández, A. S., Trull, T. W., Nodder, S. D., Flores, J. A., Bostock, H., Abrantes, F., Eriksen, R. S., Sierro, F. J., Davies, D. M., Ballegeer, A.-M., Fuertes, M. A. and Northcote, L. C.: Coccolithophore biodiversity controls carbonate export in the Southern Ocean, *Biogeosciences*, 17(1), 245–263, doi:10.5194/bg-17-245-2020, 2020.

Roberts, J., McCave, I. N., McClymont, E. L., Kender, S., Hillenbrand, C.-D., Matano, R., Hodell, D. A. and Peck, V. L.: Deglacial changes in flow and frontal structure through the Drake Passage, *Earth Planet. Sci. Lett.*, 474, 397–408, doi:10.1016/j.epsl.2017.07.004, 2017.

Saavedra-Pellitero, M., Baumann, K. H., Lamy, F. and Köhler, P.: Coccolithophore variability across Marine Isotope Stage 11 in the Pacific sector of the Southern Ocean and its potential impact on the carbon cycle, *Paleoceanography*, 32(8), 864–880, doi:10.1002/2017PA003156, 2017.

Saavedra-Pellitero, M., Baumann, K. H., Fuertes, M. Á., Schulz, H., Marcon, Y., Manon Vollmar, N., Flores, J. A. and Lamy, F.: Calcification and latitudinal distribution of extant coccolithophores across



the Drake Passage during late austral summer 2016, *Biogeosciences*, 16(19), 3679–3702, doi:10.5194/bg-16-3679-2019, 2019.

Schlitzer, Reiner, Ocean Data View, <https://odv.awi.de>, 2021

Schlüter, M. and Rickert, D.: Effect of pH on the measurement of biogenic silica, *Mar. Chem.*, 63(1–2), 81–92, doi:10.1016/S0304-4203(98)00052-8, 1998.

Schroth, A. W., Crusius, J., Sholkovitz, E. R. and Bostick, B. C.: Iron solubility driven by speciation in dust sources to the ocean, *Nat. Geosci.*, 2(5), 337–340, doi:10.1038/ngeo501, 2009.

Shoenfelt, E. M., Sun, J., Winckler, G., Kaplan, M. R., Borunda, A. L., Farrell, K. R., Moreno, P. I., Gaiero, D. M., Recasens, C., Sambrotto, R. N. and Bostick, B. C.: High particulate iron(II) content in glacially sourced dusts enhances productivity of a model diatom, *Sci. Adv.*, 3(6), e1700314, doi:10.1126/sciadv.1700314, 2017.

Shoenfelt, E. M., Winckler, G., Lamy, F., Anderson, R. F. and Bostick, B. C.: Highly bioavailable dust-borne iron delivered to the Southern Ocean during glacial periods, *Proc. Natl. Acad. Sci. U. S. A.*, 115(44), 11180–11185, doi:10.1073/pnas.1809755115, 2018.

Shoenfelt, E. M., Winckler, G., Annett, A. L., Hendry, K. R. and Bostick, B. C.: Physical Weathering Intensity Controls Bioavailable Primary Iron(II) Silicate Content in Major Global Dust Sources, *Geophys. Res. Lett.*, 46(19), 10854–10864, doi:10.1029/2019GL084180, 2019.

Sigman, D. M., Hain, M. P. and Haug, G. H.: The polar ocean and glacial cycles in atmospheric CO<sub>2</sub> concentration, *Nature*, 466(7302), 47–55, doi:10.1038/nature09149, 2010.

Sprenk, D., Weber, E. M., Kuhn, G., Rosén, P., Frank, M., Molina-Kescher, M., Liebetrau, V. and Röhling, H. G.: Southern Ocean bioproductivity during the last glacial cycle - New detection method and decadal-scale insight from the Scotia Sea, *Geol. Soc. Spec. Publ.*, 381(1), 245–261, doi:10.1144/SP381.17, 2013.

Strub, P. T., James, C., Montecino, V., Rutllant, J. A. and Blanco, J. L.: Ocean circulation along the southern Chile transition region (38°–46°S): Mean, seasonal and interannual variability, with a focus on 2014–2016, *Prog. Oceanogr.*, 172(May 2018), 159–198, doi:10.1016/j.pocean.2019.01.004, 2019.

Sugden, D. E., McCulloch, R. D., Bory, A. J.-M. and Hein, A. S.: Influence of Patagonian glaciers on Antarctic dust deposition during the last glacial period, *Nat. Geosci.*, 2(4), 281–285, doi:10.1038/ngeo474, 2009.

Sulpis, O., Boudreau, B. P., Mucci, A., Jenkins, C., Trossman, D. S., Arbic, B. K. and Key, R. M.: Current CaCO<sub>3</sub> dissolution at the seafloor caused by anthropogenic CO<sub>2</sub>, *Proc. Natl. Acad. Sci.*, 115(46), 11700–11705, doi:10.1073/pnas.1804250115, 2018.

Suman, D. O. and Bacon, M. P.: Variations in Holocene sedimentation in the North American Basin determined from 230Th measurements, *Deep Sea Res. Part A, Oceanogr. Res. Pap.*, 36(6), 869–878, doi:10.1016/0198-0149(89)90033-2, 1989.

Tapia, R., Ho, S. L., Núñez-Ricardo, S., Marchant, M., Lamy, F. and Hebbeln, D.: Increased marine productivity in the southern Humboldt Current System during MIS 2–4 and 10–11, *Paleoceanogr. Paleoclimatology*, 33(0), 2–31, doi:10.1029/2020PA004066, 2021.

Thöle, L. M., Amsler, H. E., Moretti, S., Auderset, A., Gilgannon, J., Lippold, J., Vogel, H., Crosta, X., Mazaud, A., Michel, E., Martínez-García, A. and Jaccard, S. L.: Glacial-interglacial dust and export production records from the Southern Indian Ocean, *Earth Planet. Sci. Lett.*, 525, 115716, doi:10.1016/j.epsl.2019.115716, 2019.

Toyos, M. H., Lamy, F., Lange, C. B., Lembke-Jene, L., Saavedra-Pellitero, M., Esper, O. and Arz, H. W.: Antarctic Circumpolar Current Dynamics at the Pacific Entrance to the Drake Passage Over the Past 1.3 Million Years, *Paleoceanogr. Paleoclimatology*, 35(7), 1–20, doi:10.1029/2019PA003773, 2020.

Turekian, K. K. and Wedepohl, K. H.: Distribution of the Elements in Some Major Units of the Earth's Crust, *GSA Bull.*, 72(2), 175–192, doi:10.1130/0016-7606(1961)72[175:DOTAIS]2.0.CO;2, 1961.

Turnewitsch, R., Reys, J.-L., Nycander, J., Waniek, J. J. and Lampitt, R. S.: Internal tides and sediment dynamics in the deep sea—Evidence from radioactive 234Th/238U disequilibria, *Deep Sea Res. Part I Oceanogr. Res. Pap.*, 55(12), 1727–1747, doi:10.1016/j.dsr.2008.07.008, 2008.

Vernet, M., Sines, K., Chakos, D., Cefarelli, A. O. and Ekern, L.: Impacts on phytoplankton dynamics by free-drifting icebergs in the NW Weddell Sea, *Deep. Res. Part II Top. Stud. Oceanogr.*, 58(11–12), 1422–1435, doi:10.1016/j.dsr2.2010.11.022, 2011.

Wadhams, J. L., Hawkings, J. R., Tarasov, L., Gregoire, L. J., Spencer, R. G. M., Gutjahr, M., Ridgwell, A. and Kohfeld, K. E.: Ice sheets matter for the global carbon cycle, *Nat. Commun.*, 10(1), 3567, doi:10.1038/s41467-019-11394-4, 2019.

Wengler, M., Lamy, F., Struve, T., Borunda, A., Böning, P., Geibert, W., Kuhn, G., Pahnke, K., Roberts, J., Tiedemann, R. and Winckler, G.: A geochemical approach to reconstruct modern dust fluxes and

sources to the South Pacific, *Geochim. Cosmochim. Acta*, 264, 205–223, doi:10.1016/j.gca.2019.08.024, 2019.

Winckler, G., Anderson, R. F., Fleisher, M. Q., McGee, D. and Mahowald, N.: Covariant glacial-interglacial dust fluxes in the equatorial Pacific and Antarctica., *Science*, 320(5872), 93–96, doi:10.1126/science.1150595, 2008.

Winckler, G., Anderson, R. F., Jaccard, S. L. and Marcantonio, F.: Ocean dynamics, not dust, have controlled equatorial Pacific productivity over the past 500,000 years, *Proc. Natl. Acad. Sci. U. S. A.*, 113(22), 6119–6124, doi:10.1073/pnas.1600616113, 2016.

Wu, S.Y. and Hou, S.: Impact of icebergs on net primary productivity in the Southern Ocean, *Cryosph.*, 11(2), 707–722, doi:10.5194/tc-11-707-2017, 2017.

Wu, S., Kuhn, G., Diekmann, B., Lembke-Jene, L., Tiedemann, R., Zheng, X., Ehrhardt, S., Arz, H. W. and Lamy, F.: Surface sediment characteristics related to provenance and ocean circulation in the Drake Passage sector of the Southern Ocean, *Deep Sea Res. Part I Oceanogr. Res. Pap.*, 154(December), 103135, doi:10.1016/j.dsr.2019.103135, 2019.

Wu, S., Lembke-Jene, L., Lamy, F., Arz, H. W., Nowaczyk, N., Xiao, W., Zhang, X., Hass, H. C., Titschack, J., Zheng, X., Liu, J., Dumm, L., Diekmann, B., Nürnberg, D., Tiedemann, R. and Kuhn, G.: Orbital- and millennial-scale Antarctic Circumpolar Current variability in Drake Passage over the past 140,000 years, *Nat. Commun.*, 12(1), 3948, doi:10.1038/s41467-021-24264-9, 2021.

*Supplement of*

**Variations in export production, lithogenic sediment transport and iron fertilization in the Pacific sector of Drake Passage over the past 400 ka**

**María H. Toyos et al.**

*Correspondence to:* María H. Toyos (mtoyos@udec.cl)

The copyright of individual parts of the supplement might differ from the article licence.



**Table S1.** Correlation matrix between <sup>230</sup>Th-normalized MARs of export production proxies and lithogenic indicators for core PS97/093-2.

<b>Litho. MAR (g/cm<sup>2</sup>/kyr)</b>	<b>Lithogenic MAR (g/cm<sup>2</sup>/kyr)</b>					
<b>Fe MAR (mg/cm<sup>2</sup>/kyr)</b>	$r^2=0.98$ $P<0.0001$ $n=60$	<b>Fe MAR (mg/cm<sup>2</sup>/kyr)</b>				
<b>Ba<sub>exc</sub> MAR (mg/cm<sup>2</sup>/kyr)</b>	$r^2=0.44$ $P<0.0001$ $n=60$	$r^2=0.46$ $P<0.0001$ $n=60$	<b>Ba<sub>exc</sub> MAR (mg/cm<sup>2</sup>/kyr)</b>			
<b>TOC MAR (mg/cm<sup>2</sup>/kyr)</b>	$r^2=0.81$ $P<0.0001$ $n=60$	$r^2=0.80$ $P<0.0001$ $n=60$	$r^2=0.48$ $P<0.0001$ $n=60$	<b>TOC MAR (mg/cm<sup>2</sup>/kyr)</b>		
<b>Opal MAR (g/cm<sup>2</sup>/kyr)</b>	$r^2=0.89$ $P<0.0001$ $n=60$	$r^2=0.85$ $P<0.0001$ $n=60$	$r^2=0.47$ $P<0.0001$ $n=60$	$r^2=0.57$ $P<0.0001$ $n=60$	<b>Opal MAR (g/cm<sup>2</sup>/kyr)</b>	
<b>CaCO<sub>3</sub> MAR (g/cm<sup>2</sup>/kyr)</b>	$r^2=0.11$ $P=0.009$ $n=60$	$r^2=0.10$ $P=0.009$ $n=60$	$r^2=0.03$ $P=0.128$ $n=60$	$r^2=0.02$ $P=0.208$ $n=60$	$r^2=0.04$ $P=0.059$ $n=60$	<b>CaCO<sub>3</sub> MAR (g/cm<sup>2</sup>/kyr)</b>

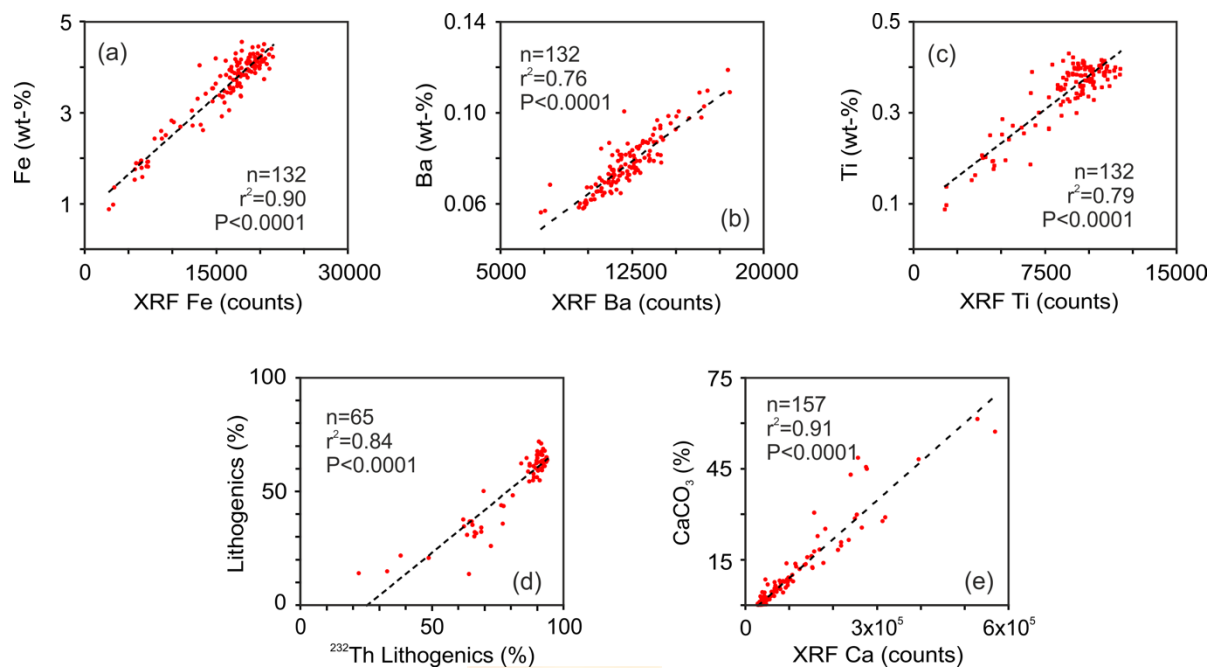


**Figure S1.** a, b, c: Linear regressions between XRF and measured element concentrations (Fe, Ba, Ti) used to obtain high-resolution element content records. d: Linear regression between lithogenic content obtained by subtraction (Litho %= 100 - [CaCO<sub>3</sub> % + opal % + (2xTOC %)]), and lithogenic content obtained by <sup>232</sup>Th concentrations. e: Linear regression between XRF Ca and measured CaCO<sub>3</sub> percentage used to obtain a high-resolution carbonate content record.

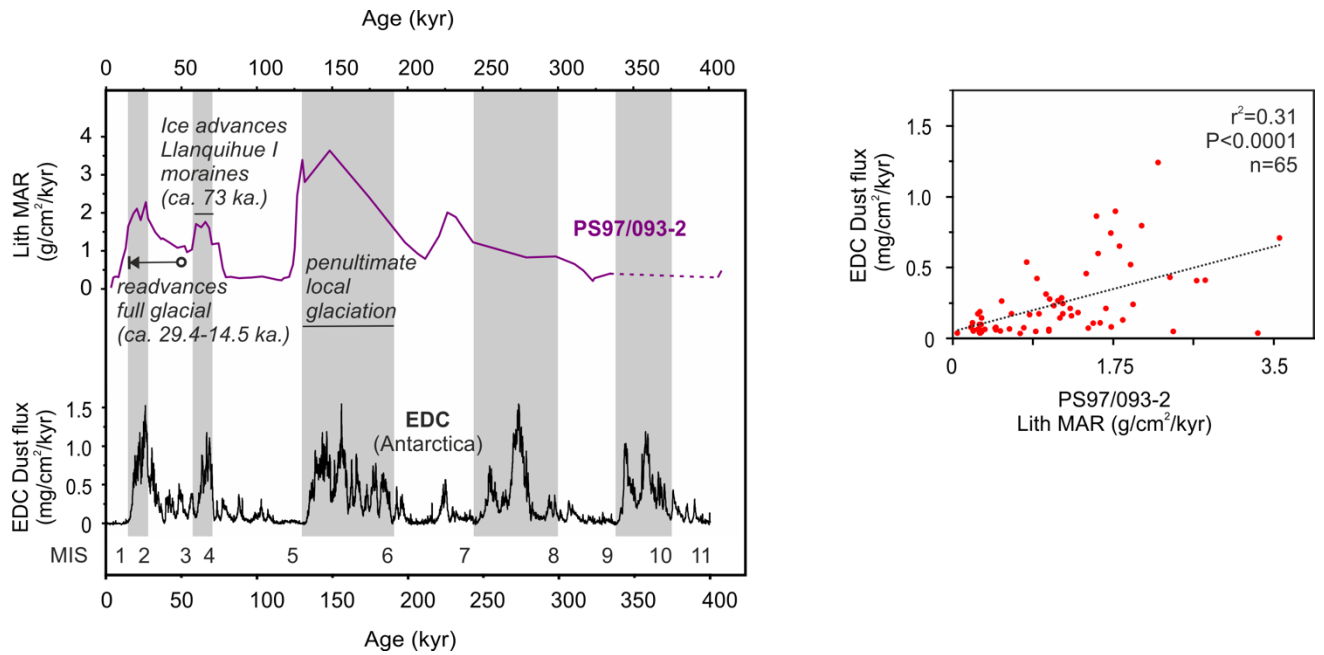


**Figure S2.** Left: Changes in <sup>230</sup>Th-normalized Lithogenic MARs of core PS97/093-2 compared to dust fluxes in the EPICA Dome C ice core (Lambert et al., 2008). The inset texts indicate the chronology of the ice advances in Patagonia and Tierra del Fuego according to Rabassa (2008). Vertical grey bars mark glacial stages according to Lisiecki & Raymo (2005). Marine Isotope Stage (MIS). Right: Linear correlation between PS97/093-2 lithogenic MARs and EDC dust flux.

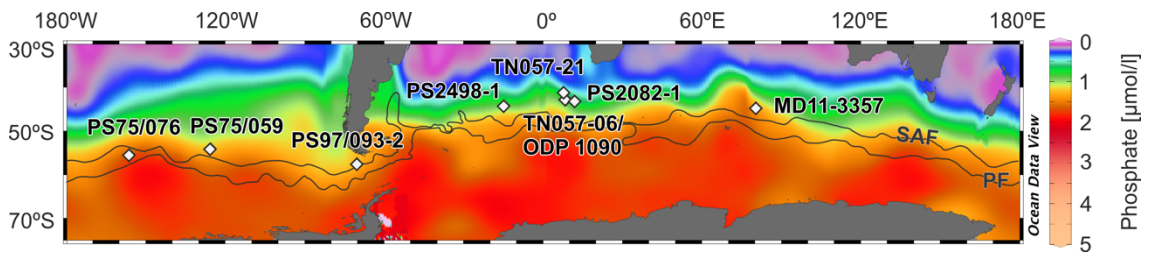


**Figure S3.** Southern Ocean average surface concentration of phosphate (data from Gouretski & Koltermann, 2004); Black lines indicate the modern location of the Subantarctic Front (SAF), and Polar Front (PF, Orsi et al., 1995); White diamonds indicate the core locations (PS75/076 and PS75/059, Lamy et al. 2014; PS97/093-2, this study; PS2498-1, TN057-21 and TN057-06, Anderson et al., 2014; ODP1090, Martínez-García et al. 2014; PS2082-1, Nürnberg, 1997 and Frank, 2002; MD11-3357, Thöle et al., 2019).

## References

- Anderson, R. F., Barker, S., Fleisher, M., Gersonde, R., Goldstein, S. L., Kuhn, G., Mortyn, P. G., Pahnke, K. and Sachs, J. P.: Biological response to millennial variability of dust and nutrient supply in the Subantarctic South Atlantic Ocean, *Philos. Trans. R. Soc. A Math. Phys. Eng. Sci.*, 372(2019), doi:10.1098/rsta.2013.0054, 2014.
- Frank, M.: Accumulation rate and vertical rain rate of sediment core PS2082-1. PANGAEA, <https://doi.org/10.1594/PANGAEA.81101>, 2002.
- Gouretski, V. V. and Koltermann, K. P.: The World Ocean Circulation Experiment (WOCE) Global Hydrographic Climatology, 35th ed., edited by B. BHS, Hamburg. [online] Available from: <http://rda.ucar.edu/datasets/ds285.4/>, 2004.
- Lambert, F., Delmonte, B., Petit, J. R., Bigler, M., Kaufmann, P. R., Hutterli, M. A., Stocker, T. F., Ruth, U., Steffensen, J. P. and Maggi, V.: Dust - Climate couplings over the past 800,000 years from the EPICA Dome C ice core, *Nature*, 452(7187), 616–619, doi:10.1038/nature06763, 2008.
- Lamy, F., Gersonde, R., Winckler, G., Esper, O., Jaeschke, A., Kuhn, G., Ullermann, J., Martinez-Garcia, A., Lambert, F. and Kilian, R.: Increased Dust Deposition in the Pacific Southern Ocean During Glacial Periods, *Science.*, 343(6169), 403–407, doi:10.1126/science.1245424, 2014.
- Lisiecki, L. E. and Raymo, M. E.: A Pliocene-Pleistocene stack of 57 globally distributed benthic  $\delta^{18}\text{O}$  records, *Paleoceanography*, 20(1), doi:10.1029/2004PA001071, 2005.
- Martínez-García, A., Sigman, D. M., Ren, H., Anderson, R. F., Straub, M., Hodell, D. A., Jaccard, S. L., Eglinton, T. I. and Haug, G. H.: Iron Fertilization of the Subantarctic Ocean During the Last Ice Age, *Science.*, 343(6177), 1347–1350, doi:10.1126/science.1246848, 2014.
- Nürnberg, C. C., Bohrmann, G., Schlüter, M. and Frank, M.: Barium accumulation in the Atlantic sector of the Southern Ocean: Results From 190,000-year records, *Paleoceanography*, 12(4), 594–603, doi:10.1029/97PA01130, 1997.
- Rabassa, J.: Late Cenozoic Glaciations in Patagonia and Tierra del Fuego, *Dev. Quat. Sci.*, 11, 151–204, doi:10.1016/S1571-0866(07)10008-7, 2008.
- Thöle, L. M., Amsler, H. E., Moretti, S., Auderset, A., Gilgannon, J., Lippold, J., Vogel, H., Crosta, X., Mazaud, A., Michel, E., Martínez-García, A. and Jaccard, S. L.: Glacial-interglacial dust and export production records from the Southern Indian Ocean, *Earth Planet. Sci. Lett.*, 525, doi:10.1016/j.epsl.2019.115716, 2019.



### 4.3. Chapter 3/ Capítulo 3

#### **Manuscript 3 (in preparation): 1.4 Ma productivity reconstruction at the Pacific entrance of the Drake Passage determined from mass accumulation rates corrected for syndepositional redistribution of sediments**

María H. Toyos, Frank Lamy, Carina B. Lange, Helge W. Arz, Lester Lembke-Jene, and Gisela Winckler: 1.4 Ma productivity reconstruction at the Pacific entrance of the Drake Passage determined from mass accumulation rates corrected for syndepositional redistribution of sediments. To be submitted to *Paleoceanography and Paleoclimatology* (in preparation)

#### **Motivación**

**Reconstrucción de la productividad biológica en la Zona Subantártica en la entrada del Paso de Drake basada en tasas de acumulación corregidas por el fenómeno de redistribución lateral de sedimentos durante los últimos 1.4 millones de años.**

El aumento de la productividad primaria en la Zona Subantártica ha sido uno de los mecanismos propuestos para explicar la captación de carbono por parte del océano Austral durante periodos glaciales. Sin

embargo, a causa de la vigorosidad de la Corriente Circumpolar Antártica, la redistribución lateral de sedimentos en el fondo marino es un fenómeno común aquí, y las reconstrucciones basadas en tasas de acumulación derivadas del modelo de edad (*BMAR*, por sus siglas en inglés) pueden estar sesgadas. En este estudio, se han evaluado los cambios en la productividad biológica en la Zona Subantártica a la entrada del Paso de Drake durante los últimos 1.4 millones de años. Este estudio se basa en una novedosa combinación *BMAR* de bario biogénico, carbono orgánico, opal biogénico, carbonatos y hierro en las que se ha corregido el efecto de redistribución lateral de sedimentos en el testigo de sedimentos PS97/093-2.

Los resultados presentados en este capítulo servirán de base para un manuscrito en preparación que se someterá en la revista *Paleoceanography and Paleoclimatology* (Diciembre 2021).

## **1.4 Ma productivity reconstruction at the Pacific entrance of the Drake Passage determined from mass accumulation rates corrected for syndepositional redistribution of sediments**

**María H. Toyos<sup>1,2,3</sup>, Frank Lamy<sup>3</sup>, Carina B. Lange<sup>2,4,5,6</sup>, Helge W. Arz<sup>7</sup>,  
Lester Lembke-Jene<sup>3</sup>, and Gisela Winckler<sup>8,9</sup>**

<sup>1</sup> Programa de Postgrado en Oceanografía, Departamento de Oceanografía, Facultad de Ciencias Naturales y Oceanográficas, Universidad de Concepción, Concepción, Chile

<sup>2</sup> Centro de Investigación Dinámica de Ecosistemas Marinos de Altas Latitudes (IDEAL), Universidad Austral de Chile, Valdivia, Chile

<sup>3</sup> Alfred-Wegener-Institut, Helmholtz-Zentrum für Polar und Meeresforschung, Bremerhaven, Germany

<sup>4</sup> Centro Oceanográfico COPAS Sur-Austral, Universidad de Concepción, Concepción, Chile

<sup>5</sup> Departamento de Oceanografía, Universidad de Concepción, Chile

<sup>6</sup> Scripps Institution of Oceanography, La Jolla, California 92037

<sup>7</sup> Leibniz-Institut für Ostseeforschung Warnemünde (IOW), Rostock-Warnemünde, Germany

<sup>8</sup> Lamont-Doherty Earth Observatory, Columbia University, Palisades, NY 10964

<sup>9</sup> Department of Earth and Environmental Sciences, Columbia University, New York, NY 10027

## **Motivation**

Increased export production in the Subantarctic Zone of the Southern Ocean has been proposed as a key mechanism for explaining carbon drawdown during glacial times. However, syndepositional redistribution of sediments is common here due to the dynamic bottom water circulation of the Antarctic Circumpolar Current, leading to biased stratigraphy-based mass accumulation rates (BMAR). Here, we provide an evaluation of export production linked to the Earth's fundamental climate changes over the past ~1.4 Ma. in the Subantarctic Zone, at the Pacific entrance of the Drake Passage. We base our study on a novel combination of BMAR of biogenic barium, organic carbon, biogenic opal, calcium carbonate, and iron corrected for syndepositional redistribution from sediment core PS97/093-2.

## **1 Introduction**

The Southern Ocean (SO) plays an essential role in modulating glacial-interglacial variations of atmospheric  $p\text{CO}_2$  (Sigman et al., 2010) and in global ocean biogeochemistry by supplying nutrients to the surface, and thereby influencing primary export production (e.g., Henley et al., 2020). The main feature of the SO is the Antarctic Circumpolar Current (ACC). Through induced pronounced upwelling of nutrient- and  $\text{CO}_2$ -rich

subsurface water masses and enhancing the air-sea exchange of CO<sub>2</sub> (Chapman et al., 2020), the ACC fundamentally affects the strength of the biological carbon pump. Its flow is concentrated along several fronts, which are the Subantarctic Front (SAF), Polar Front (PF), and Southern ACC Front (SACCF; Orsi et al., 1995; figure 1). In the SO, the fronts act as barriers, inhibiting the exchange of the upwelled waters and their associated nutrients with neighboring fronts (Paparazzo, 2016). Therefore, their positions usually indicate the boundary of some of the main biogeochemical provinces that comprise the SO (Tréguer & Jacques, 1992). Specifically, the region between the SAF and the PF, known as the Polar Frontal Zone (PFZ), is characterized by a significant increase in phytoplankton biomass in the frontal area and high abundances of large diatoms (Kopczynska et al., 2001). In contrast, the Subantarctic Zone (SAZ, the area north of the SAF) is defined as a carbonate-dominated regime, where the biological pump is predominantly driven by carbonate-producing organisms (Honjo, 2004; Rigual-Hernández et al., 2015). Furthermore, in the SAZ, iron (Fe) and silica limit the phytoplankton growth (Boyd et al., 1999), and mean chlorophyll-*a* concentrations are relatively low, being only above 2 mg m<sup>-3</sup> within 50km off a continental or island coastline (figure 1; Graham et al., 2015).

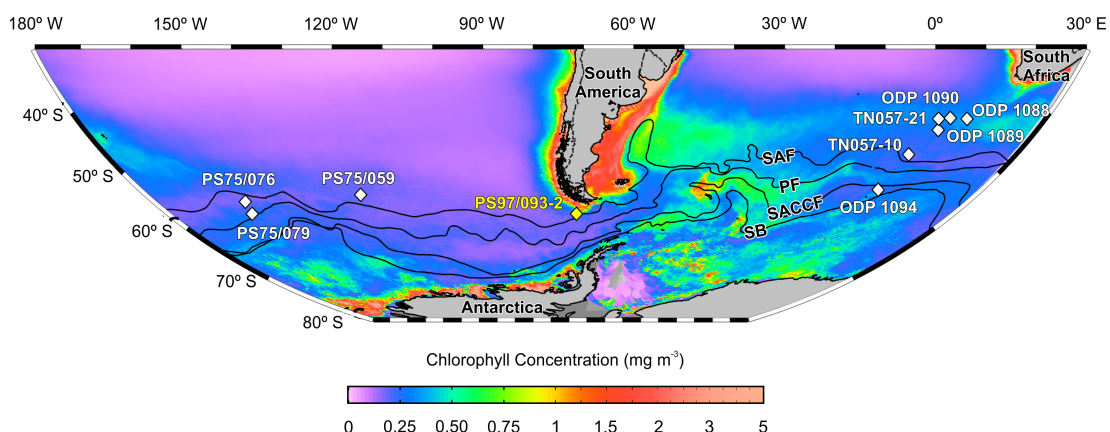


**Figure 1.** Map of Southern Ocean mean chlorophyll-*a* concentrations for the years 2009–2019 with core locations. Yellow diamond indicates the location of core PS97/093-2 (this study), and white diamonds the location of published records discussed in the text: PS75/079, PS75/076 and PS75/059 (Saavedra-Pellitero, 2017a); TN057-10, TN057-21 and ODP 1089 (Gottschalk et al., 2018); ODP 1088 (Farmer et al., 2019a); ODP 1090 (Farmer et al., 2019a; Lawrence et al., 2013; Martínez-García et al., 2011), and ODP 1094 (Jaccard et al., 2013). Black lines mark ACC modern fronts (Orsi et al., 1995). SAF, Subantarctic Front; PF, Polar Front; SACCF, southern Antarctic Circumpolar Current Front, and SB, southern boundary of the ACC. We used the MODIS-Aqua Level-3 Mapped Chlorophyll Data Version 2018 (data/10.5067/AQUA/MODIS/L3M/CHL/2018), in 4 km resolution monthly mean chlorophyll-*a* concentrations between March 2009 to March 2019 (available from NASA Ocean Color website, <https://oceancolor.gsfc.nasa.gov/l3/>).

Today, the SO represents the main leak in the marine carbon cycle, as indicated by the inefficient nutrient utilization, partly because phytoplankton growth is limited by the scarcity of Fe (de Baar et al., 1995). However, increased biological activity from enhanced Fe fertilization in a stratified SO is thought to have been a key driver of the increased glacial carbon storage (Jaccard et al., 2013). Several studies have provided evidence for more significant Fe deposition and higher export production in the SAZ during glacial intervals (Anderson et al., 2014; Kohfeld et al., 2005; Lamy et al., 2014; Martínez-García et al.,

2009; Thöle et al., 2019, Toyos et al., accepted). A spatial comparison between subantarctic fluxes shows that glacial export production at the Pacific entrance to the Drake Passage (DP) was lower than in the Atlantic and Indian sectors of the SO, despite having the highest glacial lithogenic fluxes. Since at the Pacific entrance to the DP, due to the proximity of the South American continent and related to Patagonian Ice Sheet (PIS) expansions, phytoplankton growth was not limited by Fe during such intervals (Toyos et al., accepted). It has been proposed that the glacial increase in export production was primarily regulated by silica availability due to complete consumption of the silicic acid by diatoms (Matsumoto et al., 2002; Toyos et al., accepted).

Furthermore, in this area, a detailed analysis of biological productivity changes, covering the past 400 kyr, shows that during glacials, peaks in export production are consistent with northward shifts of the SAF and PF, which would position the area closer to Si-rich waters, and additionally enhanced by a decrease in the utilization of silicic acid relative to nitrate by diatoms (Toyos et al., accepted). Whereas, during interglacials, due to a southward migration of the SAZ, primary export production was likely dominated by coccolithophores, but the absence of peaks in proxies of total export production during such intervals suggests

that export production by calcareous organism was too small to have a noticeable impact on the total export (Toyos et al., accepted). However, beyond the last 400,000 years, and despite being a non-trivial portion of the SO, the knowledge of productivity changes in the SAZ at the Pacific entrance to the DP is still unexplored.

The DP is the geographical separation between South America and the Antarctic Peninsula and constitutes the major bottleneck along the ACC path (figure 1). Here strong surface and bottom current velocities have been observed, mainly concentrated in the SAF and the PF (Meredith et al., 2011; Renault et al., 2011). Furthermore, in the SAZ and central DP, it has been reported significant glacial/interglacial changes in the ACC bottom flow speed, with reduced ACC intensity in glacials and a more vigorous circulation during interglacials (Lamy et al., 2015; Toyos et al., 2020; Wu et al., 2021). Specifically, in the vicinity of the SAZ, at the Pacific entrance to the DP, the mean glacial/interglacial variability in bottom current speeds based on sortable silt measurements during the last 1.3 Ma. was *ca.* 16% (Toyos et al., 2020). As a result, in the SO, the dynamic bottom water circulation of the ACC led to widespread and repeated syndepositional redistribution (e.g., Van Bennekom et al., 1988), where the accumulation rates of laterally redistributed sediments are often



many times larger than the fluxes of material sinking from the overlying surface waters (Francois et al., 2004). Therefore, stratigraphy-based mass accumulation rates (BMAR) and the resulting paleoceanographic interpretations may suffer from substantial errors if lateral redistribution of particles by ocean currents is not considered (e.g., Francois et al., 2004). For instance, in the Atlantic sector of the SO, Frank et al. (1999) showed that BMAR could be biased by up to a factor of 12 if sediment focusing and winnowing is ignored. In the Pacific subantarctic entrance to the DP, bottom current dynamics caused BMARs to be biased up to three (four) times in the intervals with pronounced focusing (winnowing) (Toyos et al., accepted). As a consequence, constant flux proxies, such as particle-reactive  $^{230}\text{Th}$  radionuclide, have been developed, allowing for the quantification of lateral sediment redistribution and the production of accurate vertical rain rates (e.g. Costa et al., 2020; Suman & Bacon, 1989). Since then,  $^{230}\text{Th}_{\text{XS}}$ -normalized mass accumulation rates (MAR) have been widely used in SO cores to reconstruct past changes in export production (e.g., Anderson et al., 2014; Durand et al., 2017; Lamy et al., 2014; Thöle et al., 2019). Unfortunately, the applicability of the  $^{230}\text{Th}$  constant flux proxy is limited to the last 500 kyr due to its half-life ( $t_{1/2}^{230}\text{Th} = 75.5$  kyr; Cheng et al., 2013). Thus, for the interval beyond the applicability of the

$^{230}\text{Th}$ , the reliability of paleoproductivity reconstructions by using BMAR exclusively in the SO is compromised. Understanding how bottom currents redistribute sediment components settling from the surface water is critical.

Here, we provide the first quantification of export production changes in the subantarctic SE Pacific beyond the interval where accumulation rates based on  $^{230}\text{Th}_{\text{xs}}$ -normalization are applicable (from *ca.* 400 ka to 1.37 Ma). This period includes two major climate transitions. Firstly, the Mid-Pleistocene Transition (MPT) when ice age cyclicity switched from predominantly 41 kyr to 100 kyr periodicities for yet unknown reasons (Farmer et al., 2019b). Secondly, the MIS 12/11 boundary, known as the Mid-Brunhes Event (MBE). It indicates the end of the "*lukewarm*" interglacials (MIS 13 –19, Jaccard et al., (2013)), and triggered substantially warmer interglacials with higher  $\text{CO}_2$  concentrations than previous interglacials (Holden et al., 2011; Yin & Berger, 2012).

To report export production beyond the last 400 kyr, we use a sediment core retrieved near the SAF at the DP entrance (Core PS97/093-2, figure 1). Firstly, we provide a novel approach to reduce the errors substantially for syndepositional sediment redistribution in BMAR. As a

result, we use a combination of "corrected" BMAR (BMAR-corr) of Fe, excess of barium (the fraction of Ba that is not supplied by terrigenous material,  $Ba_{xs}$ ), total organic carbon (TOC), biogenic opal, and carbonate ( $CaCO_3$ ). Secondly, we show how the variations in paleoproductivity proxies are locked to the Earth's climate fundamental changes across the MPT and the MBE.

## **2 Materials and Methods**

The methodological strategy of this work relies on the application of numerous geochemical indicators in marine sediments from piston core PS97/093-2 (57° 29.94' S; 70° 16.48' W; 3781 m water depth; length of core 16.45 m). The core was retrieved *ca.* 40 km NW of the present-day position of the SAF, within the main flow of the ACC, on the Pacific entrance of the Drake Passage during expedition PS97 "Paleo Drake" with R/V Polarstern (Lamy, 2016). Our sampling and analytical procedures are described in detail by Toyos et al. (accepted) and are briefly summarized in this section.

### **2.1 Age model**

The initial age model for sediment core PS97/093-2 was taken from (Toyos et al., 2020) and consisted of a two-step approach: 1) establishment of a preliminary age model based on biostratigraphic time markers from

calcareous nannofossils and diatoms, and 2) fine-tuning of the high-resolution XRF records of Fe and Ca counts and CaCO<sub>3</sub> contents to the LR04 benthic  $\delta^{18}\text{O}$  stack (Lisiecki & Raymo, 2005). For tuning, we assumed that low Fe contents characterize interglacial periods, whereas high represent glacials. Additionally, XRF Ca counts and CaCO<sub>3</sub> percentages were used for a finer tuning in the intervals where they are present. Nevertheless, for a better fit with the biostratigraphic time markers in the lowermost portion of the record, we slightly revisited the original age model by adding 3 tie points. Therefore, the new age model used in this study has 37 tie points, all of them within the biostratigraphic datums' age ranges, and sedimentation rates between *ca.* 0.5 and 2.5 cm/kyr. The revised age-depth relationship for core PS97/093-2 exhibits and more uniform sedimentation rates than the original age model (figure 2). All correlations were performed with the AnalySeries software (Paillard et al., 1996). The bottom of the core reaches back to 1.37 Ma.

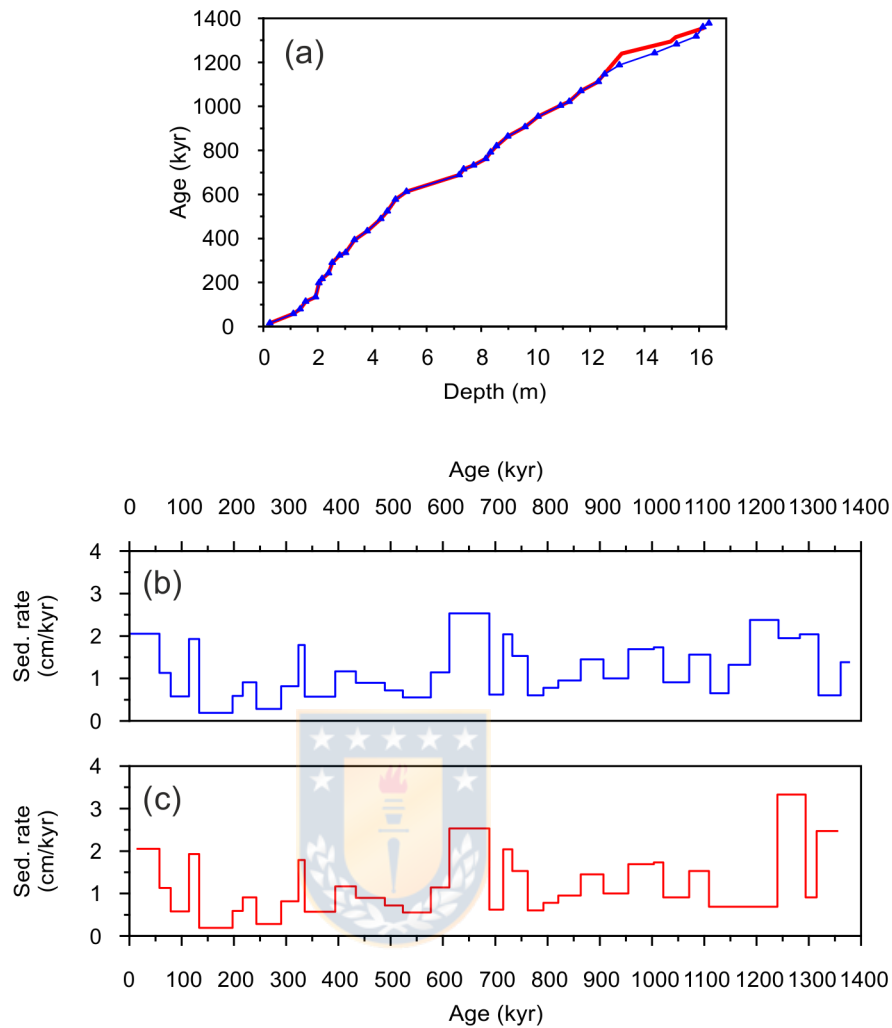


**Figure 2. a:** Age–depth relationship for core PS97/093-2, red line indicates the original age model from Toyos et al. (2020), and blue line marks the modified age model (this study), the blue triangles are the pointers. **b, c:** Sedimentation rates of core PS97/093-2 according to the update age model (b), and to the initial age model from Toyos et al. (2020) (c).

## 2.2. Bulk sediment parameters and geochemistry

Total carbon, total nitrogen (TC, TN) and total organic carbon (TOC) were quantified at the Alfred-Wegener-Institute, Bremerhaven (AWI), and biogenic opal was determined at the Laboratory of Paleoceanography, University of Concepción, Chile. The analytical procedures are described in detail by Toyos et al. (accepted).

Dry bulk densities were quantified on a total of 162 samples at AWI Bremerhaven, using freeze-dried and homogenized bulk sediment samples.

The archive half of core PS97/093-2 was measured with an AVAATECH X-Ray Fluorescence Core Scanner at AWI Bremerhaven for high-resolution semi-quantitative element intensities of Ca, Fe, Ba and Ti at 0.5 cm resolution. In this work we used the CaCO<sub>3</sub> high-resolution record calculated by Toyos et al. (2020).

### **2.3 Elements and U/Th isotope analysis**

Concentrations of Al, Fe, Ti, and Ba, along with U/Th isotopes, were determined at Lamont-Doherty Earth Observatory (LDEO) following the procedures described in Toyos et al. (accepted). In this study we used the high resolution high-resolution Fe record from Toyos et al. (accepted), obtained by calibration of the the 3-point smoothed Fe XRF intensities with bulk sediment (wt%) Fe from our discrete samples ( $r^2=0.90$ ,  $n=132$ ,  $P<0.0001$ ).

### **2.4 Excess barium and elemental ratios**

Excess barium ( $Ba_{xs}$ ) was determined via the equation:

$$Ba_{xs} = Ba_{total} - (Ti_{total} * [Ba/Ti]_{detrital})$$

where  $Ba_{total}$  is the total measured Ba,  $Ti_{total}$  is the total measured Ti, and  $[Ba/Ti]_{detrital}$  is the ratio of Ba and Ti in crustal material (assumed here to be 0.126 after Turekian & Wedepohl, (1961)). The  $Ba_{xs}$  record was obtained calibrating the 3-point smoothed Ba and Ti XRF intensities with bulk sediment (wt%) Ba ( $r^2=0.76$ ,  $n=132$ ,  $P<0.0001$ ) and Ti ( $r^2=0.79$ ,  $n=132$ ,  $P<0.0001$ ).

## **2.5 Mass accumulation rates**

Stratigraphy-based mass accumulation rates (BMAR) of individual components (Fe,  $Ba_{xs}$ , TOC,  $CaCO_3$  and biogenic opal) were obtained by multiplying the concentration of the respective component by the linear sedimentation rate and the dry bulk density. Additionally, we used the  $^{230}Th_{xs}$ -normalized mass accumulation rates (MAR) of Fe,  $Ba_{xs}$ , TOC, biogenic opal and  $CaCO_3$  from Toyos et al. (accepted). MAR were calculated by using the  $^{30}Th_{xs}$  normalization method (Bacon, 1984; Francois et al., 2004).

## **2.6 Calculation of focusing factor**

In this study, we used the focusing factors of core PS97/093-2 calculated in Toyos et al. (accepted). The degree of sediment focusing ( $\Psi$ ) was obtained following the approach of Suman & Bacon (1989).  $\Psi>1$  indicates sediment focusing, whereas  $\Psi<1$  denotes sediment winnowing.

Values of  $\Psi=1$  indicate that the amount of  $^{230}\text{Th}$  buried in the sediment is equivalent to the amount of  $^{230}\text{Th}$  produced in the water column.

### **3 Calibration strategy for calculation of “corrected” stratigraphy-based mass accumulation rates (BMAR-corr)**

3.1 Basis: lateral redistribution of sediments in response to the bottom current regime at core site PS97/93 and uncertainties

A previous study of core PS97/093-2 shows substantial discrepancies between the BMAR and MAR caused by current-driven sediment redistribution, as indicated by the corresponding current strength fluctuations compared the changing focusing factors. Specifically, our core shows a consistent pattern of winnowing (focusing) in the intervals with relatively low (high) bottom current speeds (Toyos et al., accepted; figure 3). This pattern, which at first sight seems counterintuitive, is most likely caused by a combination of factors including: i) Changes in the cohesive effects and flocculation of the fines during transport. The fine sediment fraction behaves similarly to the  $>63\ \mu\text{m}$  fraction under strong bottom current conditions because of the cohesive effects and flocculation on the fines during transport (McCave & Hall, 2006). In contrast, under slower bottom current conditions, there might be a loss of such effects in the fine sediment fraction, which triggers the winnowing (Marcantonio et



al., 2014). ii) During interglacial periods, stronger currents plausibly cause a gradual mobilization of more and more coarse-grained material that had accumulated laterally in certain areas, resulting in a coarser-grained sediment focusing at PS97/093 site (Toyos et al., accepted).

For core PS97/093-2, given the the good correlation between current strengths and focusing factors. To quantify accurately past variations in mass accumulation rates beyond the interval of applicability of  $^{230}\text{Th}$ , we propose a new approach to identify and correct for lateral redistribution of sediments. To do so, we use the relationship between the focusing factors, which indicate lateral redistribution of sediments, and the sortable silt, as a proxy for past bottom strength fluctuations. To infer the degree of sediment focusing as a function of the bottom current strength ( $\overline{SS}$ ), there are some considerations that should be taken into account:

i) Our focusing factors suggest that periods of maximum current strength during glacial times did not result in sediment erosion/winning but fostered increased sediment focusing (Toyos et al., accepted). However, intermittent winnowing intervals might start above the flow speed that indicates the height in accumulation rates (McCave & Hall, 2006), compromising the reliability of the approach for higher  $\overline{SS}$  values

than the ones used in calibration. Since the absolute  $\overline{SS}$  maxima in our record happened during MIS 9 ( $\overline{SS}= 28.9 \mu\text{m}$ , figure 3a), which belongs to the calibration interval, we have confidence that all the peaks in  $\overline{SS}$ , do not reach the point where a combination of selective deposition and winnowing takes place.

ii) By definition, focusing factors can be quite sensitive to the age model uncertainties and temporal integration periods (Stefanie S. Kienast et al., 2007). Therefore, to reduce errors and increase the reliability of the calibration, we chose the age-depth horizons of the measured  $^{230}\text{Th}_{ex}^o$  instead of the averaged  $^{230}\text{Th}_{ex}^o$  between dated horizons (tie points, figure 3b).

### 3.2 Sortable silt-focusing factor correlation

To estimate the degree of sediment focusing in core PS97/093-2 beyond the applicability interval of  $^{230}\text{Th}$ , we plotted the measured focusing factors as a  $f(\overline{SS})$  in figure 3c. Since focusing factors are always  $>0$ , and the growth rate seems to be faster in the focusing than in the winnowing interval, to get the best fit, we used an exponential regression (figure 3c,  $r^2=0.72$ ,  $n=65$ ):

$$\textit{Focusing factor} (\overline{SS}) = \exp(-11.04 + 0.58 (\overline{SS}) - 0.005 (\overline{SS})^2)$$

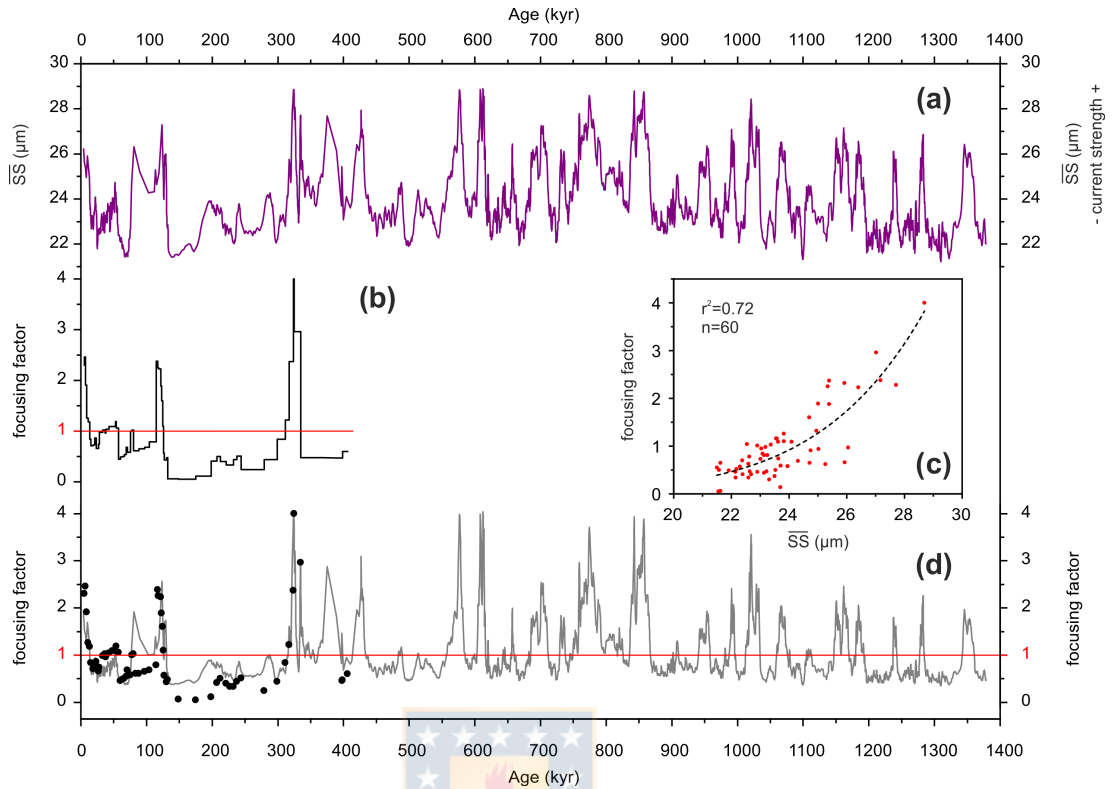


**Figure 3.** Multiproxy reconstruction at site PS97/093. **a:** Reconstructed current strength based on  $\overline{SS}$  proxy (Toyos et al., 2020); **b:** Focusing factor (Toyos et al., accepted); **c:** Exponential regression between focusing factor and  $\overline{SS}$  used to obtain focusing factors beyond the 400 ka.; **d:** High resolution focusing factors (grey line) compared to measured focusing factor (black dots). Red lines in (b) and (d) indicate focusing factor=1, values above 1 are in the focusing intervals, whereas below 1 denote winnowing.

Our new focusing factors range from a minimum value of  $\Psi=0.35$  ( $\overline{SS}=21.2 \mu\text{m}$ ) at MIS 32, to a maximum of  $\Psi=4.03$  ( $\overline{SS}=28.9 \mu\text{m}$ ) during MIS 9, whereas neutral values ( $\Psi \approx 1$ ) happen when bottom current strength is *ca.*  $\overline{SS} \approx 24.2\text{--}24.5 \mu\text{m}$  (figure 3d). The main implication of our new approach is to obtain an estimation of the degree of syndepositional redistribution beyond the interval of the applicability of  $^{230}\text{Th}$ , which allows us to decrease the associated errors in the BMAR dividing them by

the estimated focusing factors (figure 3d). Comparisons between the non-corrected BMAR and BMAR-corr with the MAR show a significant positive correlation between MAR and BMAR-corr. In contrast, there is no significant positive correlation between MAR and BMAR (table 1). Furthermore, the correspondence between MAR and BMAR-corr increases substantially when we eliminate the data from MIS 6 (table 1), which is the only interval characterized by extreme winnowing ( $\Psi=0.08$ ) that likely trigger an overestimation of the MAR, caused by the removal of part of the  $^{230}\text{Th}$  fraction (Toyos et al., accepted). A comparison between the BMAR and BMAR-corr of the individual components Fe,  $\text{Ba}_{\text{xs}}$ , TOC, opal, and  $\text{CaCO}_3$  is shown in figure 4.

**Table 1.** Comparison between the statistical parameters of the correlations between the accumulation rates ( $\text{g}/\text{cm}^2/\text{kyr}$ ) MAR ( $^{230}\text{Th}$ -based) from Toyos et al. (accepted), BMAR (stratigraphy-based) from Toyos et al. (accepted), and BMAR-corr (stratigraphy-based corrected by syndepositional redistribution, this study). BMAR were calculated multiplying the dry bulk density ( $\text{g}/\text{cm}^3$ ) by the sedimentation rates ( $\text{cm}/\text{kyr}$ ), and BMAR-corr were obtained dividing the BMAR by the focusing factor.

Correlation		Regression statistics			
		R	Adj-R <sup>2</sup>	P-value	observations-n
All points	MAR vs BMAR	0.068	-0.011	0.588	60
	MAR vs BMAR-corr	0.403	0.162	0.0008	60
MIS 6 not included	MAR vs BMAR	0.250	0.047	0.049	57
	MAR vs BMAR-corr	0.584	0.329	0.000001	57

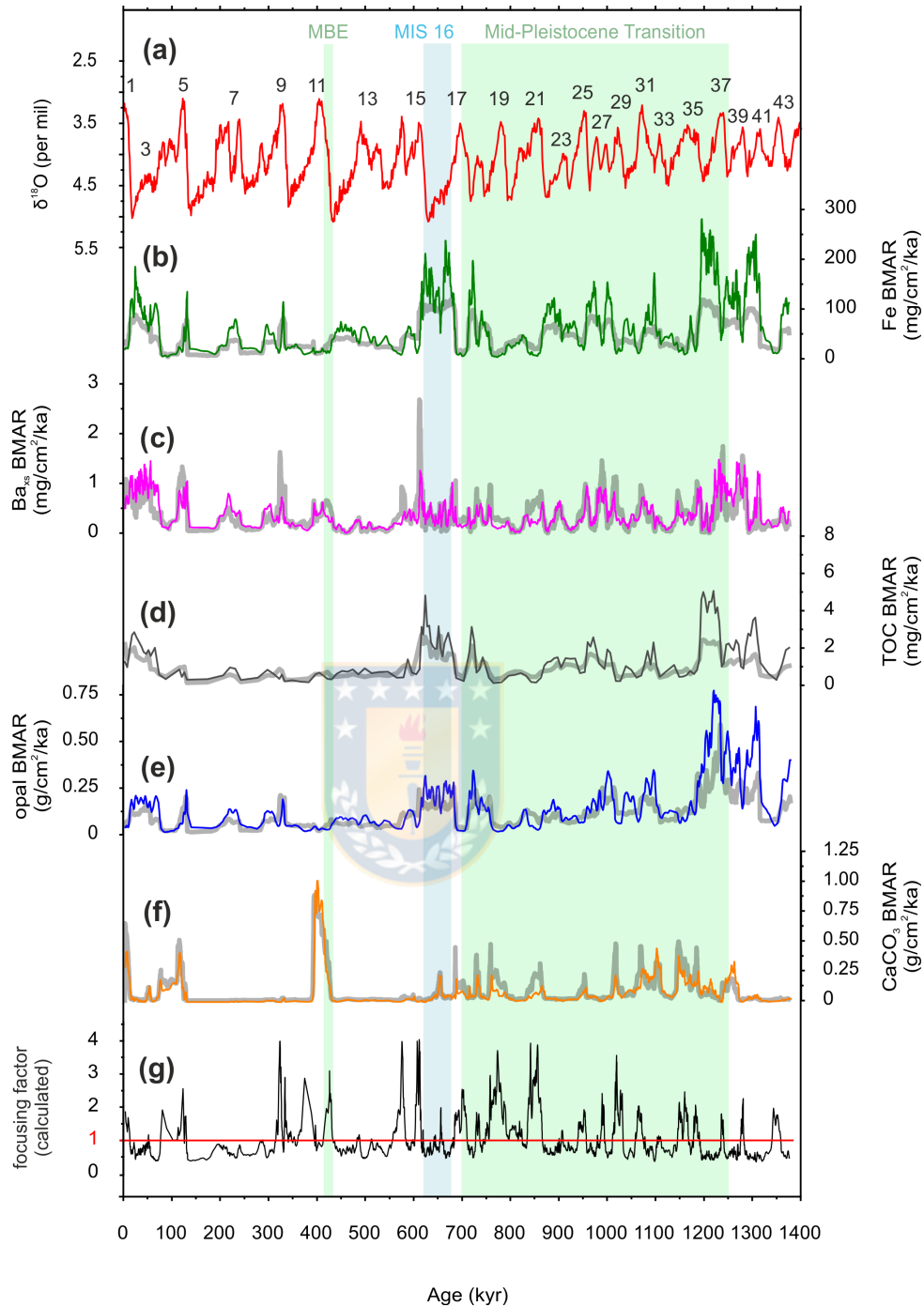


**Figure 4.** Comparison between PS97/093-2's BMAR (thick grey lines) and BMAR-corr (fine colored lines) of Fe,  $Ba_{xs}$ , TOC, opal and  $CaCO_3$ . a: LR04 benthic  $\delta^{18}O$  stack (Lisiecki & Raymo, 2005), numbers indicate interglacial Marine Isotope Stages; b: Fe BMAR-corr and BMAR; c:  $Ba_{xs}$  BMAR-corr and BMAR; d: TOC BMAR-corr and BMAR; e: biogenic opal BMAR-corr and BMAR; f:  $CaCO_3$  BMAR-corr and BMAR; g: Focusing factor (calculated) over the past 1.37 Ma.; red line indicates focusing factor=1, values above 1 are in the focusing intervals, whereas below 1 denote winnowing. Vertical bars mark the Mid-Plesistocene Transition (green), Mid-Brunhes Event (green), and Marine Isotope Stage 16 (blue).

#### **4 Results: corrected age model-based MARs records (BMAR-corr)**

Generally, we observe high glacial ( $>50 \text{ mg/cm}^2/\text{ka}$ ) and low interglacial ( $<10 \text{ mg/cm}^2/\text{ka}$ ) Fe BMAR-corr, reaching peak values in the interval MIS 40–36, and during MIS 16, whereas the lowest values are observed during MIS 5 (figure 5). A similar pattern is observed for the TOC BMAR-corr and opal BMAR-corr records in the interval MIS 40–36 with high values (up to *ca.*  $5 \text{ mg/cm}^2/\text{ka}$  and *ca.*  $0.75 \text{ g/cm}^2/\text{ka}$ , respectively). However, during MIS 16 TOC BMAR-corr peaks noticeably whereas opal BMAR-corr values are not substantially higher than in other glacials. Overall, TOC and opal MARs-corr are lower during interglacials showing minima during MIS 19 and MIS 21 for the TOC BMARs-corr, and during MIS 5 for the opal BMARs-corr (figure 5). Furthermore, Fe, TOC and opal BMARs-corr correlate positively, and most of the time the records are in good agreement exhibiting coherent patterns (figure 5).

On the other hand, the  $\text{Ba}_{\text{xs}}$  BMARs-corr record does not display a clear glacial-interglacial variability because it peaks in some glacial and interglacial intervals. The relatively high values ( $> 0.75 \text{ mg/cm}^2/\text{ka}$ ) are recorded in the intervals MIS 40–36, MIS 4–2, and spikes are observed

during MIS 28, 26, at the transition MIS 16/15, in the middle of MIS 7, at the transition of MIS 6/5, and at the beginning of MIS 5. Smaller peaks (ranging from ca. 0.5 to 0.75 mg/cm<sup>2</sup>/ka) are seen within the Holocene, MIS 9, 11, 16, 18, 22, 23, 32 and at the transitions between MIS 32/31 and MIS MIS 17/16 (figure 5c).

A completely different pattern is observed in the BMAR-corr of CaCO<sub>3</sub> record, which exhibits a strong peak during MIS 11 (ca. 1 g/cm<sup>2</sup>/kyr), and relatively high values (> 0.25 g/cm<sup>2</sup>/kyr) during MIS 5, the Holocene and interglacials at the onset of the MPT (MIS 39–MIS 31). Throughout the rest of the record, CaCO<sub>3</sub> BMAR-corr are almost null, showing only intermittent spikes of less than 0.25 g/cm<sup>2</sup>/kyr during some terminations or in random intervals where opal BMAR-corr are always low (figure 5).

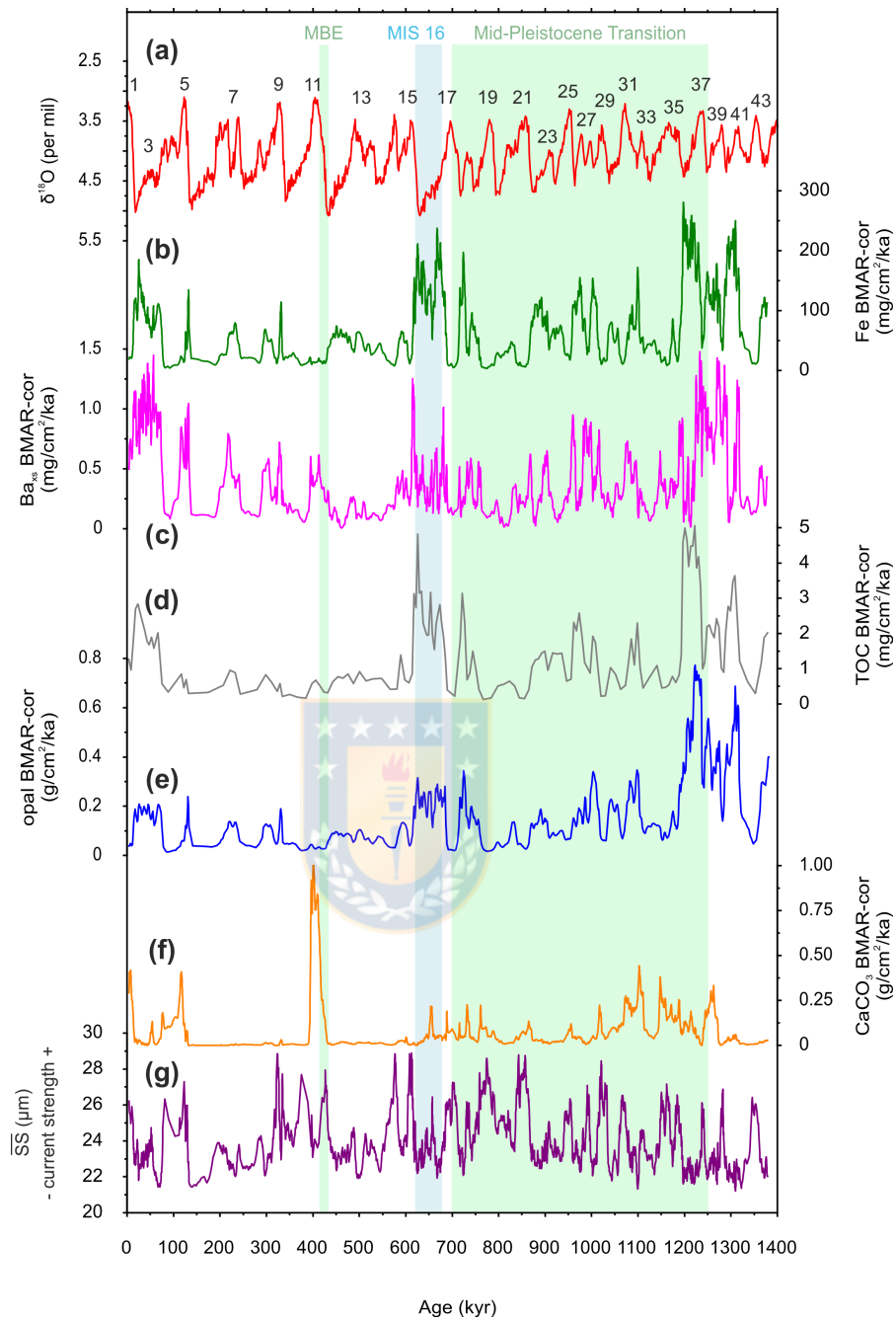


**Figure 5.** SE Pacific (PS97/093-2) stratigraphy-based mass accumulation rate corrected for syndepositional redistribution (BMAR-corr) of individual components compared to the evolution of the global ice volume (Lisiecki & Raymo, 2005), and bottom current strength fluctuations at core site (Toyos et al., 2020). **a:** LR04 benthic  $\delta^{18}\text{O}$  stack (Lisiecki & Raymo, 2005), numbers indicate interglacial Marine Isotope Stages; **b:** Fe BMAR-corr; **c:**  $\text{Ba}_{\text{xs}}$  BMAR-corr; **d:** TOC BMAR-corr; **e:** biogenic opal BMAR-corr; **f:**  $\text{CaCO}_3$  BMAR-corr; **g:** Changes in bottom current strength as indicated by the sortable silt record of site PS97/093-2. Vertical bars mark the Mid-



Pleistocene Transition (green), Mid-Brunhes Event (green), and Marine Isotope Stage 16 (blue).

## **5 Discussion (in prep)**

## **6 Conclusions (in prep)**

## **Acknowledgments**

This work was funded by the Alfred-Wegener-Institut Helmholtz-Zentrum für Polar- und Meeresforschung through its PACES-II Research programme. Additional support was provided by the Chilean oceanographic centers FONDAP-IDEAL (project number 1500003) and COPAS Sur-Austral (AFB170006) to CBL and MHT, and Lamont-Doherty Earth Observatory. MHT acknowledges support from scholarship CONICYT-PCHA/Doctorado Nacional/2016-21160454, Postgraduate Office of Universidad de Concepción, Red Clima Red (project number LPR163), and Doctorado MaReA. We thank the captain, crew and scientific party of R/V Polarstern for a successful PS97 cruise. We acknowledge A. Ávila for technical support at the Paleoceanography lab of Universidad de Concepción, R. Schwarz and M. Fleisher for assistance at Lamont-Doherty Earth Observatory, and S. Wiebe, R. Fröhlking and V. Schumacher for technical support at AWI.

## **References**

Anderson, R. F., Barker, S., Fleisher, M., Gersonde, R., Goldstein, S. L., Kuhn, G., Mortyn, P. G., Pahnke, K., & Sachs, J. P. (2014).

Biological response to millennial variability of dust and nutrient supply in the Subantarctic South Atlantic Ocean. *Philosophical Transactions of the Royal Society A: Mathematical, Physical and Engineering Sciences*, 372(2019). <https://doi.org/10.1098/rsta.2013.0054>

Bacon, M. P. (1984). Glacial to interglacial changes in carbonate and clay sedimentation in the Atlantic Ocean estimated from  $^{230}\text{Th}$  measurements. *Isotope Geoscience*, 2(2), 97–111.

Barker, S., Archer, D., Booth, L., Elderfield, H., Henderiks, J., & Rickaby, R. E. M. (2006). Globally increased pelagic carbonate production during the Mid-Brunhes dissolution interval and the  $\text{CO}_2$  paradox of MIS 11. *Quaternary Science Reviews*, 25(23–24), 3278–3293. <https://doi.org/10.1016/j.quascirev.2006.07.018>

Boyd, P., LaRoche, J., Gall, M., Frew, R., & McKay, R. M. L. (1999). Role of iron, light, and silicate in controlling algal biomass in subantarctic waters SE of New Zealand. *Journal of Geophysical Research: Oceans*, 104(C6), 13395–13408. <https://doi.org/10.1029/1999JC900009>

Chapman, C. C., Lea, M.-A., Meyer, A., Sallée, J.-B., & Hindell, M. (2020). Defining Southern Ocean fronts and their influence on biological and physical processes in a changing climate. *Nature Climate Change*, 10(3), 209–219. <https://doi.org/10.1038/s41558-020-0705-4>

Cheng, H., Lawrence Edwards, R., Shen, C.-C., Polyak, V. J., Asmerom, Y., Woodhead, J., Hellstrom, J., Wang, Y., Kong, X., Spötl, C., Wang, X., & Calvin Alexander, E. (2013). Improvements in  $^{230}\text{Th}$  dating,  $^{230}\text{Th}$  and  $^{234}\text{U}$  half-life values, and U–Th isotopic measurements by multi-collector inductively coupled plasma mass spectrometry. *Earth and Planetary Science Letters*, 371–372, 82–91. <https://doi.org/10.1016/j.epsl.2013.04.006>

Costa, K. M., Hayes, C. T., Anderson, R. F., Pavia, F. J., Bausch, A., Deng, F., Dutay, J. C., Geibert, W., Heinze, C., Henderson, G., Hillaire-Marcel, C., Hoffmann, S., Jaccard, S. L., Jacobel, A. W., Kienast, S. S., Kipp, L., Lerner, P., Lippold, J., Lund, D., ... Zhou, Y. (2020).  $^{230}\text{Th}$  Normalization: New Insights on an Essential Tool for Quantifying Sedimentary Fluxes in the Modern and Quaternary Ocean.

*Paleoceanography and Paleoclimatology*, 35(2), 1–36.  
<https://doi.org/10.1029/2019PA003820>

de Baar, H. J. W., Bathmann, U., Smetacek, V., Löscher, B. M., & Veth, C. (1995). Importance of iron for plankton blooms and carbon dioxide drawdown in the Southern Ocean. *Nature*, 373(6513), 412–415.  
<https://doi.org/10.1038/373412a0>

Durand, A., Chase, Z., Noble, T. L., Bostock, H., Jaccard, S. L., Kitchener, P., Townsend, A. T., Jansen, N., Kinsley, L., Jacobsen, G., Johnson, S., & Neil, H. (2017). Export production in the New-Zealand region since the Last Glacial Maximum. *Earth and Planetary Science Letters*, 469, 110–122. <https://doi.org/10.1016/j.epsl.2017.03.035>

Farmer, J. R., Hönisch, B., Haynes, L. L., Kroon, D., Jung, S., Ford, H. L., Raymo, M. E., Jaume-Seguí, M., Bell, D. B., Goldstein, S. L., Pena, L. D., Yehudai, M., & Kim, J. (2019a). Deep Atlantic Ocean carbon storage and the rise of 100,000-year glacial cycles. *Nature Geoscience*, 12(5), 355–360. <https://doi.org/10.1038/s41561-019-0334-6>

Farmer, Jesse R, Goldstein, S. L., Haynes, L. L., Hönisch, B., Kim, J., Pena, L., & Yehudai, M. (2019b). Data constraints on ocean-carbon cycle feedbacks at the mid-Pleistocene transition. *Past Global Changes Magazine*, 27(2). <https://doi.org/10.22498/pages.27.2.62>

Francois, R., Frank, M., Rutgers van der Loeff, M. M., & Bacon, M. P. (2004). 230Th normalization: An essential tool for interpreting sedimentary fluxes during the late Quaternary. *Paleoceanography*, 19(1), PA1018. <https://doi.org/10.1029/2003PA000939>

Frank, M., Gersonde, R., & Mangini, A. (1999). Sediment Redistribution, 230Thex- Normalization and Implications for the Reconstruction of Particle Flux and Export Paleoproductivity. In *Use of Proxies in Paleoceanography* (pp. 409–426). Springer Berlin Heidelberg. [https://doi.org/10.1007/978-3-642-58646-0\\_16](https://doi.org/10.1007/978-3-642-58646-0_16)

Gottschalk, J., Hodell, D. A., Skinner, L. C., Crowhurst, S. J., Jaccard, S. L., & Charles, C. (2018). Past Carbonate Preservation Events in the Deep Southeast Atlantic Ocean (Cape Basin) and Their Implications for Atlantic Overturning Dynamics and Marine Carbon Cycling.

*Paleoceanography and Paleoclimatology*, 33(6), 643–663.  
<https://doi.org/10.1029/2018PA003353>

Graham, R. M., De Boer, A. M., van Sebille, E., Kohfeld, K. E., & Schlosser, C. (2015). Inferring source regions and supply mechanisms of iron in the Southern Ocean from satellite chlorophyll data. *Deep-Sea Research Part I: Oceanographic Research Papers*, 104, 9–25.  
<https://doi.org/10.1016/j.dsr.2015.05.007>

Henley, S. F., Cavan, E. L., Fawcett, S. E., Kerr, R., Monteiro, T., Sherrell, R. M., Bowie, A. R., Boyd, P. W., Barnes, D. K. A., Schloss, I. R., Marshall, T., Flynn, R., & Smith, S. (2020). Changing Biogeochemistry of the Southern Ocean and Its Ecosystem Implications. *Frontiers in Marine Science*, 7 (July).  
<https://doi.org/10.3389/fmars.2020.00581>

Holden, P. B., Edwards, N. R., Wolff, E. W., Valdes, P. J., & Singarayer, J. S. (2011). The Mid-Brunhes Event and West Antarctic ice sheet stability. *Journal of Quaternary Science*, 26(5), 474–477.  
<https://doi.org/10.1002/jqs.1525>

Honjo, S. (2004). Particle export and the biological pump in the Southern Ocean. *Antarctic Science*, 16(4), 501–516.  
<https://doi.org/10.1017/S0954102004002287>

Jaccard, S. L. ., Hayes, C. T. ., Martínez-García, A. ., Hodell, D. A. ., Anderson, R. F. ., Sigman, D. M. ., & Haug, G. H. . (2013). Two Modes of Change in Southern Ocean Productivity Over the Past Million Years. *Science*, 339(6126), 1419–1423. <https://doi.org/10.1126/science.1227545>

Jaccard, S. L., Hayes, C. T., Martínez-García, A., Hodell, D. A., Anderson, R. F., Sigman, D. M., & Haug, G. H. (2013). Supplementary materials: Two modes of change in Southern Ocean productivity over the past million years. *Science*, 339(6126), 1419–1423.  
<https://doi.org/10.1126/science.1227545>

Kienast, S. S., Kienast, M., Mix, A. C., Calvert, S. E., & François, R. (2007). Thorium-230 normalized particle flux and sediment focusing in the Panama Basin region during the last 30,000 years. *Paleoceanography*, 22(2), 1–19. <https://doi.org/10.1029/2006PA001357>

Kohfeld, K. E., Le Quéré, C., Harrison, S. P., & Anderson, R. F. (2005). Role of marine biology in glacial-interglacial CO<sub>2</sub> cycles. *Science*, 308(5718), 74–78. <https://doi.org/10.1126/science.1105375>

Kopczynska, E. E., Dehairs, F., Elskens, M., & Wright, S. (2001). Phytoplankton and microzooplankton variability between the Subtropical and Polar Fronts south of Australia: Thriving under regenerative and new production in late summer. *Journal of Geophysical Research: Oceans*, 106(C12), 31597–31609. <https://doi.org/10.1029/2000JC000278>

Lamy, F., Gersonde, R., Winckler, G., Esper, O., Jaeschke, A., Kuhn, G., Ullermann, J., Martinez-Garcia, A., Lambert, F., & Kilian, R. (2014). Increased Dust Deposition in the Pacific Southern Ocean During Glacial Periods. *Science*, 343(6169), 403–407. <https://doi.org/10.1126/science.1245424>

Lamy, Frank. (2016). The expedition PS97 of the research vessel POLARSTERN to the Drake Passage in 2016. In *Reports on Polar and Marine Research*. [https://doi.org/10.2312/BzPM\\_0702\\_2016](https://doi.org/10.2312/BzPM_0702_2016)

Lamy, Frank, Arz, H. W., Kilian, R., Lange, C. B., Lembke-Jene, L., Wengler, M., Kaiser, J., Baeza-Urrea, O., Hall, I. R., Harada, N., & Tiedemann, R. (2015). Glacial reduction and millennial-scale variations in Drake Passage throughflow. *Proceedings of the National Academy of Sciences of the United States of America*, 112(44), 13496–13501. <https://doi.org/10.1073/pnas.1509203112>

Lawrence, K. T., Sigman, D. M., Herbert, T. D., Riihimaki, C. A., Bolton, C. T., Martinez-Garcia, A., Rosell-Mele, A., & Haug, G. H. (2013). Time-transgressive North Atlantic productivity changes upon Northern Hemisphere glaciation. *Paleoceanography*, 28(4), 740–751. <https://doi.org/10.1002/2013PA002546>

Lisiecki, L. E., & Raymo, M. E. (2005). A Pliocene-Pleistocene stack of 57 globally distributed benthic  $\delta^{18}\text{O}$  records. *Paleoceanography*, 20(1). <https://doi.org/10.1029/2004PA001071>

Marcantonio, F., Lyle, M., & Ibrahim, R. (2014). Particle sorting during sediment redistribution processes and the effect on 230 Th-

normalized mass accumulation rates. *Geophysical Research Letters*, 41(15), 5547–5554. <https://doi.org/10.1002/2014GL060477>

Martínez-García, A., Rosell-Melé, A., Geibert, W., Gersonde, R., Masqué, P., Gaspari, V., & Barbante, C. (2009). Links between iron supply, marine productivity, sea surface temperature, and CO<sub>2</sub> over the last 1.1 Ma. *Paleoceanography*, 24(1), n/a-n/a. <https://doi.org/10.1029/2008PA001657>

Martínez-García, A., Rosell-Melé, A., Jaccard, S. L., Geibert, W., Sigman, D. M., & Haug, G. H. (2011). Southern Ocean dust-climate coupling over the past four million years. *Nature*, 476(7360), 312–315. <https://doi.org/10.1038/nature10310>

Matsumoto, K., Sarmiento, J. L., & Brzezinski, M. A. (2002). Silicic acid leakage from the Southern Ocean: A possible explanation for glacial atmospheric pCO<sub>2</sub>. *Global Biogeochemical Cycles*, 16(3), 5-1-5–23. <https://doi.org/10.1029/2001GB001442>

McCave, I. N., & Hall, I. R. (2006). Size sorting in marine muds: Processes, pitfalls, and prospects for paleoflow-speed proxies. *Geochemistry, Geophysics, Geosystems*, 7(10). <https://doi.org/10.1029/2006GC001284>

Meredith, M. P., Woodworth, P. L., Chereskin, T. K., Marshall, D. P., Allison, L. C., Bigg, G. R., Donohue, K., Heywood, K. J., Hughes, C. W., Hibbert, A., Hogg, A. M., Johnson, H. L., Jullion, L., King, B. A., Leach, H., Lenn, Y. D., Maqueda, M. A. M., Munday, D. R., Garabato, A. C. N., Sprintall, J. (2011). Sustained monitoring of the Southern Ocean at Drake Passage: past achievements and future priorities. *Reviews of Geophysics*, 49, 8755–1209. <https://doi.org/10.1029/2010RG000348.1>

Orsi, H., Whitworth, T., & Nowlin, W. D. (1995). On the meridional extent and fronts of the Antarctic Circumpolar Current. *Deep Sea Research*, 42(5), 641–673. [https://doi.org/10.1016/0967-0637\(95\)00021-W](https://doi.org/10.1016/0967-0637(95)00021-W)

Paillard, D., Labeyrie, L., & Yiou, P. (1996). Macintosh Program performs time-series analysis. *Eos, Transactions American Geophysical Union*, 77(39), 379–379. <https://doi.org/10.1029/96EO00259>

Paparazzo, F. E. (2016). Tendencias espaciales y temporales en la distribución de macronutrientes en aguas superficiales del Pasaje Drake. *Ecología Austral*, 26(1), 027–039. <https://doi.org/10.25260/EA.16.26.1.0.142>

Renault, A., Provost, C., Sennéchaël, N., Barré, N., & Kartavtseff, A. (2011). Two full-depth velocity sections in the Drake Passage in 2006—Transport estimates. *Deep Sea Research Part II: Topical Studies in Oceanography*, 58(25–26), 2572–2591. <https://doi.org/10.1016/j.dsr2.2011.01.004>

Rigual-Hernández, A. S., Trull, T. W., Bray, S. G., Cortina, A., & Armand, L. K. (2015). Latitudinal and temporal distributions of diatom populations in the pelagic waters of the Subantarctic and Polar Frontal zones of the Southern Ocean and their role in the biological pump. *Biogeosciences*, 12(18), 5309–5337. <https://doi.org/10.5194/bg-12-5309-2015>

Saavedra-Pellitero, M., Baumann, K. H., Lamy, F., & Köhler, P. (2017). Coccolithophore variability across Marine Isotope Stage 11 in the Pacific sector of the Southern Ocean and its potential impact on the carbon cycle. *Paleoceanography*, 32(8), 864–880. <https://doi.org/10.1002/2017PA003156>

Sigman, D. M., Hain, M. P., & Haug, G. H. (2010). The polar ocean and glacial cycles in atmospheric CO<sub>2</sub> concentration. *Nature*, 466(7302), 47–55. <https://doi.org/10.1038/nature09149>

Suman, D. O., & Bacon, M. P. (1989). Variations in Holocene sedimentation in the North American Basin determined from 230Th measurements. *Deep Sea Research Part A, Oceanographic Research Papers*, 36(6), 869–878. [https://doi.org/10.1016/0198-0149\(89\)90033-2](https://doi.org/10.1016/0198-0149(89)90033-2)

Thöle, L. M., Amsler, H. E., Moretti, S., Auderset, A., Gilgannon, J., Lippold, J., Vogel, H., Crosta, X., Mazaud, A., Michel, E., Martínez-García, A., & Jaccard, S. L. (2019). Glacial-interglacial dust and export production records from the Southern Indian Ocean. *Earth and Planetary Science Letters*, 525. <https://doi.org/10.1016/j.epsl.2019.115716>

Toyos, M. H., Lamy, F., Lange, C. B., Lembke-Jene, L., Saavedra-Pellitero, M., Esper, O., & Arz, H. W. (2020). Antarctic Circumpolar Current Dynamics at the Pacific Entrance to the Drake Passage Over the Past 1.3 Million Years. *Paleoceanography and Paleoclimatology*, 35(7), 1–20. <https://doi.org/10.1029/2019PA003773>

Toyos, M. H., Winckler, G., Arz, H. W., Lembke-Jene, L., Lange, C. B., Kuhn, G., & Lamy, F. (2021). Variations in export production, lithogenic sediment transport and iron fertilization in the Pacific sector of the Drake Passage over the past 400 ka. *Climate of the Past Discussions*, 2021, 1–37. <https://doi.org/10.5194/cp-2021-85>

Tréguer, P., & Jacques, G. (1992). Dynamics of nutrients and phytoplankton, and fluxes of carbon, nitrogen and silicon in the Antarctic Ocean. *Polar Biology*, 12(2), 149–162. <https://doi.org/10.1007/BF00238255>

Turekian, K. K., & Wedepohl, K. H. (1961). Distribution of the Elements in Some Major Units of the Earth's Crust. *GSA Bulletin*, 72(2), 175–192.

Van Bennekom, A., Berger, G., Van der Gaast, S., & de Vries, R. T. (1988). Primary productivity and the silica cycle in the Southern Ocean (Atlantic sector). *Palaeogeography, Palaeoclimatology, Palaeoecology*, 67(1–2), 19–30. [https://doi.org/10.1016/0031-0182\(88\)90120-4](https://doi.org/10.1016/0031-0182(88)90120-4)

Wu, S., Lembke-Jene, L., Lamy, F., Arz, H. W., Nowaczyk, N., Xiao, W., Zhang, X., Hass, H. C., Titschack, J., Zheng, X., Liu, J., Dumm, L., Diekmann, B., Nürnberg, D., Tiedemann, R., & Kuhn, G. (2021). Orbital- and millennial-scale Antarctic Circumpolar Current variability in Drake Passage over the past 140,000 years. *Nature Communications*, 12(1), 3948. <https://doi.org/10.1038/s41467-021-24264-9>

Yin, Q. Z., & Berger, A. (2012). Individual contribution of insolation and CO<sub>2</sub> to the interglacial climates of the past 800,000 years. *Climate Dynamics*, 38(3–4), 709–724. <https://doi.org/10.1007/s00382-011-1013-5>



## 5. DISCUSSION/ DISCUSIÓN

This thesis aims to reconstruct fluctuations in the intensity of ACC flow and to improve our understanding of past export production in the subantarctic SE Pacific over the past ca.1.3 Myr. To assess a comprehensive paleoenvironmental reconstruction and its paleoclimatic implications at different timescales, we first compare our current strength reconstruction to the few existing records in the DP area and with the other two ACC current strength reconstructions that extend beyond 500 ka in the SO (section 5.1). Secondly, we briefly debate in section 5.2 how the fluctuations in ACC flow might have affected the mass accumulation rates at site PS97/093. A further focus is to enhance our understanding of the basic mechanisms that control export production at glacial-interglacial timescales and the processes that could trigger such oscillations (section 5.3). Finally, in section 5.4, we examine if the variations in current strength and productivity are linked to the Earth's climate fundamental changes across the MPT and the MBE.

### **5.1. Glacial-Interglacial changes in ACC flow strength and its global implications**

The new high-resolution current strength record from the SAZ of the Pacific entrance to the DP presented in chapter 1 (Toyos et al., 2020)

shows a consistent pattern of glacial reduction in near-bottom flow speed (approximately 6% overall and 16% when considering major shifts, based on the sortable silt proxy, figure 4 of chapter 1) during the last 1.3 Ma. Since oceanographic observations and models hint that one of the driving forces that control the strength of the ACC is the position of the SWW belt (Völker & Köhler, 2013), our record is consistent with proxy reconstruction of the expansion/contraction and thus strength of the SWW belt in the southern Chilean margin, that shows latitudinally extended and somewhat reduced winds during colder intervals (Kohfeld et al., 2013; Lamy et al., 2010). If we take winter as an analog for glacial periods in the past, this might indicate that our reported glacial reduction is linked with a weakening and northward extension of the SWW belt (figure 5.1).

Furthermore, our current strength reconstruction largely agrees with other LGM/Holocene reconstructions from the Chilean and Argentinian continental margins that also show a glacial (interglacial) reduction (increase) in ACC strength (Lamy et al., 2015; Roberts et al., 2017, figure 5 of chapter 1). The lower LGM current strength could be the product of a northward shift of the SO frontal system relative to its current position such that the SAF did not extend through the DP, but instead was truncated by South America (Roberts et al., 2017). We suggest that the

hypothesis of a northward shift during the LGM happened during most of the glacials during the last 1.3 Ma. Therefore, our observed variations in current strength might also be linked to the northward shift of the SAF during glacial intervals, locating the study site south of the strongest ACC flow in the vicinity of the SAF (figure 5.1). In order to get a full picture of the DP current strength fluctuations at glacial/interglacial timescales, we compared the subantarctic records mentioned above with other LGM/Holocene deep cores retrieved along a transect in the Scotia Sea (McCave et al., 2014). Overall, all cores located in the vicinity of the SO fronts show a Holocene increase, being much higher in those located in the SAZ close to the SAF, where one half of the total modern DP throughflow transport occurs (Koenig et al., 2016). Thus, in the geographic constriction of the DP, we postulate that the consequence of a prominent subantarctic glacial reduction in the ACC flow together with an expected glacially extended sea ice zone is a reduction in the inflow of CDW into the Atlantic, which could have affected the strength of the global MOC at timescales before the last glacial (figure 5.1). This shortfall in the supply of deep water to the Atlantic basin could have been compensated by a strong recirculation within the South Pacific causing a stronger South Pacific Gyre (Lamy et al., 2015).

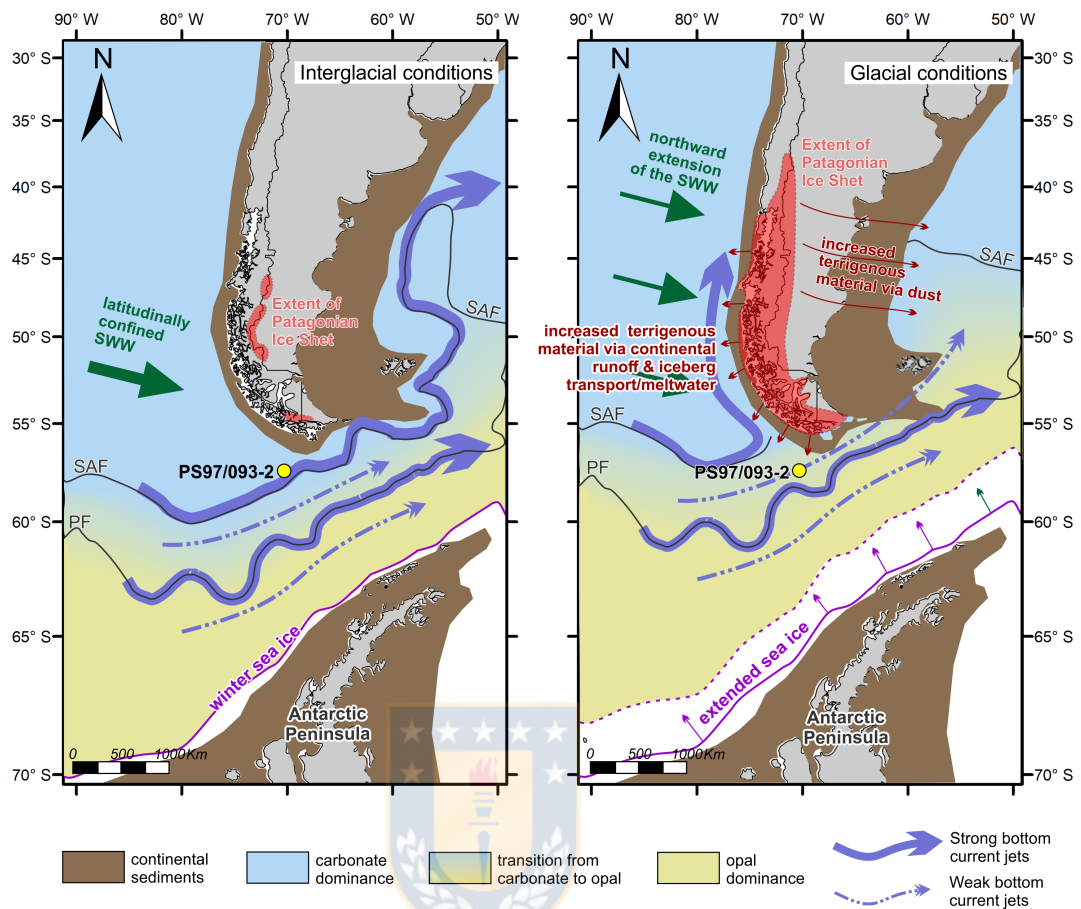


**Figure 5.1** Scheme of the hypothesized interglacial (left) and glacial (right) conditions in the Drake Passage area based on previous studies and the new paleoceanographic records presented in this thesis. Black lines indicate the expected Subantarctic Front (SAF) and Polar Front (PF) positions in each scenario. Note that we use the modern ACC front position from Orsi et al. (1995) for interglacial stages, and for glacials, we projected the Last Glacial position proposed by Roberts et al. (2017). Blue arrows show the ACC frontal jets; Red shadow areas indicate the current extension of the Patagonian and Cordillera Darwin Icefields (left) and the Patagonian Ice Sheet during the last glacial (right, taken from Glasser et al. (2008)). Purple lines mark the average modern winter sea ice position (Comiso et al., 2003). Yellow dots indicate the location of core PS97/093-2.

On the other hand, the consistent pattern of higher near-bottom current speeds during interglacials in the DP area contrasts with the 1.2 Ma record from ODP Site 1123 in the southwest Pacific east of New Zealand (Hall et al., 2001) and with a 500-ka long ACC record from the

subantarctic Indian Ocean sector (Mazaud et al., 2010). The latter is based on variations in size and abundance of magnetic grains and therefore, caution in the interpretation of this record is advised since, in addition to current strength fluctuations, variations in magnetic properties could also reflect changes in bacterial production, ice-rafted debris input, and the source of the magnetic minerals (Channell et al., 2016). If we accept that the changes in the abundance of magnetic grains studied by Mazaud et al. (2010) reflect current strength fluctuations, both records reflect faster ACC flow during glacials, and largely agree with the general view of glacial intensification of atmospheric ocean circulation of the SO (Lynch-Stieglitz et al., 2016; Toggweiler et al., 2006). However, our new record shows that the glacial intensification of the subantarctic ACC in the Indian Ocean and the Pacific SW did not extend to the SE Pacific and the DP, and that the subantarctic ACC circulation pattern has not been uniform in space, varying along its circumpolar path. In this regard, in chapter 1 (Toyos et al., 2020) we provide evidence that current strength fluctuations were out of phase between the eastern (core PS97/093-2) and western (ODP1123) Pacific over the past 1.2 Ma. (figure 8 of chapter 1). Thus, a weaker supply of deep water along the DP and into the Atlantic Ocean during glacials corresponds to an enhanced flow of the SW Pacific

DWBC. The disparity between both records might be also responding to frontal movements. Whereas our record in the SE Pacific suggests northward shifts of the SAF during glacials and thus a reduction in DP throughflow, such northward migration in the SW Pacific would have brought the ACC closer to Site 1123 and reinforced the flow of DWBC, explaining the strong glacial bottom current recorded (Hall et al., 2001).

## **5.2. Sedimentation patterns related to near-bottom current speeds.**

As indicated in chapter 1, our study area is strongly influenced by highly variable current strengths on glacial-interglacial timescales (Toyos et al., 2020, and references therein). As a result, the dynamic near-bottom water circulation of the ACC led to frequent syndepositional redistribution of sediment on the seafloor, as evidenced in core PS97/093-2. The latter implies that the accumulation rates of laterally redistributed sediments are often larger (smaller) than the fluxes of material sinking from the overlying surface waters, leading to sediment focusing (winnowing), respectively (Francois et al., 2004).

The results presented in chapter 2 (Toyos et al., accepted) indicate that winnowing occurs at our core site, during intervals with relatively low current strengths (mainly during glacials) whereas focusing occurs during interglacials characterized by rather high near-bottom flow (figure 4 of

chapter 2). Since our core has experienced strong grain size fluctuations over time, we suggest (in chapter 2) that this counterintuitive pattern is most likely due to a loss of flocculation and cohesive effects of the fine sediment fraction under relatively slow bottom currents in a generally fine-grained sediment. On the other hand, strong currents might have caused a gradual mobilization of more and more coarse-grained material that had accumulated in certain areas, resulting in a coarser grained focusing at our site.

The pattern of highly variable focusing/winningning at site PS97/093 might have some implications in the i) inferred current speeds based on the sortable silt measurements; ii)  $^{230}\text{Th}$ -derived vertical fluxes during extreme winnowed intervals, because of a preferential removal of the  $^{230}\text{Th}$ -rich fine grains, and iii) bulk stratigraphy-based mass accumulation rates reliability.

Firstly, as shown in chapter 1 (Toyos et al., 2020), variations in  $\overline{SS}$  and  $SS\%$  at our site correlate positively, suggesting that near-bottom currents are the principal driver for changes in the 10–63 $\mu\text{m}$  grain size fraction (McCave & Hall, 2006), supporting the reliability of  $\overline{SS}$  as a current speed proxy. Therefore, we suggest that the documented sediment focusing might have triggered the deposition of coarser grained sediments

(>63 $\mu\text{m}$ ). In contrast, during intervals characterized by winnowing, it is likely that part of the finer fraction (<10 $\mu\text{m}$ ) has been moved laterally.

Secondly, as a result of the winnowing, it might happen that deep-ocean currents laterally advect particles that contain excess of  $^{230}\text{Th}$ , which is preferentially accumulated in the fine fraction (Marcantonio et al., 2014). In this regard, the extreme winnowing during MIS 6 ( $\Psi=0.08$ ) might have led to a deficit of  $^{230}\text{Th}$ , causing an overestimation of the particle rain rate (Chapter 2, Toyos et al., accepted). Except for this time interval, the rest of the record does not display extreme winnowing and focusing factors exceed  $\Psi>0.24$ ; therefore,  $^{230}\text{Th}_{\text{xs}}$ -normalized accumulation rates are robust (figure 4 of chapter 2).

Thirdly, as a result of frequent syndepositional redistribution at our core site, BMARs are strongly biased in intervals with highest focusing and pronounced winnowing, and the resulting paleoceanographic interpretations may suffer from substantial errors. This issue is addressed in chapters 2 and 3. It is well known that such errors are substantially higher than those associated with  $^{230}\text{Th}$ -derived mass accumulation rates (Costa et al., 2020). Consequently, in this thesis, the paleoproductivity reconstructions younger than 400,000 years are primarily based on the  $^{230}\text{Th}$ -derived mass accumulation rates, which allows for the



quantification of lateral sediment redistribution and accurate vertical rain rates (Costa et al., 2020; Suman & Bacon, 1989). This method has been widely used in other SAZ productivity reconstructions (e.g., Anderson et al., 2014; Durand et al., 2017; Lamy et al., 2014; Martínez-García et al., 2009; Thöle et al., 2019). However, the applicability of the  $^{230}\text{Th}$  constant flux proxy is limited to the last 500 kyr due to its half-life ( $t_{1/2}^{230}\text{Th} = 75.5$  kyr; Chen et al., 2013). Thus, for the interval beyond the applicability of the  $^{230}\text{Th}$ , and given the good correlation between current strengths ( $\overline{SS}$ ) and focusing factors ( $\Psi$ ), in Manuscript 3 (in prep.) we corrected BMARs for syndepositional redistribution beyond the 400 kyr ( $\text{BMAR}_{\text{corr}}$ ). As a result, an evaluation of long-term changes in productivity and how they relate to current strength and main climatic events was possible. The results are presented in chapter 3, and briefly discussed in section 5.4.

### **5.3. Glacial-Interglacial productivity pattern based on $^{230}\text{Th}_{\text{xs}}$ -normalized mass accumulation rates**

In chapter 2 (Toyos et al., accepted) we evaluate the basic mechanisms that condition the export production response at our core site at glacial/interglacial timescales covering the last 400,000 years. We show that the multiple proxies of export production ( $\text{Ba}_{\text{xs}}$ , TOC and opal) generally co-vary, and vary in parallel with lithogenic and Fe MARs; all

proxies are higher during most glacials and lower during interglacials (figure 3 of chapter 2). In contrast, CaCO<sub>3</sub> MARs are high only during strong interglacials (Holocene, MIS 5 and MIS 11, PAGES, 2016; figure 3 of chapter 2).

It is important to consider that the accumulation rates of each of these components in the sediments is controlled by specific factors, and before assessing export production changes, it is necessary to take into account the limitations that each proxy might have at our core location. In this regard, dissolution and poor preservation conditions can affect the interpretation of reconstructed CaCO<sub>3</sub> MAR. Sediment core PS97/093-2 is bathed in CDW, which is characterized by relatively low [CO<sub>3</sub><sup>2-</sup>], being undersaturated with respect to calcium, therefore promoting carbonate dissolution (Key et al., 2004). Furthermore, the core was retrieved slightly above the water depth of the lysocline, which would shoal at least 0.5 km during glacial stages (Howard & Prell, 1994). Thus, near-zero CaCO<sub>3</sub> MAR values likely indicate carbonate dissolution rather than low export production. Limitations associated with poor preservation could have also affected our TOC MARs, given the water depth at which core PS97/093-2 was retrieved (3850 m water depth) and because preservation of organic carbon in sediments is globally scarce (Berger et al., 1989). On the other

hand, variable dissolution in the water column does not significantly affect opal burial in the SO (Chase et al., 2015), suggesting that opal MAR might be only marginally affected by preservation changes, thus providing valid information on past diatom productivity changes (Bradtmiller et al., 2009; Sprenk et al., 2013).  $Ba_{xs}$  MAR also has relatively high preservation rates (*ca.* 30% in sediments under oxic conditions, Dymond, 1992). Since  $Ba_{xs}$  rain rates are not specific to any plankton group and relate to total carbon export (Paytan, 2009), the good correspondence between  $Ba_{xs}$  and opal MARs implies that most of the glacial export production was fueled by diatoms in the study area.

### **5.3.1. Role of Fe as a driver of export production**

As mentioned above, lithogenic, Fe,  $Ba_{xs}$ , TOC and opal MARs increase in parallel mostly during glacials of the past 400 kyr (Chapter 2, Toyos et al., accepted), suggesting that an intensification of Fe supply to our core location could have alleviated the iron limitation observed in the region (Paparazzo, 2016). Hence, it is likely that at the Pacific entrance of the DP, diatoms received sufficient iron to fuel silica consumption. Conventionally, iron addition during glacial periods in other open ocean subantarctic cores has been primarily attributed to dust input (Alfredo Martínez-García et al., 2011; Shoenfelt et al., 2018). However, the glacial

peaks of lithogenic MAR in core PS97/093-2 were one order of magnitude higher than other reconstructions from the open Pacific, Atlantic and Indian SAZ (Anderson et al., 2014; Lamy et al., 2014; Martínez-García et al., 2009; Thöle et al., 2019; figure 5 of chapter 2). Since a strong contribution of dust is not expected in the study area due to the prevailing SWW (Wengler et al., 2019; Wu et al., 2019), we hypothesize that the comparatively higher lithogenic MARs are due to the proximity of our site to southern South America, which could have acted as a substantial source of fluvially-derived and glaciogenic sediments at glacial times, when Patagonia was covered by an extended PIS (e.g. Davies et al., 2020; Glasser et al., 2008; Rabassa et al., 2011; figure 5.1). This assumption is supported by i) the good correspondence between local glaciations and increases in lithogenic and Fe MARs at our core location; ii) higher ice-rafted debris contents at the Pacific entrance of the Strait of Magellan (core MD07-3128, *ca.* 620 km away from core PS97/093-2) linked to advances of the PIS (Caniupán et al., 2011); and iii) increases in Fe concentrations on the Chilean continental margin (ODP Site 1233) linked to PIS advances (Kilian & Lamy, 2012; Lamy et al., 2010). Previous studies suggest that physical weathering increases the labile primary Fe (II) content of sediments that is associated with phytoplankton fertilization

(Shoenfelt et al., 2017, 2019). Since our core site is relatively proximal to continental sources that are dominated by physical weathering, we would expect that the Fe supply delivered to site PS97/093 might have always been relatively enriched in bio-available Fe. Thus, advances of the PIS during glacial intervals (e.g. Rabassa, 2008; Rabassa et al., 2011) would have increased substantially the portion of bioavailable Fe that reached our study area, alleviating Fe limitation (figure 5.1).

### **5.3.2. Impact of frontal shifts and $\text{Si}(\text{OH})_4$ availability on the export production patterns**

In the study area, the oceanographic fronts act as barriers, and represent the limits between geochemical provinces (Chapman et al., 2020; Papparazzo, 2016). For example, the PF is associated with the northern expression of the silicate front, indicating the geographical boundary between silicate-poor waters to the north and silicate-rich waters to the south of it (Freeman et al., 2018, 2019). As discussed in section 5.1, we hypothesized a northward shift of the SO frontal system during glacials of the last 1.3 Ma at our core location. This would have positioned our core PS97/093-2 south of the SAF and closer to Si-rich waters. In contrast, during interglacials the position of the frontal system might have been similar to the present-day, and therefore the core would have been placed

in an environment where diatom production may be co-limited by silicic acid and iron, favoring a transition from diatoms to coccolithophores (Saavedra-Pellitero et al., 2019). Hence, in this thesis it is shown that re-alignments of the SO fronts have a direct impact on export production patterns at the core site, where enhanced diatom production during glacials represents a response to increased  $\text{Si(OH)}_4$  supply that was exported across the PFZ compared to interglacials (Chase et al., 2015; Freeman et al., 2019; figure 5.1). In chapter 2 (Toyos et al., accepted) we also postulate that the glacial relief in  $\text{Si(OH)}_4$  limitation might have also been favored by a reduction of the diatom Si:N uptake ratio under Fe replete conditions, as discussed in section 5.3.1 (Franck et al., 2000; Matsumoto et al., 2002).

Even though export production was enhanced during glacial times at our core site, the spatial comparison with previously published records from different locations in the SAZ suggest that the impact on export production when Fe limitation is relieved, is lower in the SE Pacific than in other SAZ sectors (figure 6 of chapter 2). Thus, in chapter 2 (Toyos et al., accepted), we support the idea that the relatively lower export production values seen in our record when compared to the Atlantic and Indian sectors, may relate to complete consumption of silicic acid.

## **5.4. Orbital scale fluctuation in current strength and productivity over the past 1.3 Ma.**

The results presented in Toyos et al. (2020) and in chapter 3 suggest that PS97/093 site has been affected by the Earth's major climate changes over the past 1.3 Ma.

### **5.4.1. Changes across the Mid-Pleistocene Transition in the Drake Passage**

Glacial-interglacial fluctuations in ACC strength at the Pacific entrance of the DP largely follow the LR04 stack (Lisiecki & Raymo, 2005), and consequently the well-known global climate changes and variations in ice volume (figure 7 of chapter 1). Our generated  $\overline{SS}$  record shows a dominance of the ca. 41-kyr cycles in the early part of the record (1.3 Ma to 850 ka.; MIS 21) followed by an increase of the spectral power of the ca. 100-kyr cycles across the MPT into the middle and late Pleistocene (from MIS 21 to the Holocene).

It has been suggested that changes in the biological pump (specifically a global increase in the primary productivity) were linked to atmospheric CO<sub>2</sub> drawdown that acted as a forcing mechanism for the glacial climatic cooling that defines the MPT (Chalk et al., 2017).

According to Martínez-García et al. (2011), in the Subantarctic South Atlantic, the rise in productivity related to dust-borne Fe fertilization increased around the beginning of the MPT (*ca.* 1.25 Ma ago, figure 5.2), and then gradually over the MPT, as a consequence of larger ice sheets. This timing differs from PS97/093 site (figure 5.2), suggesting that our core site might not have contributed significantly to the decline of atmospheric CO<sub>2</sub> associated with the MPT via dust-borne Fe fertilization.

Nevertheless, the increase in Fe and productivity from *ca.* 1.35 to 1.2 Ma at our core location, likely produced by local factors (either by glacial weathering associated with an extreme intensive PIS or by increased erosion surfaces caused by the culmination of the uplift of the Southern Patagonian Andes; Rabassa & Clapperton, 1990; Singer et al., 2004), in conjunction with the worldwide non-concurrent increased productivity during the onset of the MPT (Diester-Haass et al., 2018), may have played a role in the CO<sub>2</sub> sequestration in the deep ocean *via* enhanced biological CO<sub>2</sub> uptake.

Apart from an increase in the ocean biological productivity, another proposed pathway that might explain the atmospheric CO<sub>2</sub> drawdown during the MPT is a weaker deep ocean circulation. Related to this point, and based on neodymium isotopes, a major disruption of the MOC across



the MPT (between MIS 25 and 21) has been documented causing enhanced deep ocean carbon storage (Farmer et al., 2019b). Our ACC strength record of the entrance of the DP shows a strong reduction in the amplitude of the cycles between MIS 25 and MIS 21 (e.g., figure 7 of chapter 1). This evidence, together with the peaks in the pyrite records from Southern Ocean sites ODP 1123 (North Chatham Drift) and ODP 1090 (South Atlantic), which have been interpreted as an indicator of stagnant deep water circulation (Diester-Haass et al. (2018)), supports the idea of a sluggish MOC during the MPT (Pena & Goldstein, 2014).

It has been shown that a reduced MOC during the MPT corresponds to abrupt increases in deep-water corrosivity, as indicated by a decrease in  $\Delta[\text{CO}_3^{2-}]$  (Farmer et al., 2019b). At site PS97/093, we observe a change in the  $\text{CaCO}_3$   $\text{BMAR}_{\text{corr}}$  pattern at MIS 28 (*ca.* 1 Ma. Ago; figure 5 of chapter 3). Before that time, carbonates showed a consistent pattern of glacial/interglacial variability; interglacial peaks matched with increases in  $\text{Ba}_{\text{xs}}$ , suggesting enhanced carbonate export production during such intervals. However, from *ca.* 1 Ma ago to the MBE,  $\text{CaCO}_3$   $\text{BMAR}_{\text{corr}}$  only peaks in the shape of short-lived spikes, and with no associated peaks in any of the other proxies of export production, suggesting that the absence

or presence of carbonates primarily represent changes in the depth of the lysocline (figure 5 of chapter 3).

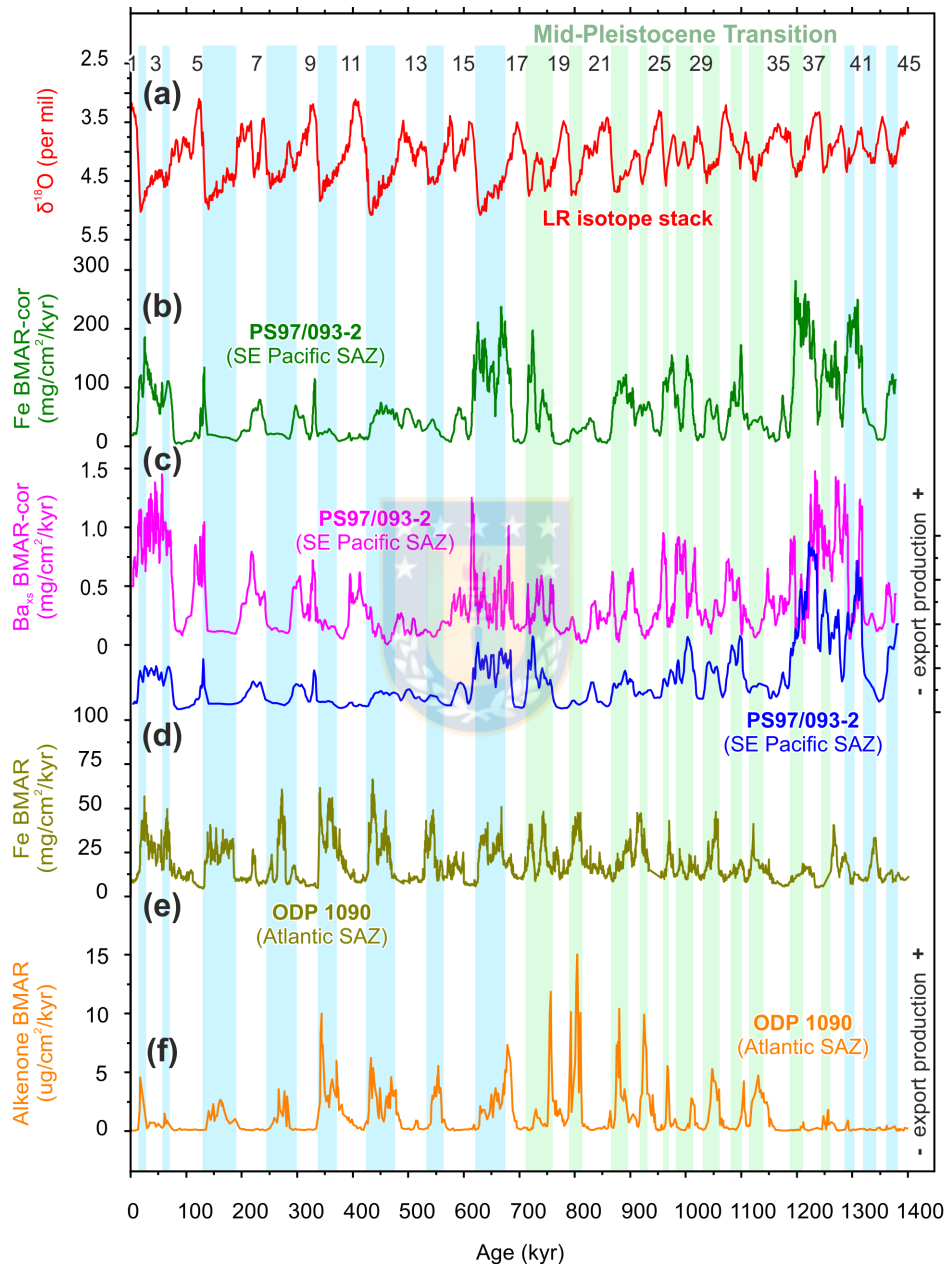


**Figure 5.2.** Accumulation rates of Fe, and export production in the SAZ, at the SE Pacific (core PS97/093-2) and in the Atlantic (ODP 1090) sectors. **a:** LR04 benthic  $\delta^{18}\text{O}$  stack (Lisiecki & Raymo, 2005), numbers indicate interglacial Marine Isotope Stages; **b:** Fe BMAR-corr (core PS97/093-2, this study); **c:**  $\text{Ba}_{\text{xs}}$  BMAR-corr (core PS97/093-2, this study); **d:** biogenic opal BMAR-corr (core PS97/093-2, this study); **e:** accumulation rates of Fe (ODP 1090; Martínez-García et al., 2011); **f:** accumulation

rates of  $C_{37}$  Alkenone (ODP 1090; Lawrence et al., 2013; Martínez-García et al., 2009). Vertical blue bars indicate Lisiecki and Raymo glacial stages, and glacials from the Mid Pleistocene Transition are marked in green.

#### **5.4.2. Ocean circulation and productivity during the 100-Kyr world and the Mid-Brunhes event**

Our current strength reconstruction indicates that the emergence of the first high-amplitude 100-kyr glacial cycle took place during interglacial MIS 21 (figure 7 of chapter 1). However, the influence of the 41-kyr cycles remain during all the space of time that encompasses our core, in agreement with a recent work that found a persistent influence of the obliquity cycle in glacial terminations since the MPT (Bajo et al., 2020). Our sortable silt record also shows that the vigor of the interglacial near-bottom circulation during the so-called 100-kyr world was higher than before, suggesting a change in the southward position of the SO fronts (Robinson et al., 2019), and/or an increase in the variability of deep water circulation with well-ventilated interglacials and poorly ventilated glacials (Venz & Hodell, 2002; figure 7 of chapter 1).

During the 100-kyr world, the amplitude of the orbital scale changes in productivity in our core largely follows the global strength of glacial/interglacial periods of the last 700,000 years (figure 5 of chapter 3). Increased export production (opal,  $Ba_{xs}$ , TOC) and Fe accumulation rates are seen during the globally strong glacial MIS 16 (Lang & Wolff,

2011), whereas carbonate production/preservation is greatest during the strong interglacials MIS 11, MIS 5, and the Holocene. In contrast, export production displays a marked reduction in amplitude during weak glacials (e.g., MIS 14) and interglacials (MIS 13, 15, and 17) (Jaccard et al., 2013; Lang & Wolff, 2011).

The substantial increase in CaCO<sub>3</sub> accumulation rates during MSI 11 in our core coincides with an ooze of *Gephyrocapsa caribbeanica* coccolithophore (Lamy, 2016; Toyos et al., 2020), suggesting either enhanced carbonate preservation or a rise in carbonate export production linked to the MBE (figure 5 of chapter 3). *Gephyrocapsa* coccolithophore oozes have also been recognized at other locations in the Pacific sector of the Southern Ocean (Cores PS75/059, PS75/076, and PS75/076; Gersonde, 2011; Saavedra-Pellitero, 2017a; Saavedra-Pellitero, 2017b). These works have suggested that such increase carbonates could have altered marine carbonate chemistry leading to enhanced outgassing and contributing to the documented rise in atmospheric CO<sub>2</sub> concentrations (Barker et al., 2006; Saavedra-Pellitero, et al., 2017a). Thus, we propose that the Subantarctic SE Pacific sector of the SO might have also contribute in the documented rise in atmospheric CO<sub>2</sub> concentrations.

Except for the extraordinary increase in the accumulation rates of carbonates at our core site, the absence of any other significant change in any of the other productivity indicators after the MBE suggests that the Pacific entrance to the DP did not suffer other modifications linked to this event (figure 5 of chapter 3).



## 6. GENERAL CONCLUSIONS/ CONCLUSIONES

### GENERALES

The research presented in this thesis significantly improved our knowledge of past glacial-interglacial changes in the strength of ACC near-bottom flow and the impact of these changes on the Atlantic MOC, as well as understanding past export production in the subantarctic SE Pacific over the past 1.3 Myr. The thesis focuses on the DP, where the ACC is constricted to its narrowest extent. In contrast to the Atlantic and Indian sectors of the ACC, information on Quaternary paleoceanography from deep-sea records in the DP area are scarce. We generated a new set of data that led us to test the hypotheses and answer the scientific questions exposed in sections 2.1 and 1.5, respectively.

We present a new high-resolution ACC near-bottom current strength reconstruction based on  $\overline{SS}$  data in core PS97/093-2. The generated record shows that at the DP entrance, the  $\overline{SS}$  record varied by ~6–16% on glacial-interglacial timescales, showing a consistent pattern of stronger ACC during interglacials over the past 1.3. Myr. Our results also highlight a weaker ACC during glacial periods due to a northward shift of the SAF accompanied by an expansion the sea-ice zone in the southern sector of the DP, resulting in a glacial weakening of the total DP

throughflow. Therefore, we might infer a glacial decrease in the inflow of CDW into the Atlantic through the DP and a weakening of the cold-water route, altering the global MOC. According to these results, Hypothesis A0 “*At the Drake Passage entrance, the strength of the Antarctic Circumpolar Current does not vary significantly at glacial-interglacial timescales, and therefore, changes in the global Meridional Overturning Circulation originating from the ACC are not expected*” is rejected.

Because of a highly dynamic near-bottom flow of the ACC at glacial-interglacial timescales, lateral redistribution of sediments frequently occurred at our core site. Contrary to expectation, the results presented in this thesis show that winnowing usually happened during glacial periods when ACC flow strength was relatively low whereas increased focusing was concurrent with strengthened near-bottom currents. We postulate that winnowing likely occurred because of a loss of the flocculation and cohesive effects of the fine sediment fraction under relatively slow bottom currents. Stronger flow, on the other hand, probably caused a gradual mobilization of coarse-grained material that had laterally accumulated at our site. As a result of the syndepositional redistribution, this thesis demonstrates that stratigraphy-based mass accumulation rates are strongly biased in core PS97/093-2. Based on the

arguments mentioned above, Hypothesis B0 “*Although the subantarctic Drake Passage is an area of highly dynamic bottom currents, sediment accumulation rates are not influenced by redistribution processes (focusing/winnowing)*” is rejected.

We generated the first paleoproductivity reconstruction for the Pacific entrance of the DP, based on  $^{230}\text{Th}_{\text{xs}}$  normalized mass accumulation rates. We show that during glacial, export production responds to glaciogenic Fe supply from the extensive Patagonian Ice Sheet and silica availability due to northward shifts in oceanic fronts leading to enhanced diatom production. In contrast to the Atlantic and Indian Ocean SAZ, dust, as a source of iron to our core site, plays a minor role. Therefore, Hypothesis C0 “*Dust-borne iron fertilization is the main driver of enhanced export production during glacial times in the subantarctic Drake Passage*” is rejected.

This study also demonstrates that both near-bottom current strength and productivity have responded to the Earth’s major climate changes over the past 1.3 Ma. The generated current strength record shows a dominance of the 41-kyr cycles from 1.3 Ma to the MPT (*ca.* 850 Ka, MIS 21), followed by an increase of the spectral power of the 100-kyr cycles thereafter. The productivity records display increases during the onset of



the MPT (from *ca.* 1.35 to 1.2 Ma), and carbonates show enhanced dissolution since the mid-point of the MPT. Carbonates increase substantially after the MBE, coinciding with the extensive propagation of the *Gephyrocapsa* coccolithophore seen in other areas of the South Pacific. Therefore, the fluctuations in our core were, to some extent, related to global changes, either by contributing to the reorganization of the Earth's internal climate system or as a part of the cascading effects that characterized such events. For the reasons exposed above Hypothesis D0: *“The amplitude and pattern of glacial-interglacial changes in the Antarctic Circumpolar Current strength and export production in the subantarctic Drake Passage have not been influenced by the Earth's major climate changes (Mid-Pleistocene Transition and Mid-Brunhes Event) over the past 1.3 Ma.”* is rejected.

## **7. PERSPECTIVES/ PERSPECTIVAS PARA FUTURAS INVESTIGACIONES**

The results presented in this thesis contribute with new knowledge on Southern Ocean Quaternary paleoceanography and constitute a valuable reference for future paleoclimatic and/or palaeoceanographic research in this remote area of the world. While this thesis was developing, further research challenges and new questions that could not be addressed in the scope of this study arose, for instance:

Current strength fluctuations in the SE Pacific along the southern Chilean coastline are not well constrained since there are remarkably few records (cores MD07-3128 and MR0806-PC09 (Lamy et al., 2015)) that have reconstructed current strength changes there during the past glacial cycles previous to this thesis. Furthermore, the previously published reconstructions are from the southernmost American continental slope (Cape Horn current) and northern DP. This thesis, based on core PS97/093-2 (Toyos et al., 2020), reconstructed ACC flow changes at the entrance of the DP during the past glacial cycles of the past 1.3 Ma. There is still a lack of knowledge of glacial-interglacial changes for the Humboldt Current System and the northern part of the southward flowing Cape Horn Current.

$^{230}\text{Th}_{\text{xs}}$ -normalized mass accumulation rates are considered a valuable paleoceanographic tool and have been widely used in SO cores to reconstruct past changes in export production. Unfortunately, this is not the case for export production reconstructions offshore Chile in the SE Pacific, where there is only one study previous to this thesis that has applied  $^{230}\text{Th}_{\text{xs}}$ -normalized mass accumulation rates (Cores GeoB 7101-1 and GeoB 3375-1; Dezileau et al., 2004). This thesis contributed with new knowledge (Toyos et al., accepted) on the effects of sediment redistribution that have not been taken into account in most of the existing paleoceanographic reconstructions in the SE Pacific. Since the applicability of  $^{230}\text{Th}$  normalization in shallow waters is challenging, to better understand past export production in the region, future work is needed in marine sediment cores recovered at  $\geq 1.000$  m. A first step might be to re-study existing records using the  $^{230}\text{Th}$  isotopes approach.

Additionally, as indicated in Toyos et al. (2020) and Toyos et al. (accepted), respectively, there are still no clear answers for the reduction in current strength observed during MIS 11 and its implications, as well as for the reach of Fe fertilization in the SE Pacific linked to PIS dynamics.

As a result, the following research questions will need to be solved in the future:

How was the ocean circulation in the SE South Pacific and Cape Horn-Humbolt current systems at glacial/interglacial timescales?

Why is the ACC flow weaker at the subantarctic Pacific entrance of the Drake Passage during the exceptionally warm MIS 11? Is this weakening part of an extended pattern in the subantarctic SE Pacific? Did the reduced ACC near-bottom flow permit the increase in coccolith accumulation rates during this time interval along the subantarctic SE Pacific?

How far offshore did the released Fe from the PIS extended and what was the impact on productivity during glacial times? Did the export production increase enough during glacials to be comparable to the Atlantic and Indian sectors of the SO?

The study of further sediment cores along the SE Pacific, parallel and perpendicular to the Chilean coastline, are needed to better constrain the dynamics involved in ocean circulation related to the Cape Horn-Humboldt current systems and the reach of Fe fertilization linked to PIS dynamics during the past glacial/interglacial cycles. Given the complexity of the region and the strong influence of teleconnections, the greatest potential for progress lies in facilitating further cross-disciplinary collaboration instead of compartmentalizing it into specialties.

## 8. REFERENCES/REFERENCIAS

Anderson, R. F., Barker, S., Fleisher, M., Gersonde, R., Goldstein, S. L., Kuhn, G., Mortyn, P. G., Pahnke, K., & Sachs, J. P. (2014). Biological response to millennial variability of dust and nutrient supply in the Subantarctic South Atlantic Ocean. *Philosophical Transactions of the Royal Society A: Mathematical, Physical and Engineering Sciences*, 372(2019). <https://doi.org/10.1098/rsta.2013.0054>

Anderson, R. F., Chase, Z., Fleisher, M. Q., & Sachs, J. (2002). The Southern Ocean's biological pump during the Last Glacial Maximum. *Deep-Sea Research Part II: Topical Studies in Oceanography*, 49(9–10), 1909–1938. [https://doi.org/10.1016/S0967-0645\(02\)00018-8](https://doi.org/10.1016/S0967-0645(02)00018-8)

de Baar, H. J. W., Bathmann, U., Smetacek, V., Löscher, B. M., & Veth, C. (1995). Importance of iron for plankton blooms and carbon dioxide drawdown in the Southern Ocean. *Nature*, 373(6513), pp. 412–415. <https://doi.org/10.1038/373412a0>

Bacon, M. P. (1984). Glacial to interglacial changes in carbonate and clay sedimentation in the Atlantic Ocean estimated from 230Th measurements. *Isotope Geoscience*, 2(2), 97–111.

Barker, P. F. (2001). Scotia Sea regional tectonic evolution: implications for mantle flow and palaeocirculation. *Earth-Science Reviews*, 55(1–2), 1–39. [https://doi.org/10.1016/S0012-8252\(01\)00055-1](https://doi.org/10.1016/S0012-8252(01)00055-1)

Barker, P. F., Filippelli, G. M., Florindo, F., Martin, E. E., & Scher, H. D. (2007). Onset and role of the Antarctic Circumpolar Current. *Deep Sea Research Part II: Topical Studies in Oceanography*, 54(21–22), 2388–2398. <https://doi.org/10.1016/j.dsr2.2007.07.028>

Barker, S., Archer, D., Booth, L., Elderfield, H., Henderiks, J., & Rickaby, R. E. M. (2006). Globally increased pelagic carbonate production during the Mid-Brunhes dissolution interval and the CO<sub>2</sub> paradox of MIS 11. *Quaternary Science Reviews*, 25(23–24), 3278–3293. <https://doi.org/10.1016/j.quascirev.2006.07.018>

Becker, J. J., Sandwell, D. T., Smith, W. H. F., Braud, J., Binder, B., Depner, J., Fabre, D., Factor, J., Ingalls, S., Kim, S.-H., Ladner, R., Marks, K., Nelson, S., Pharaoh, A., Trimmer, R., Von Rosenberg, J., Wallace, G., & Weatherall, P. (2009). Global Bathymetry and Elevation Data at 30 Arc Seconds Resolution: SRTM30\_PLUS. *Marine Geodesy*, 32(4), 355–371. <https://doi.org/10.1080/01490410903297766>

Berger, W. H., Smetacek, V., & Wefer, G. (1989). Ocean Productivity and Paleoproductivity - An Overview. In W. Berger, V. Smetacek, & G. Wefer (Eds.), *Productivity of the Ocean: Present and Past* (Issue January 1989, pp. 1–34). John Wiley & Sons Limited.

Bianchi, G. G., Hall, I. R., McCave, I. N., & Joseph, L. (1999). Measurement of the sortable silt current speed proxy using the Sedigraph 5100 and Coulter Multisizer II: Precision and accuracy. *Sedimentology*, 46, 1001–1014. <https://doi.org/10.1046/j.1365-3091.1999.00256.x>

Bohoyo, F., Larter, R. D., Galindo-Zaldívar, J., Leat, P. T., Maldonado, A., Tate, A. J., Flexas, M. M., Gowland, E. J. M., Arndt, J. E., Dorschel, B., Kim, Y. D., Hong, J. K., López-Martínez, J., Maestro, A., Bermúdez, O., Nitsche, F. O., Livermore, R. A., & Riley, T. R. (2019). Morphological and geological features of Drake Passage, Antarctica, from a new digital bathymetric model. *Journal of Maps*. <https://doi.org/10.1080/17445647.2018.1543618>

Bouttes, N., Swingedouw, D., Roche, D. M., Sanchez-Goni, M. F., & Crosta, X. (2018). Response of the carbon cycle in an intermediate complexity model to the different climate configurations of the last nine interglacials. *Climate of the Past*, 14(2), 239–253. <https://doi.org/10.5194/cp-14-239-2018>

Boyd, P. W., Arrigo, K. R., Strzepek, R., & Van Dijken, G. L. (2012). Mapping phytoplankton iron utilization: Insights into Southern Ocean supply mechanisms. *Journal of Geophysical Research: Oceans*, 117(6), 1–18. <https://doi.org/10.1029/2011JC007726>

Boyd, Philip W. (2002). Environmental factors controlling phytoplankton processes in the Southern Ocean. *Journal of Phycology*, 38(5), 844–861. <https://doi.org/10.1046/j.1529-8817.2002.t01-1-01203.x>

Bradt Miller, L. I., Anderson, R. F., Fleisher, M. Q., & Burckle, L. H. (2009). Comparing glacial and Holocene opal fluxes in the Pacific sector of the Southern Ocean. *Paleoceanography*, 24(2), 1–20. <https://doi.org/10.1029/2008PA001693>

Cárdenas, P., Lange, C. B., Vernet, M., Esper, O., Srain, B., Vorrath, M.-E., Ehrhardt, S., Müller, J., Kuhn, G., Arz, H. W., Lembke-Jene, L., & Lamy, F. (2019). Biogeochemical proxies and diatoms in surface sediments across the Drake Passage reflect oceanic domains and frontal systems in the region. *Progress in Oceanography*, 174, 72–88. <https://doi.org/10.1016/j.pocean.2018.10.004>

Carter, L., & McCave, I. N. (1997). The sedimentary regime beneath the deep western boundary current inflow to the southwest Pacific ocean. *Journal of Sedimentary Research, Section B: Stratigraphy and Global Studies*, 67(6), 1005–1017. <https://doi.org/10.1306/d42686b2-2b26-11d7-8648000102c1865d>

Carter, R. M., McCave, I. N., & Carter, L. (2004). Leg 181 synthesis: Fronts, flows, drifts, volcanoes, and the evolution of the southwestern gateway to the Pacific Ocean, eastern New Zealand. In C. Richter (Ed.), *Proc. ODP, Sci. Results* (Vol. 181, pp. 1–111). College Station, TX: ocean drilling program. <https://doi.org/10.2973/odp.proc.sr.181.210.2004>

Carter, L., McCave, I. N., & Williams, M. J. M. (2008). Chapter 4 Circulation and Water Masses of the Southern Ocean: A Review. In F. Florindo & M. Soegert (Eds.), *Developments in Earth and Environmental Sciences* (Vol. 8, pp. 85–114). Elsevier B.V. [https://doi.org/10.1016/S1571-9197\(08\)00004-9](https://doi.org/10.1016/S1571-9197(08)00004-9)

Chalk, T. B., Hain, M. P., Badger, M. P. S., Martínez-García, A., Sexton, P. F., Hasenfratz, A. P., Jaccard, S. L., Cherry, S. G., Rohling, E. J., & Pälike, H. (2017). Causes of ice age intensification across the Mid-Pleistocene Transition. *Proceedings of the National Academy of Sciences*, 114(50), 13114–13119. <https://doi.org/10.1073/pnas.1702143114>

Channell, J. E. T., Harrison, R. J., Lascu, I., McCave, I. N., Hibbert, F. D., & Austin, W. E. (2016). Magnetic record of deglaciation using FORC-PCA, sortable-silt grain size, and magnetic excursion at 26 ka, from the Rockall Trough (NE Atlantic). *Geochemistry, Geophysics, Geosystems*, *17*(11), 4517–4533. <https://doi.org/10.1002/2015GC006171>.

Chapman, C. C., Lea, M.-A., Meyer, A., Sallée, J.-B., & Hindell, M. (2020). Defining Southern Ocean fronts and their influence on biological and physical processes in a changing climate. *Nature Climate Change*, *10*(3), 209–219. <https://doi.org/10.1038/s41558-020-0705-4>

Chase, Z., Kohfeld, K. E., & Matsumoto, K. (2015). Controls on biogenic silica burial in the Southern Ocean. *Global Biogeochemical Cycles*, *29*(10), 1599–1616. <https://doi.org/10.1002/2015GB005186>

Cheng, H., Lawrence Edwards, R., Shen, C.-C., Polyak, V. J., Asmerom, Y., Woodhead, J., Hellstrom, J., Wang, Y., Kong, X., Spötl, C., Wang, X., & Calvin Alexander, E. (2013). Improvements in <sup>230</sup>Th dating, <sup>230</sup>Th and <sup>234</sup>U half-life values, and U–Th isotopic measurements by multi-collector inductively coupled plasma mass spectrometry. *Earth and Planetary Science Letters*, *371–372*, 82–91. <https://doi.org/10.1016/j.epsl.2013.04.006>

Clark, P. U., Archer, D., Pollard, D., Blum, J. D., Rial, J. A., Brovkin, V., Mix, A. C., Pisias, N. G., & Roy, M. (2006). The middle Pleistocene transition: characteristics, mechanisms, and implications for long-term changes in atmospheric pCO<sub>2</sub>. *Quaternary Science Reviews*, *25*(23–24), 3150–3184. <https://doi.org/10.1016/j.quascirev.2006.07.008>

Comiso, J. C., Cavalieri, D. J., & Markus, T. (2003). Sea ice concentration, ice temperature, and snow depth using AMSR-E data. *IEEE Transactions on Geoscience and Remote Sensing*, *41*(2), 243–252. <https://doi.org/10.1109/TGRS.2002.808317>

Cortese, G., & Gersonde, R. (2008). Plio/Pleistocene changes in the main biogenic silica carrier in the Southern Ocean, Atlantic Sector. *Marine Geology*, *252*(3–4), 100–110. <https://doi.org/10.1016/j.margeo.2008.03.015>



Costa, K. M., Hayes, C. T., Anderson, R. F., Pavia, F. J., Bausch, A., Deng, F., Dutay, J. C., Geibert, W., Heinze, C., Henderson, G., Hillaire-Marcel, C., Hoffmann, S., Jaccard, S. L., Jacobel, A. W., Kienast, S. S., Kipp, L., Lerner, P., Lippold, J., Lund, D., ... Zhou, Y. (2020). 230Th Normalization: New Insights on an Essential Tool for Quantifying Sedimentary Fluxes in the Modern and Quaternary Ocean. *Paleoceanography and Paleoclimatology*, 35(2), 1–36. <https://doi.org/10.1029/2019PA003820>

Davies, B. J., Darvill, C. M., Lovell, H., Bendle, J. M., Dowdeswell, J. A., Fabel, D., García, J.-L., Geiger, A., Glasser, N. F., Gheorghiu, D. M., Harrison, S., Hein, A. S., Kaplan, M. R., Martin, J. R. V., Mendelova, M., Palmer, A., Pelto, M., Rodés, Á., Sagredo, E. A., ... Thorndycraft, V. R. (2020). The evolution of the Patagonian Ice Sheet from 35 ka to the present day (PATICE). *Earth-Science Reviews*, 204, 103152. <https://doi.org/10.1016/j.earscirev.2020.103152>

Deacon, G. (1984). The Antarctic Circumpolar Ocean. Studies in Polar Research Series, viii. In Cambridge University Press. (Ed.), *Geological Magazine* (VIII, Vol. 122, Issue 3, pp. 306–306). <https://doi.org/10.1017/S0016756800031575>

Demidov, A. B., Mosharov, S. A., Gagarin, V. I., & Romanova, N. D. (2011). Spatial variability of the primary production and chlorophyll a concentration in the drake passage in the austral spring. *Oceanology*, 51(2), 281–294. <https://doi.org/10.1134/S0001437011020056>

Deppeler, S. L., & Davidson, A. T. (2017). Southern Ocean phytoplankton in a changing climate. *Frontiers in Marine Science*, 4(FEB). <https://doi.org/10.3389/fmars.2017.00040>

Dezileau, L., Ulloa, O., Hebbeln, D., Lamy, F., Reyss, J.L., & Fontugne, M. (2004). Iron control of past productivity in the coastal upwelling system off the Atacama Desert, Chile. *Paleoceanography*, 19(3). <https://doi.org/10.1029/2004PA001006>

Diester-Haass, L., Billups, K., & Lear, C. (2018). Productivity changes across the mid-Pleistocene climate transition. *Earth-Science*

*Reviews*, 179(July 2017), 372–391.  
<https://doi.org/10.1016/j.earscirev.2018.02.016>

Donohue, K. A., Tracey, K. L., Watts, D. R., Chidichimo, M. P., & Chereskin, T. K. (2016). Mean Antarctic Circumpolar Current transport measured in Drake Passage. *Geophysical Research Letters*, 43(22), 11,760–11,767. <https://doi.org/10.1002/2016GL070319>

Durand, A., Chase, Z., Noble, T. L., Bostock, H., Jaccard, S. L., Kitchener, P., Townsend, A. T., Jansen, N., Kinsley, L., Jacobsen, G., Johnson, S., & Neil, H. (2017). Export production in the New-Zealand region since the Last Glacial Maximum. *Earth and Planetary Science Letters*, 469, 110–122. <https://doi.org/10.1016/j.epsl.2017.03.035>

Dymond, J., Suess, E., & Lyle, M. (1992). Barium in deep sea sediments: A geo-chemical proxy for paleoproductivity: Paleoceanography. *Paleoceanography*, 7, 163–181. <https://doi.org/10.1029/1992PA00181>

Dypvik, H., & Harris, N. B. (2001). Geochemical facies analysis of fine-grained siliciclastics using Th/U, Zr/Rb and (Zr + Rb)/Sr ratios. *Chemical Geology*, 181(1–4), 131–146. [https://doi.org/10.1016/S0009-2541\(01\)00278-9](https://doi.org/10.1016/S0009-2541(01)00278-9)

Elderfield, H., Ferretti, P., Greaves, M., Crowhurst, S. J., McCave, I. N., Hodell, D., & Piotrowski, A. M. (2012). Evolution of Ocean Temperature and Ice Volume Through the Mid-Pleistocene Climate Transition. *Science*, 337, 704–709. <https://doi.org/10.1126/science.1218211>

Farmer, J. R., Goldstein, S. L., Haynes, L. L., Hönisch, B., Kim, J., Pena, L., & Yehudai, M. (2019a). Data constraints on ocean-carbon cycle feedbacks at the mid-Pleistocene transition. *Past Global Changes Magazine*, 27(2). <https://doi.org/10.1002/pag.27.2.62>

Farmer, J. R., Hönisch, B., Haynes, L. L., Kroon, D., Jung, S., Ford, H. L., Raymo, M. E., Jaume-Seguí, M., Bell, D. B., Goldstein, S. L., Pena, L. D., Yehudai, M., & Kim, J. (2019b). Deep Atlantic Ocean carbon

storage and the rise of 100,000-year glacial cycles. *Nature Geoscience*, 12(5), 355–360. <https://doi.org/10.1038/s41561-019-0334-6>

Fitzsimmons, J. N., Boyle, E. A., & Jenkins, W. J. (2014). Distal transport of dissolved hydrothermal iron in the deep South Pacific Ocean. *Proceedings of the National Academy of Sciences*, 111(47), 16654–16661. <https://doi.org/10.1073/pnas.1418778111>

Fleisher, M. Q., & Anderson, R. F. (2003). Assessing the collection efficiency of Ross Sea sediment traps using <sup>230</sup>Th and <sup>231</sup>Pa. *Deep-Sea Research*, 50, 693–712. [https://doi.org/10.1016/S0967-0645\(02\)00591-X](https://doi.org/10.1016/S0967-0645(02)00591-X)

Fralick, P. W., & Kronberg, B. I. (1997). Geochemical discrimination of clastic sedimentary rock sources. *Sedimentary Geology*, 113(1–2), 111–124. [https://doi.org/10.1016/S0037-0738\(97\)00049-3](https://doi.org/10.1016/S0037-0738(97)00049-3)

Francois, R., Frank, M., Rutgers van der Loeff, M. M., & Bacon, M. P. (2004). <sup>230</sup>Th normalization: An essential tool for interpreting sedimentary fluxes during the late Quaternary. *Paleoceanography*, 19(1), PA1018. <https://doi.org/10.1029/2003PA000939>

Frank, M., Gersonde, R., & Mangini, A. (1999). Sediment Redistribution, <sup>230</sup>Thex- Normalization and Implications for the Reconstruction of Particle Flux and Export Paleoproductivity. In *Use of Proxies in Paleoceanography* (pp. 409–426). Springer Berlin Heidelberg. [https://doi.org/10.1007/978-3-642-58646-0\\_16](https://doi.org/10.1007/978-3-642-58646-0_16)

Freeman, N. M., Lovenduski, N. S., Munro, D. R., Krumhardt, K. M., Lindsay, K., Long, M. C., & Maclennan, M. (2018). The Variable and Changing Southern Ocean Silicate Front: Insights From the CESM Large Ensemble. *Global Biogeochemical Cycles*, 32(5), 752–768. <https://doi.org/10.1029/2017GB005816>

Freeman, N. M., Munro, D. R., Sprintall, J., Mazloff, M. R., Purkey, S., Rosso, I., DeRanek, C. A., & Sweeney, C. (2019). The Observed Seasonal Cycle of Macronutrients in Drake Passage: Relationship to Fronts and Utility as a Model Metric. *Journal of Geophysical Research: Oceans*, 124(7), 4763–4783. <https://doi.org/10.1029/2019JC015052>

Frölicher, T. L., Sarmiento, J. L., Paynter, D. J., Dunne, J. P., Krasting, J. P., & Winton, M. (2015). Dominance of the Southern Ocean in Anthropogenic Carbon and Heat Uptake in CMIP5 Models. *Journal of Climate*, 28(2), 862–886. <https://doi.org/10.1175/JCLI-D-14-00117.1>

Geibert, W., Rutgers van der Loeff, M. M., Usbeck, R., Gersonde, R., Kuhn, G., & Seeberg-Elverfeldt, J. (2005). Quantifying the opal belt in the Atlantic and southeast Pacific sector of the Southern Ocean by means of <sup>230</sup>Th normalization. *Global Biogeochemical Cycles*, 19(4). <https://doi.org/10.1029/2005GB002465>

Gersonde, R. (2011). *The expedition of the research vessel “Polarstern” to the polar South Pacific in 2009/2010 (ANT-XXVI/2 - BIPOMAC)* (H. Bornemann; & B. Chiaventone (eds.); Gersonde, Vol. 632). *Berichte zur Polar- und Meeresforschung (Reports on Polar and Marine Research)*, Bremerhaven, Alfred Wegener Institute for Polar and Marine Research. [https://doi.org/10.2312/BzPM\\_0632\\_2011](https://doi.org/10.2312/BzPM_0632_2011)

Glasser, N. F., Jansson, K. N., Harrison, S., & Kleman, J. (2008). The glacial geomorphology and Pleistocene history of South America between 38°S and 56°S. *Quaternary Science Reviews*, 27(3–4), 365–390. <https://doi.org/10.1016/j.quascirev.2007.11.011>

Gordon, A. L. (1975). An Antarctic oceanographic section along 170°E. *Deep-Sea Research and Oceanographic Abstracts*, 22, 357–377. [https://doi.org/10.1016/0011-7471\(75\)90060-1](https://doi.org/10.1016/0011-7471(75)90060-1)

Gordon, A. L. (1986). Interocean Exchange of Thermocline Water. *Journal of Geophysical Research*, 91(C4), 5037–5046. <https://doi.org/10.1063/1.475313>

Gottschalk, J., Hodell, D. A., Skinner, L. C., Crowhurst, S. J., Jaccard, S. L., & Charles, C. (2018). Past Carbonate Preservation Events in the Deep Southeast Atlantic Ocean (Cape Basin) and Their Implications for Atlantic Overturning Dynamics and Marine Carbon Cycling. *Paleoceanography and Paleoclimatology*, 33(6), 643–663. <https://doi.org/10.1029/2018PA003353>

Gouretski, V. V., & Koltermann, K. P. (2004). *The World Ocean Circulation Experiment (WOCE) Global Hydrographic Climatology* (B. BHS (ed.); 35th ed.). <http://rda.ucar.edu/datasets/ds285.4/>

Graham, R. M., De Boer, A. M., van Sebille, E., Kohfeld, K. E., & Schlosser, C. (2015). Inferring source regions and supply mechanisms of iron in the Southern Ocean from satellite chlorophyll data. *Deep-Sea Research Part I: Oceanographic Research Papers*, 104, 9–25. <https://doi.org/10.1016/j.dsr.2015.05.007>

Hall, I. R., McCave, I. N., Shackleton, N. J., Weedon, G. P., & Harris, S. E. (2001). Intensified deep Pacific inflow and ventilation in Pleistocene glacial times. *Nature*, 412(6849), 809–812. <https://doi.org/10.1038/35090552>

Hasenfratz, A. P., Jaccard, S. L., Martínez-García, A., Sigman, D. M., Hodell, D. A., Vance, D., Bernasconi, S. M., Kleiven, H. F., Haumann, F. A., & Haug, G. H. (2019). The residence time of Southern Ocean surface waters and the 100,000-year ice age cycle. *Science*, 363, 1080–1084. <https://doi.org/10.1126/science.aat7067>

Ho, S. L., Mollenhauer, G., Lamy, F., Martínez-García, A., Mohtadi, M., Gersonde, R., Hebbeln, D., Nunez-Ricardo, S., Rosell-Melé, A., & Tiedemann, R. (2012). Sea surface temperature variability in the Pacific sector of the Southern Ocean over the past 700 kyr. *Paleoceanography*, 27(4), PA4202. <https://doi.org/10.1029/2012PA002317>

Hodell, D. A., Charles, C. D., & Ninnemann, U. S. (2000). Comparison of interglacial stages in the South Atlantic sector of the Southern Ocean for the past 450 kyr: Implications for Marine Isotope Stage (MIS) 11. *Global and Planetary Change*, 24(1), 7–26. [https://doi.org/10.1016/S0921-8181\(99\)00069-7](https://doi.org/10.1016/S0921-8181(99)00069-7)

Holden, P. B., Edwards, N. R., Wolff, E. W., Valdes, P. J., & Singarayer, J. S. (2011). The Mid-Brunhes Event and West Antarctic ice sheet stability. *Journal of Quaternary Science*, 26(5), 474–477. <https://doi.org/10.1002/jqs.1525>

Honjo, S. (2004). Particle export and the biological pump in the Southern Ocean. *Antarctic Science*, 16(4), 501–516. <https://doi.org/10.1017/S0954102004002287>

Hopwood, M. J., Carroll, D., Höfer, J., Achterberg, E. P., Meire, L., Le Moigne, F. A. C., Bach, L. T., Eich, C., Sutherland, D. A., & González, H. E. (2019). Highly variable iron content modulates iceberg-ocean fertilisation and potential carbon export. *Nature Communications*, 10(1). <https://doi.org/10.1038/s41467-019-13231-0>

Howard, W. R., & Prell, W. L. (1994). Late Quaternary CaCO<sub>3</sub> production and preservation in the Southern Ocean: Implications for oceanic and atmospheric carbon cycling. *Paleoceanography*, 9(3), 453–482. <https://doi.org/10.1029/93PA03524>

Jaccard, S. L., Hayes, C. T., Martinez-Garcia, A., Hodell, D. A., Anderson, R. F., Sigman, D. M., & Haug, G. H. (2013). Two Modes of Change in Southern Ocean Productivity Over the Past Million Years. *Science*, 339(6126), 1419–1423. <https://doi.org/10.1126/science.1227545>

Jouzel, J., Masson-Delmotte, V., Cattani, O., Dreyfus, G., Falourd, S., Hoffmann, G., Minster, B., Nouet, J., Barnola, J. M., Chappellaz, J., Fischer, H., Gallet, J. C., Johnsen, S., Leuenberger, M., Loulergue, L., Luethi, D., Oerter, H., Parrenin, F., Raisbeck, G., Wolff, E. W. (2007). Orbital and millennial Antarctic climate variability over the past 800,000 years. *Science*, 317(5839), 793–796. <https://doi.org/10.1126/science.1141038>

Kienast, S. S., Winckler, G., Lippold, J., Albani, S., & Mahowald, N. M. (2016). Tracing dust input to the global ocean using thorium isotopes in marine sediments: ThoroMap. *Global Biogeochemical Cycles*, 30(10), 1526–1541. <https://doi.org/10.1002/2016GB005408>

Klunder, M. B., Laan, P., Middag, R., De Baar, H. J. W., & van Ooijen, J. C. (2011). Dissolved iron in the Southern Ocean (Atlantic sector). *Deep Sea Research Part II: Topical Studies in Oceanography*, 58(25–26), 2678–2694. <https://doi.org/10.1016/j.dsr2.2010.10.042>

Koenig, Z., Provost, C., Park, Y., Ferrari, R., & Sennéchaël, N. (2016). Anatomy of the Antarctic Circumpolar Current volume transports through Drake Passage. *Journal of Geophysical Research: Oceans*, *121*(4), 2572–2595. <https://doi.org/10.1002/2015JC011436>

Kohfeld, K. E., Graham, R. M., de Boer, A. M., Sime, L. C., Wolff, E. W., Le Quéré, C., & Bopp, L. (2013). Southern Hemisphere westerly wind changes during the Last Glacial Maximum: Paleo-data synthesis. *Quaternary Science Reviews*, *68*(April 2013), 76–95. <https://doi.org/10.1016/j.quascirev.2013.01.017>

Kohfeld, Karen E., Le Quéré, C., Harrison, S. P., & Anderson, R. F. (2005). Role of marine biology in glacial-interglacial CO<sub>2</sub> cycles. *Science*, *308*(5718), 74–78. <https://doi.org/10.1126/science.1105375>

Kopczynska, E. E., Dehairs, F., Elskens, M., & Wright, S. (2001). Phytoplankton and microzooplankton variability between the Subtropical and Polar Fronts south of Australia: Thriving under regenerative and new production in late summer. *Journal of Geophysical Research: Oceans*, *106*(C12), 31597–31609. <https://doi.org/10.1029/2000JC000278>

Kylander, M. E., Ampel, L., Wohlfarth, B., & Veres, D. (2011). High-resolution X-ray fluorescence core scanning analysis of Les Echets (France) sedimentary sequence: New insights from chemical proxies. *Journal of Quaternary Science*, *26*(1), 109–117. <https://doi.org/10.1002/jqs.1438>

Lambert, F., Delmonte, B., Petit, J. R., Bigler, M., Kaufmann, P. R., Hutterli, M. A., Stocker, T. F., Ruth, U., Steffensen, J. P., & Maggi, V. (2008). Dust - Climate couplings over the past 800,000 years from the EPICA Dome C ice core. *Nature*, *452*(7187), 616–619. <https://doi.org/10.1038/nature06763>

Lamy, F., Gersonde, R., Winckler, G., Esper, O., Jaeschke, A., Kuhn, G., Ullermann, J., Martinez-Garcia, A., Lambert, F., & Kilian, R. (2014). Increased Dust Deposition in the Pacific Southern Ocean During Glacial Periods. *Science*, *343*(6169), 403–407. <https://doi.org/10.1126/science.1245424>

Lamy, Frank. (2016). The expedition PS97 of the research vessel POLARSTERN to the Drake Passage in 2016. In *Reports on Polar and Marine Research*. [https://doi.org/10.2312/BzPM\\_0702\\_2016](https://doi.org/10.2312/BzPM_0702_2016)

Lamy, F., Arz, H. W., Kilian, R., Lange, C. B., Lembke-Jene, L., Wengler, M., Kaiser, J., Baeza-Urrea, O., Hall, I. R., Harada, N., & Tiedemann, R. (2015). Glacial reduction and millennial-scale variations in Drake Passage throughflow. *Proceedings of the National Academy of Sciences of the United States of America*, *112*(44), 13496–13501. <https://doi.org/10.1073/pnas.1509203112>

Lamy, F., Kilian, R., Arz, H. W., Francois, J. P., Kaiser, J., Prange, M., & Steinke, T. (2010). Holocene changes in the position and intensity of the southern westerly wind belt. *Nature Geoscience*, *3*(10), 695–699. <https://doi.org/10.1038/ngeo959>

Lang, N., & Wolff, E. W. (2011). Interglacial and glacial variability from the last 800 ka in marine, ice and terrestrial archives. *Climate of the Past*, *7*(2), 361–380. <https://doi.org/10.5194/cp-7-361-2011>

Lawrence, K. T., Sigman, D. M., Herbert, T. D., Riihimaki, C. A., Bolton, C. T., Martinez-Garcia, A., Rosell-Mele, A., & Haug, G. H. (2013). Time-transgressive North Atlantic productivity changes upon Northern Hemisphere glaciation. *Paleoceanography*, *28*(4), 740–751. <https://doi.org/10.1002/2013PA002546>

Li, F., Ginoux, P., & Ramaswamy, V. (2008). Distribution, transport, and deposition of mineral dust in the Southern Ocean and Antarctica: Contribution of major sources. *Journal of Geophysical Research*, *113*(D10), D10207. <https://doi.org/10.1029/2007JD009190>

Li, F., Ginoux, P., & Ramaswamy, V. (2010). Transport of Patagonian dust to Antarctica. *Journal of Geophysical Research Atmospheres*, *115*(18), 1–9. <https://doi.org/10.1029/2009JD012356>

Lisiecki, L. E., & Raymo, M. E. (2005). A Pliocene-Pleistocene stack of 57 globally distributed benthic  $\delta^{18}\text{O}$  records. *Paleoceanography*, *20*(1). <https://doi.org/10.1029/2004PA001071>



Livermore, R., Nankivell, A., Eagles, G., & Morris, P. (2005). Paleogene opening of Drake Passage. *Earth and Planetary Science Letters*, 236, 459–470. <https://doi.org/10.1016/j.epsl.2005.03.027>

Lynch-Stieglitz, J., Ito, T., & Michel, E. (2016). Antarctic density stratification and the strength of the circumpolar current during the Last Glacial Maximum. *Paleoceanography*, 31(5), 539–552. <https://doi.org/10.1002/2015PA002915>

Mantyla, A. W., & Reid, J. L. (1983). Abyssal characteristics of the World Ocean waters. *Deep-Sea Research*, 30(8). [https://doi.org/https://doi.org/10.1016/0198-0149\(83\)90002-X](https://doi.org/https://doi.org/10.1016/0198-0149(83)90002-X)

Marcantonio, F., Lyle, M., & Ibrahim, R. (2014). Particle sorting during sediment redistribution processes and the effect on <sup>230</sup>Th-normalized mass accumulation rates. *Geophysical Research Letters*, 41(15), 5547–5554. <https://doi.org/10.1002/2014GL060477>

Martínez-García, A., Sigman, D. M., Ren, H., Anderson, R. F., Straub, M., Hodell, D. A., Jaccard, S. L., Eglinton, T. I., & Haug, G. H. (2014). Iron Fertilization of the Subantarctic Ocean During the Last Ice Age. *Science*, 343(6177), 1347–1350. <https://doi.org/10.1126/science.1246848>

Martínez-García, Alfredo, Rosell-Melé, A., Geibert, W., Gersonde, R., Masqué, P., Gaspari, V., & Barbante, C. (2009). Links between iron supply, marine productivity, sea surface temperature, and CO<sub>2</sub> over the last 1.1 Ma. *Paleoceanography*, 24(1), n/a-n/a. <https://doi.org/10.1029/2008PA001657>

Martínez-García, Alfredo, Rosell-Melé, A., Jaccard, S. L., Geibert, W., Sigman, D. M., & Haug, G. H. (2011). Southern Ocean dust-climate coupling over the past four million years. *Nature*, 476(7360), 312–315. <https://doi.org/10.1038/nature10310>

Matsumoto, K., Sarmiento, J. L., & Brzezinski, M. A. (2002). Silicic acid leakage from the Southern Ocean: A possible explanation for

glacial atmospheric p CO<sub>2</sub>. *Global Biogeochemical Cycles*, 16(3), 5-15–23. <https://doi.org/10.1029/2001GB001442>

Mazaud, A., Michel, E., Dewilde, F., & Turon, J. L. (2010). Variations of the Antarctic Circumpolar Current intensity during the past 500 ka. *Geochemistry, Geophysics, Geosystems*, 11(8), 1–10. <https://doi.org/10.1029/2010GC003033>

McCave, I. N., Carter, L., & Hall, I. R. (2008). Glacial–interglacial changes in water mass structure and flow in the SW Pacific Ocean. *Quaternary Science Reviews*, 27(19–20), 1886–1908. <https://doi.org/10.1016/j.quascirev.2008.07.010>

McCave, I. N., Crowhurst, S. J., Kuhn, G., Hillenbrand, C.-D., & Meredith, M. P. (2014). Minimal change in Antarctic Circumpolar Current flow speed between the last glacial and Holocene. *Nature Geoscience*, 7(2), 113–116. <https://doi.org/10.1038/ngeo2037>

McCave, I. N., & Hall, I. R. (2006). Size sorting in marine muds: Processes, pitfalls, and prospects for paleoflow-speed proxies. *Geochemistry, Geophysics, Geosystems*, 7(10). <https://doi.org/10.1029/2006GC001284>

McCave, I. N., Manighetti, B., & Robinson, S. G. (1995). Sortable Silt and Fine Sediment Size/Composition Slicing: Parameters for Paleocurrent Speed and Paleoceanography. *Paleoceanography*, 10(3), 593–610.

McGee, D., Winckler, G., Borunda, A., Serno, S., Anderson, R. F., Recasens, C., Bory, A., Gaiero, D., Jaccard, S. L., Kaplan, M., McManus, J. F., Revel, M., & Sun, Y. (2016). Tracking eolian dust with helium and thorium: Impacts of grain size and provenance. *Geochimica et Cosmochimica Acta*, 175, 47–67. <https://doi.org/10.1016/j.gca.2015.11.023>

Mollenhauer, G., Schneider, R. R., Müller, P. J., Spieß, V., & Wefer, G. (2002). Glacial/interglacial variability in the Benguela upwelling system: Spatial distribution and budgets of organic carbon

accumulation. *Global Biogeochemical Cycles*, 16(4), 81-1-81-15. <https://doi.org/10.1029/2001GB001488>

Moore, C. M., Mills, M. M., Arrigo, K. R., Berman-Frank, I., Bopp, L., Boyd, P. W., Galbraith, E. D., Geider, R. J., Guieu, C., Jaccard, S. L., Jickells, T. D., La Roche, J., Lenton, T. M., Mahowald, N. M., Marañón, E., Marinov, I., Moore, J. K., Nakatsuka, T., Oschlies, A., Ulloa, O. (2013). Processes and patterns of oceanic nutrient limitation. *Nature Geoscience*, 6(9), 701–710. <https://doi.org/10.1038/ngeo1765>

Mortlock, R. A., & Froelich, P. N. (1989). A simple method for the rapid determination of biogenic opal in pelagic marine sediments. *Deep Sea Research Part A, Oceanographic Research Papers*, 36(9), 1415–1426. [https://doi.org/10.1016/0198-0149\(89\)90092-7](https://doi.org/10.1016/0198-0149(89)90092-7)

Nozaki, Y., Horibe, Y., & Tsubota, H. (1981). The water column distributions of thorium isotopes in the western North Pacific. *Earth and Planetary Science Letters*, 54(2), 203–216. [https://doi.org/10.1016/0012-821X\(81\)90004-2](https://doi.org/10.1016/0012-821X(81)90004-2)

Nürnberg, C. C., Bohrmann, G., Schlüter, M., & Frank, M. (1997). Barium accumulation in the Atlantic sector of the Southern Ocean: Results From 190,000-year records. *Paleoceanography*, 12(4), 594–603. <https://doi.org/10.1029/97PA01130>

Orsi, H., Whitworth, T., & Nowlin, W. D. (1995). On the meridional extent and fronts of the Antarctic Circumpolar Current. *Deep Sea Research*, 42(5), 641–673. [https://doi.org/10.1016/0967-0637\(95\)00021-W](https://doi.org/10.1016/0967-0637(95)00021-W)

PAGES, Past Interglacials Working Group of PAGES (2016). Interglacials of the last 800,000years. *Reviews of Geophysics*, 54, 162–219. <https://doi.org/10.1002/2015RG000482>.Received

Palter, J. B., Marinov, I., Sarmiento, J. L., & Gruber, N. (2013). *Large-Scale, Persistent Nutrient Fronts of the World Ocean: Impacts on Biogeochemistry* (pp. 1–38). Springer Berlin Heidelberg. [https://doi.org/10.1007/698\\_2013\\_241](https://doi.org/10.1007/698_2013_241)

Paparazzo, F. E. (2016). Tendencias espaciales y temporales en la distribución de macronutrientes en aguas superficiales del Pasaje Drake. *Ecología Austral*, 26(1), 027–039. <https://doi.org/10.25260/EA.16.26.1.0.142>

Paytan, A.: Ocean Paleoproductivity, in *Encyclopedia of Paleoclimatology and Ancient Environments*. Encyclopedia of Earth Sciences Series., edited by V. Gornitz, pp. 643–651, Springer Netherlands, Dordrecht., 2009.

Pena, L. D., & Goldstein, S. L. (2014). Thermohaline circulation crisis and impacts during the mid-Pleistocene transition. *Science*, 345(6194), 318–322. <https://doi.org/10.1126/science.1249770>

Pfuhl, H. A., & McCave, I. N. (2005). Evidence for late Oligocene establishment of the Antarctic Circumpolar Current. *Earth and Planetary Science Letters*, 235(3–4), 715–728. <https://doi.org/10.1016/j.epsl.2005.04.025>

Pollard, R. T., Lucas, M. I., & Read, J. F. (2002). Physical controls on biogeochemical zonation in the Southern Ocean. *Deep-Sea Research Part II: Topical Studies in Oceanography*, 49(16), 3289–3305. [https://doi.org/10.1016/S0967-0645\(02\)00084-X](https://doi.org/10.1016/S0967-0645(02)00084-X)

Provost, C., Renault, A., Barré, N., Sennéchaël, N., Garçon, V., Sudre, J., & Huhn, O. (2011). Two repeat crossings of Drake Passage in austral summer 2006: Short-term variations and evidence for considerable ventilation of intermediate and deep waters. *Deep Sea Research Part II: Topical Studies in Oceanography*, 58(25–26), 2555–2571.

Rabassa, J., & Clapperton, C. M. (1990). Quaternary glaciations in the southern hemisphere: An overview. *Quaternary Science Reviews*, 9(2–3), 299–304. [https://doi.org/10.1016/0277-3791\(90\)90024-5](https://doi.org/10.1016/0277-3791(90)90024-5)

Rabassa, J. (2008). Late Cenozoic Glaciations in Patagonia and Tierra del Fuego. *Developments in Quaternary Science*, 11, 151–204. [https://doi.org/10.1016/S1571-0866\(07\)10008-7](https://doi.org/10.1016/S1571-0866(07)10008-7)

Rabassa, J., Coronato, A., & Martínez, O. (2011). Late Cenozoic glaciations in Patagonia and Tierra del Fuego: An updated review. *Biological Journal of the Linnean Society*, *103*(2), 316–335. <https://doi.org/10.1111/j.1095-8312.2011.01681.x>

Renault, A., Provost, C., Sennéchaël, N., Barré, N., & Kartavtseff, A. (2011). Two full-depth velocity sections in the Drake Passage in 2006—Transport estimates. *Deep Sea Research Part II: Topical Studies in Oceanography*, *58*(25–26), 2572–2591. <https://doi.org/10.1016/j.dsr2.2011.01.004>

Richter, T. O., van der Gaast, S., Koster, B., Vaars, A., Gieles, R., de Stigter, H. C., De Haas, H., & van Weering, T. C. E. (2006). The Avaatech XRF Core Scanner: technical description and applications to NE Atlantic sediments. *Geological Society, London, Special Publications*, *267*(1), 39–50. <https://doi.org/10.1144/GSL.SP.2006.267.01.03>

Rigual-Hernández, A. S., Trull, T. W., Bray, S. G., Cortina, A., & Armand, L. K. (2015). Latitudinal and temporal distributions of diatom populations in the pelagic waters of the Subantarctic and Polar Frontal zones of the Southern Ocean and their role in the biological pump. *Biogeosciences*, *12*(18), 5309–5337. <https://doi.org/10.5194/bg-12-5309-2015>

Rintoul, R., & Trull, W. (2001). Water mass properties along a north-south hydrographic. *Journal of Geophysical Research*, *106*(C12), 31447–31462.

Rintoul, S. R., & da Silva, C. E. (2019). Antarctic Circumpolar Current. In *Encyclopedia of Ocean Sciences* (Issue May). Elsevier Inc. <https://doi.org/10.1016/b978-0-12-409548-9.11298-9>

Roberts, J., McCave, I. N., McClymont, E. L., Kender, S., Hillenbrand, C.-D., Matano, R., Hodell, D. A., & Peck, V. L. (2017). Deglacial changes in flow and frontal structure through the Drake Passage. *Earth and Planetary Science Letters*, *474*, 397–408. <https://doi.org/10.1016/j.epsl.2017.07.004>

Robinson, R. S., Jones, C. A., Kelly, R. P., Rafter, P., Etourneau, J., & Martinez, P. (2019). A Cool, Nutrient-Enriched Eastern Equatorial Pacific During the Mid-Pleistocene Transition. *Geophysical Research Letters*, 46(4), 2187–2195. <https://doi.org/10.1029/2018GL081315>

Rühs, S., Schwarzkopf, F. U., Speich, S., & Biastoch, A. (2019). Cold vs. warm water route – sources for the upper limb of the Atlantic Meridional Overturning Circulation revisited in a high-resolution ocean model. *Ocean Science*, 15(3), 489–512. <https://doi.org/10.5194/os-15-489-2019>

Saavedra-Pellitero, M., Baumann, K. H., Fuertes, M. Á., Schulz, H., Marcon, Y., Manon Vollmar, N., Flores, J. A., & Lamy, F. (2019). Calcification and latitudinal distribution of extant coccolithophores across the Drake Passage during late austral summer 2016. *Biogeosciences*, 16(19), 3679–3702. <https://doi.org/10.5194/bg-16-3679-2019>

Saavedra-Pellitero, M., Baumann, K. H., Lamy, F., & Köhler, P. (2017a). Coccolithophore variability across Marine Isotope Stage 11 in the Pacific sector of the Southern Ocean and its potential impact on the carbon cycle. *Paleoceanography*, 32(8), 864–880. <https://doi.org/10.1002/2017PA003156>

Saavedra-Pellitero, M., Baumann, K. H., Ullermann, J., & Lamy, F. (2017b). Marine Isotope Stage 11 in the Pacific sector of the Southern Ocean; a coccolithophore perspective. *Quaternary Science Reviews*, 158, 1–14. <https://doi.org/10.1016/j.quascirev.2016.12.020>

Sallée, J. B. (2018). Southern Ocean Warming. *Oceanography*, 31(2), 0–27. <https://doi.org/10.5670/oceanog.2018.215>

Sarmiento, J. L., & Toggweiler, J. R. (1984). A new model for the role of the oceans in determining atmospheric P CO<sub>2</sub>. *Nature*, 308(5960), 621–624. <https://doi.org/10.1038/308621a0>

Schlüter, M., & Rickert, D. (1998). Effect of pH on the measurement of biogenic silica. *Marine Chemistry*, 63(1–2), 81–92. [https://doi.org/10.1016/S0304-4203\(98\)00052-8](https://doi.org/10.1016/S0304-4203(98)00052-8)

Shaw, T. J., Raiswell, R., Hexel, C. R., Vu, H. P., Moore, W. S., Dudgeon, R., & Smith, K. L. (2011). Input, composition, and potential impact of terrigenous material from free-drifting icebergs in the Weddell Sea. *Deep-Sea Research Part II: Topical Studies in Oceanography*, 58(11–12), 1376–1383. <https://doi.org/10.1016/j.dsr2.2010.11.012>

Shi, J. R., Talley, L. D., Xie, S. P., Peng, Q., & Liu, W. (2021). Ocean warming and accelerating Southern Ocean zonal flow. *Nature Climate Change*, 11(12), 1090–1097. <https://doi.org/10.1038/s41558-021-01212-5>

Shoenfelt, E. M., Sun, J., Winckler, G., Kaplan, M. R., Borunda, A. L., Farrell, K. R., Moreno, P. I., Gaiero, D. M., Recasens, C., Sambrotto, R. N., & Bostick, B. C. (2017). High particulate iron(II) content in glacially sourced dusts enhances productivity of a model diatom. *Science Advances*, 3(6), e1700314. <https://doi.org/10.1126/sciadv.1700314>

Shoenfelt, E. M., Winckler, G., Annett, A. L., Hendry, K. R., & Bostick, B. C. (2019). Physical Weathering Intensity Controls Bioavailable Primary Iron(II) Silicate Content in Major Global Dust Sources. *Geophysical Research Letters*, 46(19), 10854–10864. <https://doi.org/10.1029/2019GL084180>

Shoenfelt, E. M., Winckler, G., Lamy, F., Anderson, R. F., & Bostick, B. C. (2018). Highly bioavailable dust-borne iron delivered to the Southern Ocean during glacial periods. *Proceedings of the National Academy of Sciences of the United States of America*, 115(44), 11180–11185. <https://doi.org/10.1073/pnas.1809755115>

Singer, B. S., Ackert, R. P., & Guillou, H. (2004).  $^{40}\text{Ar}/^{39}\text{Ar}$  and K-Ar chronology of Pleistocene glaciations in Patagonia. *Bulletin of the Geological Society of America*, 116(3–4), 434–450. <https://doi.org/10.1130/B25177.1>

Sokolov, S., & Rintoul, S. R. (2009). Circumpolar structure and distribution of the antarctic circumpolar current fronts: 2. Variability and relationship to sea surface height. *Journal of Geophysical Research: Oceans*, 114(11), 1–15. <https://doi.org/10.1029/2008JC005248>

Sprenk, D., Weber, E. M., Kuhn, G., Rosén, P., Frank, M., Molina-Kescher, M., Liebetrau, V., & Röhling, H. G. (2013). Southern Ocean bioproductivity during the last glacial cycle - New detection method and decadal-scale insight from the Scotia Sea. *Geological Society Special Publication*, 381(1), 245–261. <https://doi.org/10.1144/SP381.17>

Strub, P. T., James, C., Montecino, V., Rutllant, J. A., & Blanco, J. L. (2019). Ocean circulation along the southern Chile transition region (38°–46°S): Mean, seasonal and interannual variability, with a focus on 2014–2016. *Progress in Oceanography*, 172(May 2018), 159–198. <https://doi.org/10.1016/j.pocean.2019.01.004>

Studer, A. S., Sigman, D. M., Martínez-García, A., Benz, V., Winckler, G., Kuhn, G., Esper, O., Lamy, F., Jaccard, S. L., Wacker, L., Oleynik, S., Gersonde, R., & Haug, G. H. (2015). Antarctic Zone nutrient conditions during the last two glacial cycles. *Paleoceanography*, 30(7), 845–862. <https://doi.org/10.1002/2014PA002745>

Suman, D. O., & Bacon, M. P. (1989). Variations in Holocene sedimentation in the North American Basin determined from 230Th measurements. *Deep Sea Research Part A, Oceanographic Research Papers*, 36(6), 869–878. [https://doi.org/10.1016/0198-0149\(89\)90033-2](https://doi.org/10.1016/0198-0149(89)90033-2)

Thöle, L. M., Amsler, H. E., Moretti, S., Auderset, A., Gilgannon, J., Lippold, J., Vogel, H., Crosta, X., Mazaud, A., Michel, E., Martínez-García, A., & Jaccard, S. L. (2019). Glacial-interglacial dust and export production records from the Southern Indian Ocean. *Earth and Planetary Science Letters*, 525. <https://doi.org/10.1016/j.epsl.2019.115716>

Toggweiler, J. R., Russell, J. L., & Carson, S. R. (2006). Midlatitude westerlies, atmospheric CO<sub>2</sub>, and climate change during the ice ages. *Paleoceanography*, 21(2), 1–15. <https://doi.org/10.1029/2005PA001154>

Toyos, M. H., Lamy, F., Lange, C. B., Lembke-Jene, L., Saavedra-Pellitero, M., Esper, O., & Arz, H. W. (2020). Antarctic Circumpolar Current Dynamics at the Pacific Entrance to the Drake Passage Over the



Past 1.3 Million Years. *Paleoceanography and Paleoclimatology*, 35(7), 1–20. <https://doi.org/10.1029/2019PA003773>

Toyos, M. H., Winckler, G., Arz, H. W., Lembke-Jene, L., Lange, C. B., Kuhn, G., & Lamy, F. (2021). Variations in export production, lithogenic sediment transport and iron fertilization in the Pacific sector of the Drake Passage over the past 400 ka. *Climate of the Past Discussions*, 2021, 1–37. <https://doi.org/10.5194/cp-2021-85>

Tréguer, P., & Jacques, G. (1992). Dynamics of nutrients and phytoplankton, and fluxes of carbon, nitrogen and silicon in the Antarctic Ocean. *Polar Biology*, 12(2), 149–162. <https://doi.org/10.1007/BF00238255>

Turekian, K. K., & Wedepohl, K. H. (1961). Distribution of the Elements in Some Major Units of the Earth's Crust. *GSA Bulletin*, 72(2), 175–192. [https://doi.org/10.1130/0016-7606\(1961\)72](https://doi.org/10.1130/0016-7606(1961)72)

Venables, H., & Moore, C. M. (2010). Phytoplankton and light limitation in the Southern Ocean: Learning from high-nutrient, high-chlorophyll areas. *Journal of Geophysical Research*, 115(C02015). <https://doi.org/10.1029/2009JC005361>

Venz, K. A., & Hodell, D. A. (2002). New evidence for changes in Plio-Pleistocene deep water circulation from Southern Ocean ODP Leg 177 Site 1090. *Palaeogeography, Palaeoclimatology, Palaeoecology*, 182(3–4), 197–220. [https://doi.org/10.1016/S0031-0182\(01\)00496-5](https://doi.org/10.1016/S0031-0182(01)00496-5)

Völker, C., & Köhler, P. (2013). Responses of ocean circulation and carbon cycle to changes in the position of the Southern Hemisphere westerlies at Last Glacial Maximum. *Paleoceanography*, 28(4), 726–739. <https://doi.org/10.1002/2013PA002556>

Wadham, J. L., Hawkings, J. R., Tarasov, L., Gregoire, L. J., Spencer, R. G. M., Gutjahr, M., Ridgwell, A., & Kohfeld, K. E. (2019). Ice sheets matter for the global carbon cycle. *Nature Communications*, 10(1). <https://doi.org/10.1038/s41467-019-11394-4>

Wengler, M., Lamy, F., Struve, T., Borunda, A., Böning, P., Geibert, W., Kuhn, G., Pahnke, K., Roberts, J., Tiedemann, R., & Winckler, G. (2019). A geochemical approach to reconstruct modern dust fluxes and sources to the South Pacific. *Geochimica et Cosmochimica Acta*, 264, 205–223. <https://doi.org/10.1016/j.gca.2019.08.024>

Whitworth, T. I. (1988). The Antarctic Circumpolar Current. *Oceanus*, 31(2), 53–58.

Winckler, G., Anderson, R. F., Jaccard, S. L., & Marcantonio, F. (2016). Ocean dynamics, not dust, have controlled equatorial Pacific productivity over the past 500,000 years. *Proceedings of the National Academy of Sciences of the United States of America*, 113(22), 6119–6124. <https://doi.org/10.1073/pnas.1600616113>

Wu, L., Wilson, D. J., Wang, R., Yin, X., Chen, Z., Xiao, W., & Huang, M. (2020). Evaluating Zr/Rb Ratio From XRF Scanning as an Indicator of Grain-Size Variations of Glaciomarine Sediments in the Southern Ocean. *Geochemistry, Geophysics, Geosystems*, 21(11). <https://doi.org/10.1029/2020GC009350>

Wu, S.-Y., & Hou, S. (2017). Impact of icebergs on net primary productivity in the Southern Ocean. *The Cryosphere*, 11(2), 707–722. <https://doi.org/10.5194/tc-11-707-2017>

Wu, S., Kuhn, G., Diekmann, B., Lembke-Jene, L., Tiedemann, R., Zheng, X., Ehrhardt, S., Arz, H. W., & Lamy, F. (2019). Surface sediment characteristics related to provenance and ocean circulation in the Drake Passage sector of the Southern Ocean. *Deep Sea Research Part I: Oceanographic Research Papers*, 154(December), 103135. <https://doi.org/10.1016/j.dsr.2019.103135>

Wu, S., Lembke-Jene, L., Lamy, F., Arz, H. W., Nowaczyk, N., Xiao, W., Zhang, X., Hass, H. C., Titschack, J., Zheng, X., Liu, J., Dumm, L., Diekmann, B., Nürnberg, D., Tiedemann, R., & Kuhn, G. (2021). Orbital- and millennial-scale Antarctic Circumpolar Current variability in Drake Passage over the past 140,000 years. *Nature Communications*, 12(1), 3948. <https://doi.org/10.1038/s41467-021-24264-9>

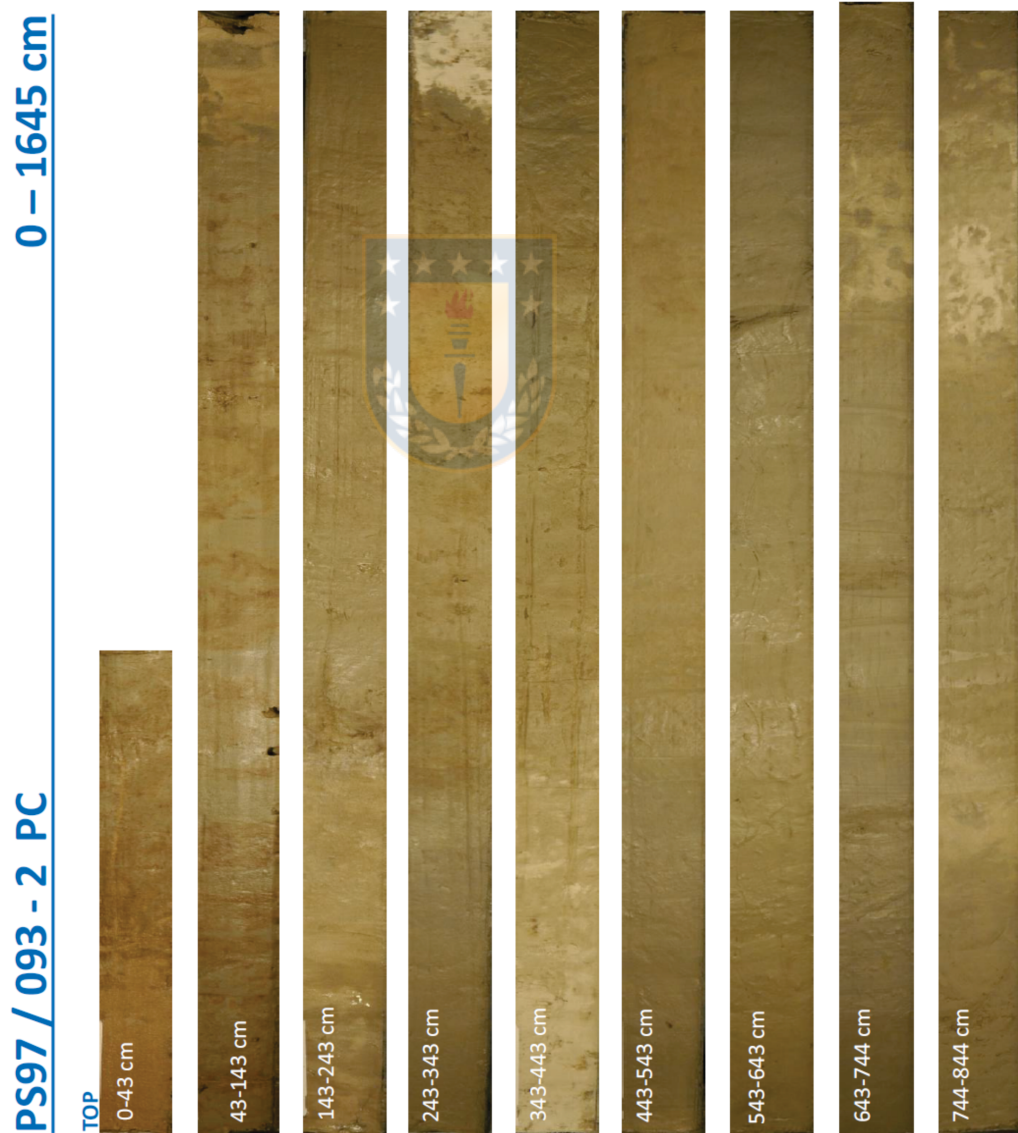
Yin, Q. Z., & Berger, A. (2012). Individual contribution of insolation and CO<sub>2</sub> to the interglacial climates of the past 800,000 years. *Climate Dynamics*, 38(3–4), 709–724. <https://doi.org/10.1007/s00382-011-1013-5>

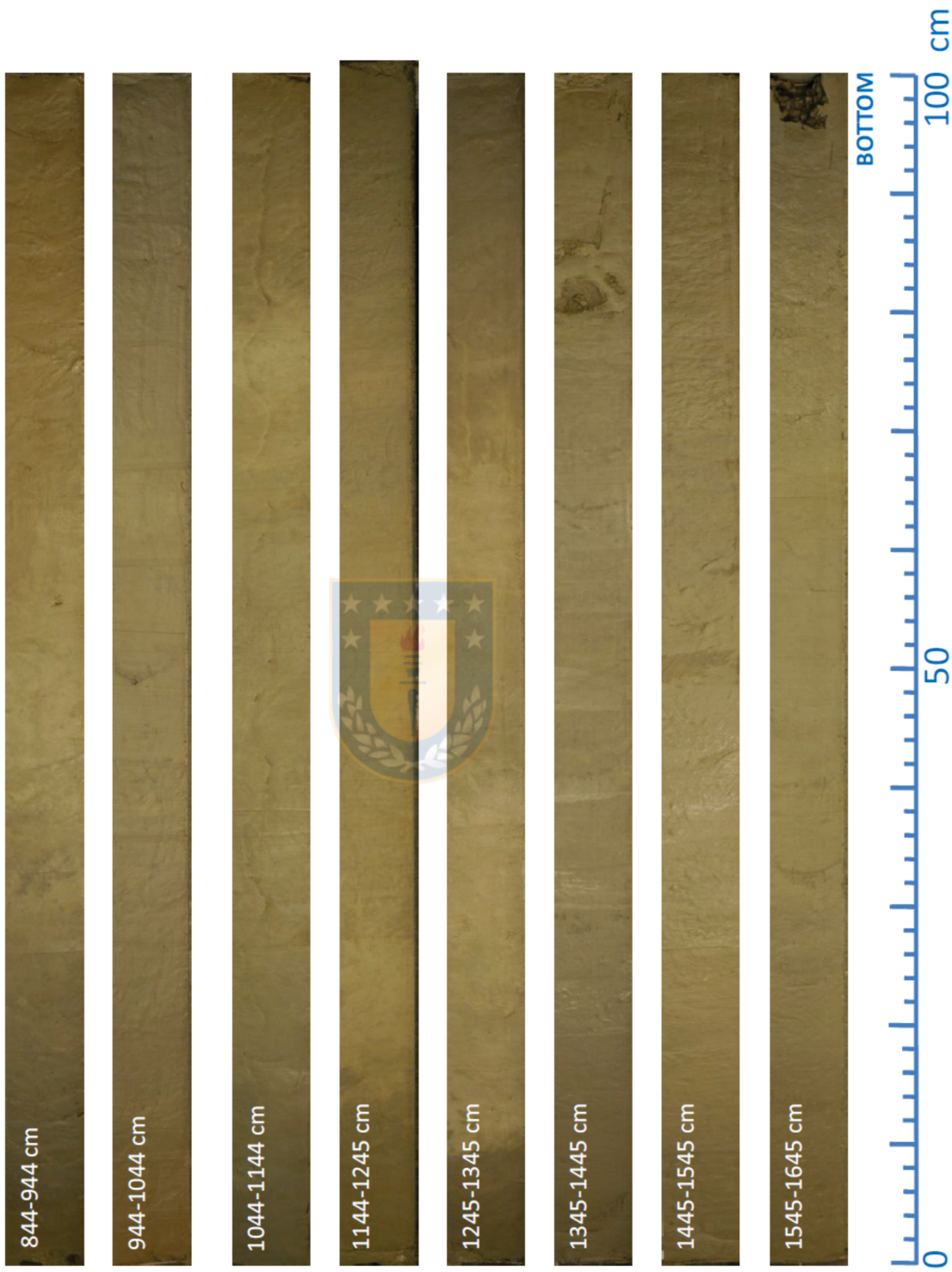


## 9. APPENDICES/ANEXOS

### A.1. Core photos

Photos of core PS97/093-2 were taken from the Appendix A.5 of the PS97 Cruise Report (Lamy, 2016).

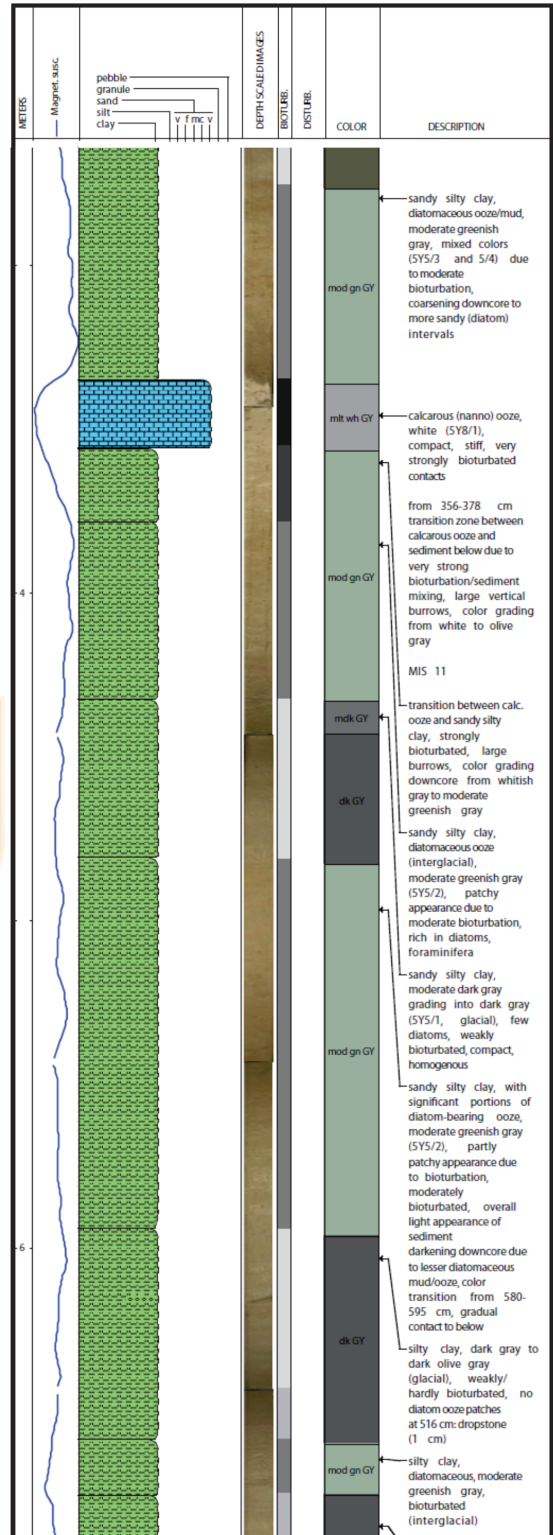
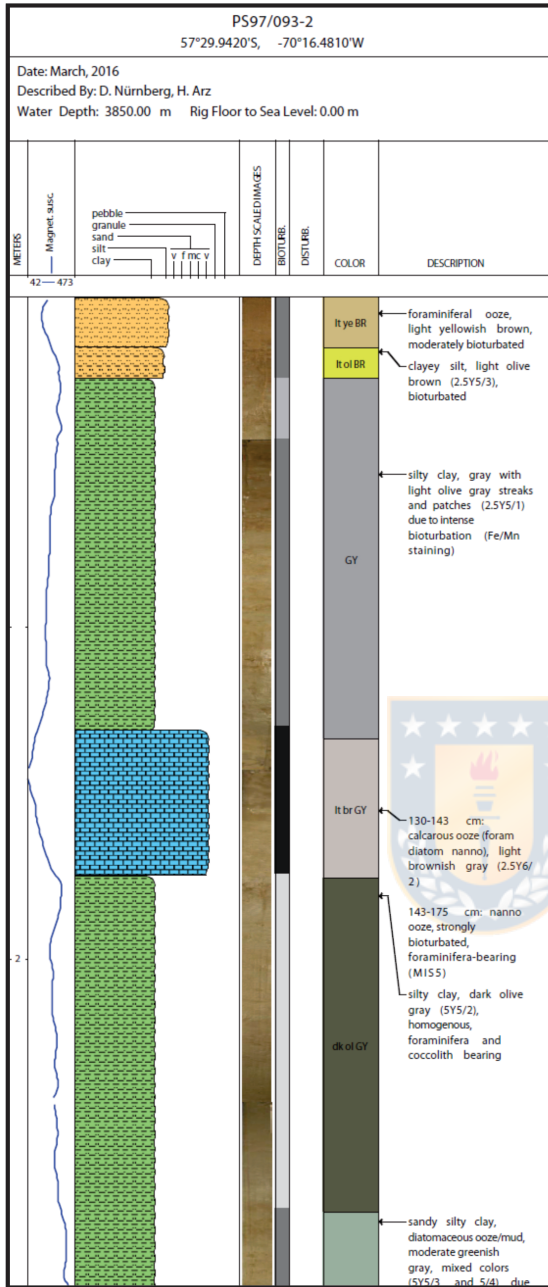




## **A.2. Onboard core description**

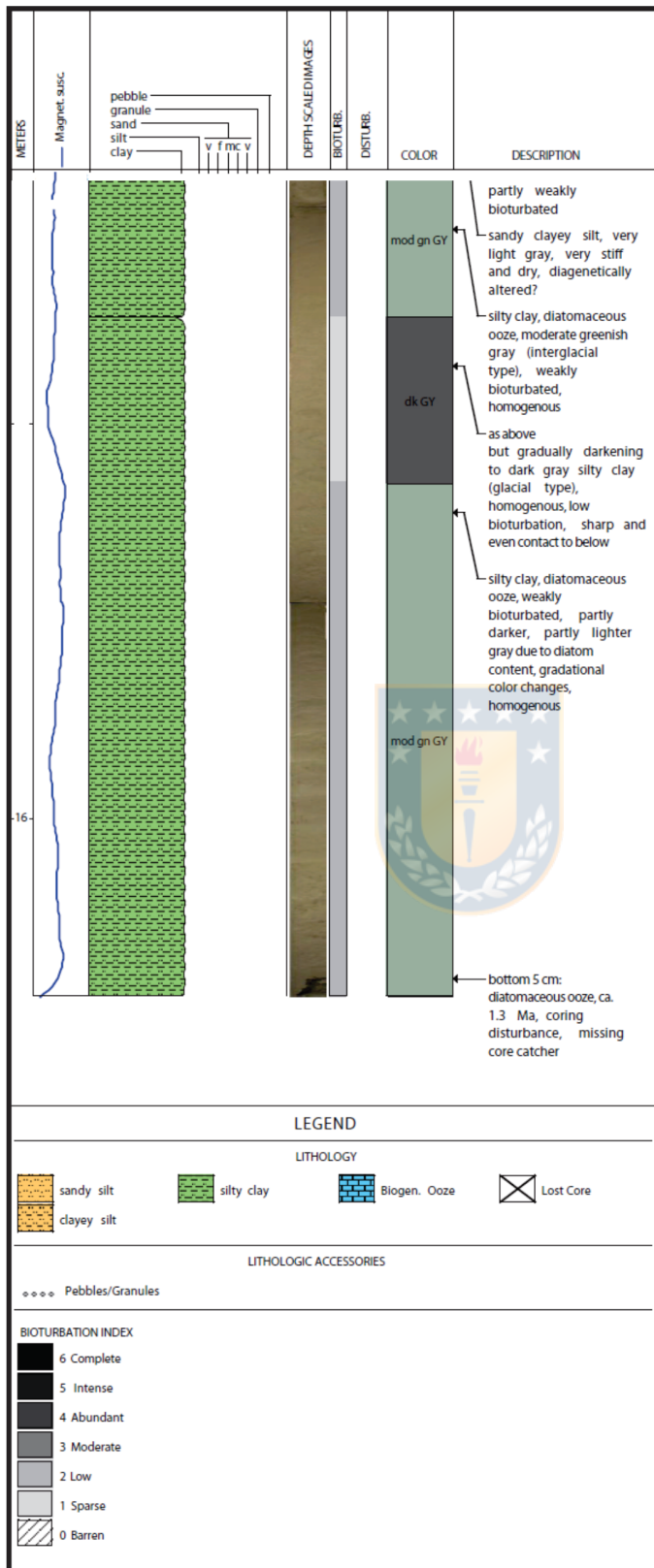
The description of core PS97/093-2 was taken from the Appendix A.6 of the PS97 Cruise Report (Lamy, 2016).

“Sediment core PS97/093-2 typically consists of a recurring sequence of distinct lithologies: At the base of such a sequence, a whitish gray calcareous ooze is developed, which is pervasive of coccoliths and planktonic foraminifera with only minor portions of diatoms. In parts, the calcareous ooze develops into a pure, white nannofossil ooze, which is compact, stiff, and difficult to cut. The nannofossil ooze is only 20 cm thick. Either, the commonly strongly bioturbated calcareous (nannofossil) ooze changes rapidly into a weakly bioturbated dark clay void of biogenic components, or a transitional diatomaceous fine-grained sediment of various thickness is intercalated. The dark gray clay gradually changes into a diatomaceous silt, which is moderately bioturbated and clearly more greenish gray. Subsequently, calcareous ooze is deposited again, with the transition zone to the sediment below being very strongly bioturbated. The calcareous oozes are clearly reflected in the magnetic susceptibility records by minimum values. In core PS97/93-2, we observe ~10 well-define calcareous oozes.” (Lamy, 2016, pp. 48).



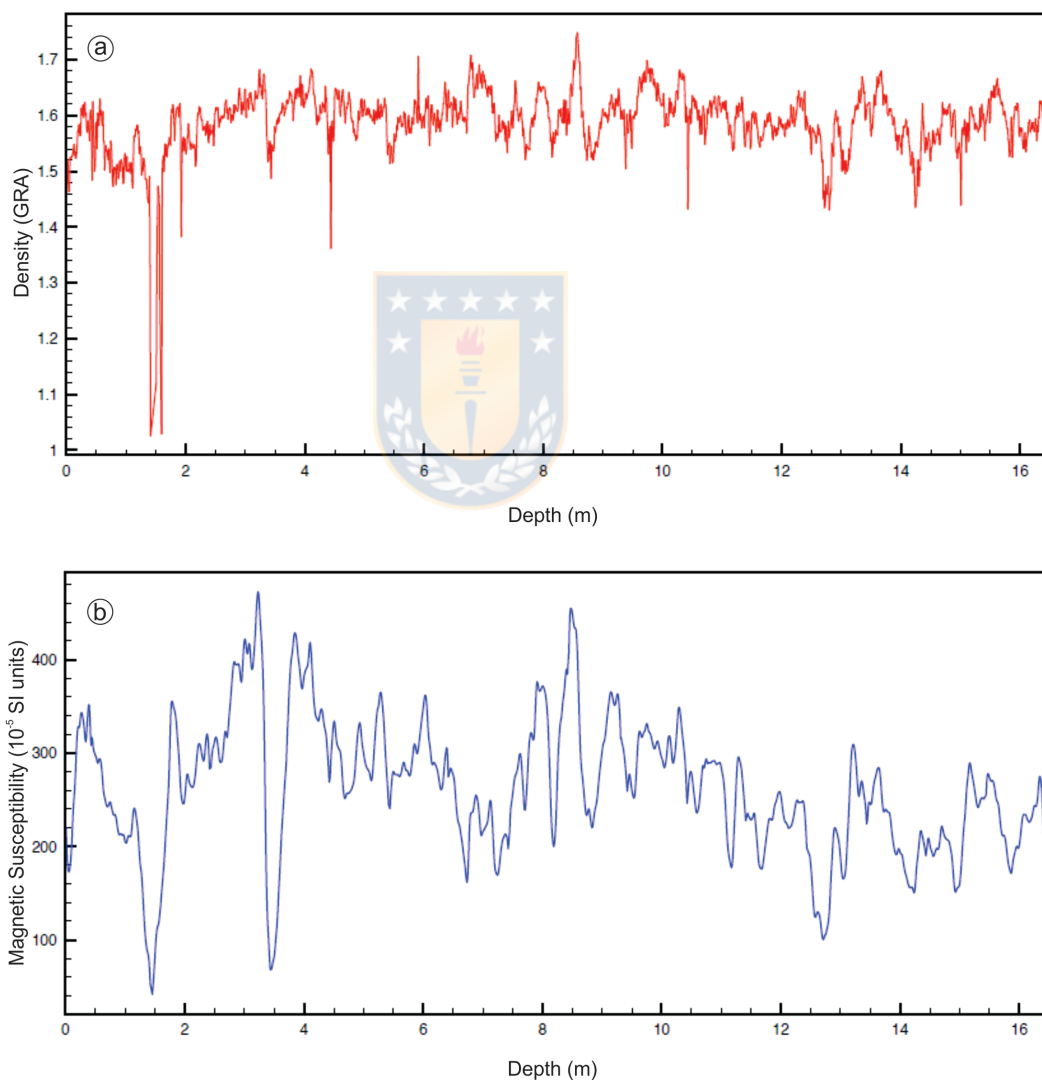






### A.3. Onboard physical properties

Physical properties (wet bulk density and magnetic susceptibility) of core PS97/093-2 were taken from the Appendix A.9 of the PS97 Cruise Report (Lamy, 2016).



**Appendix A.3** Physical properties measured onboard of core PS97/093-2. (a) Wet bulk density record; (b) Magnetic susceptibility record.